Thermal Diffusion of Dopants in Silicon Carbide

by

Balapuwaduge Suwan Pathum Mendis

A dissertation submitted to the Graduate Faculty of
Auburn University
in partial fulfillment of the
requirements for the Degree of
Doctor of Philosophy

Auburn, Alabama
August 4, 2012

Keywords: SiC, Thermal diffusion, Phosphorus, Ohmic contacts
Specific contact resistance

Copyright 2012 by Balapuwaduge Suwan Pathum Mendis

Approved by

Chin-Che Tin, Chair, Professor of Physics
Jianjun Dong, Professor of Physics
Michael J Bozack, Professor of Physics
Barton C Prorok, Associate Professor of Materials Engineering

Abstract

Despite considerable advancement in SiC material and device technology, there are still vital issues to be resolved such as metallization and doping. In SiC, ohmic contacts require high concentration doping. Commonly used doping methods in SiC device processing include *in-situ* doping during epitaxial growth, thermal diffusion, and ion implantation. These methods require specialized equipment and elaborate processing protocols involving high temperature annealing in excess of 1900 K. High temperature processes are detrimental to the material and device performance. Therefore, a low temperature process is needed.

The successful development of a low temperature technique called vacancy assisted impurity doping (VAID) is presented. The objective of VAID is to create vacancies, or vacancy injection, at the surface to allow impurities to diffuse more easily into the surface region. The implementation of this technique using phosphorus for n-type doping of SiC will be described. Phosphorus is an important n-type dopant for both silicon and silicon carbide. While solid-state diffusion of phosphorus in silicon is an experimentally proven method, solid-state diffusion of phosphorus in silicon carbide is relatively unproven, especially at lower temperatures. When subjected to favorable thermodynamic conditions, the presence of metal oxides in contact with SiC can lead to the introduction of impurities in to SiC at optimal temperature annealing. A detailed thermodynamic study confirmed the possibility of phosphorus and boron diffusion in silicon carbide using phosphorus oxide and boron oxide as sources of phosphorus and boron dopants.

Another variation of the VAID technique is to use the formation of silicides to assist in the vacancy creation process. Ternary phase diagrams of stability have been used to study nickel as a potential catalyst for the process. In this study, a silcidation assisted doping process has been described using nickel.

Experimental results show successful phosphorus impurity incorporation and activation in 4H-SiC at temperatures below 1400°C. Phosphorus was incorporated in SiC at temperatures as low as 900°C using the silicidation assisted VAID technique, which is significant progress in thermal diffusion in SiC. SIMS results are presented, showing dopant concentrations in the range of 10^{19} cm^{-3} while EDX analyses have also confirmed the presence of phosphorus. Specific contact resistivity values in the range of 10^{-5} ~ 10^{-6} Ωcm^2 resulted from $Ni_{93\%}V_{7\%}$ contacts to phosphorus doped 4H-SiC.

A different variation of the VAID process that uses silicidation of metal without oxidation was demonstrated. Electroless nickel plating was investigated as an ohmic contact to n-type 4H-SiC. Electroless nickel film contains 5-14% phosphorus by weight. Due to its high concentration of phosphorus atoms, electroless nickel can be a useful and convenient source of phosphorus dopant in the fabrication of n-type ohmic contact for SiC. Specific contact resistivity on lightly-doped samples with carrier concentration of 2.5×10^{16} cm^{-3} is 5.3×10^{-6} Ωcm^2 without any need for ion implantation. This metallization technique is especially useful in broad area ohmic contact formation on the highly doped layer at the back of an n-type SiC substrate.

Acknowledgments

I would like to express my deepest appreciation to my supervisor, Dr. Chin-Che Tin, for his guidance and support throughout the last five years. Without his patience, wisdom and persistence, it would not have been possible for me to succeed in this program. I am also grateful to Dr. Michael Bozack, Dr. Jianjun Dong, and Dr. Bart Prorok for agreeing to serve on my dissertation committee and for evaluating this work. I would like to thank Dr. Michael Miller for agreeing to be the university reader for my dissertation. I am also grateful to Dr. Prorok and Dr. Miller for their guidance in helping me obtain the EDX spectra, and Dr. Bozack for his assistance with AES profiles.

I would also like to thank Dr. Claude Ahyi for training me in standard microfabrication processes and for our numerous insightful discussions. I would also like to express my thanks to Michelle Tin and Erika Crandall for their assistance in the summer of 2011. I also appreciate Mrs. Tamara Isaac-Smith for her assistance in providing the RBS analyses and Mr. Max Cichon for his contribution in building and maintaining the essential equipment.

I would like to express my sincerest thanks to my wife, Kanchana, for her support and understanding throughout my time at Auburn University. I would also like to thank my daughter Saneli, and my parents Pemsiri and Premila for their support, patience and encouragement during the compilation of this manuscript. Finally, I thank God for giving me guidance.

Table of Contents

Abstract ... ii

Acknowledgments ... iv

List of Tables ... ix

List of Figures ... xi

Chapter 1 Introduction ... 1

1.1 Background ... 1

1.2 Properties of Silicon Carbide ... 2

1.2.1 Structures ... 2

1.2.2 Properties ... 5

1.2.3 Crystal Growth ... 7

1.2.4 Devices and Application ... 8

1.3 Objectives and Scope of this Thesis ... 11

1.4 References ... 13

Chapter 2 Metal Semiconductor Contacts ... 16

2.1 Schottky Contacts ... 18

2.2 Ohmic Contacts ... 21

2.2.1 Ohmic Contacts to n-type 4H Silicon Carbide ... 27

2.2.2 Ohmic Contacts to p-type 4H Silicon Carbide ... 30

2.3 References ... 31

Chapter 3 Analytical Techniques 34
3.1 Electrical Characterization 34
3.1.1 Linear Transmission Line Method 34
3.1.2 C-V Measurements 42
3.2 Physical Analysis 44
3.2.1 Electron Dispersive X-ray Spectroscopy 44
3.2.2 Secondary Ion Mass Spectrometry 49
3.2.3 Rutherford Backscattering Spectrometry 54
3.3 References 58
Chapter 4 Diffusion and Doping in SiC 61
4.1 Diffusion in Semiconductors 61
4.1.1 Mathematical Basis 61
4.1.2 Diffusion Mechanisms 66
4.2 Defects in Silicon Carbide 71
4.3 Current Doping Techniques 76
4.3.1 Doping by Ion Implantation 76
4.3.2 Doping by Thermal Diffusion 83
4.3.3 In-situ Doping During Crystal Growth 87
4.3.4 Laser Doping 90
4.4 References 92
Chapter 5 Vacancy Assisted Impurity Doping (VAID) 96
5.1 VAID Technique 96
5.2 Thermodynamic Basis for VAID 100

5.2.1 Free Energy Calculations 100
5.2.2 Ternary Phase Diagrams of Stability 111
5.3 Dopant Sources for the VAID technique 121
5.3.1 Phosphorus and Boron 121
5.3.2 Electroless Plating 127
5.4 References 128
Chapter 6 Basic Experimental Methods 131
6.1 Standard Procedures 131
6.1.1 Sample Cleaning 131
6.1.2 Photolithography 133
6.1.3 Metal Sputter Deposition 135
6.1.4 Thermal Evaporation 137
6.1.5 Thermal Annealing 139
6.1.5.1 Alumina Furnace 139
6.1.5.1.1 VAID Process 139
6.1.5.1.2 Electroless Nickel Plating 143
6.1.5.2 Vacuum Annealing 145
6.1.5.2.1 Contact Annealing 146
6.1.5.2.2 Dopant Activation 146
6.1.6 Reactive Ion Etching 146
6.1.7 Ohmic Contact Fabrication for LTLM 148
6.1.8 Schottky Contact Fabrication for CV Measurements 148
6.2 References 150

Chapter 7 Results and Discussion 152

7.1 VAID Process 152

7.1.1 Schottky Barrier Diodes on n^-/n^+ 4H-SiC 152

7.1.2 SIMS Profiles 157

7.1.3 Activation of N Implants Using VAID 159

7.1.4 Ohmic Contact Characterization 164

7.2 Silicidation Assisted Impurity Doping 172

7.2.1 Schottky Barrier Diodes on n^-/n^+ 4H-SiC 172

7.2.2 SIMS Profile and RBS Spectra 178

7.2.3 Activation of N Implants Using Silicidation Assisted Impurity Doping 183

7.2.4 Ohmic Contact Characterization 188

7.3 Electroless Nickel Plating for Ohmic Contacts 196

7.4 References 202

Chapter 8 Conclusions and Future Work 203

8.1 Conclusions 203

8.2 Future Work 205

8.3 References 205

List of Tables

1.1. Structural characteristics of common SiC polytypes 5

1.2. Comparison of important electronic properties of semiconductors 6

2.1. Work function dependence of MS contacts 17

2.2. Work function and calculated barrier heights for selected metals 21

2.3. Ohmic contacts to n-type α-SiC and reported ρ_c values 29

2.4. Ohmic contacts to p-type α-SiC and reported ρ_c values 31

5.1. Gibbs free energies for 5.31-5.34 at 1200 K 116

5.2. Gibbs free energies for 5.35-5.39 at 1200 K 118

7.1. Atomic percentages of elements in the SBD sample obtained using EDX 155

7.2. R_c, R_{sh} and ρ_c values for ohmic anneal at 1000°C 160

7.3. R_c, R_{sh} and ρ_c values for ohmic anneal at 1100°C 162

7.4. R_c, R_{sh} and ρ_c values for ohmic anneal at 1200°C 164

7.5. Atomic percentages of elements obtained using EDX 166

7.6. R_c, R_{sh} and ρ_c values for the sample (a) annealed at 1300°C in oxygen (b) annealed at 1400°C in oxygen 168

7.7. Atomic percentages of elements in the SBD sample obtained using EDX for the sample (a) with nickel annealed at 650°C (b) with nickel annealed at 800°C 176

7.8. R_c, R_{sh} and ρ_c values for ohmic anneal at 1000°C 184

7.9. R_c, R_{sh} and ρ_c values for the 1100°C ohmic anneal 186

7.10. R_c, R_{sh} and ρ_c values for the 1200°C ohmic anneal 188

7.11. Atomic percentages of elements obtained using EDX for the sample............................ 189

7.12. R_c, R_{sh} and ρ_c values for the sample (a) activated at 1400°C in argon (b) activated at 1500°C in argon 192

7.13. Surface composition of the 4H-SiC sample, as-plated and after anneal.......................... 197

7.14. R_c, R_{sh} and ρ_c values for the sample (a) annealed at 1000°C (b) annealed at 1100°C 201

List of Figures

1.1. Tetrahedral structure of a carbon atom with the four nearest neighboring silicon atoms.... 3

1.2. The structure and stacking sequence of 3C, 4H and 6H-SiC.. 4

1.3. Basic structure of a MOSFET.. 9

1.4. Basic Structure of a SiC photodiode 10

2.1. I-V characteristics of Schottky and ohmic contacts.. 17

2.2. Energy band diagram of a metal and semiconductor (a) in close proximity and (b) in contact 19

2.3. (a) n-type semiconductor in close proximity to a metal (b) MS contact 23

2.4. (a) p-type semiconductor in close proximity to a metal (b) MS contact 24

3.1. (a) Top view of the LTLM contacts (b) Cross-sectional view of the semiconductor with LTLM contact 35

3.2. TLM resistive network.. 37

3.3. (a) Typical LTLM pattern (b) Plot of total resistance (R_T) vs gap length (L) 41

3.4. (a) top view of C-V pattern (b) Cross-sectional view of C-V measurement sample.......... 44

3.5. Cross-sectional view of the EDX analysis area 47

3.6. Schematic of an EDX system 48

3.7. Si(Li) crystal detector 49

3.8. Schematic of the ion bombardment process 50

3.9. Schematic diagram of the Mattauch-Herzog magnetic sector instrument capable of simultaneous mass detection.. 54

3.10. Collision between the accelerated ion and the stationary target 55

3.11. Schematic diagram of an RBS system 58

4.1. Constant-source diffusion profiles 64

4.2. Limited-source diffusion profile 66

4.3. Substitutional diffusion in a two dimensional lattice 67

4.4. Direct interstitial diffusion mechanism 68

4.5. Kickout mechanism 69

4.6. Structural diagram of the vacancies in 4H-SiC: (a) V_{Si} at a cubic lattice site. (b) V_{Si} at a hexagonal lattice site. (c) V_C at a cubic lattice site. (d) V_C at a hexagonal lattice site ... 72

4.7. Di-vacancy complex at a hexagonal site 74

4.8. Gaussian distribution of the implanted ion profile for the impurity completely below the surface 78

4.9. Schematic diagram of an ion implanter 79

4.10. Schematic diagram of diffusion mechanism through vapor phase 84

4.11. Schematic diagram of experimental setup for thermal diffusion doping 86

4.12. Schematic diagram of the CVD system at Auburn University 88

4.13. Schematic diagram of the ECR-CVD system 89

4.14. Schematic diagram of a laser doping system 91

5.1. Schematic diagram of the VAID process for (a) phosphorus (b) boron 99

5.2. Schematic diagram of the silicidation assisted impurity doping process for phosphorus 100

5.3. Ellingham diagram for the oxidation reactions of SiC between temperatures of 700 K and 2400 K. The vertical line represents the 1700 K line 104

5.4. Ellingham diagram for the most probable reactions between SiC and phosphorus oxide below 1700 K 106

5.5. Temperature dependence of the enthalpy of the reactions between SiC and boron oxide 109

5.6. Temperature dependence of the Gibbs free energy of formation for common oxides 110

5.7. Ellingham diagram for the silicide formation reactions 113

5.8. Ni-Si-C ternary phase diagram at 900°C 114

5.9. Ni-O-P ternary phase diagram at 1200 K 117

5.10. Ni-O-Si ternary phase diagram at 1200 K 119

5.11. P-Si-C ternary phase diagram at 1200 K 120

5.12. Mass Spectrum of the phophorus dopant solution 123

5.13. Nomarski micrographs for (a) 0.25 g (b) 0.497 g (c) 0.792 g of B_2O_3 in 20 ml of 1:1:2 ethanol, methanol and isopropanol solution. (d) After annealing sample shown in b at 1300°C.. 125

5.14. Triethylborate spin coated at (a) 1000 rpm (b) 2000 rpm. (c) Sample spin coated at 1000 rpm after anneal in O_2 at 1300°C 126

6.1. Schematic diagram for mask aligner.. 134

6.2. Schematic diagram of the DC sputtering process 136

6.3. Schematic diagram of thermal evaporation system 138

6.4. Schematic diagram of alumina furnace.. 140

6.5. Experimental process for phosphorus diffusion (VAID)... 141

6.6. Experimental process for silicidation assisted phosphorus diffusion 142

6.7. Experimental process for boron diffusion (VAID) 143

6.8. Experimental process for the electroless nickel plating for ohmic contacts 144

6.9. Basic schematic diagram of an RIE system 147

6.10. Sequential process for ohmic contact fabrication 149

6.11. Sequential process for Schottky contact fabrication.. 150

7.1. Depth profile of concentration using C-V measurements for the Schottky barrier diode.. 153

7.2. I-V characteristic of a Schottky contact pad 154

7.3. EDX spectrum of the SBD sample 155

7.4. Depth profile of dopant concentration using C-V measurements after dopant activation 156

7.5. SIMS analyses of the samples annealed at 1200°C and 1400°C 158

7.6. TLM data for ohmic anneal at 1000°C 160

7.7. TLM data for ohmic anneal at 1100°C 161

7.8. I-V characteristic curve for the ohmic contacts annealed at 1100°C 162

7.9. TLM data for ohmic anneal at 1200°C 163

7.10. EDX spectrum for (a) sample annealed at 1300°C (b) sample annealed at 1400°C 165

7.11. TLM data for n-type doped sample (a) annealed at 1300°C in oxygen (b) annealed at 1400°C in oxygen 167

7.12. I-V characteristics of the top surface for the sample (a) annealed at 1300°C (b) annealed at 1400°C 170

7.13. p-n junction I-V characteristics for the sample (a) annealed at 1300°C (b) annealed at 1400°C 171

7.14. Depth profile of concentration using C-V measurements for the Schottky barrier diode on the sample (a) annealed at 650°C (b) annealed at 800°C 173

7.15. I-V characteristic of a Schottky contact pad on the sample annealed at 800°C 174

7.16. EDX spectrum of the SBD sample (a) annealed at 650°C (b) annealed at 800°C. 175

7.17. Depth profile of dopant concentration using C-V measurements after sample activation for the sample with nickel annealed at 800°C. 177

7.18. Nomarski microscope image of (a) the sample with nickel annealed at 800°C (b) the VAID process sample. 178

7.19. RBS spectrum of the sample with the deposited layer before annealing in argon. 179

7.20. RBS analysis for the sample with nickel annealed in argon at (a) 700°C (b) 900°C (c) 1000°C. 180

7.21. SIMS analysis of the sample with nickel annealed at 900°C. 182

7.22. TLM data for 1000°C ohmic anneal. 184

7.23. TLM data for 1100°C ohmic anneal. 185

7.24. I-V characteristic curve for the $Ni_{93\%}V_{7\%}$ ohmic contacts annealed at 1100°C............. 186

7.25. TLM data for 1200°C ohmic anneal. 187

7.26. EDX spectrum for the sample with nickel annealed at 900°C. 189

7.27. TLM data for n-type doped sample (a) activated at 1400°C in argon (b) activated at 1500°C in argon. 191

7.28. I-V characteristics of the top surface for the sample (a) activated at 1400°C (b) activated at 1500°C. 194

7.29. p-n junction I-V characteristics for the sample (a) activated at 1400°C (b) activated at 1500°C. 195

7.30. Fabricated blue LED using silicidation assisted impurity doping technique................. 196

7.31. EDX spectrum of an as-plated 4H-SiC sample... 197

7.32. RBS spectra of a Ni:P plated sample before and after annealing at 1000°C. 198

7.33. I-V data for the sample annealed at 1000°C and 1100°C. 199

7.34. TLM data plated sample (a) annealed at 1000°C (b) annealed at 1100°C. 200

Chapter 1

Introduction

1.1 Background

The most widely used semiconductor for electronic devices is silicon, which shows great material properties for efficient device fabrication. Therefore, for mass scale production, silicon is undoubtedly the ideal material. However, for certain specific tasks like operating at high temperatures or high power, silicon devices leave much to be desired in terms of performance. For several decades, research scientists have been studying wide band gap semiconductor materials such as silicon carbide (SiC), gallium nitride (GaN) and aluminium nitride (AlN) for high power, high frequency, high temperature and short wavelength applications [1-3].

SiC is a wide band gap semiconductor with physical and electronic properties highly suitable for high power, high temperature, and high frequency electronics. Progress in silicon carbide device technology during the last few decades has led to the fabrication of various devices such as metal semiconductor field effect transistors (MESFET), metal oxide field effect transistors (MOSFET), thyristors, and static induction thyristors (SIT) [4]. Despite this progress, there are still critical issues in metallization that necessitate reliable ohmic contacts [5] and high concentration doping [6].

1.2 Properties of Silicon Carbide

1.2.1 Structures

Since the late 19th century, silicon carbide has been known to occur naturally and was historically referred to as moissanite. Its early prominence was due to its thermal, chemical and mechanical properties [7]. Initially, Acheson [8] devised a method to produce SiC for large scale use as an abrasive. Other uses, such as using SiC as material for heating elements with longer lifetimes, high strength structural materials and semiconductor materials were discovered later. It was first used in electrical systems in polycrystalline form as lightning arrestors to protect electrical equipment from power surges [7,8].

SiC is known to exist in different forms generally referred to as polytypes. Polytypism in SiC is defined as the ability of SiC to crystallize in to a number of unique structures, in which two dimensions of a unit cell are identical whereas the third dimension varies as an integral multiple of a common length [7]. These various polytypes can be differentiated by the stacking sequence of the tetrahedrally–bonded Si-C bilayers. The neighboring Si or C bonds have an approximate bond length of 3.078 Å [9]. All polytypes have a tetrahedral frame with three Si atoms arranged in a triangle at the base with a C atom at the center of the triangle, slightly elevated. The fourth Si, which belongs to the next layer of the Si crystal structure, is directly above the C atom. All C-Si bonds have a bond length of 1.89 Å and the spacing between two adjacent Si layers is 2.52 Å [10]. Fig. 1.1 shows the tetragonal structure of one carbon atom bonded to four silicon atoms.

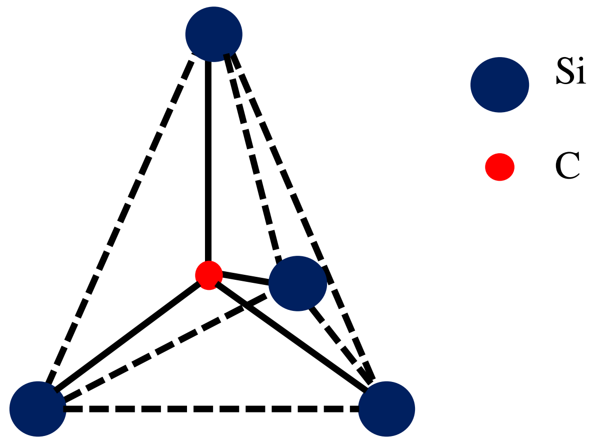

Fig. 1.1: Tetrahedral structure of a carbon atom with the four nearest neighboring silicon atoms

There are more than 200 known polytypes of SiC and some do not have repeating stacking patterns for over hundreds of layers [11]. The most common method used to describe these polytypes is the Ramsdell notation, which consists of a number followed by a letter. The number denotes the number of bilayers of silicon and carbon that occur before a repeating sequence. The letter represents the crystal structure, with C used for cubic, R for rhombohedral and H for hexagonal [12,13]. The only purely cubic structure is 3C (β-SiC) and the only purely hexagonal structure is 2H (α-SiC). Of the numerous polytypes, 3C, 4H and 6H are the most important ones being developed for electronic applications mainly because of the availability of these as substrate materials. The structure and stacking sequence of these polytypes are shown in Figure 1.2.

Fig. 1.2: The structure and stacking sequence of 3C, 4H and 6H-SiC [14]

The first bilayer is referred to as the A position following which a layer is placed on the B position or the C position according to closely packed structure. This sequence is used to distinguish between the different polytypes. Structural characteristics of some of the common polytypes are displayed in Table 1.1 below.

Table 1.1: Structural characteristics of common SiC polytypes [12,15]

Ramsdell notation	Stacking sequence	Atoms per unit cell	Lattice constants (Å)
3C	ABC…………	2	a= 4.349
2H	AB……………	4	a= 3.080 c= 5.048
4H	ABCB…………	8	a= 3.080 c= 10.050
6H	ABCACB……….	12	a= 3.080 c= 15.079
15R	ABCACBCABACABCB…..	10	a= 3.080 c= 37.7

1.2.2 Properties

The exceptional semiconducting properties of SiC make it an ideal candidate for electronic device applications. It has a wide band gap of 2.2-3.3 eV when compared to silicon, which has a band gap of 1.1 eV. Although there are other wide band gap semiconductors like gallium nitride (band gap, E_g= 3.4 eV) and aluminum nitride (E_g= 6.2 eV), SiC is the only wide band gap semiconductor that can be oxidized to form native silicon dioxide (SiO_2). For electronic device applications, p-type epitaxial SiC can be obtained by introducing boron or aluminum into the SiC lattice, while n-type epitaxial SiC can be obtained by introducing phosphorus or nitrogen into the SiC lattice. Recently, SiC has shown further promise as a potential semiconductor for quantum computing due to intrinsic defects that can be used to form qubits [16].

Table 1.2 shows a comparison of the electrical properties of SiC with other common semiconductors such as Si and GaN. The most important properties for high temperature, high frequency and high power applications are compared to show the advantages of using SiC. As a rough estimate of the effect of the band gap on device operation, the maximum operating temperatures of different semiconductor material are listed. The maximum operating temperature is defined as the temperature at which the intrinsic carrier concentration equals $5x10^{15}$ cm^{-3} [17]. The high thermal conductivity, high breakdown field and the high operating temperature allow SiC devices to work at high power density conditions. Furthermore, SiC has high thermal stability, is chemically inert and has a very high tolerance to radiation, which enables it to function effectively in harsh environments [12,18].

Table 1.2: Comparison of important electronic properties of semiconductors [19-21]

Property	Si	GaN	3C SiC	4H SiC	6H SiC
Bandgap at 300 K (eV)	1.1	3.39	2.39	3.26	3.02
Max. Operating Temperature (K)	600	--	1200	900	1580
Electron mobility (cm^2/Vs)	1400	900	1000	800	600
Hole mobility (cm^2/Vs)	600	150	40	115	101
Breakdown field (MV/cm)	0.3	5	1.5	3	3.2
Thermal conductivity (W/cm)	1.5	51.3	3.2	3.7	4.9
Dielectric constant	11.8	9	9.7	9.7	10.3

1.2.3 Crystal Growth

Since SiC was first grown in the 1890's by Acheson [8], there have been concerted efforts to produce high quality, single crystalline substrates. High quality SiC wafers have been in the market for a few decades due to university researchers and semiconductor companies like Northrop-Grumman, ATMI, CREE Incorporated, and Nippon Steel Corporation in Japan actively developing monocrystalline SiC growth [22]. Silicon carbide growth processes that have been developed by such researchers constitute one of the main advantages when compared to other wide band gap semiconductors.

Generally, the growth of semiconductor boules from a melt or a solution is one common process, but for SiC, this involves pressures of over 100000 atm and temperatures in excess of 3200°C, making it an impractical method for commercial purposes. Therefore, researchers have been investigating other methods of SiC growth by using various forms of physical vapor transport (PVT). Liquid-phase epitaxy (LPE) was used as one of the earlier methods due to its lower growth temperatures in the range of 1500- 1700°C, compared to 2000°C when grown by sublimation, but the use of graphite crucibles during the process meant that C contamination occurred [23,24]. This problem was solved by using a C-enriched Si melt suspended in an electromagnetic field [25]. In another method, growth occurs through sublimation, in which a vapor phase source of Si and C is transported to a seed crystal with the aid of a carrier gas such as argon. The seed crystal is kept at a temperature of 1800°C while the source is set at a temperature of 2000°C.

Chemical vapor deposition (CVD) has become the preferred method of SiC epitaxial growth, while the "modified Lely-method" [26] is preferred for SiC bulk growth. For SiC

epitaxial growth, the methods used include low pressure chemical vapor deposition (LPCVD), atmospheric pressure chemical vapor deposition (APCVD), metallorganic chemical vapor deposition (MOCVD) and molecular beam epitaxy (MBE) [27].

1.2.4 Devices and Applications

SiC devices have been used for a variety of applications including high temperature, high power, radio frequency, microwave, optoelectronic and optical sensing. A few of these devices are discussed in the following section.

Field Effect Transistors

Several types of SiC field effect transistors (FET) are available commercially. The importance of FETs can be attributed to their power-switching capabilities and the ease of large scale integration. The basic structure of a metal oxide semiconductor field effect transistor (MOSFET) is shown in Figure 1.3.

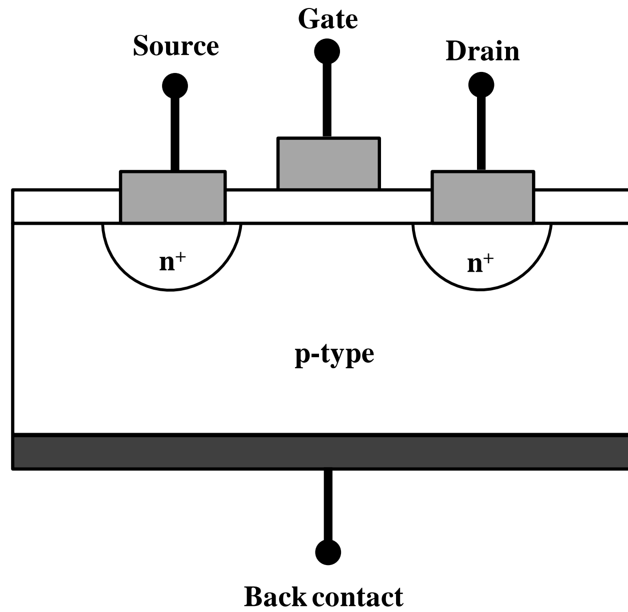

Fig. 1.3: Basic structure of a MOSFET

Higher breakdown fields, low leakage currents, and high operating temperatures make SiC FETs attractive for certain specific applications [28–31]. Although there has been considerable success in the fabrication of SiC MOSFETs, the quality of the thermal oxide grown has limitations compared to Si MOSFETs. A significant limitation is at the SiO_2/SiC interface, where high fixed oxide charge densities, high interface state densities, charge trapping, and carrier oxide tunneling have posed problems affecting MOSFET operation [32]. Researchers have recently used nitrogen (N) to passivate the SiO_2/SiC interface with and considerable success has been achieved [33].

Photodiodes

SiC photodiodes were among the first commercially available wide band gap devices. Because of their small dark current levels and their sensitivity to shorter wavelengths, SiC photodiodes are ideal candidates for ultra violet (UV) solar-blind light detection. Figure 1.4 shows the basic structure of a SiC photodiode.

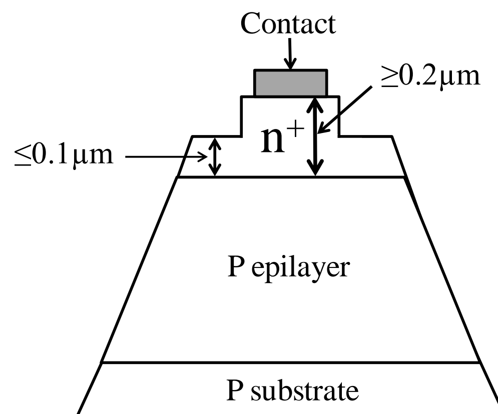

Fig. 1.4: Basic structure of a SiC photodiode

These photodiodes can operate at higher temperatures compared to Si UV detectors, which provides an additional advantage. Due to their low dark currents, SiC UV detectors have a very high sensitivity ($\geq 10^4$) relative to Si UV detectors [34]. Also, because UV detection often requires detectors to be placed in harsh environments, the physical stability of SiC makes it a preferred choice.

Light Emitting Diodes (LEDs)

The development of LEDs has moved swiftly since Brander and Sutton [35] produced the first blue SiC LED. Although SiC LEDs can be doped with various impurities to emit light in the entire visible range, it is mostly used for blue light. Presently, companies including CREE, Sanyo, Siemens AG, and Sharp are commercially fabricating blue SiC LEDs, but the efficiency of these devices are low due to the indirect band gap of SiC [1].

The mechanisms that produce light in SiC LEDs are donor-to-acceptor pair recombination, bound exciton recombination and free exciton recombination [10]. However, at present, SiC blue LEDs have been replaced by the more efficient gallium nitride LEDs.

1.3 Objectives and Scope of this Thesis

Current techniques of doping SiC require dedicated apparatus and extremely high temperatures ($\geq 1700^{o}C$), which increase the cost of SiC fabrication. The goal of this research is to develop a low cost, efficient method to introduce impurities in to SiC, based on the vacancy assisted impurity doping (VAID) process, where impurity incorporation in SiC is achieved by selectively creating favorable vacancies and defect complexes and using thermodynamically favorable dopant compounds to send the dopants in to these created vacancies [36].

Contrary to the popular belief that thermal diffusion is only achievable at extremely high temperatures in SiC [10], this research investigates the possibilities of introducing impurities at temperatures lower than $1400^{o}C$. Metal oxides in contact with SiC can lead to the introduction of impurities in to SiC at optimal temperature annealing due to favorable thermodynamic

conditions. A detailed thermodynamic investigation confirmed the possibility of phosphorus and boron incorporation in silicon carbide using the VAID process. The potential of using nickel as a catalyst for the VAID process has been studied using ternary phase diagrams of stability.

Dopant solutions were used to deposit phosphorus oxide onto SiC substrates. Annealing at temperatures within a range of 1100°C to 1400°C in an oxygen ambient was investigated. Nickel was used as a catalyst to introduce phosphorus at temperatures less than 900°C due to the favorable thermodynamics of silicide formation. Electron dispersive x-ray spectroscopy (EDX) and secondary ion mass spectroscopy (SIMS) were used to confirm the presence of phosphorus in silicon carbide. Electrical characterization provided a description of the nature of the contacts. Annealing in oxygen at 1400°C produced a phosphorus concentration in the range of 10^{19} cm^{-3} up to a depth of 0.1 μm, while annealing at 900°C in argon using silicidation assisted doping process increased phosphorus incorporation. Using nickel in the process allowed the phosphorus to diffuse to a depth of 0.3 μm at a surface concentration of approximately 3 x 10^{19} cm^{-3}.

As a measure of the effectiveness of the VAID process, ohmic contact metallization was used to confirm the high doping levels obtained by SIMS. A high doping concentration in the range of 10^{18} ~ 10^{19} cm^{-3} is expected to produce specific contact resistivity in the range of 10^{-5} ~ 10^{-6} Ωcm^{2}. Contact resistance was measured via the linear transmission line method (LTLM) to characterize the contacts. LTLM measurements conducted on ohmic contacts fabricated using the VAID process show contact resistivity in the range of 10^{-5}-10^{-6} Ωcm^{2}. Electroless nickel plating was also used to fabricate ohmic contacts to SiC based on the silicidation-assisted doping process, and specific contact resistivity of approximately 5 x 10^{-6} Ωcm^{2} was reported.

1.4 References

1. J. A. Edmond, H. S. Kong, and C. H. Carter, Jr., *Physica B* **185**, 453 (1993).

2. R. W. Brander and R. P. Sutton, *J. Phys*. **D 2**, 309 (1969).

3. H. Amano, M. Kito, K. Hiramatsu and I. Akasaki, *Jpn*, *J. Appl. Phys*. **28**, L2112 (1989).

4. C. E. Weitzel, J. W. Palmour, C. H. Carter, K. Moore, K. J. Nordquist, S. Allen and C. Thero, *IEEE Trans. Electron Devices*, **43**, 1732 (1996).

5. F. Roccaforte, F. La Via V. Ranieri, *Int. J. High Speed Electron. Syst*. **15** (4), 781 (2005).

6. E. Rauls, U. Gerstmann, Th. Frauenheim, H. Overhof, *Physica B* **340-342**, 184 (2003).

7. J. Feitknecht, *Silicon carbide as a semiconductor: Springer Tracts in Modern Physics* G. Höhler (ed), **58,** 48 (1971).

8. G. Acheson, *Brit. Pat*. 17911 (1892).

9. W. F. Knippenberg, *Philips Research Reports*, **18**, No. 3, 161 (1963).

10. M. Li, *Ohmic Contacts to Implanted (0001) 4H-SiC*, Dissertation, Department of Physics, Auburn University (2009).

11. T. N. Oder, *Fabrication and Characterization of Ohmic Contacts to p- and n-type Silicon Carbide with Applications to p-n Junction Diodes*, Dissertation, Department of Physics, Auburn University (1999).

12. J. A. Powell, *Mat. Res. Soc. Symp. Proc. Vol.* **97**, 159 (1987).

13. R. S. Ramsdell, *Am. Min.* **32**, 39 (1945).

14. http://en.wikipedia.org/wiki/Silicon_carbide

15. W. J. Choyke and G. Pensl, *M.R.S. Bulletin*, **22** No. 3, 25 (1997).

16. A. G. Smart, *Phys. Today*, **65** No. 1, 10 (2012).

17. H. Morkoç, S. Strite, G. B. Gao, M. E. Lin, B. Sverdlov and M. Burns, *J. Appl. Phys*. **76**, 1363 (1994).

18. R. B. Campbell and H. C. Chang, in *Semiconductors and Semimetals*, R.K.Willardson and A. C. Beer (eds) (Academic Press, New York, 1971), Vol. 7 Part B, Chap. 9.

19. S. M. Sze, *Physics of Semiconductor Devices*, 2nd ed., New York: John Wiley & Sons, (1981).

20. G. L. Harris, in *Properties of Silicon Carbide*, G. L. Harris (ed), EMIS Data Review Series 13, (INSPECT, London 1995) p. vii.

21. D. Pelletier, D. Gervais and C. Pomot, *J. Appl. Phys.* **55**(4), 999 (1984).

22. R.C. Glass, D. Henshall, V. F. Svetkov and C. H. Carter Jr., *M.R.S Bulletin*, **22** No.3, 30 (1997).

23. M. Ikeda, T. Hayakawa, Z. Yamagiva, H. Matsunami and T. Tanaka, *J. Appl. Phys*. **50**, 8215 (1979).

24. W. Muench and W. Kurzinger, *Solid State Electron*. **21**, 1129 (1978).

25. V. A. Dmitriev, P. A. Ivanov, I. Korkin, Y. Morozenko, I. Popov, T. A. Sidorova, A. M. Strslchuk and E. Chelnokov, *Sov. Phys. Technol. Lett*. **11**, 98 (1985).

26. Y. M. Tairov and V. M. Tsvetkv, *J. Cryst. Growth* **43**, 209 (1978).

27. D. J. Larkin, *M.R.S Bulletin*, **22** No.3, 36 (1997).

28. M. Ghezzo, D. M. Brown, E. Downey, J. Kretchmer, W. Hennessy, D. L. Polla and H. Bakhn I, *IEEE Electron. Device Lett*. **EDL-13**, 639 (1992).

29. M. Bhatnagar, P. McLarty, and B. J. Baliga, *IEEE Electron. Device Lett*. **EDL-13**, 501 (1992).

30. P. G. Neudeck, D. J. Larkin, J. E. Starr, J. A. Powell, C. S. Zalupo, and L. G. Matus, *IEEE Electron. Device Lett*. **EDL-14**, 136 (1993).

31. R. F. Davis, G. Kelner, M. Shur, J. W. Palmour, and J. A. Edmond, *Proc. IEEE* **79**, 677 (1991).

32. P. G. Neudeck, *Silicon Carbide Electronic Devices*, in *Encyclopedia of Materials: Science and Technology*, K. H. J. Bushchow, R. W. Cahn, M. C. Flemming, B. Ilschner, E. J. Kramer and S. Mahajan (eds) (Oxford: Elsevier Science) **9**, 8508 (2001).

33. G. Y. Chung, J. R. Williams, T. Isaacs-Smith, F. Ren, K. McDonald and L. C. Feldman, *Appl. Phys. Lett*. **81**, 4266 (2002).

34. D. M. Brown, E.T. Downey, M. Ghezzo, J.W. Kretchmer, R.J. Saia and Y.S. Liu, *IEEE Trans.* **ED 40** (2), 325 (1993).

35. R. W. Brander and R. P. Sutton, J. Phys. **D 2**, 309 (1969).

36. C. C. Tin, A. V. Adedeji, I. G. Atabayev, B. G. Atabaev, T. M. Saliev, E. N. Bakhranov, M. Li, S. P. Mendis and C. A. Ahyi, *U.S. Patent* 7,999,268. (2011).

Chapter 2

Metal Semiconductor Contacts

The most important aspect of semiconductor electronics is the metal-semiconductor (MS) contact, which can be either rectifying or non-rectifying. Low resistive non-rectifying (ohmic) contacts are necessary in electronics to connect semiconductor devices to external circuits, while rectifying (Schottky) contacts are required for switching and rectification [1]. Relative to the resistance of the bulk device, which is referred to as the "device on-resistance", the resistance of the contact must be extremely low to minimize the voltage drop at the contact. A large voltage drop increases the power dissipation of the device and thereby decreases its effectiveness [2].

An ideal MS contact should be devoid of any interdiffusion between the two layers and there should be no accumulated surface charge at the interface. However, ideal conditions are very rarely achieved, which adversely affects the barrier height[3]. Controlling surface variables that affect the Schottky barrier height dictate the behavior of ohmic and Schottky contacts [4]. If the work functions of both materials are known, it should be possible to theoretically predict the behavior of a metal-semiconductor contact, but since most of the material properties of SiC that control the metal-SiC contact are not fully understood, predicting the contact behavior is difficult [4].

Figure 2.1 shows the characteristic current-voltage (I-V) curve of both a Schottky contact and an ohmic contact. Shottky contacts are characterized by the non-linear asymmetric curve, while ohmic contacts are characterized by the linear curve.

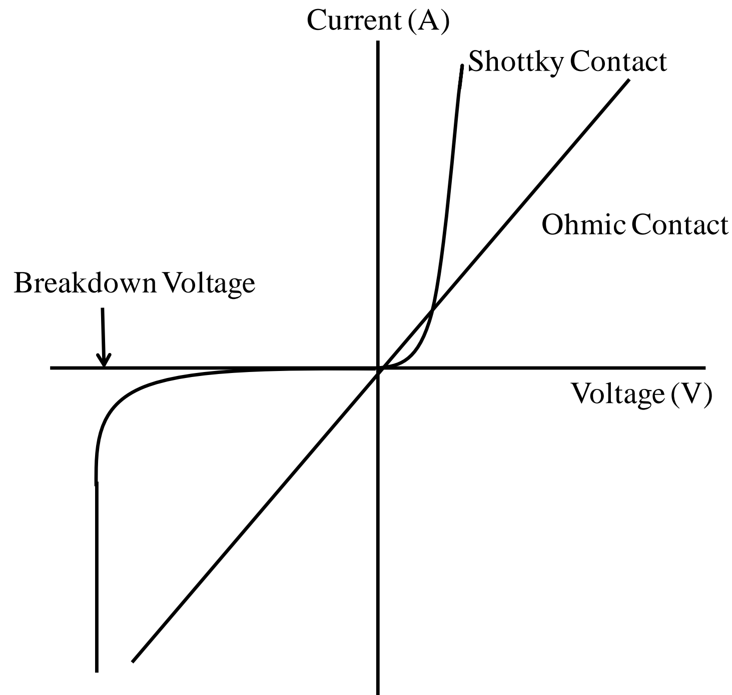

Fig. 2.1: I-V characteristics of Schottky and ohmic contacts

Ideally, the values of the work function of the metal (Φ_m) and the work function of the semiconductor (Φ_s) will dictate the behavior of the contact. Table 2.1 shows the general rule for differentiating between Schottky contacts and ohmic contacts.

Table 2.1: Work function dependence of MS contacts

Semiconductor type	$\Phi_m > \Phi_s$	$\Phi_m < \Phi_s$
n-type	Schottky	Ohmic
p-type	Ohmic	Schottky

2.1 Schottky Contacts

A semiconductor with low doping concentration in contact with a metal that produces a large barrier height (Φ_B), which is referred to as a Schottky barrier. Figure 2.2(a) shows the energy band diagram for a metal and a semiconductor in close proximity. As shown in Figure 2.2(a), the vacuum energy levels (E_o) are the same while the Fermi energy levels are separated. But when the metal is put in contact with the semiconductor as shown in Figure 2.2(b), the Fermi levels coincide as the metal and semiconductor reach thermal equilibrium while the conduction and valence bands bend at the interface. This band bending creates an energy barrier for the electrons, which is referred to as the Schottky barrier.

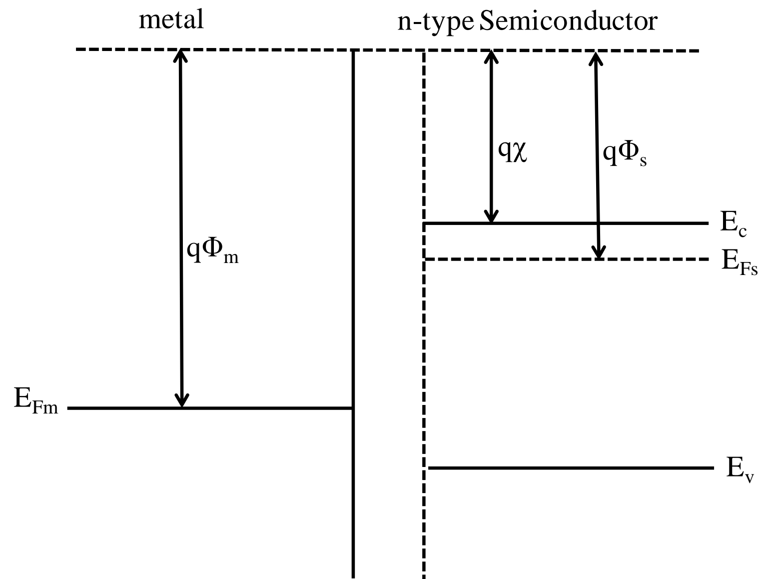

(a)

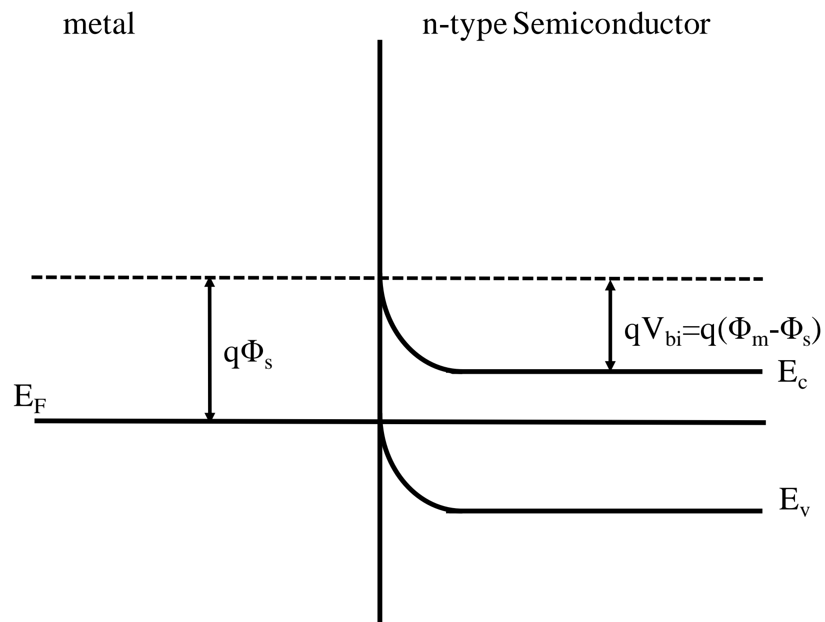

(b)

Fig. 2.2: Energy band diagram of a metal and semiconductor (a) in close proximity and (b) in contact.

For n-type semiconductors, the Schottky barrier height is defined as the potential difference between the Fermi energy and the conduction band energy level at the MS interface. This is shown in Equation 2.1, while Equation 2.2 shows the Schottky barrier height for a p-type semiconductor in contact with a metal and it is defined as the potential difference between the Fermi energy level and the valence band energy level at the MS interface:

$$\Phi_B = \Phi_m - \chi \tag{2.1}$$

$$\Phi_B = \frac{E_g}{q} + \chi - \Phi_m \tag{2.2}$$

The electron affinity is represented by χ and E_g is the energy gap. Therefore, an MS contact will form a Schottky barrier if the Fermi level is located between the conduction and valence bands at the interface.

Table 2.2 shows the work function of selected metals (in vacuum) and the calculated Schottky barrier height from Equations 2.1 and 2.2. Because the calculated values assume ideal conditions, the actual experimental values are often different [6,7]. This difference can be attributed to chemical reactions between the two materials and interfacial layers such as thin oxides and other contaminants, which lead to a change in the barrier height.

Table 2.2: Work function and calculated barrier heights for selected metals.

	Al	Ti	Zn	W	Cu	Mo	Ni	Au	Pt
Φ_m (eV)	4.28	4.33	4.33	4.55	4.65	4.69	5.10	5.15	5.65
Φ_B (eV)	1.01	1.06	1.06	1.28	1.38	1.33	1.63	1.68	2.08

When a voltage is applied to an n-type semiconductor in contact with a metal, in which the work function of the metal is greater than that of the semiconductor, electrons flow from the semiconductor to the metal, leaving positive donor ions. This leads to the accumulation of charge at the surface of the metal. For a uniformly-doped semiconductor, the charge density will be uniform in the depletion layer and the electric field will display a linear profile over a distance. Electrons travelling from the metal to the semiconductor will have to surmount the Schottky barrier (Φ_B) while the electrons travelling in the opposite direction will encounter the built-in potential (V_b), which is determined by the band bending at equilibrium. Therefore, the I-V characteristics (Figure 2.1) of a Schottky contact can be explained by the dependence of V_b on the applied bias and the lack thereof for Φ_B [8].

2.2 Ohmic Contacts

For an n-type semiconductor, if the work function of the metal is less than the work function of the semiconductor ($\Phi_m<\Phi_s$), the contact is ohmic under ideal conditions as mentioned earlier in Table 2.1. Figure 2.3(b) shows the energy band diagram for an n-type semiconductor in

contact with a metal with a work function that would produce an ohmic contact under ideal conditions. When the metal is put in contact with the semiconductor, the Fermi levels on both materials line up together when in thermal equilibrium, which leads to an adjustment of the conduction band near the Fermi level at the interface. This produces an ohmic contact.

On the other hand, for a p-type semiconductor, the contact is ohmic under ideal conditions if work function of the metal is greater than the work function of the semiconductor ($\Phi_s < \Phi_m$). Figure 2.4(b) shows the energy band diagram for a p-type semiconductor in contact with a metal with a work function that would produce an ohmic contact under ideal conditions. The figure also illustrates that the Fermi levels on both materials line up together in thermal equilibrium after contact, which leads to an adjustment of the valence band near the Fermi level at the interface, producing an ohmic contact.

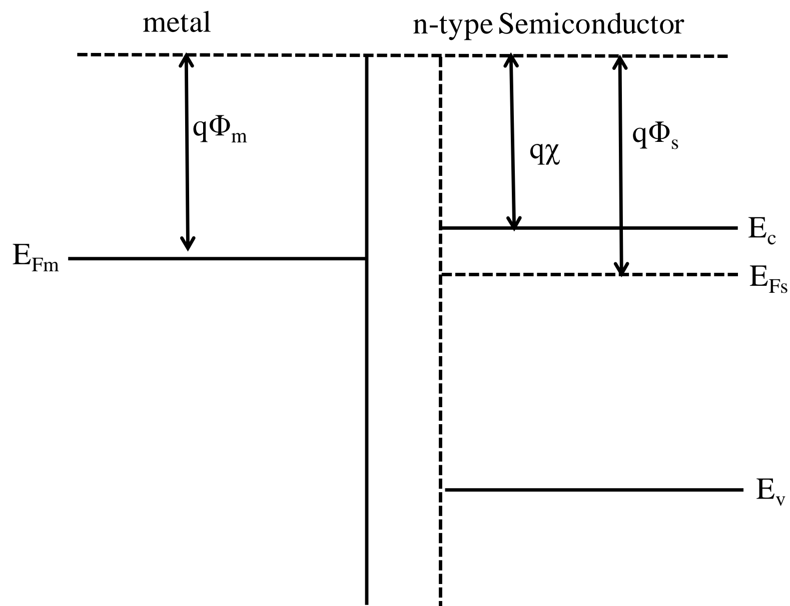

(a)

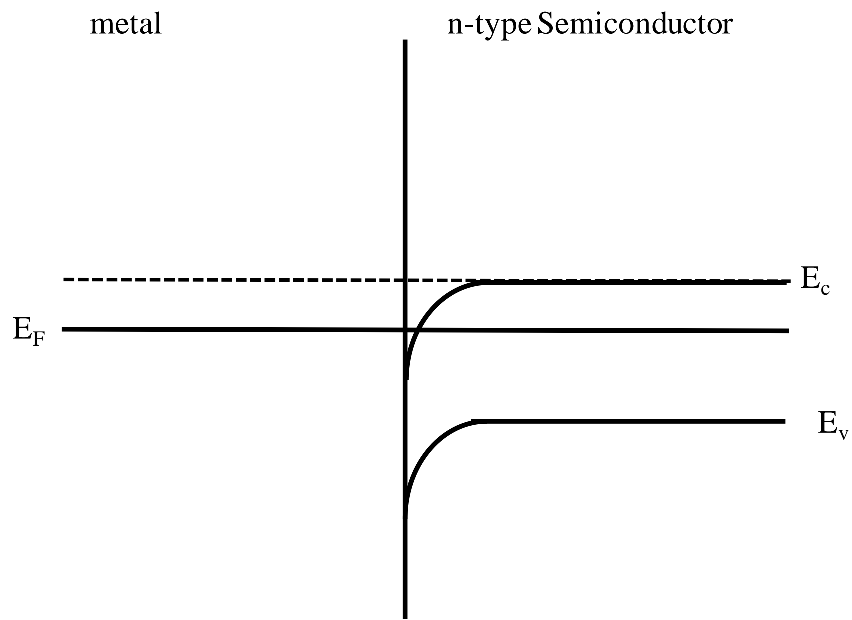

(b)

Fig. 2.3: (a) n-type semiconductor in close proximity to a metal (b) MS contact

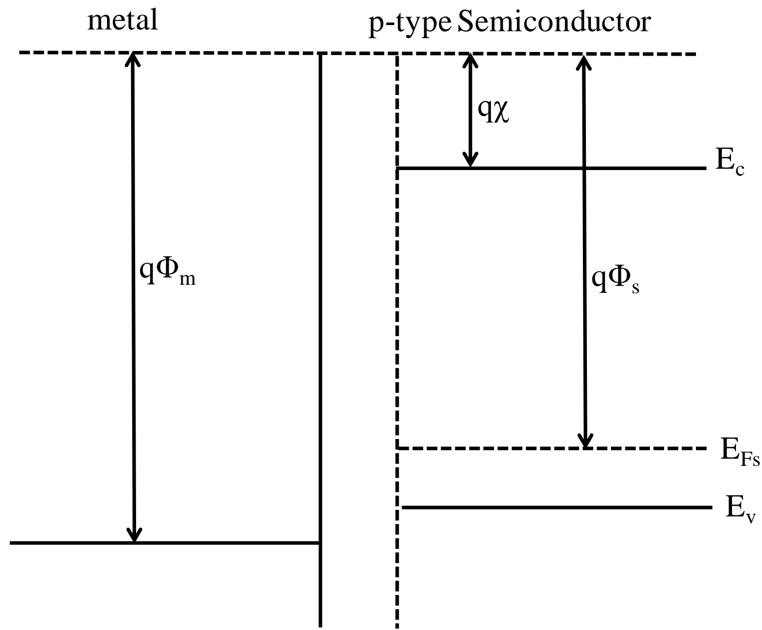

(a)

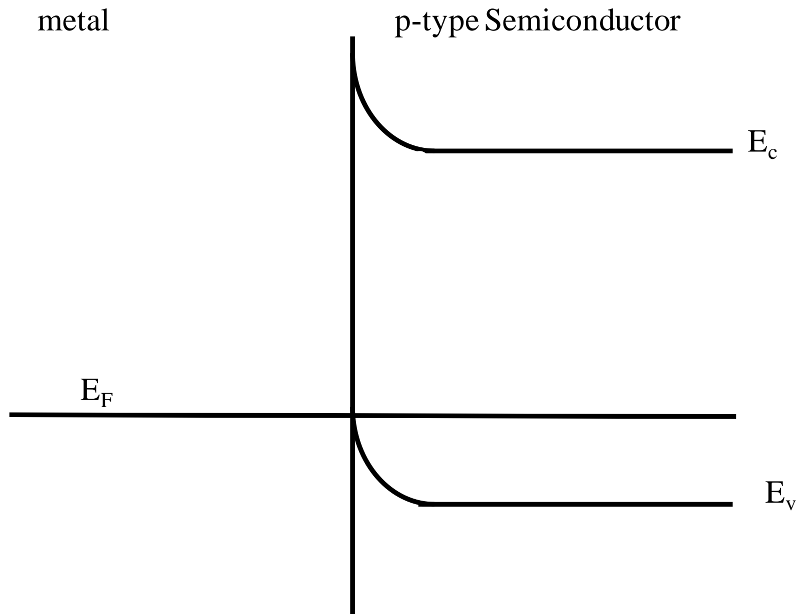

(b)

Fig. 2.4: (a) p-type semiconductor in close proximity to a metal (b) MS contact

An MS contact can be manipulated to show ohmic characteristics by controlling the shape of the Schottky barrier through specific processing steps to reduce either the barrier height or the width of the barrier itself. The doping concentration of the semiconductor in the surface region dictates the behavior of the contact. Although the barrier height would not change for the same metal in contact with a highly doped or a lightly doped semiconductor, the width of the depletion region reduces as the doping level is increased. This allows the carriers to tunnel through the barrier instead of going over it [9].

For ohmic contacts, the contact potential (Φ_s) at the metal semiconductor interface is given by Equation 2.3, where Φ_m is the work function of the metal and Ψ_{bi} is the built-in potential [10]. Equation 2.4 defines Ψ_{bi} in terms of the net dopant concentration (N) and the variables N_1 and N_2:

$$\phi_s = \phi_m + \psi_{bi} \tag{2.3}$$

$$\psi_{bi} = -\frac{k_B \cdot T_L}{q} \cdot \ln\left(\frac{1}{2N_1}\left(N + \sqrt{N^2 + 4N_1N_2}\right)\right) - \frac{k_B \cdot T_L}{q} \cdot \ln\left(\frac{1}{2N_2}\left(-N + \sqrt{N^2 + 4N_1N_2}\right)\right) \tag{2.4}$$

K_B is the Boltzmann constant and $T_L$is the lattice temperature. Variables N_1 and N_2 are given by Equations 2.5 and 2.6:

$$N_1 = N_c \cdot \exp\left(\frac{-E_c}{k_B \cdot T_L}\right) \tag{2.5}$$

$$N_2 = N_v \cdot \exp(\frac{-E_v}{k_B \cdot T_L}) \tag{2.6}$$

where N_c is defined as the effective density-of-states of electrons in the conduction band and N_v is defined as the effective density-of-states of holes in the valence band. For an ideal ohmic contact, the carrier concentration in the semiconductor can be assumed to be equal to the carrier concentration at the contact. The carrier concentrations in the semiconductor, n_s and p_s, can be written as:

$$n_s = N_c \cdot \exp\left(\frac{-E_c + q \cdot \Psi_{bi}}{k_B \cdot T_L}\right) \tag{2.7}$$

$$p_s = N_v \cdot \exp\left(\frac{-E_v - q \cdot \Psi_{bi}}{k_B \cdot T_L}\right) \tag{2.8}$$

Ohmic contact resistance is especially important in SiC devices due to its wide band gap, which tends to make large Schottky barrier heights at the interface with most metals. For instance, in Si the barrier height problem can be solved by using the most advantageous metal to make reliable ohmic contacts, but in SiC there is minimal room to maneuver because of its wide band gap and the positioning of the Fermi level [9]. Development of ohmic contacts to 4H SiC is discussed in the following section.

2.2.1 Ohmic Contacts to n-type 4H Silicon Carbide

The development of ohmic contacts for α-SiC started with 6H-SiC, but 4H-SiC is gradually replacing 6H-SiC as the choice of material because of its higher bulk mobility [11]. For lightly to moderately doped ($\approx 10^{17}$-10^{18} cm^{-3}) SiC, specific contact resistivity (ρ_c) values are limited to a range of 10^{-4} to 10^{-3} $\Omega \cdot cm^2$ [11], but recent developments have led to a gradual decrease in ρ_c values ($\approx 10^{-6}$–10^{-5} $\Omega \cdot cm^2$) on highly doped (> 10^{19} cm^{-3}) α-SiC. This range of ρ_c is generally adequate for a good ohmic contact [12].

Specific contact resistance (ρ_c) can be calculated using Equation 2.9, in which A^{**} is the Richardson constant [2]. The Richardson constant is given by Equation 2.10, in which q is the charge of an electron, m is the mass of an electron, and h is Planck's constant:

$$\rho_c = \frac{k_B}{qA^{**}T} \exp\left(\frac{q\Phi_B}{k_B T}\right) \quad (2.9)$$

$$A^{**} = \frac{4\pi \cdot q \cdot m \cdot {k_B}^2}{h^3} \quad (2.10)$$

The most important aspect of forming an ohmic contact to SiC is the formation of metal silicide at the interface. Nickel is the most frequently used material for ohmic contacts to n-type SiC. Annealing Ni-based contacts on SiC at temperatures ranging between 800 to 1150°C has

shown to form nickel silicides [13]. Reportedly, the ohmic contact is formed due to the solid state chemical reaction between Ni and SiC forming nickel silicide at the MS contact, which changes the key properties of SiC near the interface region [14,15].

Other metals such as cobalt and tantalum have been used to produce ohmic contacts [11]. More recently, metal alloys and multilayered contacts have been investigated as ohmic contacts to n-type 4H-SiC. Lee et al. [16] reports on titanium-based ohmic contacts to 4H-SiC, in the form of titanium carbide (TiC) and titanium tungsten (TiW). Epitaxially grown TiC has been used on epitaxial layers and specific contact resistance ρ_c, measured at 300 K while using the transmission line method (TLM), was found to be as low as $5 \times 10^{-6}\ \Omega cm^2$ for n^+ epilayer [16]. Table 2.3 shows a list of metals used as ohmic contacts to n-type α-SiC with the reported values for ρ_c.

Table 2.3: Ohmic contacts to n-type α-SiC and reported ρ_c values

Contact metal	SiC carrier conc. (cm^{-3})	Annealing condition	ρ_c ($\Omega\cdot cm^2$)	Method of ρ_c measurement	Ref.
Ni	4.5×10^{17}	1000°C, 20s	1.7×10^{-4}	TLM	[17]
Ni	4.7×10^{18}	950°C, 5 min	mid 10^{-2}	4-pt probe	[18]
Ni	7.9×10^{18}	950°C, 2 min	$< 5 \times 10^{-6}$	TLM	[19]
Ni	9.8×10^{17}	1050°C, 5 min	10^{-3}-10^{-4}	TLM	[12]
Ni	4.5×10^{20}	1000°C, 5 min	1×10^{-6}	contact area	[20]
Ni	3.2×10^{17}	1000°C-1200°C, 1 min	1×10^{-5} – 3.6×10^{-6}	TLM	[21]
Ni	2×10^{18} – 2×10^{19}	950-1000°C	4×10^{-4} - 10^{-6}	TLM	[22]
Mo	2×10^{18} – 2×10^{19}	950-1000°C	4×10^{-4} - 10^{-5}	TLM	[22]
Mo	$>1 \times 10^{19}$	as-deposited	$\approx 10^{-4}$	4-pt probe	[23]
Ti	2×10^{18} – 1×10^{20}	as-deposited	10^{-2} -10^{-5}	Circ. TLM	[24]
W	3×10^{18} – 1×10^{19}	1200°C-1600°C	5×10^{-3} – 1×10^{-4}	4-pt probe	[25]
Ta	$>1 \times 10^{19}$	as-deposited	$\approx 10^{--4}$	4-pt probe	[23]
0.6Ni-0.4Cr	4.7×10^{18}	950°C, 5 min	1.8×10^{-3}	Circ. TLM	[18]
TiW	4.7×10^{18}	600°C, 5 min	7.8×10^{-4}	Circ. TLM	[18]
TiC	4×10^{19}	etched at 1300°C 15 min in H_2	1.3×10^{-5}	TLM	[26]
Ni, Ni/W Ni/Ti/W	10^{18} –10^{19}	1000°C-1050°C 5-10 min	10^{-3} –10^{-6}	TLM	[27]
Cr/W Cr/Mo/W	10^{18} –10^{19}	1000°C-1050°C 5-10 min	10^{-3} –10^{-4}	TLM	[27]

2.2.2 Ohmic Contacts to p-type 4H Silicon Carbide

Forming ohmic contacts on p-type α-SiC is more challenging due to their relatively higher Schottky barrier heights compared to n- type SiC. Therefore high concentration doping is used to reduce the width Schottky barrier so that tunneling can occur.

Aluminum (Al) and its alloys are the most commonly used metal ohmic contacts on p-type α-SiC. Al diffuses into the semiconductor during the annealing process to increase the doping concentration at the surface to make the reduce the Schottky barrier. Pure Al metal is typically not used due to its low melting point and the fact that it is easily oxidized. Therefore, Al binary alloys are used to increase the melting point. A 90-10 alloy of Al and Ti was deposited on p-type SiC and subsequently annealed at 1000°C for 2 min, led to specific contact resistance ranging between 5 x 10^{-6} to 3 x 10^{-5} Ωcm^2. The initial alloy thickness was found to be crucial to controlling the Al-Ti sheet resistance [28].

Other binary alloys and multilayer structures have been investigated as ohmic contacts. Following annealing at 900°C, Au/Ti(30%)/Al(70%) ohmic contact on p-type SiC can achieve a specific contact resistance of 1.4 x 10^{-5} Ωcm^2. This ohmic contact shows a maximum operating temperature of approximately 450°C and maximum current densities of up to 10^3 A/cm^2 [29]. Mohammad et al. [30] reported that Pt/SiC and Pt/Si/SiC contacts to p-type SiC were rectifying in the as-deposited state, but after annealing at 1100°C and 1000°C respectively for Pt/SiC and Pt/Si/SiC, these transformed into ohmic contacts. Pure Ti has also been considered as a contact. Annealing at 800°C for 1 minute after deposition of Ti showed a specific contact resistance in the range of 2 x 10^{-5} and 4 x 10^{-5} Ωcm^2 [28]. Table 2.4 shows a list of metals used as ohmic contacts to p-type α-SiC with the reported values for ρ_c.

Table 2.4: Ohmic contacts to p-type α-SiC and reported ρ_c values

Contact Metal	SiC carrier conc. (cm^{-3})	Annealing condition	ρ_c ($\Omega \cdot cm^2$)	Method of ρ_c measurement	Ref.
Al	1.8 x 10^{18}	700°C, 10 min	1.7 x 10^{-3}	TLM	[18]
Al	8 x 10^{18}	800°C, 10 min	10^{-2} -10^{-3}	TLM	[12]
Ta	>1 x 10^{19}	as-deposited	7 x 10^{-4}	TLM	[23]
Ti	>1 x 10^{19}	as-deposited	3 x 10^{-4}	TLM	[23]
Mo	>1 x 10^{19}	as-deposited	2 x 10^{-4}	TLM	[23]
Al-Ti	5 x 10^{15} – 2 x 10^{19}	1000°C, 5 min	2.9 x10^{-2} – 1.5 x 10^{-5}	Circ. TLM	[31]
Al-Ti/Al	2 x 10^{18} – 2 x 10^{19}	950-1000°C	4 x10^{-4} -10^{-5}	TLM	[32]

2.3 References

1. V. Saxena and A. J. Steckl, in *SiC Materials and Devices*, Y. S. Park (ed), **52**, 77 (1998).

2. F. Roccaforte, F. La Via and V. Raineri, *Int. J. of High Speed Electron. Syst.* **15,** 781 (2005).

3. R. F. Pierret, *Semiconductor Device Fundementals,* Addison-Wiley Publishing Company inc., (1996).

4. M. J. Bozack, *Phys. Stat. Sol.* (b), **202**, 549 (1997).

5. A. Tesfaye, *SiC Semiconductor Devices Technology, Modeling, and Simulation*, Dissertation, Universitat Wien Fakultat fur Elektrotechnik and Informationstechnik (2004).

6. A. Itoh, O. Takemura, T. Kimoto, and H. Matsunami, *Inst. Phys. Conf. Ser.* **142**, 685 (1996).

7. D. Defives, O. Durand, F. Wyczisk, O. Noblanc, C. Brylinski, and F. Meyer, *Microelectronic Engineering,* **55**, **No** 1-4, 369 (2001).

8. A. V. Adedeji, *Composite Contact Metallization on SiC for High Temperature Applications in Air,* Dissertation, Department of Physics, Auburn University (2005).

9. M. Li, *Ohmic Contacts to Implanted (0001) 4H-SiC*, Dissertation, Department of Physics, Auburn University (2009).

10. C. Fischer, *Bauelementsimulation in einer computergestützten Entwurfsumgebung*, Dissertation, TU Vienna (1994).

11. J. Crofton, L. M. Porter and J. R. Williams, *Phys. Stat. Sol*. (b) **202**, 581 (1997).

12. L. M. Porter and R. F. Davis, *Mater. Sci. Eng.* **B34**, 83 (1995).

13. S. Liu, K. Reinhardt, J. Scofield and C. Severt, *Workshop on High Temperature Power Electronics for Vehicles* (1995).

14. Y. Cao, L. Nyborg, D. Q. Yi, U. Jelvestam, *Mater. Sci. Tech.* **22**, 1227 (2006).

15. I. P. Nikitina, K. V. Vassilevski, N. G. Wright, A. B. Horsfall, A. G. O'Neill and C. M. Johnson, *J. Appl. Phys.* **97**, 083709 (2005).

16. S. K. Lee, C. M. Zetterling, M. Östling, J. P. Palmquist and U. Jansson, *Microelectron. Eng.* **60**, 261 (2002).

17. G. Kelner, S. Binari, M. Shur, and J. W. Palmmour, *Electronic Lett*. **27**, 1038 (1991).

18. J. Crofton, J. M. Ferrero, P. A. Barnes, J. R. Williams, M. J. Bozack, C. C. Tin, C. D. Ellis, J. A. Spitznagel, and P. G. McMullin, *Amorphous Crystalline Silicon Carbide IV*, C. Y. Yang, M. M. Rahman, and G. L. Harris (eds), SpringerVerlag, Berlin, p.176, (1992).

19. J. Crofton, P. G. McMullin, J. R. Williams and M. J. Bozack, *J. Appl. Phys*. **77 (3),** 1317 (1995).

20. T. Uemoto, *J. Appl. Phys*. **34,** L7 (1995).

21. J. Crofton, E. D. Lukowski, J. R. Williams, T. Isaacs-Smith, M. J. Bozack, and R. Siergiej, (in: Silicon Carbide and Related Materials VI-Kyoto 1995) *Inst. of Phys.Conf. Ser.* **142**, 569 (1996).

22. C. Arnodo, S. Tyc, F. Wyczisk, and C. Brylinski, (in: Silicon Carbide and Related Materials VI- Kyoto 1995) *Inst. of Phys. Conf. Ser.* **142**, 577 (1996).

23. J. B. Petit, P. G. Neudeck, C. S. Salupo, D. J. Larkin, and J. A. Powell, *Inst. of Phys.*149 *Conf. Ser*. **137**, 679 (1994).

24. D. Alok, B. J. Baliga, and P. K. Mclarty, *IEDM* 691 (1993).

25. M. M. Anikin, M. G. Rastegaeva, A. L. Syrkin, and I. V. Chuiko, *Amorphous Crystalline Silicon Carbide III-Springer-Verlag, Berlin*, F. L. Jarris, M. G. Spencer, and C. Y. Yang (eds) **56,** 183 (1992).

26. A. K. Chaddha, J. D. Parsons, and G. B. Kruaval, *Appl. Phys. Lett*. **66**, 760 (1995).

27. S. Liu, K. Reinhardt, C. Svert and J. Scofield (in: Silicon Carbide and Related Materials VI-Kyoto 1995) *Inst. of Phys. Conf. Ser.* **142**, 589 (1996).

28. J. Crofton, L. Beyer, J. R. Williams, E. D. Luckowski, S. E. Mohney and J. M. Delucca, *Solid State Electron.* **41**, 1725 (1997).

29. L. Kolaklieva, R. Kakanakov, G. Lepoeva and J. B. Gomes, *International Conference on Microelectronics* Vol **2,** 321 (*MIEL* 2004).

30. F. A. Mohammad, Y. Cao and L. M. Porter, *Appl. Phys. Lett.* **87**, 161908 (2005).

31. J. Crofton, P. A. Barnes, and J. R. Williams, *Appl. Phys. Lett*. **62**, 384 (1993).

32. N. Nordell S. Savage, and A. Schönder, *Inst. of Phys. Conf. Ser.* **142**, 573 (1996).

Chapter 3

Analytical Techniques

3.1 Electrical Characterization

The most important parameters in characterizing ohmic contacts are contact resistance (R_c), specific contact resistivity (ρ_c) and the sheet resistance (R_{sh}) of a semiconductor material. These parameters are used as an indication of whether the doping concentration of the sample is sufficient to produce ohmic contacts. The following sections discuss the methods used to calculate the contact parameters in this work.

3.1.1 Linear Transmission Line Method

The linear transmission line method (LTLM) is the most widely used method to measure contact resistance due to its simplicity. Other methods such as circular TLM, the van der Pauw method, or the collinear four point probe method, can also be used to measure the contact resistance and specific contact resistivity. The LTLM measurement involves calculating the total resistance (R_T) as a function of the length between two adjacent contact pads (L).

As seen in Figure 3.1(b), the total resistance between two adjacent contact pads can be given by, where R_s is the resistance of the semiconductor between the 2 adjacent contacts and R_c is the resistance of the contacts [1]:

$$R_T = R_s + 2R_c \tag{3.1}$$

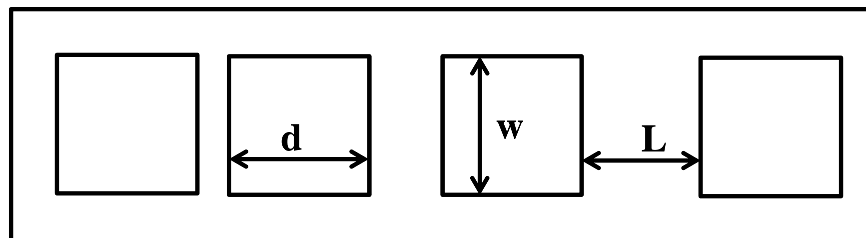

(a)

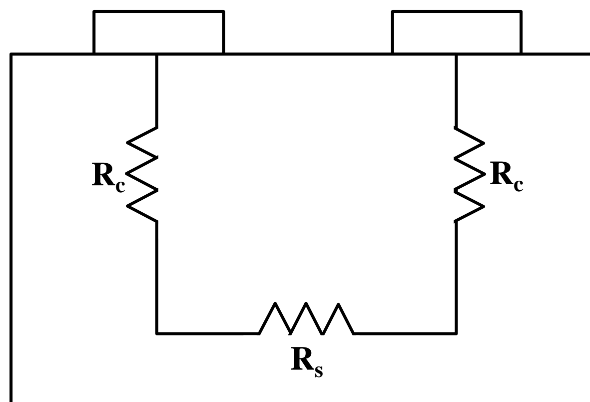

(b)

Fig. 3.1: (a) Top view of the LTLM contacts (b) Cross-sectional view of the semiconductor with LTLM contacts.

R_s can be written in terms of the sheet resistance R_{sh}:

$$R_S = \frac{R_{sh} L}{W} \tag{3.2}$$

where W is the width of a contact pad as seen in Figure 3.1(a). Therefore Equation 3.1 can be modified as:

$$R_T = \frac{R_{sh} L}{W} \tag{3.3}$$

R_c at the MS contact can be depicted by the resistor network shown in Figure 3.2, and R_1 and R_2 can be written as [2]:

$$R_1 = \frac{\rho_c}{W\Delta x} \tag{3.4}$$

$$R_2 = R_{sk} \frac{\Delta x}{W} \tag{3.5}$$

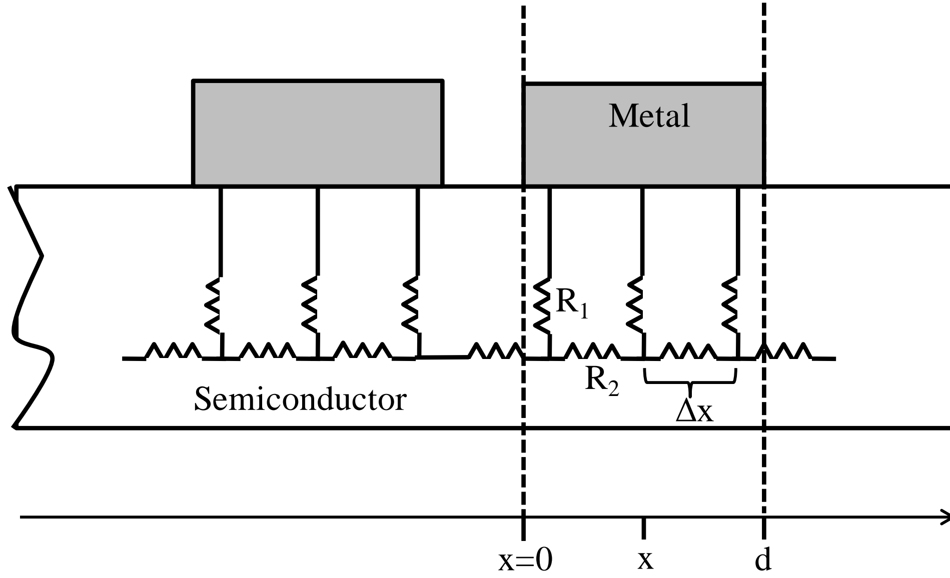

Fig. 3.2: TLM resistive network [2].

where R_{sk} is defined as the modified sheet resistance of the contact and W is the width of the contact as shown in Figure 3.1(a). By applying Kirchoff's law to the resistive network shown in Figure 3.2, the voltage and the current for an interval of Δx can be written as:

$$V(x + \Delta x) - V(x) = I(x)R_2 = I(x)R_{sk}\frac{\Delta x}{W} \tag{3.6}$$

When Δx →0,

$$\frac{dV}{dx} = I(x)\frac{R_{sk}}{W} \tag{3.7}$$

Similarly,

$$I(x + \Delta x) - I(x) = \frac{V(x)}{R_1} = V(x)\frac{W}{\rho_C}\Delta x \tag{3.8}$$

When $\Delta x \rightarrow 0$,

$$\frac{dI(x)}{dx} = V(x)\frac{W}{\rho_C} \tag{3.9}$$

Differentiating Equation 3.9 gives:

$$\frac{d^2I(x)}{dx^2} = \frac{W}{\rho_C}\frac{dV}{dx} \tag{3.10}$$

Integrating Equations 3.7 and 3.10 gives the following second order differential equation:

$$\frac{d^2I(x)}{dx^2} = \frac{W}{\rho_C}\ I(x)\frac{R_{sk}}{W} \rightarrow \frac{d^2I(x)}{dx^2} = \frac{R_{sk}}{\rho_C}\ I(x) \tag{3.11}$$

This can also be written as:

$$\frac{d^2I(x)}{dx^2} = \frac{I(x)}{L_T^2}; L_T = \sqrt{\frac{\rho_C}{R_{SK}}} \tag{3.12}$$

L_T is defined as the transfer length and the value can be obtained from the plot shown in Figure 3.3(b). The general solutions to Equation 3.12 can be written as:

$$I(x) = I_0 \frac{\sinh(\frac{d-x}{L_T})}{\sinh(\frac{d}{L_T})} \tag{3.18}$$

$$V(x) = I_0 \frac{L_T R_{SK}}{W} \frac{\cosh(\frac{d-x}{L_T})}{\sinh(\frac{d}{L_T})} \tag{3.14}$$

where d is the length of a contact pad, which is shown in Figure 3.1(a). Therefore, the contact resistance can be given by the following equation:

$$R_c = \frac{V(0)}{I(0)} = \frac{L_T R_{SK}}{W} \coth(\frac{d}{L_T}) \tag{3.15}$$

When $d >> 2L_T$, $\coth(d/L_T) \approx 1$:

$$R_c = \frac{L_T R_{SK}}{W} \tag{3.16}$$

Then R_T can be written as:

$$R_T = \frac{R_{sh} L}{W} + \frac{2 L_T R_{sk}}{W} \tag{3.17}$$

If the sheet resistance under the contact is not significantly modified, for the case of $d >> L_T$, $R_{sk} \approx R_{sh}$. Therefore Equation 3.17 becomes:

$$R_T = \frac{R_{sh} L}{W} + \frac{\sqrt{R_{sh} \rho_C}}{W} \quad (3.18)$$

Equation 3.18 can be fitted to the plot in Figure 3.3(b) and Equations 3.19 and 3.20 can be used to calculate the sheet resistance (R_{sh}) and specific contact resistance (ρ_c) respectively:

$$R_{sh} = (\text{slope})\ W \quad (3.19)$$

$$\rho_C = \frac{(\text{Intercept})^2 W^2}{4R_{sh}} \quad (3.20)$$

In certain MS contacts, the semiconductor under the contact has a modified sheet resistance, which implies that $R_{sh} \neq R_{sk}$. In this special case, an additional measurement of the contact end resistance (R_E) is required to find ρ_c. R_E is defined as [3]:

$$R_E = \frac{V}{I} = \frac{\sqrt{R_{SK} \rho_C}}{W} \frac{1}{\sinh(\frac{d}{L_T})} \quad (3.21)$$

However, since $L_T = \sqrt{\frac{\rho_C}{R_{sk}}}$, R_E can be written as:

$$\frac{R_C}{R_E} = \cosh(\frac{d}{L_T}) \quad (3.22)$$

Implementation

A typical LTLM pattern is shown in Figure 3.3(a), which illustrates that multiple lines of contact pads are generally used to improve accuracy. Figure 3.3(b) shows the plot of R_T vs L, where the sheet resistance (R_{sh}) can be derived from the slope while the intercept can be used to calculate the contact resistance (R_c).

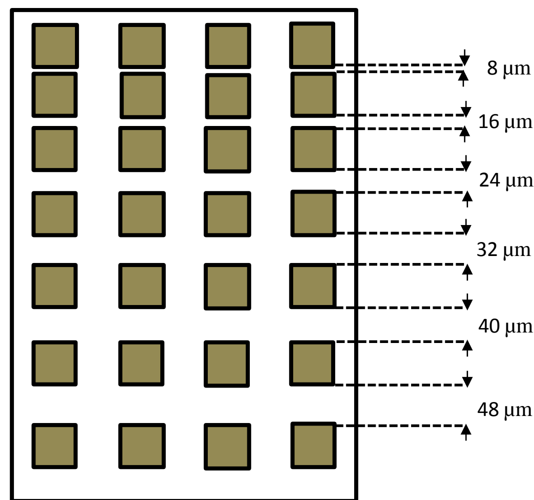

3.3(a)

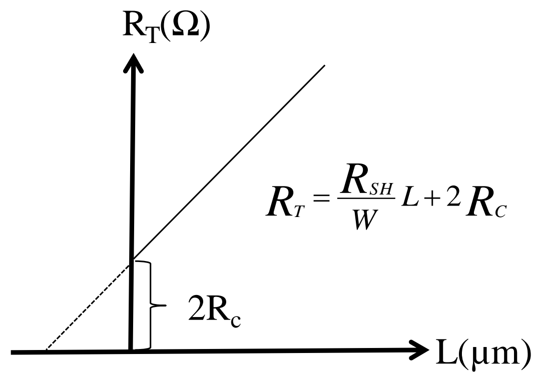

3.3(b)

Fig. 3.3(a): Typical LTLM pattern (b) Plot of total resistance (R_T) vs gap length (L) [1]

3.1.2 C-V Measurements

C-V (capacitance-voltage) measurements can be used to calculate the carrier concentration as a function of depth below the surface [4]. The capacitance of a metal semiconductor contact with a known area (A) can be measured by superimposing an AC voltage onto a DC bias [5]. Equation 3.23 shows the relationship between the capacitance (C) and the DC bias voltage (V) and Equation 3.24 shows the relationship between the depth from the surface and the capacitance:

$$\frac{1}{C^2} = -\left(\frac{2}{q\varepsilon_s N_D A^2}\right)V + \frac{2(V_{bi} - \frac{kT}{q})}{q\varepsilon_s N_D A^2} \tag{3.23}$$

$$w = \frac{\varepsilon_s A}{C} \tag{3.24}$$

In the above equations, q represents the charge of a proton, ε_s is the permittivity of the semiconductor material, N_D is the carrier concentration, A is the area under the contact, k is the Boltzmann constant, W is the depth from the surface of the semiconductor and V_{bi} is the built in potential. N_D can be obtained from the slope of the plot of $1/C^2$ vs V. After the carrier concentration is calculated, V_{bi} can be determined by using the intercept of the plot. Subsequently, the depth of the Fermi level beneath the conduction band can also be calculated using Equation 3.25:

$$V_n = -\left(\frac{kT}{q}\right)\ln(\frac{N_C}{N_D}) \tag{3.25}$$

where N_C is defined as the effective density of states of the conduction band of the semiconductor and is given by the following equation:

$$N_C = 2[\frac{2\pi mkT}{h^2}]^{\frac{3}{2}} \tag{3.26}$$

where m is the mass of an electron, h is Planck's constant, and g is defined as the number of conduction band minima. For 3C SiC the value of g is 6, while it has a value of 3 for 4H SiC [6]. Additionally, the barrier height (Φ_B) can be calculated by using Equation 3.27:

$$\Phi_B = V_{bi} + V_n \tag{3.27}$$

Implementation

CV measurements can be made by fabricating metal contacts with a known area on the surface of a lightly doped (n^-) semiconductor epitaxial layer that covers a highly doped (n^+) layer. Figure 3.4(a) shows a typical C-V measurement pattern in which the circular dots have a

known diameter and area and are used to obtain the C-V profile. Figure 3.4(b) shows the cross-sectional view of a typical C-V measurement sample.

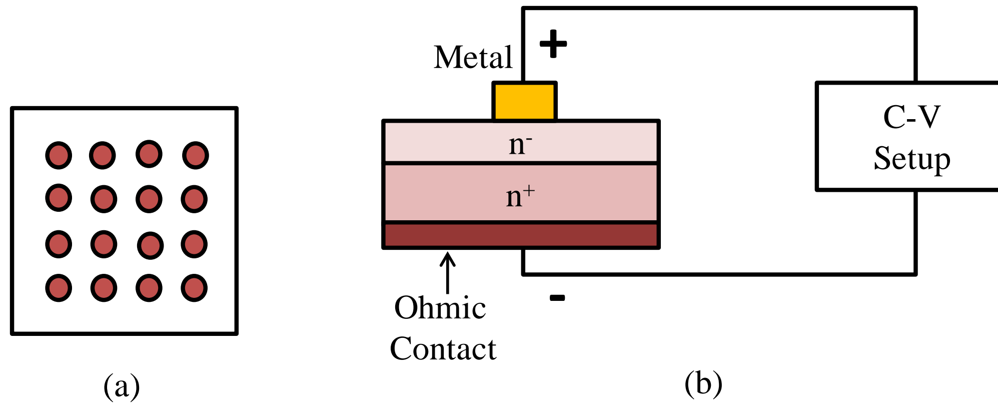

Fig. 3.4: (a) top view of C-V pattern (b) Cross-sectional view of C-V measurement sample.

3.2 Physical Analysis

3.2.1 Energy Dispersive X-ray Spectroscopy

Energy dispersive X-ray spectroscopy (EDX or EDS) is a widely used physical analysis technique for quantitative characterization of the elemental composition of a sample. The use of EDX coupled with a scanning electron microscope (SEM) has developed into a routine method for quantitative as well as qualitative chemical analysis of a surface [7]. Elements with a medium to high atomic number can be detected with high resolution using EDX. Due to its importance as a chemical analysis tool and the application possibilities, considerable research has been dedicated to EDX [8,9]

Principle

Using EDX for quantitative analysis involves the counting of net intensities of characteristic X-ray energy peaks in the range of 0-20 KeV, but it will also determine the background contribution for each spectrum and subtract them from the net intensities. One method used to determine the background contribution is to assume a straight line contribution and subtract it over the full spectrum, but a more widely accepted method is the use of Kramer's law [10]:

$$N_{Back} = CZ\frac{E_0 - E}{E} \qquad (3.28)$$

where N_{Back} represents the number of bremsstrahlung photons, E is the photon energy, Z is the mean atomic number, and E_o is the primary energy of the electrons. C is a factor that involves the original Kramer's constant and corrections according to the efficiency of the detector and the absorption of X-rays in the sample.

Castaing [11] was the first to outline the procedure used for the quantization of EDX spectra. The ratio of the concentration of a certain element in a given sample (C_{SP}) and the concentration of the same element in a standard sample (C_{ST}) can be given by the following equation:

$$\frac{C_{SP}}{C_{ST}} = K\frac{I_{SP}}{I_{ST}} \qquad (3.29)$$

where I_{SP} and I_{ST} are the X-ray intensities from the unknown sample and standard sample, respectively. K is a factor that is accounted for by X-ray intensities, differences in X-ray absorption, and X-ray fluorescence. However, for thin films the absorption and fluorescence effects can be neglected [12]. Therefore, for a thin sample composed of two elements A and B, the concentration ratio of C_A and C_B can be written in terms of the intensities I_A and I_B and is given by the following equation [7]:

$$\frac{C_A}{C_B} = k_{AB}\frac{I_A}{I_B} \tag{3.30}$$

k_{AB} is referred to as the Cliff-Lorimer factor, which depends on the accelerating voltage, the microscope and the EDX detector system being employed.

Limitations

X-ray intensity versus energy is the method used to plot EDX spectra. Gaussian shaped characteristic peaks for the elements present in samples are superimposed on a bremsstrahlung continuum. Although EDX can detect most of the chemical elements, light elements ($Z<11$) are beyond its limitations. Furthermore, EDX has a minimum detectable limit of approximately 0.01 atomic percent, and the accuracy of the spectrum can be affected by overlapping peaks as well as the nature of the sample [7].

Apparatus

EDX systems are commonly coupled with SEM systems. When electrons strike a sample in an SEM, X-rays characteristic of each element are emitted [7]. The energy of the emitted X-rays gives a specific signal due to the unique atomic structure of elements. Depending on the energy of the electron beam, it is possible to chemically analyze an area near the surface of a sample with a depth of 1-3 μm as shown in Figure 3.5.

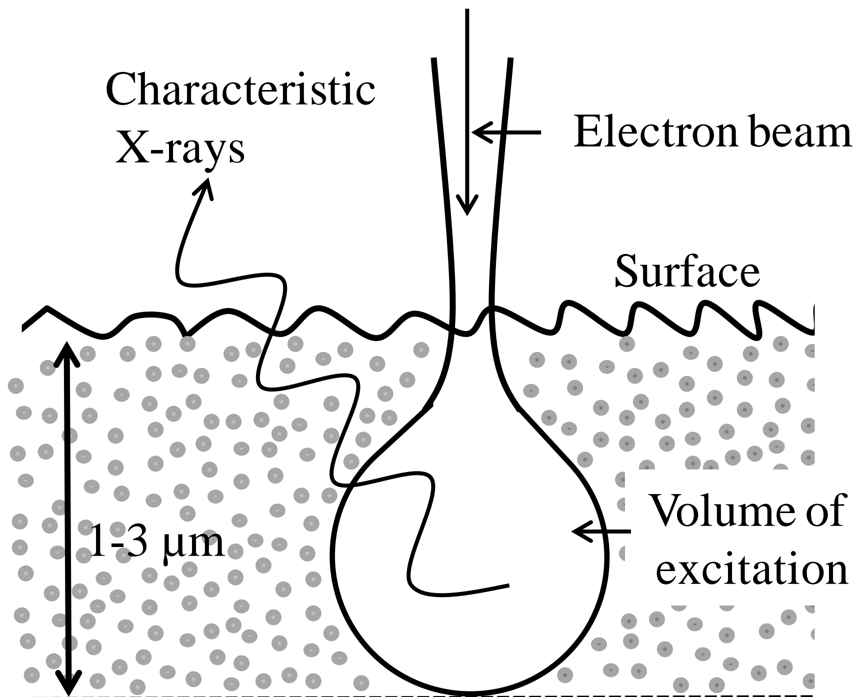

Fig. 3.5: Cross-sectional view of the EDX analysis area

A typical EDX system would consist of a semiconductor detector that converts the energy of the emitted X-rays into voltage signals. The two most commonly used semiconductor detector materials are lithium-drifted Si crystal and high purity Ge crystal [13]. Li is used to

compensate for any impurity effects of Si and to subsequently produce an intrinsic region in the Si(Li) crystal, which is necessary to detect X-rays. Figure 3.6 shows a schematic of an EDX system. Following the emission of characteristic X-rays due to the bombardment of the electron beam on the sample, a semiconductor crystal detects the X-ray energies and converts them into a voltage signal. The signal subsequently undergoes amplification and reaches a multi-channel analyzer (MCA),depicted in Figure 3.6.

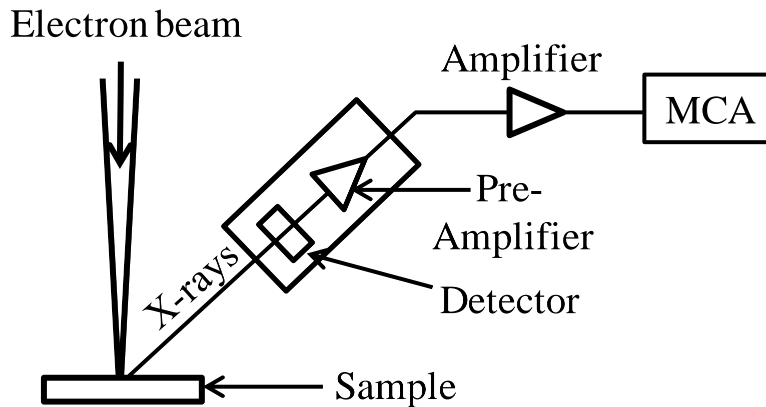

Fig. 3.6: Schematic of an EDX system.

When X-rays hit the detector, electron-hole pairs are generated inside the crystal. The energy required to produce one electron-hole pair in Si(Li) is 3.8 eV. An X-ray photon will have energy in the range of KeV, meaning that there will be thousands of electron-hole pairs generated within the crystal. EDX analysis uses the count of these electron-hole pairs and the count is directly proportional to the energy of the X-rays. A negative bias of about 1 KeV is applied on the crystal to separate the electron-hole pairs. Gold is used as the contact for the detector crystal and liquid nitrogen is used to cool the detector crystal, minimizing the

occurrence of thermally activated electron-hole pairs [7]. A schematic of an Si(Li) detector is shown in Figure 3.7.

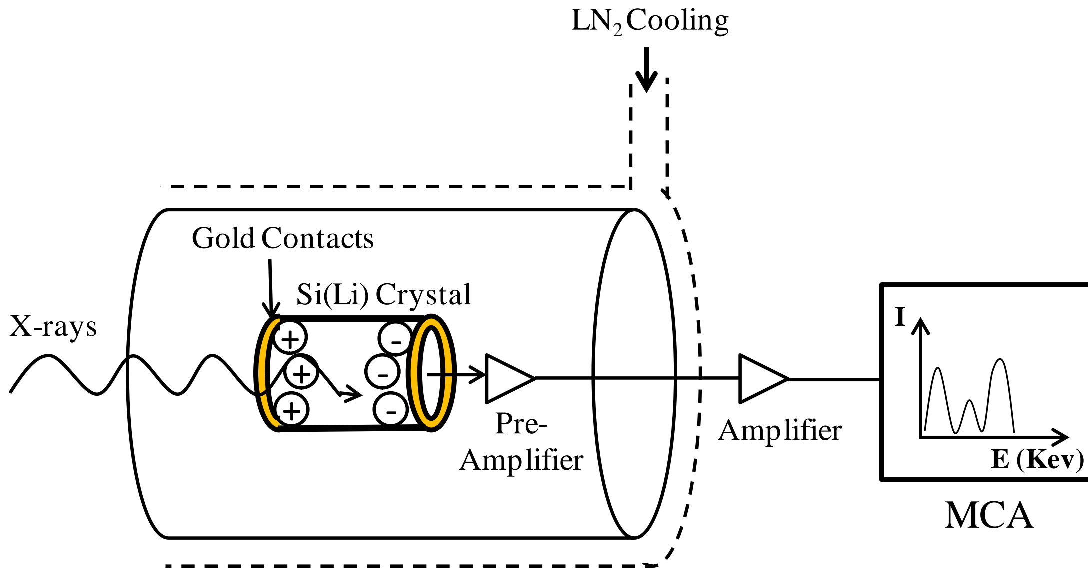

Fig 3.7: Si(Li) crystal detector [7].

3.2.2 Secondary Ion Mass Spectrometry

Secondary ion mass spectrometry (SIMS) is the standard technique used to measure the concentration of trace elements in a semiconductor. The main advantages of this technique over others such as EDX (Section 3.2.1) are its high sensitivity, its capability to detect all elements and its inherent capacity to measure depth profiles.

The first SIMS apparatus was designed and built by Herzog and Viehböck [14] in 1949. The first sophisticated SIMS instruments were built concurrently in the 1960s by Herzog et al. [15] and Castaing et al. [16]. The acronym SIMS was first used by Benninghoven in 1970 [17].

Principle

SIMS involves bombarding the surface of a sample with a positive ion beam, also known as a primary ion beam. This leads to interactions that emit various types of secondary particles including Auger electrons, photons, positive secondary ions and negative secondary ions. The basis of this technique is the analysis of negative and positive secondary ions using mass spectrometry. The mass spectra of characteristic peaks can be used to identify the substrate material, impurities or any form of contamination in the surface region.

When a heavy energetic ion strikes a surface, it penetrates into the surface until all the energy is lost due to collisions and scattering. On its way into the material, it displaces some of the atoms from the original crystalline structure, leading to more collisions and more displaced atoms. This is referred to as a collision cascade [7] and is illustrated in Figure 3.9. The emission of atoms from a surface during sputtering can be explained theoretically using Sigmund's collision cascade model [18].

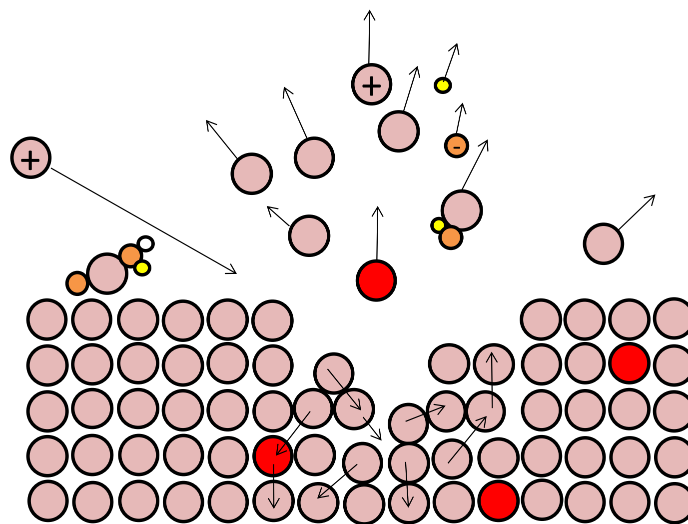

Fig. 3.8: Schematic of the ion bombardment process.

When bombarding the surface of a material A with energetic primary ions, particles of A in the near surface regions are either driven deeper in or completely removed. The disappearance yield $Y_D(A)$ is given by the following equation:

$$Y_D(A) = \frac{\text{No. of sputtered A}}{\text{No. of primary ions}} \tag{3.31}$$

During the bombardment process, some of the emitted particles are charged while others are neutral. Emitted particles can be either complete or fragmented molecules. The transformation probability gives the likelihood of desorption of A into the emission channel (X_i^q), and is shown in Equation 3.32. Here, i represents the index to distinguish between different emission channels while q is the integer charge of the particle X_i:

$$P(A \rightarrow X_i^q) = \frac{\text{No. of emitted particles } X_i^q}{\text{No. of sputtered A}} \tag{3.32}$$

However, the transformation probability cannot be measured directly because of its dependence on the concentration and the matrix, which is the primary impediment in SIMs analysis. This is referred to as the "matrix effect" [7]. Therefore, a more appropriate criteria would be the secondary yield $Y^{(q)}(X_i^q)$, which is defined in Equation 3.33 as the average number of emitted particles for each primary ion:

$$Y^q(X_i^q) = \frac{\text{No. of emitted particles } X_i^q}{\text{No. of primary ions}} \quad (3.33)$$

The detected yield Y (X_i^q), which is the number of detected particles for each primary ion, is given by:

$$Y^q(X_i^q) = \frac{\text{No. of emitted particles } X_i^q}{\text{No. of primary ions}} \quad (3.34)$$

Another important parameter is the useful yield Y_u (X_i^q), which indicates the extent to which the material is used during analysis. It is used to estimate the sensitivity of the mass spectrometric method:

$$Y_u\left(X_i^q(A)\right) = \frac{\text{No. of detected } X_i^q}{\text{No. of sputtered A}} \quad (3.35)$$

The product of the transmission of the mass spectrometer T (X_i^q) and the detections probability D (X_i^q) gives the probability of detecting one sputtered particle. For a TOF mass spectrometer, both values range between 10 and 50 percent [7].

Apparatus

A SIMS instrument can be divided into two main parts: a primary ion source and a mass analyzer. The primary ion source generates the ion beam that is aimed at the sample. There are a variety of ion sources being used in SIMS instrumentation and electron impact (EI) ion sources are the simplest type. In an EI ion source, O_2 or Ar gas flows through an ionization region where an incandescent filament accelerates electrons, which then collide with the gas atoms to produce O_2^+ or Ar^+ ions. These ions are accelerated towards electrostatic focusing lenses by means of an extraction cathode. Another widely used type of source is the Duoplasmatron, in which O_2 or Ar ions are bombarded using gas-discharge ion sources. Research has shown that the molecular secondary ion yields can be increased considerably by using primary ions of polyatomic molecules like SF_5^+ created in EI ion sources [19, 20].

Mass analyzers are used to extract the emitted secondary ions, then separate and detect the masses. An important aspect of a SIMS mass spectrometer is minimization of the surface damage by having a high yield of detected secondary ions. Two of the most commonly used mass spectrometer systems are quadrupole mass spectrometers and the time of flight (TOF) mass spectrometers. Recently, TOF mass spectrometers have been more widely used due to its ability to analyze large molecules on the surfaces of heavy metals and alloys. Another advantage of TOF mass spectrometers is the simultaneous detection of all masses of equal polarity. The possibility of reconstructing TOF spectra for any ion species as a function of the depth from the surface and its lateral position is possible by acquiring raw data [21]. The Mattauch-Herzog mass analyzer, which is capable of detecting several masses simultaneously [22], is shown in Figure 3.8.

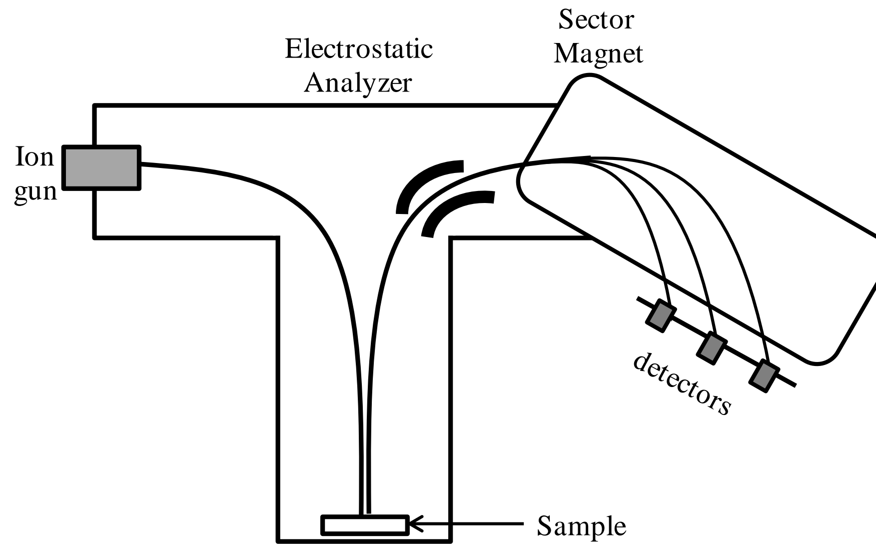

Fig 3.9: Schematic diagram of the Mattauch-Herzog magnetic sector instrument capable of simultaneous mass detection [7]

3.2.3 Rutherford Backscattering Spectrometry

Rutherford Backscattering Spectrometry (RBS) is one of the most widely used techniques for quantitative characterization of thin films in the near-surface regions. Due to its quantitative nature, it is often accepted as the standard for other techniques [7]. The 'gold foil experiment' performed by Geiger and Marsden in the early twentieth century under the guidance of Ernest Rutherford [23], is the basis for the physical process of RBS. Since then it has developed in to a major characterization technique.

Principle

When a beam of monoenergetic ions (He^{+}) with an energy of 1 eV to 3eV hits a target, the energies of the ions scattered back are analyzed. In a backscattering collision, energy is transferred from the accelerated particle to a stationary particle. Since the energy range (1–3 MeV) is below the requirement for a nuclear reaction, only coulomb interactions ensue and the collisions are considered elastic. Figure 3.10 shows the collision between an accelerated particle with mass M_1 and the stationary sample with mass M_2.

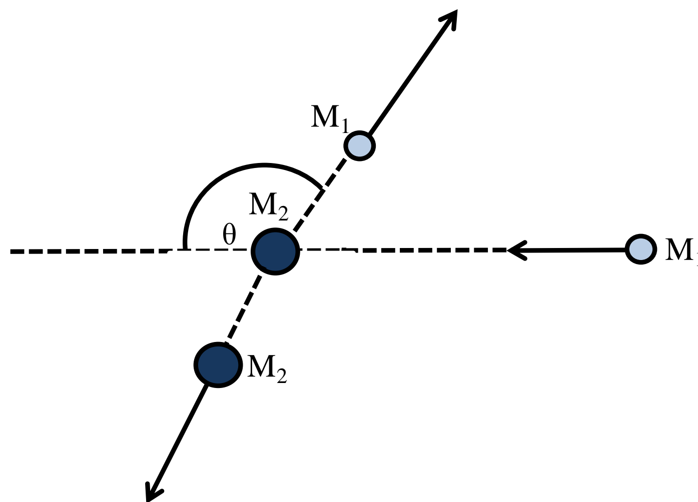

Fig. 3.10: Collision between the accelerated ion and the stationary target.

Since the collisions are considered elastic, conservation of momentum and conservation of energy both apply. The ratio of the energy of an accelerated ion before the collsion (E_o) and after the collision (E_1) is given by [24]:

$$\frac{E_1}{E_0} = K = [\frac{(M_2^2 - M_1^2 \sin^2\theta)^{1/2} + M_1\cos\theta}{M_2 + M_1}]^2 \quad (3.36)$$

where K is referred to as the kinematic factor. If M_1, E_o and θ are known, M_2 can be calculated and the target element can be identified. When the scattering angle (defined later in Figure 3.11), is 180°, Equation 3.36 becomes:

$$\frac{E_1}{E_0} = (\frac{M_2 - M_1}{M_2 + M_1})^2 \quad (3.37)$$

When M_1=M_2, there is a complete energy transfer. If M_2 is less than M_1, backscattering will not occur. For an ion beam with a total number of Q ions hitting the surface of a sample with element A, the number of backscattered ions being detected (Q_A) is given by:

$$Q_A = Y_A = QN_A\sigma_A\Delta\Omega \quad (3.38)$$

where N_A represents the surface density of A type atoms on the surface, σ_A is the differential scattering cross-section and ΔΩ is the solid angle of the detector. σ_A is defined as the probability of a projectile being scattered through an angle of θ to a solid angle of dΩ. The scattering cross-section can be given by:

$$\sigma(E,\theta) = \left(\frac{Z_1 Z_2 e^2}{4E}\right) \frac{4[(M_2^2 - M_1^2 \sin^2\theta)^{1/2} + M_2 \cos\theta]^2}{M_2 \sin^4\theta\,(M_2^2 - M_1^2 \sin^2\theta)^{1/2}} \tag{3.39}$$

where Z_1 represents the atomic number of the accelerated particle and Z_2 is the atomic number of the target atom.

For a known primary ion under controlled experimental conditions, the scattering cross-section depends only on the mass and atomic number of the scattering atom, which can be easily calculated. Therefore, for a compound film with a composition of A_mB_n, the ratio between m and n can be given by [7]:

$$\frac{n}{m} = \frac{N_B}{N_A} = \frac{Q_B \sigma_A}{Q_A \sigma_B} \tag{3.40}$$

When targets contain multiple elements that can produce overlapping peaks, computer simulations are necessary to analyze RBS spectra. The accuracy of RBS is less than 1% when analyzing stoichiometric ratios and close to 3% for analyzing areal densities [7].

Apparatus

RBS analysis systems are usually coupled with linear accelerators. Typical energy values of the accelerated ions range from 1 MeV to 3 MeV. The other important part of an RBS system is the detector, so a solid state detector is generally used to detect the back scattered ions. Two of

the most widely used detectors are silicon surface barrier detectors and passivated implanted planar silicon detectors (PIPS). The PIPS detector has better energy resolution for RBS using He^+ ions compared to surface barrier detectors [25]. Figure 3.11 shows a schematic diagram of a simple RBS system.

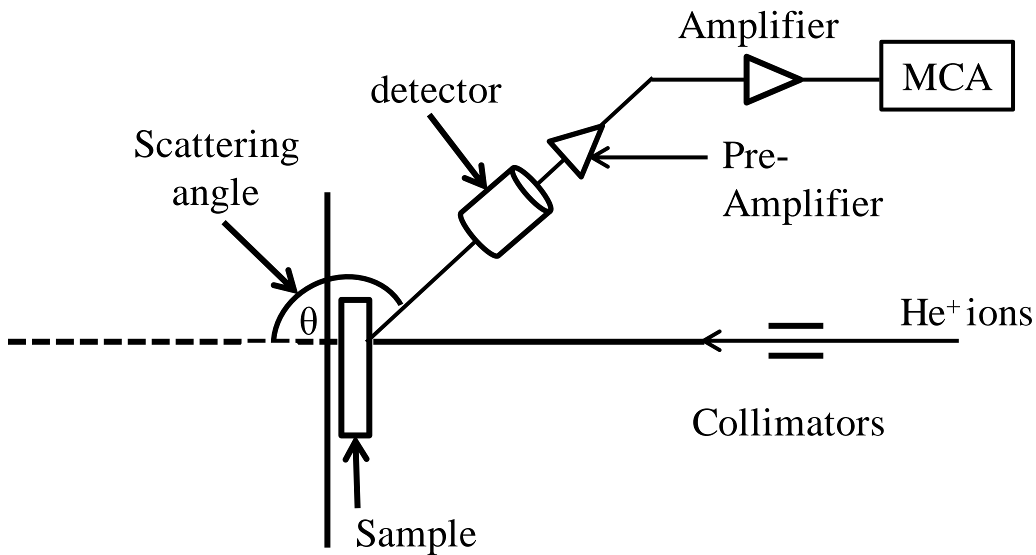

Fig: 3.11: Schematic diagram of an RBS system

3.3 References

1. G. K. Reeves and H. B. Harrison, *IEEE Electron Device Letters*, **EDL 3** (5) 111 (1982).
2. http://ecee.colorado.edu/~bart/book/book/chapter3/ch3_5.htm
3. H. B. Harrison, *Proc. IREE Aust*. **41**, 95 (1980).
4. S. M. Sze, *Physics of Semiconductor Devices*, 2nd ed. , New York: John Wiley & Sons, (1981).

5. T. N. Oder, *"Fabrication and Characterization of Ohmic Contacts to p- and n-type Silicon Carbide with Applications to p-n Junction Diodes"*, Dissertation, Department of Physics, Auburn University (1999).

6. S. Yoshida, *Properties of Silicon Carbide,* G. L. Harris (ed.), EMIS Datareviews Series No. 13, INSPEC, London, pp 74 (1995).

7. *Surface and Thin Film Analysis*, H. Bubert and H. Jennet (eds.), Wiley-VCH Verlag GmbH D-69469 Weinheim (2002).

8. L. Reimer in: *Scanning Electron Microscopy: Physics of Image Formation and Microanalysis,* Springer-Verlag, Berlin-Heidelberg-New York, (1998).

9. D. B. Williams and C. B. Carter in: *Transmission Electron Microscopy – A Textbook for Material Science,* Plenum Press, New York and London, (1996).

10. H. A. Kramers, *Phil. Mag.* **46**, 836 (1923).

11. R. Castaing, *"Application of Electronic Sensors to a Method for Analyzing Chemical and Crystallographic point"*, Dissertation, University of Paris (1951).

12. G. Cliff and G. W. Lorimer, J. Microsc. **103**, 203 (1975).

13. K. F. J. Heinrich, *Electron Beam X-ray Microanalysis,* Van Nostrand, New York, (1981).

14. R. F. K. Herzog and F. P. Viehböck, *Phys. Rev.* **76**, 855L (1949).

15. R. F. K. Herzog and H. Liebl, *J. Phys.* **34**, 2893 (1963).

16. R. Castaing, G. Slodzian, *J. de Microscopie* **1**, 395 (1962).

17. A. Benninghoven, *Z. Phys.* **239**, 403 (1970).

18. P. Sigmund in: *Inelastic Ion-Surface Collisions,* N. H. Tolk, J. C. Tully, W. Heiland, C. W. White (eds.), Academic Press, New York (1977).

19. D. Stapel, O. Brox and A. Benninghoven, *Appl. Surf. Sci.* **140**, 156 (1999).

20. K. Kötter and A. Benninghoven, *Appl. Surf. Sci.* **133**, 47 (1998).

21. K. Iltgen, C. Bendel, E. Niehuis and A. Benninghoven, *J. Vac. Sci. Technol.* A **15**, 460 (1997).

22. J. Mattauch and R. Herzog, *Z. Phys.* **89**, 786 (1934).

23. H. Geiger and E. Marsden, *Phil. Mag.* **25**, 606 (1913).

24. L. C. Feldman and J. W. Mayer, *Fundementals of Surface and Thin Film Anaysis,* North Holland, New York (1986).

25. E. Steinbauer, P. Bauer, M. Geretschlă, G. Bortels, J. P. Biersack and P. Burger, *Nucl. Instr. Meth.* B **85,** 642 (1994)

Chapter 4

Diffusion and Doping in Silicon Carbide

4.1 Diffusion in Semiconductors

High temperature diffusion has been one of the most important processing steps in the fabrication of semiconductor devices. Thermal diffusion was the preferred method of introducing impurities such as boron and phosphorus into silicon in the 1960s until it was replaced by ion implantation in the 1970s [1]. However, thermal diffusion is still an essential mechanism in the diffusion of impurities within a semiconductor and in the activation of dopants introduced using ion implantation.

4.1.1 Mathematical Basis

The diffusion process follows Fick's first law of diffusion, which states that the impurity flux goes from regions of high concentration to regions of low concentration with a magnitude that is proportional to the concentration gradient in the region. Fick's first law in one–dimension is given by:

$$J = -D \frac{\partial N}{\partial X} \tag{4.1}$$

where J represents the particle flux of the donor or acceptor impurity atoms, D is the diffusion coefficient and N is the concentration of the impurity. The diffusion coefficient depends exponentially on temperature and follows the Arrhenius behavior according to:

$$D = D_0 e^{\left(\frac{-E_A}{kT}\right)} \tag{4.2}$$

where D_o represents the maximum diffusion coefficient, E_A is the activation energy, k is the Boltzmann constant and T is the temperature.

Fick's second law of diffusion, which explains the time dependence of the diffusant concentration, can be derived from the continuity equation below:

$$\frac{\partial N}{\partial t} = -\frac{\partial J}{\partial x} \tag{4.3}$$

Fick's second law is obtained by combining Equation 4.1 and Equation 4.3, and is shown in Equation 4.4:

$$\frac{\partial N}{\partial t} = -D\frac{\partial^2 N}{\partial x^2} \tag{4.4}$$

The second order partial differential equation can be solved for the time and spatial dependence of the impurity concentration. Two specific types of boundary conditions are important in modeling impurity diffusion in semiconductor and they are defined as constant-source diffusion and limited-source diffusion. In constant-source diffusion, the surface concentration of the

impurity is held constant while in limited-source diffusion, a thin layer of the impurity is deposited on the surface to provide a fixed quantity of the dopant [2].

During the constant-source diffusion, the solution to Equation 4.4 can be obtained by:

$$N(x,t) = N_0 \operatorname{erfc}\left(\frac{x}{2\sqrt{Dt}}\right) \tag{4.5}$$

where N_o represents the impurity concentration of the surface of the wafer. The solution is referred to as a complimentary error function (erfc) diffusion and is shown in Figure 4.1. As time progresses, the diffusion front moves into the wafer while the surface concentration remains constant. As seen in Figure 4.1, the diffusion front moves deeper into the wafer as the Dt product increases, which can be due to increasing diffusion time, increasing temperature or a combination of both.

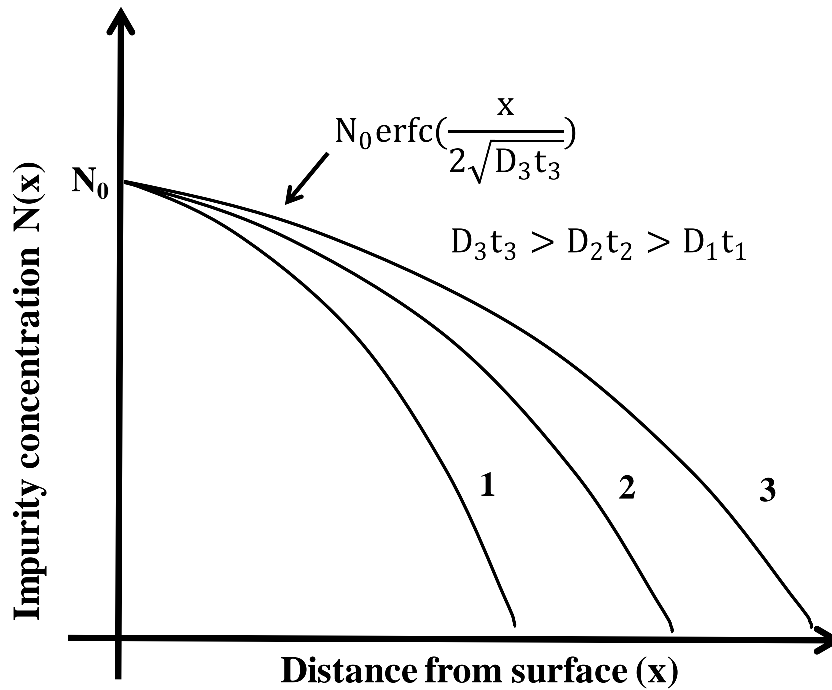

Fig. 4.1: Constant-source diffusion profiles

The total number of impurity atoms per unit area in the semiconductor is referred to as the dose, Q [2]. In a constant-source diffusion, an external impurity source supplies a continuous flow to the surface of the wafer, which leads to increasing dose over time. The dose can be calculated by integrating the depth and time-dependent impurity concentrations through the depth of the wafer and is given by:

$$Q = \int_0^{\infty} N(x,t)dx = 2N_0\sqrt{\frac{Dt}{\pi}} \quad (4.6)$$

For a limited-source diffusion with a thin layer of impurity placed on the surface of the wafer, Equation 4.4 is solved by using an impulse function at the surface of the wafer [3]. The impulse function, which is also referred to as the Dirac delta function, has a real line number that is zero at every location except at the origin, which has an integral of 1 over the entire real line. Since there is a thin layer of the impurity at the surface of the wafer, an impulse function can be used to describe the boundary conditions at the surface. Therefore, the solution can be found through the Gaussian distribution given by:

$$N(x,t) = \frac{Q}{\sqrt{\pi Dt}} e^{-(\frac{x}{2\sqrt{Dt}})^2} \quad (4.7)$$

A typical diffusion profile for a limited-source diffusion is shown in figure 4.2. In a limited-source diffusion process, the dose remains constant throughout, which causes the area under the curve to remain the same. As the impurity diffuses in to the sample, the surface concentration decreases. A typical diffusion profile for a limited-source diffusion, including a decrease in surface concentration, is shown in Figure 4.2.

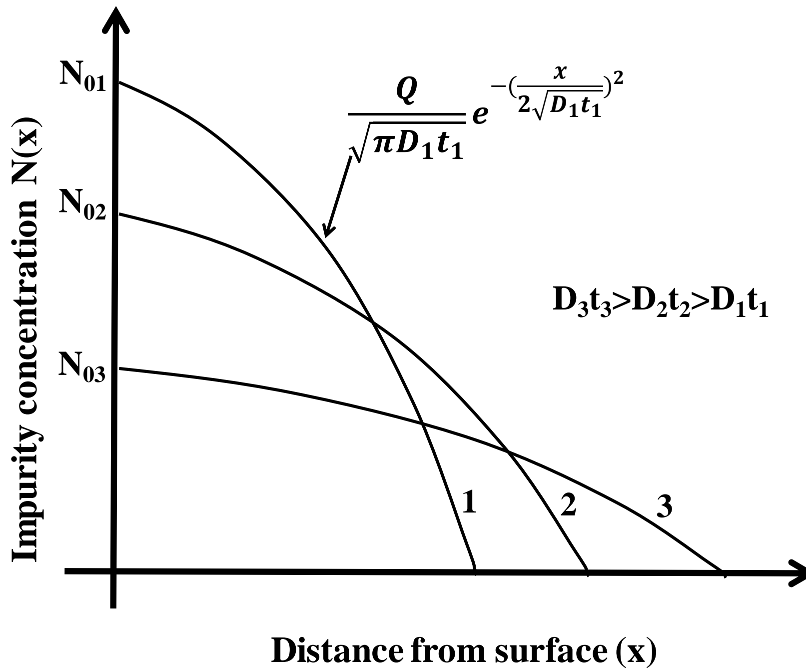

Fig. 4.2: Limited-source diffusion profile [1].

4.1.2 Diffusion Mechanisms

There are various mechanisms by which impurity atoms diffuse in a material. Three of the most important are the substitutional diffusion mechanism, the direct interstitial diffusion mechanism, and the kickout mechanism. The impurity atoms in contact with or in close proximity to the surface of a semiconductor, when provided with favorable conditions, move into the semiconductor crystal via substitutional (vacancy) or interstitial diffusion mechanisms.

In the process of substitutional diffusion, an impurity atom jumps from one crystalline lattice vacancy to another, substituting for the semiconductor atoms. Vacancies must be available in the semiconductor lattice in order for substitutional diffusion to occur. Although a certain

number of vacancies occur statistically in a semiconductor, additional vacancies can be created at high temperatures [1]. Figure 4.3 shows the process of substitutional diffusion of impurity atoms.

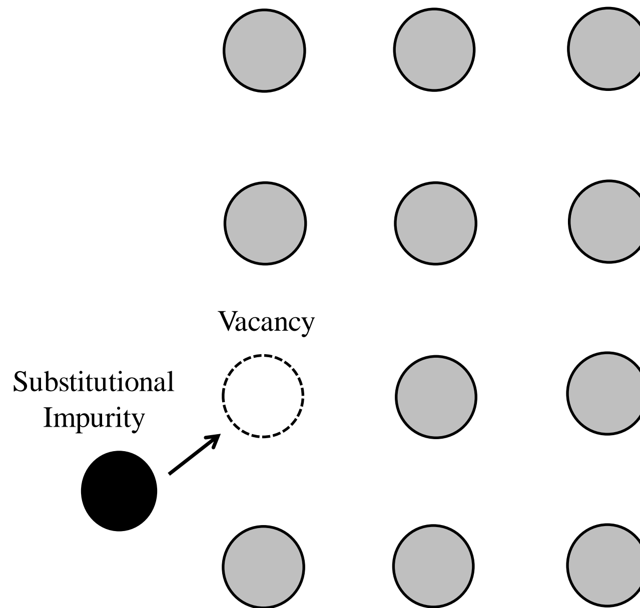

Fig. 4.3: Substitutional diffusion in a two dimensional lattice.

Considerable space exists between the atoms in a semiconductor lattice, and these spaces are referred to as interstitial sites. In direct interstitial diffusion, some impurity atoms diffuse through the crystal structure by hopping through these interstitial sites. Figure 4.4 shows the direct interstitial process, where the impurity atom moves through the interstitial sites on a random path.

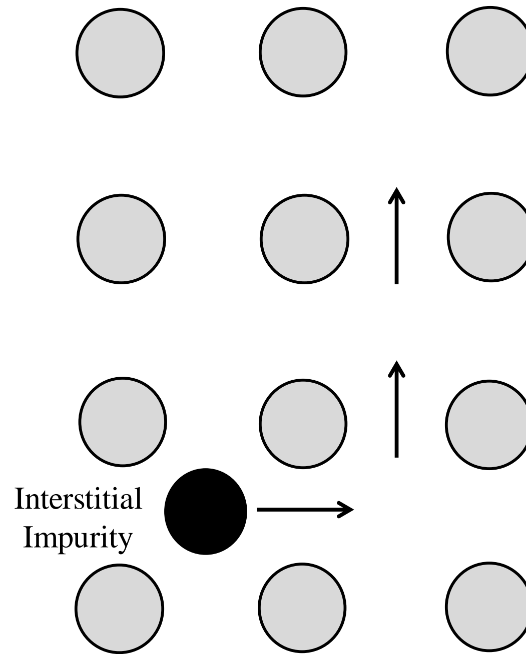

Fig. 4.4: Direct interstitial diffusion mechanism.

Another important diffusion process is the kickout mechanism, where the impurity atom replaces a semiconductor atom from the crystalline lattice. The released semiconductor atom is moved to an interstitial site. In this mechanism, the impurity atom may have moved through the lattice via the direct interstitial mechanism prior to replacing the semiconductor atom. Figure 4.5 shows the process of the kickout mechanism. Following the kickout mechanism, a self-interstitial (semiconductor atom at an interstitial site) and a substitutional impurity atom are created.

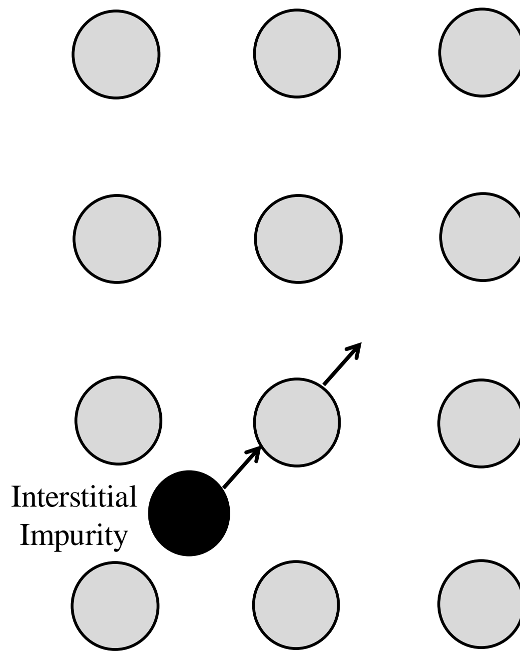

Fig. 4.5: Kickout mechanism.

Direct interstitial diffusion is a fast process compared to substitutional diffusion due to the latter requiring vacancies in the crystalline lattice. However, the slower mechanism is advantageous because substitutional diffusion affords more control of the process, while the rapid diffusion rate of direct interstitial diffusion makes it difficult to control. Another important aspect is that the impurity atoms need to be in substitutional positions in order to conduct electricity, making substitutional diffusion the preferred process. The kickout mechanism can be explained as a combination of the interstitial and substitutional processes. This mechanism for phosphorus diffusion in silicon carbide is given by Equations 4.8, where P_i represents a

phosphorus atom at an interstitial site, P_{Si} is a phosphorus atom occupying a silicon lattice site, and Si_i is a silicon atom at an interstitial site.

$$P_i \leftrightarrow P_{Si} + Si_i \quad (4.8)$$

De Souza et al. [4] reported the study of the characteristics of the kickout mechanism in silicon under thermodynamic equilibrium conditions and concluded that it is applicable in dilute impurities. The kickout mechanism for boron diffusion in silicon carbide has been studied both theoretically [5] and experimentally [6,7]. Rurali et al. [4] reported theoretical evidence that substitutional boron (B_{Si}) is readily replaced by a nearby silicon interstitial (Si_i) via a kickout mechanism. The fast diffusion of boron in SiC, compared with other dopants, can be attributed to this mechanism and the preference of boron to occupy subtitutional silicon sites [7]. Bockstedte et al. [6] reported various effects of silicon and carbon interstitials on boron acceptors in silicon and carbon sub lattices. The dominant formation of B_C in the diffusion tails of the boron profiles can be attributed to the fact that a larger kick-in barrier into silicon sites exists relative to the carbon sites [6]. Several defects that occur in silicon carbide are discussed further in the next section.

4.2 Defects in Silicon Carbide

Point defects in semiconductors are vital for controlling the electronic properties of materials according to specific requirements. Shallow substitutional impurity elements such as boron and phosphorus act as p-type and n-type dopants, respectively, for conduction in SiC. Shallow dopants in SiC, such as nitrogen and aluminum, have been studied extensively and the properties of these defects are well understood [8]. There are also intrinsic deep level defects in the band gap of SiC. Because it is a compound semiconductor, SiC has two kinds of main vacancies; those at silicon sites V_{Si} and the others at carbon sites V_C. There are two inequivalent sites of 4H-SiC, one with cubic surroundings and the other with hexagonal surroundings. These different sites are expected to cause site-dependent impurity levels. Figure 4.6 shows the vacancies at lattice sites with local cubic or hexagonal formations.

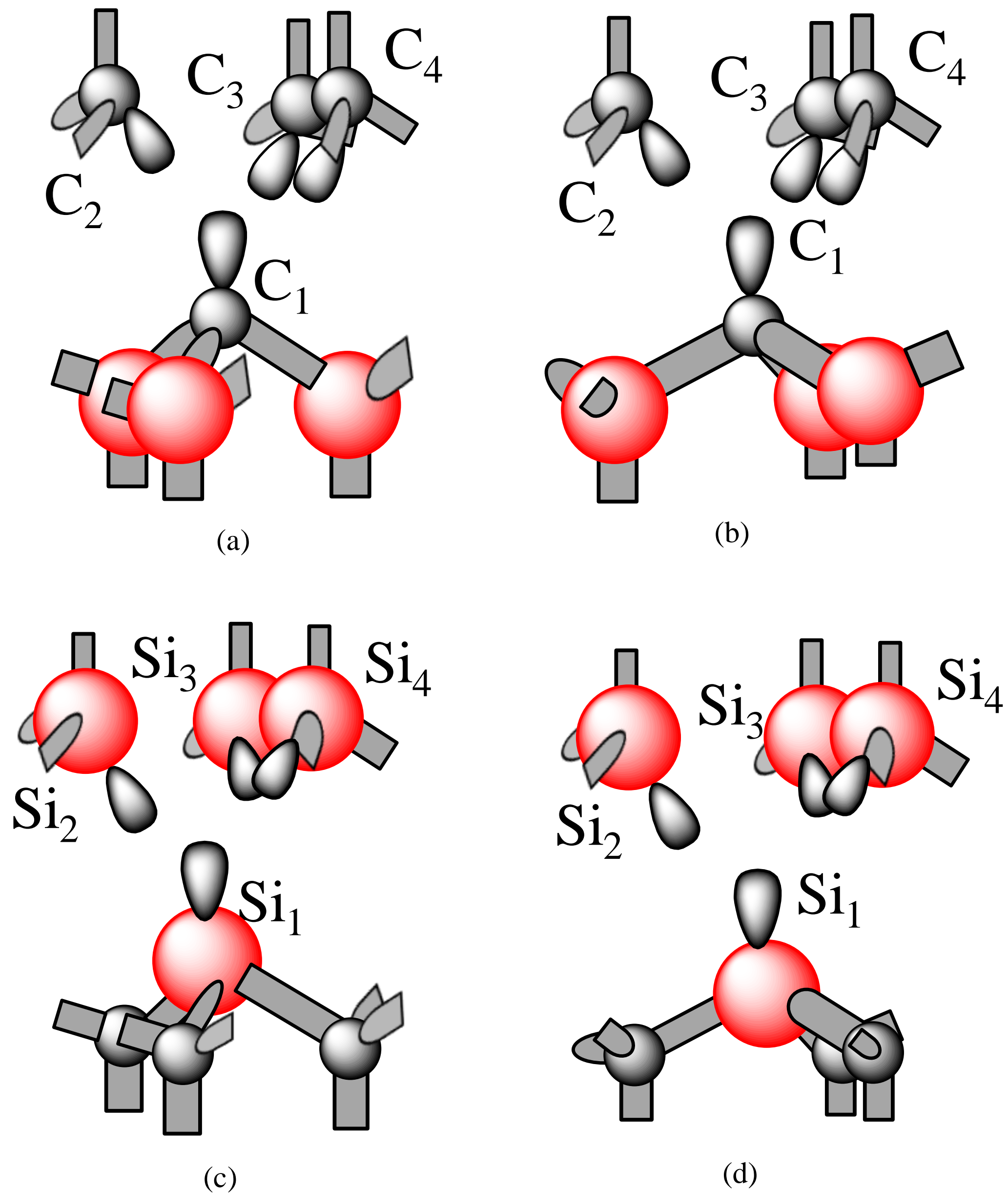

Fig. 4.6: Structural diagram of the vacancies in 4H-SiC: (a) V_{Si} at a cubic lattice site. (b) V_{Si} at a hexagonal lattice site. (c) V_C at a cubic lattice site. (d) V_C at a hexagonal lattice site [9].

Because of the elements' varying electronegativity values, the silicon vacancy V_{Si} corresponds to the cation vacancy in III–V compounds and V_C corresponds to the anion vacancy in these materials [9]. This conclusion is based on the preference of V_{Si} for high spin ground states and the fact that V_{Si} is a metastable defect for specific doping conditions [10-12], while V_C is stable for all doping conditions [11]. The metastable nature of V_{Si} makes it appropriate for use in intrinsic and positively doped situations. When the two vacancies, V_{Si} and V_C, occur in the nearest neighbor it is referred to as a di-vacancy. This di-vacancy is a generic example of the intrinsic vacancy complexes that occur in elemental and compound semiconductors [9]. Figure 4.7 shows the di-vacancy complex at a hexagonal site in 4H-SiC. A dissociation energy of 4.5 eV, derived from density functional theory, has been reported for this di-vacancy, which is predicted to be a thermally stable defect [13,14].

Chatterjee et al. [15] identified the electrically active point defects and characterized the defect energetics. Passivation techniques have also been proposed for the highly probable electrically active defects. The intrinsic point defects of SiC have been recorded as being electrically active with energy levels within the band gap of 4H-SiC. While hydrogen has been successfully used to passivate the Si vacancies, attempts to passivate C vacancies using a similar method have not been successful.

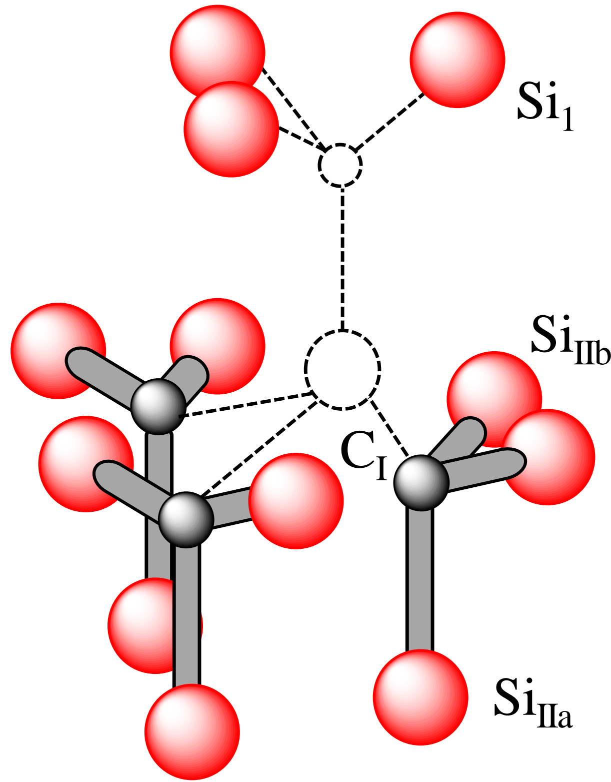

Fig. 4.7: Di-vacancy complex at a hexagonal site [9].

An antisite is another possible defect. It is either a silicon atom occupying a carbon site or a carbon atom occupying a silicon site. More complicated complexes, such as vacancy-antisite pairs and antisite-antisite pairs, have been known to form from antisites,. If more than one carbon atom occupies a silicon site, a defect complex such as a di-carbon antisite, a tri-carbon antisite, or a tetra-carbon antisite can be formed which in turn have the potential to form a carbon cluster together with the surrounding carbon atoms [16]. Also, the silicon vacancy can be observed in irradiated p-type material in spite of its metastability because the associated transformation that changes the vacancy into a carbon vacancy-antisite complex is a process that is activated only at higher temperatures [9].

Point defects such as vacancies, antisites and interstitials are important components of the diffusion of impurities in semiconductors. The efficiency of doping in semiconductors can

be controlled by the presence of specific defects, and there are several methods to create them in a controlled manner. Troffer et al. [17] reported the co-implantation of Si/B and C/B, and Gao et al. discussed the co-diffusion of aluminum and boron [18] for the generation of specific defects. An additional method is changing the composition of the gas during epitaxial growth [19]. Rauls et al. [8] studied the different behaviors of nitrogen and phophorus impurities in 4H-SiC, which have been attributed to the recombination behaviors of the corresponding split interstitials and vacancies. Evidence suggests that while nitrogen almost exclusively occupies a carbon site (N_C), phosphorus occupies both carbon and silicon sites (P_C and P_{Si}), and that nitrogen forms inactive defect complexes while phosphorus has shown no evidence of inactive complexes, which leads to the conclusion that phosphorus is a better n-type dopant in SiC than nitrogen [8].

Gao et al. [20] completed classical molecular dynamic studies of elementary defect formations in 4H-SiC. The formation energy of a silicon vacancy (V_{Si}) is given as 3.3 eV while the formation of a carbon vacancy (V_C) requires 2.7 eV. Bockstedte et al. [6] discussed the interstitial and vacancy mediated diffusion of boron in 4H-SiC. Studies show that boron diffusion is mainly due to the interstitialcy mechanism followed by the kickout mechanism. The formation of specific dominant defect complex with a boron atom at a silicon site coupled with a vacancy at a carbon site ($B_{Si} + V_C$) is also reported with a migration energy of 4.3 eV [6].

4.3 Current Doping Techniques

As with any semiconductor device fabrication, doping is an important processing step to make ohmic contacts, p-n junctions, and the active layers of SiC devices. Doping consists of the controlled introduction of specific impurities, generally referred to as dopants, into a semiconductor to alter its electrical properties such as type of conductivity, electrical conductivity, and charge carrier lifetime [19]. Dopants are used to form either ohmic or rectifying contacts. Transition metals have a tendency to form rectifying contacts on SiC in the as-deposited state unless dopants can be introduced into SiC in high concentrations [21]. A dopant concentration of at least $\approx 10^{19}$ cm^{-3} is required to produce ohmic contacts [21,22]. The four most commonly used doping methods in SiC device processing include ion implantation [24-26], thermal diffusion [18,23], *in-situ* doping during epitaxial growth [27,28] and laser doping [29-31].

4.3.1 Doping by Ion Implantation

Ion implantation is the most frequently used method for doping in SiC device fabrication. It was first patented by Shockley [32] in 1957. The process can cause significant lattice damage, so it is followed by high temperature activation annealing in the range of 1500-2200°C. Post-implantation annealing is necessary for both re-crystallization and implanted ion activation [33].

This doping method requires the bombardment of a sample with energetic ions for the purpose of changing both its electrical and chemical properties [34], but its main use is to modify only the electrical properties.

Principle

When an energetically positive ion enters the surface of a wafer, it collides with the atoms in the SiC crystalline structure and interacts with their electrons. These collisions and interactions reduce the energy of the ion until it comes to rest at a certain depth. This is a statistical process in which the distribution of the implanted ions follows a Gaussian profile given by:

$$N(x) = N_p \exp\left[-\frac{(x - R_p)}{2\Delta R_p^2}\right] \tag{4.9}$$

where N(x) represents the impurity concentration, N_p is the peak impurity concentration, x is the depth from the surface of the sample, and R_p is the projected range of the average distance traveled by an ion. Therefore, by definition, N_p occurs at a depth of $x=R_p$. The spread of the distribution is characterized by ΔR_p (standard deviation), which is referred to as the straggle [32]. Figure 4.8 shows the Gaussian distribution resulting from ion implantation.

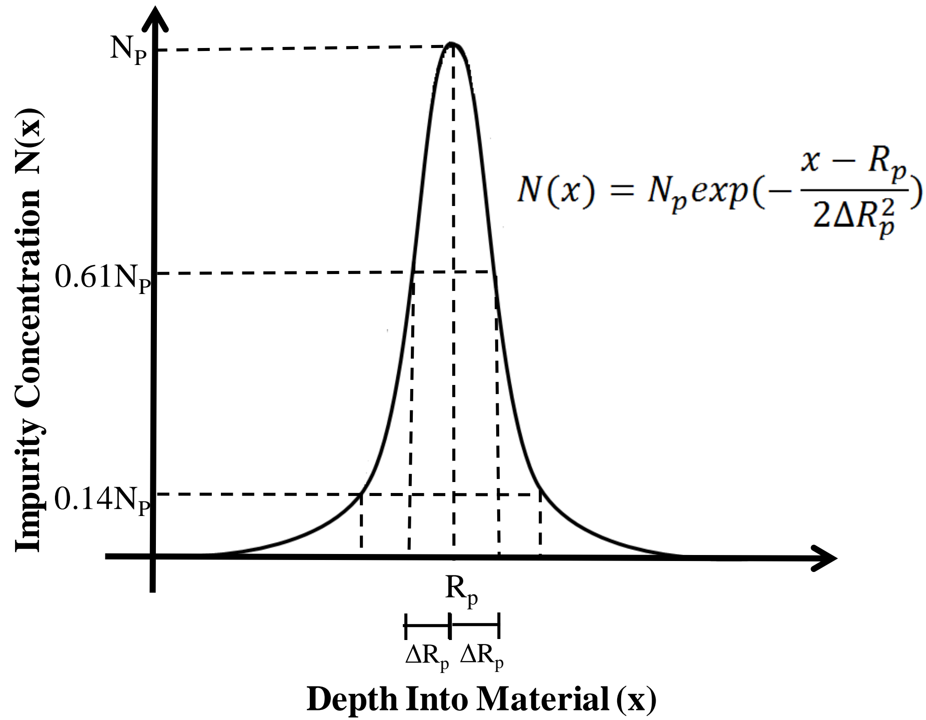

Fig. 4.8: Gaussian distribution of the implanted ion profile for the impurity completely below the surface.

The area under the impurity profile curve is defined as the implanted dose and is given by:

$$Q = \int_0^\infty N(x)\, dx \tag{4.10}$$

where Q represents the implanted dose. Equation 4.11 gives the implanted dose, Q, for an implant completely contained within the intended target wafer:

$$N_p = \frac{Q}{\sqrt{2\pi\Delta R_P}} \tag{4.11}$$

The projected range of a particular ion can be defined as a function of the ion's energy, its mass and atomic number, and the mass and the atomic number of the target material. has been developed by Lindhard et al.[35] developed the LSS theory to explain the range and straggle. These can be approximated to be proportional to the energy of the ions over a broad range.

Implementation

An ion implanter requires a high voltage particle accelerator that is capable of producing a high velocity ion beam that can penetrate the target SiC surface. Figure 4.9 shows a basic schematic diagram of a typical ion implantation system.

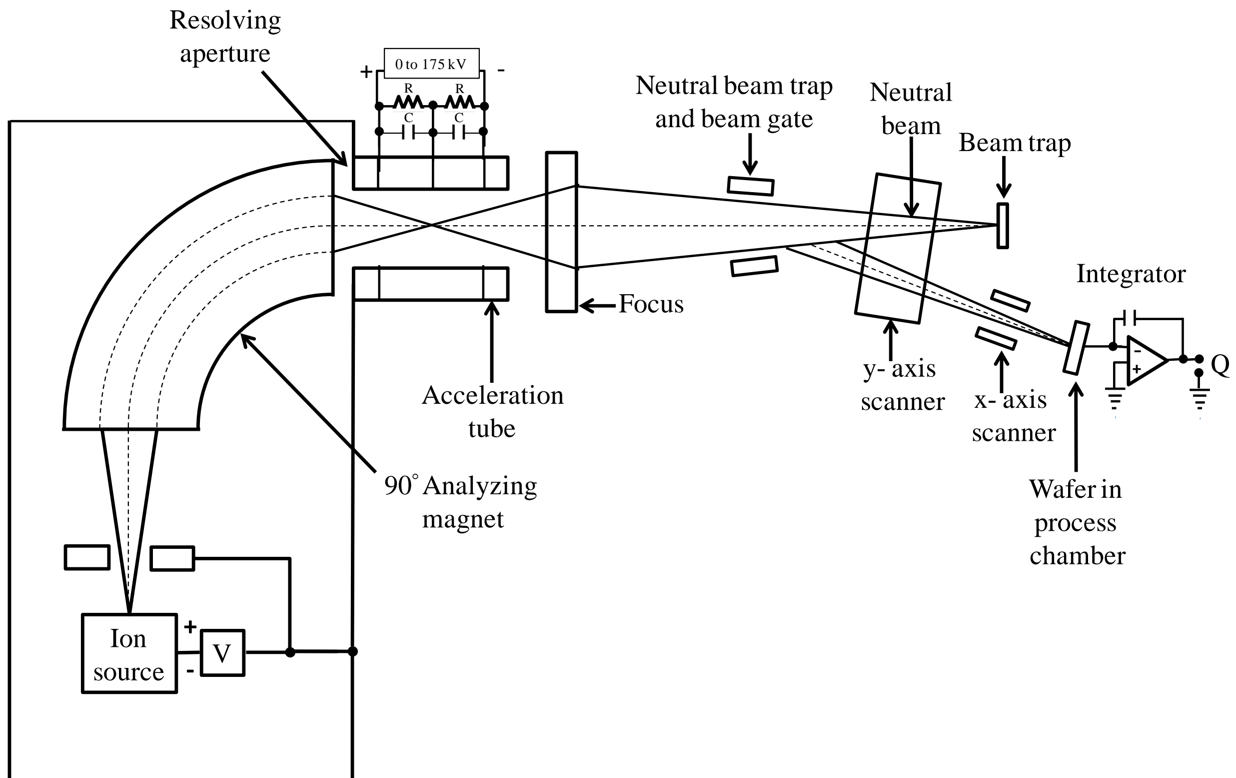

Fig. 4.9: Schematic diagram of an ion implanter [1]

A typical apparatus consists of five main components. These include the ion source, mass spectrometer, high voltage acceleration chamber, x- and y-axis deflection system and the target chamber. Each part and its function in the system is given below.

Ion source – This operates at a high voltage in the range of approximately 25 KeV to produce a plasma containing the desired impurity.

Mass spectrometer – A mass analyzing magnet is used to bend the ion beam 90° to select the required impurity ion, which moves through a slit into the linear accelerator chamber.

Accelerator – The ion beam is accelerated to high velocities in the chamber operating at a very high voltage. Typically, the ion source and the accelerator are mounted inside a shield to provide protection from X-ray emissions.

Scanning system – The x-axis and y-axis deflection plates are used to ensure uniform doping on the total surface area and to build up the desired dose.

Target chamber – While the complete system operates under vacuum conditions, the target wafers are maintained at ground potential due to safety considerations.

When a charged particle with a velocity **v** moves through the magnetic field **B,** it will experience a force **F** which causes the particle to undergo circular motion. Equation 4.4 gives **F** in terms of **v**, **B** and q, which is the charge of the particle.

$$\mathbf{F} = q(\mathbf{v} \times \mathbf{B}) \tag{4.12}$$

When the velocity is perpendicular to the magnetic field

$$qvB = \frac{mv^2}{r} \tag{4.13}$$

where m represents the mass of the charged particle and r is the radius of the path taken. Equation 4.14 is obtained using conservation of energy for the charged particle, where V represents the accelerating voltage of the linear accelerator.

$$\frac{mv^2}{2} = qV \tag{4.14}$$

Therefore, according to Equation 4.15, the magnitude of the magnetic field can be adjusted by changing the DC current to the analyzer magnet, which leads to the selection of an ion with a specific mass.

$$|\mathbf{B}| = \sqrt{\frac{2mV}{qr^2}} \tag{4.15}$$

The wafer is typically maintained in steady electrical contact with the sample holder to allow for the flow of electrons to and from the wafer so that the implanted ions will be neutralized. The current generated by this flow of electrons is used to determine the dose Q given by:

$$Q = \frac{1}{nqA}\int_0^T I\,dt \tag{4.16}$$

where I represents the beam current, A is the area of the wafer, n is the ionization of the charged particle and T is the total implantation time.

The energies used for the ion beam can vary in the KeV to MeV range while typical ion doses for SiC vary from 10^{11} to $>10^{16}$ ions/cm^2 up to a depth of 20-50 μm. Due to lower activation energies in SiC, aluminum (Al) and nitrogen (N) are the preferred implants compared to other impurities [36]. Nitrogen implants provide reliable n-type dopants with low sheet resistance values [37,38], while attempted p-type doping by implantation of either aluminum or boron have resulted in high sheet resistance values and low activation efficiency [25,36]. However, Zhao et al.[39] showed the possibility of achieving low specific contact resistance in the range of 10^{-5} Ωcm^2 for Al contacts on 6H-SiC by making highly doped ohmic contact regions using ion implantation.

Although ion implantation can reach a concentration of $>10^{16}$ /cm^3, it is time-consuming to produce a high concentrations in a high volume. The implantation process is also known to damage the surface, and a post-annealing step in excess of 1500°C has become a necessity to remove the effects of this damage. Heft et al. [40] demonstrated rapid accumulation of damage up to amorphization for a dose between 1 x 10^{14} cm^{-2} to 1 x 10^{16} cm^{-2}. Due to the high post

annealing temperatures, the SiC surface tends to decompose, and this surface roughness leads to potentially adverse effects on device performance [19,41]. The cost of the necessary equipment for ion implantation is a notable disadvantage, but overall, when considering the flexibility and process control achievable with controlled selective doping of SiC, this technique remains the preferred method for doping SiC.

4.3.2 Doping by Thermal Diffusion

Thermal diffusion is another conventional method of introducing dopants into a semiconductor. Although this process has been considerably developed for Si doping at temperatures ranging from 900°C to 1100°C [42,43], doping SiC using this method requires temperatures in excess of 1800°C due to the low impurity diffusion rates in SiC. It usually involves either flowing an impurity containing gas over the SiC sample or flowing an inert gas through the chamber while the SiC sample is placed in close proximity to a solid impurity source. This leads to the deposition of a thin metal film on the surface of the sample, which then has to be heated to a temperature between 1800°C and 2200°C to diffuse the impurity into SiC.

Gao et al. [18] presented the successful codiffusion of aluminum and boron for selective p-type doping of 4H-SiC. Codiffusion is used to simultaneously form a shallow, highly doped layer and a linearly graded deep layer. A vertical, double-walled, water-cooled quartz chamber with inductive heating has been used and the diffusion temperatures are documented to be between 1800°C and 2100°C in an Ar ambient. The samples were glued face-down to the top lid of the graphite crucible. Figure 4.10 shows a schematic of selective doping of 4H-SiC from the vapor phase.

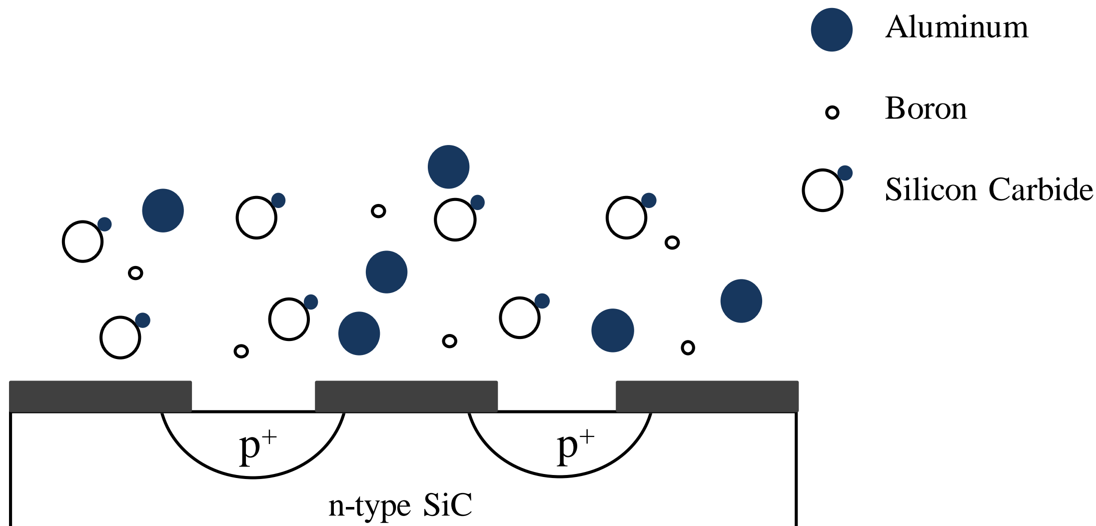

Fig. 4.10: Schematic diagram of diffusion mechanism through vapor phase.

Since the diffusion process has been carried out at approximately 2000°C, which is higher than the sublimation point of SiC, powdered SiC was charged in the crucible to form a SiC equilibrium vapor ambient to prevent the evaporation of Si atoms from the substrate [18]. A graphite mask has been used for selective doing and surface doping concentration in the range of 10^{19} cm^{-3} has been documented for both aluminum and boron using secondary ion mass spectrometry. A surface doping concentration of 5 x 10^{19} cm^{-3} has been achieved for aluminum, which shows a very shallow doping profile, while boron has displayed a linearly graded doping profile with a maximum value of approximately 2 x 10^{19} cm^{-3}, up to a depth of several micrometers. This can be attributed to the fact that boron has a higher diffusion coefficient in SiC than aluminum, and aluminum is more soluble than boron in SiC [18]. Electrical characteristics have been described using Hall effect measurements in which samples with a carrier concentration of 1 x 10^{19} cm^{-3} was used.

Soloviev et al. [44] demonstrated the selective diffusion of boron in 6H-SiC at a temperature range of 1800°C to 2100°C. A graphite film was used as the protective mask and a diffused planar p-n junction diode based on a p-type emitter region was fabricated, showing good rectification J-V characteristics. The p-type doping of 6H-SiC at temperatures higher than 1900°C has also been investigated [23]. Evidence shows that the doping profiles are clearly divided in to a steep region and a long-tailed region with different diffusion coefficients, and that the boron acceptors in the steep region are mostly located at shallow energy levels (~300 meV) and those in the long-tailed region are located at deep energy levels (~700 meV) [23].

More recently, boron and aluminum doping of SiC using elemental boron and aluminum carbide have been reported [45]. Thermal diffusion has been used to selectively dope 4H-SiC. Figure 4.3 shows the high temperature oven used by Kubiak et al. to carry out this process[45].

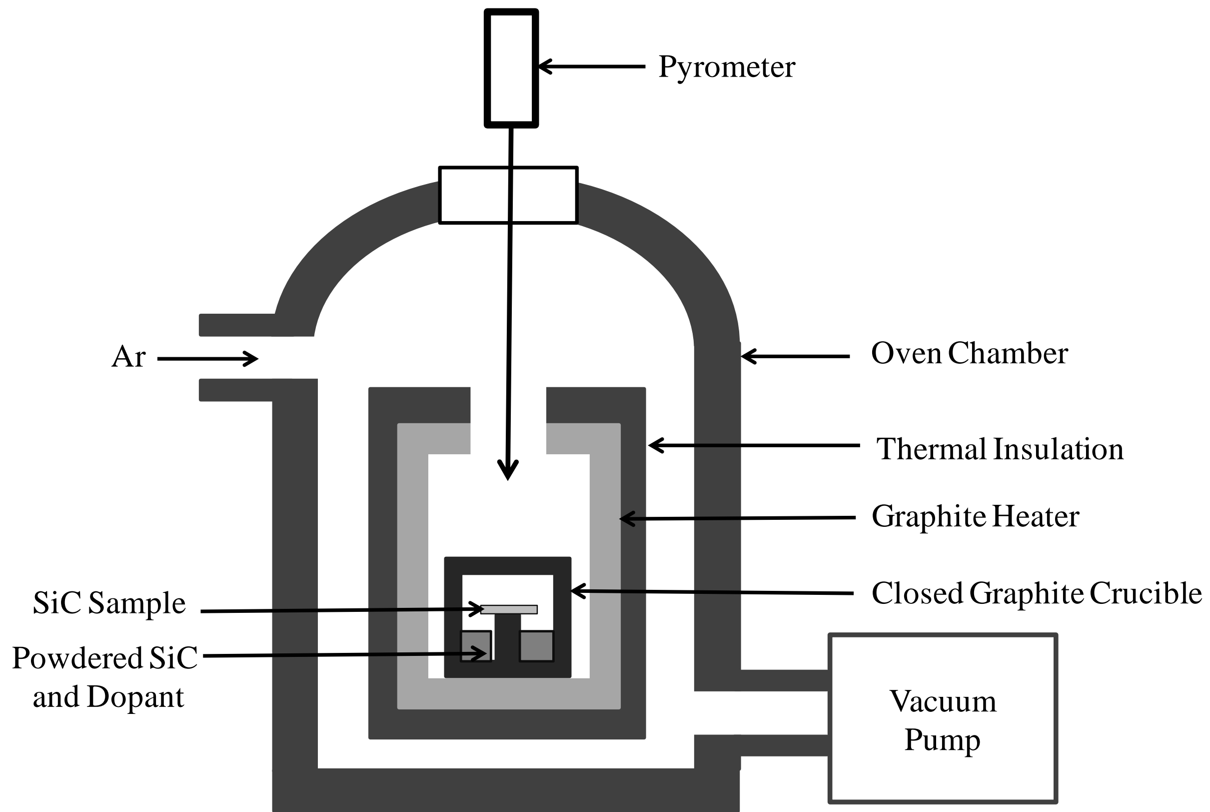

Fig. 4.11: Schematic diagram of experimental setup for thermal diffusion doping [45].

When a vertical graphite reactor with resistive heating is used,the SiC sample is placed inside a closed graphite crucible charged with powdered SiC. The diffusion of boron and aluminum is conducted at a temperature range of 1800°C to 2000°C with solid powdered sources of boron and aluminum carbide mixed in with the powdered SiC inside the crucible. Studies suggest that boron must be elemental in order to diffuse into SiC because a boron carbide (B_4C) source was found to be ineffective. Evidence shows a boron doping concentration of 6×10^{19} cm^{-3} for diffusion at 2000°C and an aluminum doping concentration 8×10^{19} cm^{-3} in the near surface region [45].

4.3.3 *In-Situ* Doping During Crystal Growth

Another frequently used technique involves dopants that are introduced during a physical vapor transport process. For example, in epitaxial growth of SiC by chemical vapor deposition, the dopants are usually introduced in the form of gas or liquid sources. Nitrogen can be introduced by using either nitrogen gas or ammonia. In aluminum doping, a metalorganic source such as trimethylaluminumis used, whereas phosphorus doping requires phosphine gas and boron doping requires diborane gas [19]. The impurity source is usually incorporated as a part of the crystal growth system. Figure 4.12 shows a schematic diagram of the chemical vapor deposition system at the semiconductor physics laboratory at Auburn University in Auburn, Alabama.

Deposition of SiC films using chemical vapor deposition (CVD) is the most common method of SiC crystal growth. Several variations of CVD include low pressure chemical vapor deposition (LPCVD), plasma enhanced chemical vapor deposition (PECVD) and atmospheric pressure chemical vapor deposition (APCVD). The basic growth processes and developments are discussed in Section 1.2.3.

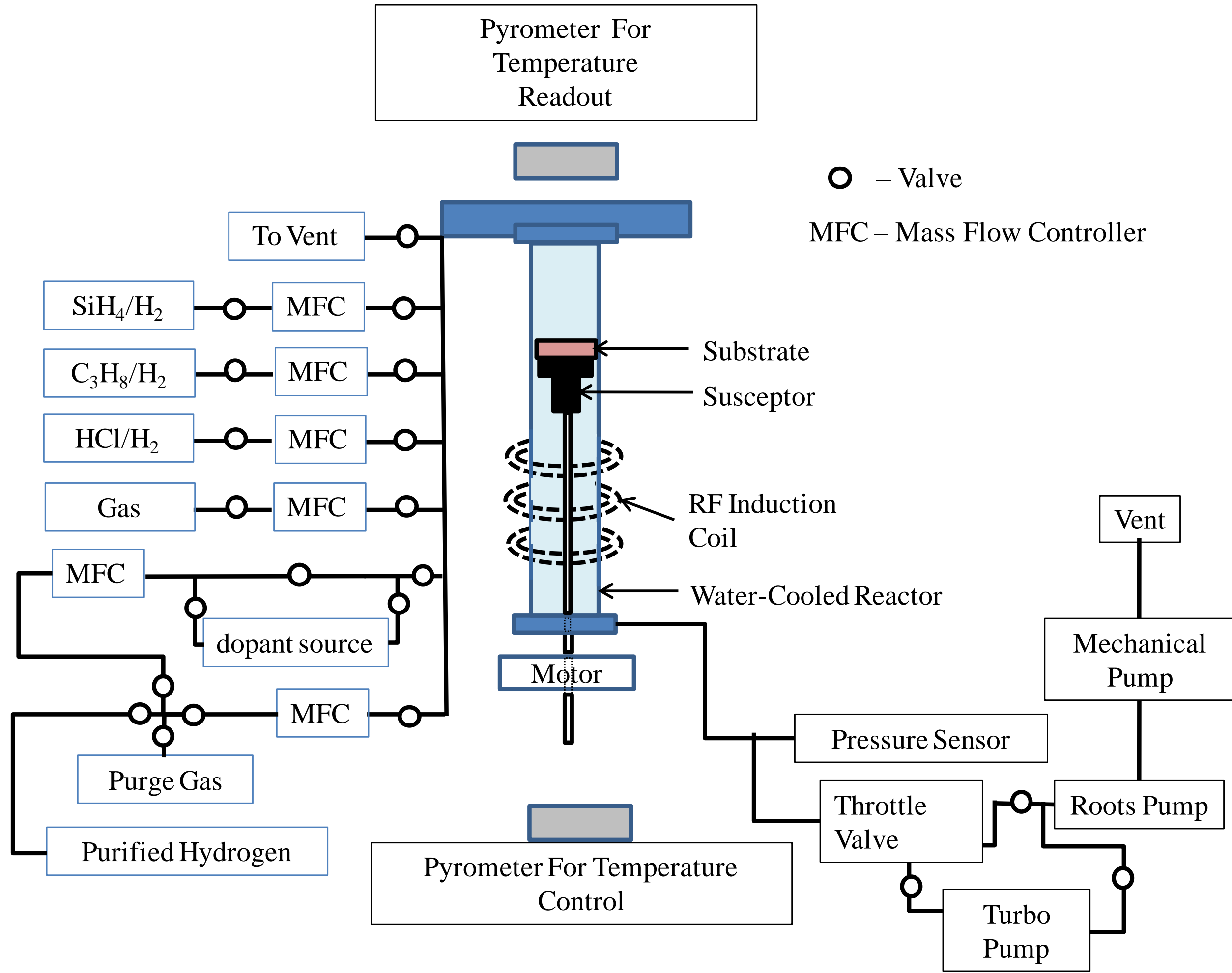

Fig. 4.12: Schematic diagram of the CVD system at Auburn

Research has been conducted on the incorporation of impurity sources into these processes. Ji et al. [46] showed the effects of phosphorus doping of SiC by using electron cyclotron resonance chemical vapor deposition (ECR-CVD), which involves the deposition of doped SiC films from a mixture of methane, silane, hydrogen, and phosphine as the dopant gas. Thin films deposited at low and high microwave powers were studied [46,47], and while SiC grown at low microwave power (150 W) was amorphous in nature its microcrystallanity increased with a corresponding increase in the phosphine fraction. SiC grown at high microwave

power (600 W) entered a strong microcrystalline phase. Figure 4.12 shows a schematic diagram of the ECR-CVD system.

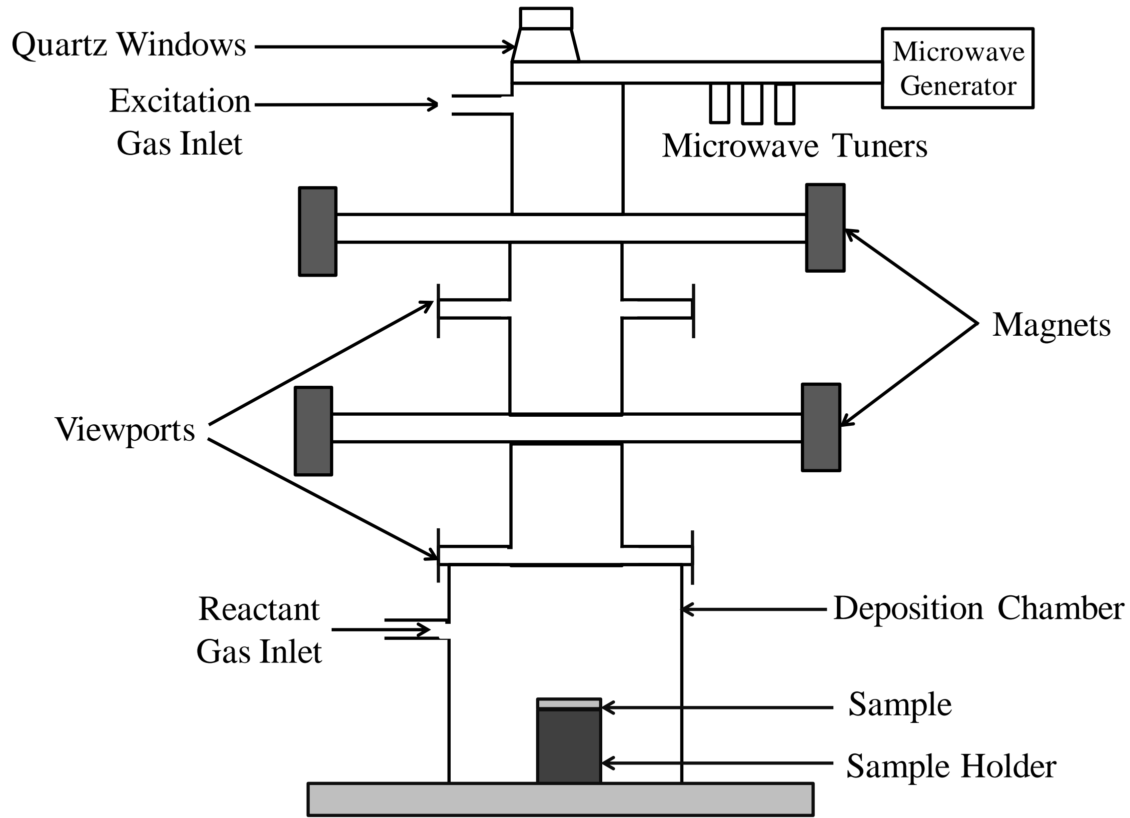

Fig. 4.13: Schematic diagram of the ECR-CVD system [46].

Similar work by Yoon et al. [48], showed that boron-doped SiC can be grown using ECR-CVD, which was possible through the use of diborane gas as the impurity source. This work showed that SiC film was completely amorphous when grown at low microwave power (150 W) while the films grown at high microwave power (800 W) showed some microcrystalline nature. However, unlike the findings of the aforementioned study, an increase in the impurity fraction made the film amorphous.

Wijesundara et al. [49] investigated the LPCVD growth of nitrogen-doped SiC films. The doped SiC was grown using 1,3-disilabutane and NH_3, which resulted in a resistivity value of 0.02 Ωcm for a thin film deposited at 800°C. Myong et. al. [50] studied the low temperature preparation of boron-doped nanocrystalline SiC films using a mercury-sensitized photo-CVD technique.

The doping of SiC using *in-situ* crystal growth techniques is preferred when uniform large area doping is required, but it is not suitable for selective area doping.

4.3.4 Laser Doping

In this method, lasers are used to introduce dopants in to semiconductor wafers. Some of the more frequently used laser doping techniques include laser thermal processing (LTP), laser-induced solid-phase doping (LISPD) and gas immersion laser doping (GILD) [29]. Figure 4.13 shows a schematic diagram of a typical laser doping system.

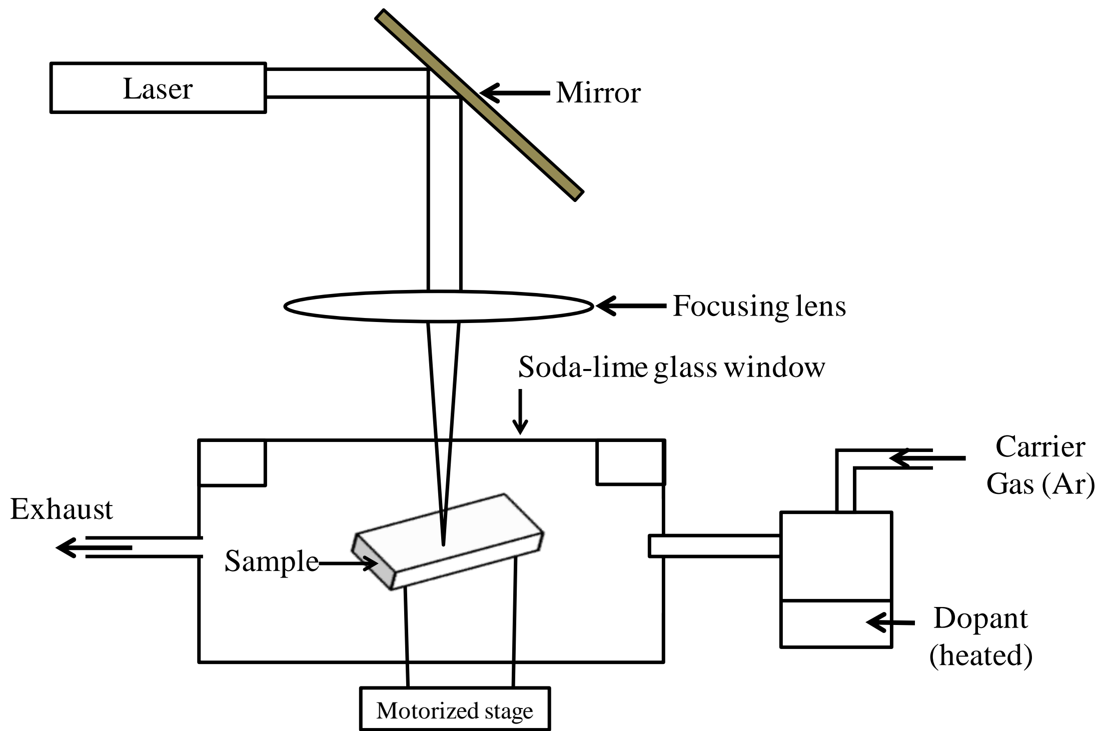

Fig. 4.14: Schematic diagram of a laser doping system [29].

The LTP method involves two steps; the dopants are introduced using ion implantation, then a pulsed laser beam induces a melting and solidification cycle over a given depth of a sample. Very high boron-doping concentrations of up to 3 x 10^{21} cm^{-3} have been reported using this technique [51].

The LISPD method is based on a solid-state diffusion process for dopant incorporation through either the dopant film method or the dopant gas method. In the first method, a thin film of the dopant material is deposited on the sample's surface and is heated with a laser beam to diffuse the dopant atoms. In the latter method, a dopant-containing vapor is supplied with the aid of an inert gas before the sample is heated with a laser beam. A suitable liquid dopant source can also be used during the LISPD method instead of a vapor medium [50]. Salama et al. [55–57]

successfully fabricated Schottky contacts, Ohmic contacts, and Schottky diodes by using the LISPD method.

The GILD method involves the diffusion of dopants into the molten layer of the semiconductor created by a laser beam. The dopant-containing gas is adsorbed at the wafer surface and pyrolyzed by a laser beam to produce the dopant atoms. The molten region allows for a faster impurity diffusion rate, so the dopant atoms are able to diffuse into the molten semiconductor layer and electrically occupy active sites during the epitaxial recrystallization of the melt [52].

Another laser doping method is a laser direct write technique [53–56], which creates fewer defects in the wafer compared to ion implantation. Sengupta et al. [54] found conductive tracks on an insulating SiC substrate surface by using the same method.

4.4 References

1. R. C. Jaeger, *Introduction to Microelectronic Fabrication,* 2nd Edition, G. W. Neudeck and R. F. Pierret (eds.) Prentice-Hall Inc. (2002).

2. D. Gupta, *Diffusion Phenomena in Thin Films and Microelectronic Materials*, D. Gupta and P.S. Ho (eds.), Noyes publications, USA, (1988).

3. D. Gupta, *Phys. Rev.* **7**, 586 (1973).

4. M. M. De Souza and G. A. Amaratunga, *Solid State Electron.* **38**, 867 (1995).

5. R. Rurali, P. Godignon, J. Rebollo, P. Ordejon and E. Hernandez, *Appl. Phys. Lett.* **81**, 2989 (2002).

6. M. Bockstedte, A. Mattausch and O. Pankratov, *Phys. Rev. B* **70**, 115203 (2004).

7. H. Bracht, N. A. Stolwijk, M. Laube and G. Pensl, *Appl. Phys. Lett.* **77**, 3188 (2000).

8. E. Rauls, U. Gerstmann, Th. Frauenheim and H. Overhof, *Physica B* **340-342**, 184 (2003).

9. M. Bockstedte, A. Gali, A. Mattausch, O. Pankratov and J. W. Steeds, *Phys. Stat. Sol.* (b) **245**, 1281 (2008).

10. E. Rauls, T. Lingner, Z. Hajnal, S. Greulich-Weber, T. Frauenheim and J. M. Spaeth, *Phys. Stat. Sol.* (b) **217**, R1 (2000).

11. M. Bockstedte and O. Pankratov, *Mater. Sci. Forum* **338–342**, 949 (2000).

12. M. Bockstedte, A. Mattausch, and O. Pankratov, *Phys. Rev. B* **68**, 205201 (2003).

13. L. Torpo, T. E. M. Staab, and R. M. Nieminen, *Phys. Rev. B* **65**, 85202 (2002).

14. M. Bockstedte, A. Mattausch, and O. Pankratov, *Phys. Rev. B* **69**, 235202 (2004).

15. A. Chatterjee, A. Bhat and K. Matocha, *Physica B* **401-402**, 81 (2007).

16. F. Yan, *Low Temperature Photoluminescence Study on Defect Centers in Silicon Carbide*, Dissertation, University of Pittsburgh (2009).

17. T. Troffer, M. Schadt, T. Frank, H. Itoh, G. Pensl, J. Heindl, H. P. Strunk and M. Maier, *Phys. Stat. Sol. (a)* **162**, 277 (1997).

18. Y. Gao, S. I. Soloviev, T. S. Sudarshan and C. C. Tin, *J. Appl. Phys.* **90** (11), 5647 (2001).

19. C. C. Tin, A. V. Adedeji, I. G. Atabayev, B. G. Atabaev, T. M. Saliev, E. N. Bakhranov, M. Li, S. P. Mendis and C. A. Ahyi, *U.S. Patent* 7,999,268. (2011).

20. F. Gao, M. Posselt, V. Belko, Y. Zhang and W. J. Weber, *Nucl. Instrum. Meth.* B **218**, 74 (2004).

21. F. A. Mohammad, Y. Cao and L. M. Porter, *Appl. Phys. Lett.* **87**, 161908 (2005).

22. I. P. Nikitina, K. V. Vassilevski, N. G. Wright, A. B. Horsfall, A. G. O'Neill and C. M. Johnson, *J. Appl. Phys.* **97**, 083709 (2005).

23. Y. Gao, S. I. Soloviev and T. S. Sudarshan, *Appl. Phys. Lett.* **83** (5), 905 (2003).

24. J. Meier, N. Achtziger, T. Licht, M. Uhrmacher and W. Witthuhn, *Physica B* **185** (1-4), 207 (1993).

25. T. Kimoto, A. Itoh, H. Matsunami, T. Nakata and M. Watanabe, *J. Electron. Mater.* **25** (5), 879 (1996).

26. M. V. Rao, P. Griffiths, O. W. Holland, G. Kelner, J. A. Freitas Jr., D. S. Simons, P. H. Chi and M. Ghezzo, *J. Appl. Phys.* **77** (6), 2479 (1995).

27. D. J. Larkin, P. G. Neudeck, J. A. Powell and L. G. Matus in *Institute of Physics Conf. Series 137: Silicon Carbide and Related Materials*, The 5th SiC and Related Materials Conf., Washington, DC, pp. 51 (1993).

28. R. S. Kern and R. F. Davis, *Appl. Phys. Lett.* **71** (10), 1356 (1997).

29. Z. Tian, I. A. Salama, N. R. Quick and A. Kar, *Acta. Mater*. **53**, 2835 (2005).

30. J. Venturini, M. Hernandez, G. Kerrien, C. Laviron, D. Camel, J. L. Santailler, T. Sarnet and J. Boulmer, *Thin Solid Films* **453-454**, 145 (2004).

31. G. Kerrien, M Hernandez, C. Laviron, T. Sarnet, D. Debarre, T. Noguchi, D. Zahorski, J. Venturini, M. N. Semeria and J. Boulmer, *Appl. Surf. Sci.* **208-209**, 277 (2003).

32. W. Shockley, *U.S. Patent* 2,787,564 (1957).

33. H. Ryssel and I. Ruge, *Ion Implantation*, John Wiley and Sons, New York (1986).

34. P. G. Neudeck, "SiC Technology", The Electrical Engineering Handbook, 2nd ed. (1998).

35. J. Lindhard, M. Scharff and H. Schiott, *Mat. Fys. Med. Dan. Vid. Selsk*. **33**, 14 (1963).

36. M. V. Rao, J. Gardner, A. Edwards, N. A. Papanicolaou, G. Kelner, O. W. Holland, M. Ghezzo and J. Kretchmer, *Mater. Sci. Forum* **264-268**, 717 (1998).

37. M. Ghezzo, D. M. Brown, E. Downey, J. Kretchmer, W. Hennessy, D. L. Polla and H. Bakhru, *IEEE Electron Device Lett*. **13**, 639 (1992).

38. J. Gardner, M. V. Rao, O. W. Holland, G. Kelner and Simons, *J. of Electron. Mater*. **25**, 885 (1996).

39. J. H. Zhao, K. Tone, S. R. Weiner, M. A. Caleca, H. Du and S. P. Withrow, *IEEE Electron Device Lett*. **18**, 375 (1997).

40. A. Heft, E. Wendler, T. Bachmann, E. Glaser and W. Wesch, *Mater. Sci. Eng. B* **29**, 142 (1995).

41. M. A. Capano, S. Ryu, J. A. Cooper, M. R. Melloch, K. Rottner, S. Karlsson, N. Nordell, A. Powell and D. E. Walker, *J. Electron. Mater*. **28**, 214 (1999).

42. D. Mathiot, A. Lachiq, A. Slaoui, S. Noel, J. C. Muller and C. Dubois, *Mat. Sci. Semicon. Proc*. **1**, 231 (1998).

43. B. Kalkofen, M. Lisker and E. P. Burte, *Mater. Sci. Eng. B* **114-115**, 362 (2004).

44. S. I. Soloviev, Y. Gao and T. S. Sudarshan, *Appl. Phys. Lett.* **77** (24), 4004 (2000).

45. A. Kubiak and J. Rogowski, *Mater. Sci. Eng.* B **176**, 297 (2011).

46. R. Ji, S. F. Yoon, J. Ahn and W. I. Milne, *Mater. Sci. Eng. B* **48**, 215 (1997).

47. S. F. Yoon, R. Ji and J. Ahn, *Mater. Chem. Phys*. **49**, 234 (1997).

48. S. F. Yoon, R. Ji and J. Ahn, *J. Non-Cryst. Solids* **211**, 173 (1997).

49. M. B. J. Wijesundara, D. Gao, C. Carraro, R. T. Howe and R. Maboudian, *J. Cryst. Growth* **259**, 18 (2003).

50. S. Y. Myong, T. H. Kim, K. S. Lim, K. H. Kim, B. T. Ahn, S. Miyajima and M. Konagai, *Sol. Energ. Mat. Sol. C.* **81**, 485 (2003).

51. G. Kerrien, M. Hernandez, C. Laviron, T. Sarnet, D. Debarre, T. Noguchi, D. Zahorski, J. Venturini, M. N. Semeria and J. Boulmer, *Appl. Surf. Sci.* **277**, 208 (2003).

52. E. C. Jones and E. Ishida, *Mater. Sci. Eng. R* **1**, 24 (1998).

53. N. R. Quick, *U.S. Patent* 5,837,607 (1998).

54. D. K. Sengupta, N. R. Quick, A. Kar, *J. Laser Appl.* **26**, 13 (2001).

55. I. A. Salama, N. R. Quick and A. Kar in: Proceedings of the 21st International Congress on Applied of Lasers & Electro-Optics (2002).

56. I. A. Salama, N. R. Quick and A. Kar, *Mater. Res. Soc. Symp. Proc.* **75**, 764 (2003).

57. I. A. Salama, C. F. Middleton, N. R. Quick, G. D. Boreman and A. Kar in: Symposium on nitride and wide bandgap semiconductors for sensors, photonics and electronics IV, 204th meeting of the Electrochemical Society, Orlando (FL), 12 (October 2003).

Chapter 5

Vacancy Assisted Impurity Doping (VAID)

5.1 VAID Technique

The rate of impurity diffusion and the doping efficiency can be mediated or enhanced by vacancies. By intentionally creating vacancies, the process of impurity incorporation in a semiconductor can be controlled. Tin et al. [1] developed the vacancy assisted impurity doping (VAID) technique, which allows low temperature impurity incorporation in silicon. This study further investigated this technique and results are presented in this work. Vacancies can be formed during silicidation. Therefore, another version of VAID, which is the silicidation assisted impurity doping technique was also studied. The experimental procedures used for both techniques are reported in Chapter 6 and the results are presented in Chapter 7.

As described in Chapter 4, point defects in SiC such as silicon vacancies (V_{Si}), carbon vacancies (V_C), di-vacancies (V_{Si}-V_C) [2], antisite defects (C_{Si} or Si_C) [3], or a combination of the aforementioned defects can interact with extrinsic impurities to alter the electrical properties of SiC.

Miyajima et al. [4] described the behavior of boron as a dopant in SiC, and claimed that boron has two main acceptor levels in SiC, of which the shallow acceptor level is due to boron occupying a silicon vacancy (B_{Si}) while the deeper acceptor level is to the result of boron occupying a carbon vacancy (B_C). However, Gao et al. [5] suggested that the deeper boron acceptor level could be due to a defect complex of boron and carbon vacancies (B_{Si}+V_C), and it is further stated that the higher carbon vacancy density in SiC can be used to explain the long tail

in the boron diffusion profile. Because of its more shallow energy level, B_{Si} is the favored acceptor level for more efficient dopant activation in SiC. Various methods have been used to create the preferential B_{Si} defect, including the co-implantation of boron and carbon and controlling of the ratio of carbon and silicon atoms during epitaxial growth during *in-situ* doping by chemical vapor deposition. Laube et al. [6] researched the co-implantation of boron and carbon in SiC for the suppressed diffusion of boron while Moroz et al. [7] fabricated p^+/n junctions through point defect and stress engineering by co-implantating boron, carbon and germanium in silicon. Larkin et al. [8] explained how doping in SiC can be controlled during chemical vapor deposition by varying the Si/C ratio to change the amount of silicon or carbon vacancies.

The VAID technique involves the creation of these vacancies or vacancy complexes by an efficient use of energy. Creating preferred vacancies such as V_{Si} or V_C requires an elevated temperature because the number of vacancies created is directly dependent on the temperature. The formation energy of such vacancies is positive, which leads to an endothermic reaction. By definition, energy has to be added into the system to create the vacancies. As an example, the formation energy of V_{Si} in 4H-SiC is between a range of 3.30 - 3.31 eV, depending on the lattice site [9].

However, vacancies can also be created by utilizing another simultaneous chemical reaction that has a lower, or preferably negative formation energy, to offset the energy required for vacancy formation through an exothermic process. In the case of SiC, the reaction between silicon and oxygen atoms leads to the formation of silicon dioxide (SiO_2), which is exothermic and thus provides an energy gain of about 8.3 eV at room temperature (298 K) [1]. Therefore, by heating silicon carbide in the presence of oxygen, the process of silicon dioxide formation while

leaving behind silicon vacancies in the SiC crystal is an energetically favorable process. Equation 5.1 shows the most probable reaction between SiC and oxygen at temperatures below 1700 K [8].

$$SiC + O_2 = C + SiO_2 \quad (5.1)$$

One variation of the VAID technique uses an oxide layer of an impurity used in SiC doping (B_2O_3, P_2O_5, etc.), which is deposited on top of the silicon carbide surface and heated to a sufficiently high temperature. This causes the silicon atoms in the silicon carbide to diffuse into the oxide layer above to form silicon dioxide, leaving behind silicon vacancies. Because this reaction is exothermic, it facilitates the creation of vacancies, which in turn help the impurity atoms in the deposited oxide layer to diffuse into the silicon carbide crystal by allowing the dopant atoms to occupy the vacant silicon sites. The formation energy of a neutral phosphorus dopant occupying a silicon vacancy (P_{Si}) in 4H-SiC is 9.2 eV, while a neutral boron atom occupying a silicon vacancy (B_{Si}) has a formation energy of 6.7 eV [10]. Although this process requires an energy input, the overall energy required is still less than that of a process without oxidation [1].

Therefore, the VAID technique combines the process of oxide-assisted vacancy creation with the process of external impurity diffusion to enable low temperature impurity incorporation in SiC. Figure 5.1 shows a schematic diagram of the VAID process for phosphorus and boron.

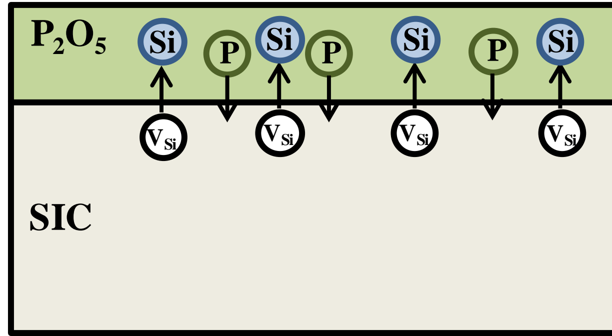

(a)

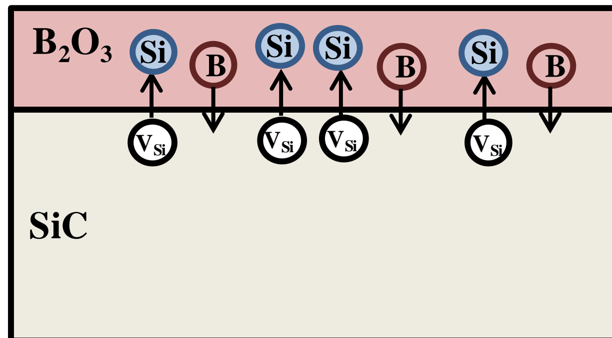

(b)

Fig. 5.1: Schematic diagram of the VAID process for (a) phosphorus (b) boron

The theoretical, thermodynamic basis of this technique requires a comparison of the relative stability of various oxides and carbides in the presence of SiC. This is possible by comparing Gibb's free energy of formation or the enthalpy of formation for the compounds for a broad temperature range. This concept is analyzed in detail in the following section for phosphorus and boron.

The silicidation assisted impurity doping technique, which is a variation of the VAID technique, described earlier in this section involves the use of a metal (such as nickel) as a catalyst for the Si vacancy creation reactions of the VAID technique. Nickel has been included in the process as thin layer on top of the impurity oxide layer with the SiC substrate at the bottom. Figure 5.2 shows a schematic diagram of the silicidation assisted impurity doping process. The

favorable thermodynamics of the silicide creation process, which relates to the negative Gibb's free energies of reactions (Section 5.2.1) for silicide formation on silicon carbide, have been used to aid in the diffusion of phosphorus. The favorable thermodynamic considerations are discussed in Section 5.2.2 in terms of ternary phase diagrams of stability.

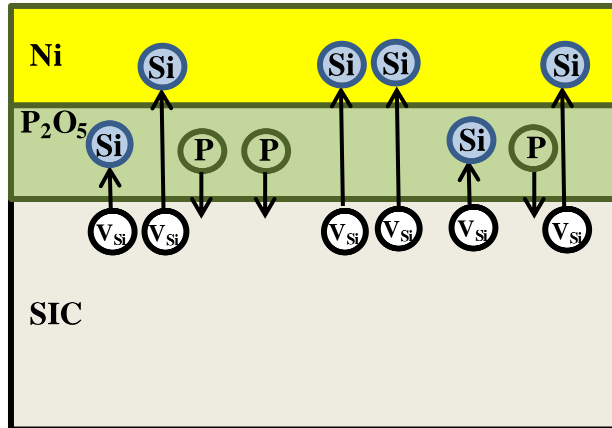

Fig. 5.2: Schematic diagram of the silicidation assisted impurity doping process for phosphorus

5.2 Thermodynamic Basis for VAID

5.2.1 Free Energy Calculations

The Gibbs free energy (G) and Enthalpy (H) are two of the most important criteria in thermodynamics when considering the proclivity of a chemical reaction. The change in Gibbs free energy is defined as the minimized chemical potential energy as a system reaches equilibrium conditions under constant pressure and temperature [11]. The free energy of the system is given by:

$$G = H - TS \tag{5.2}$$

where T represents the temperature measured in Kelvin and S is the Entropy. To consider the possibility of a chemical reaction occurring, it is necessary to take into account the change in Gibbs free energy (ΔG_r) of the reaction. The Gibbs free energy of reaction in terms of the enthalpy change and the entropy change is given by:

$$\Delta G_r = \Delta H_r - T\Delta S_r \tag{5.3}$$

The Gibbs free energy of reaction at a specific temperature can be calculated by considering the free energy of formation of the reactants and products. The Gibbs free energy of formation (ΔG_f) of a compound is defined as the Gibbs free energy change for the formation of 1 mole of the compound from its elements at a constant temperature. The Gibbs free energy change of a reaction can be given as:

$$\Delta G_r = \Sigma\Delta G_{fp} - \Sigma\Delta G_{fr} \tag{5.4}$$

where $\Sigma\Delta G_{fp}$ represents the summation of the free energy of product formation of the reaction and $\Sigma\Delta G_{fr}$ is the summation of the free energy change of formation of the reactants. If ΔG_r is

negative, the reaction is defined as a spontaneous reaction that favors the formation of the products, but if ΔG_r is positive, the reaction is characterized as non-spontaneous [11], with the reactants being more stable than the products. Other favorable conditions for a reaction to occur are a negative enthalpy of reaction (ΔH_r) and a positive value for the entropy change of the reaction (ΔS_r).

The incorporation of phosphorus into SiC using the reaction between phosphorus oxide and SiC can be studied thermodynamically. The decomposition of SiC in an oxygen-rich atmosphere is due to the oxidation of SiC [12] and all of the possible oxidation reactions for SiC are shown below. By considering the Gibbs free energy of reaction for Reactions 5.5–5.12 (ΔG_5-ΔG_{12}), the most probable reaction(s) can be identified.

$$\mathrm{SiC} + \mathrm{O_2} = \mathrm{SiO_2} + \mathrm{C} \tag{5.5}$$

$$\frac{2}{3}\mathrm{SiC} + \mathrm{O_2} = \frac{2}{3}\mathrm{SiO_2} + \frac{2}{3}\mathrm{CO} \tag{5.6}$$

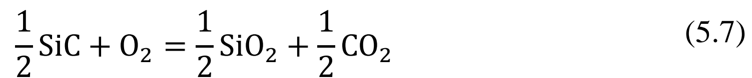

$$\frac{1}{2}\mathrm{SiC} + \mathrm{O_2} = \frac{1}{2}\mathrm{SiO_2} + \frac{1}{2}\mathrm{CO_2} \tag{5.7}$$

$$\mathrm{SiC} + \mathrm{O_2} = \mathrm{Si} + \mathrm{CO_2} \tag{5.8}$$

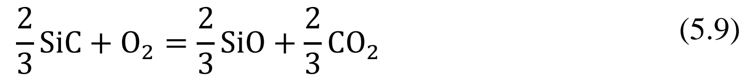

$$\frac{2}{3}\mathrm{SiC} + \mathrm{O_2} = \frac{2}{3}\mathrm{SiO} + \frac{2}{3}\mathrm{CO_2} \qquad (5.9)$$

$$\mathrm{SiC} + \mathrm{O_2} = \mathrm{SiO} + \mathrm{CO} \qquad (5.10)$$

$$\mathrm{2SiC} + \mathrm{O_2} = \mathrm{2Si} + \mathrm{2CO} \qquad (5.11)$$

$$\mathrm{2SiC} + \mathrm{O_2} = \mathrm{2SiO} + \mathrm{2C} \qquad (5.12)$$

The temperature dependence of the standard free energies of all reactions were calculated using published thermodynamic data [13,14], which is illustrated in the Ellingham diagram below (Figure 4.3). This diagram is the standard method of plotting the temperature dependence of the Gibbs free energy of reaction to explain the stability of compounds.

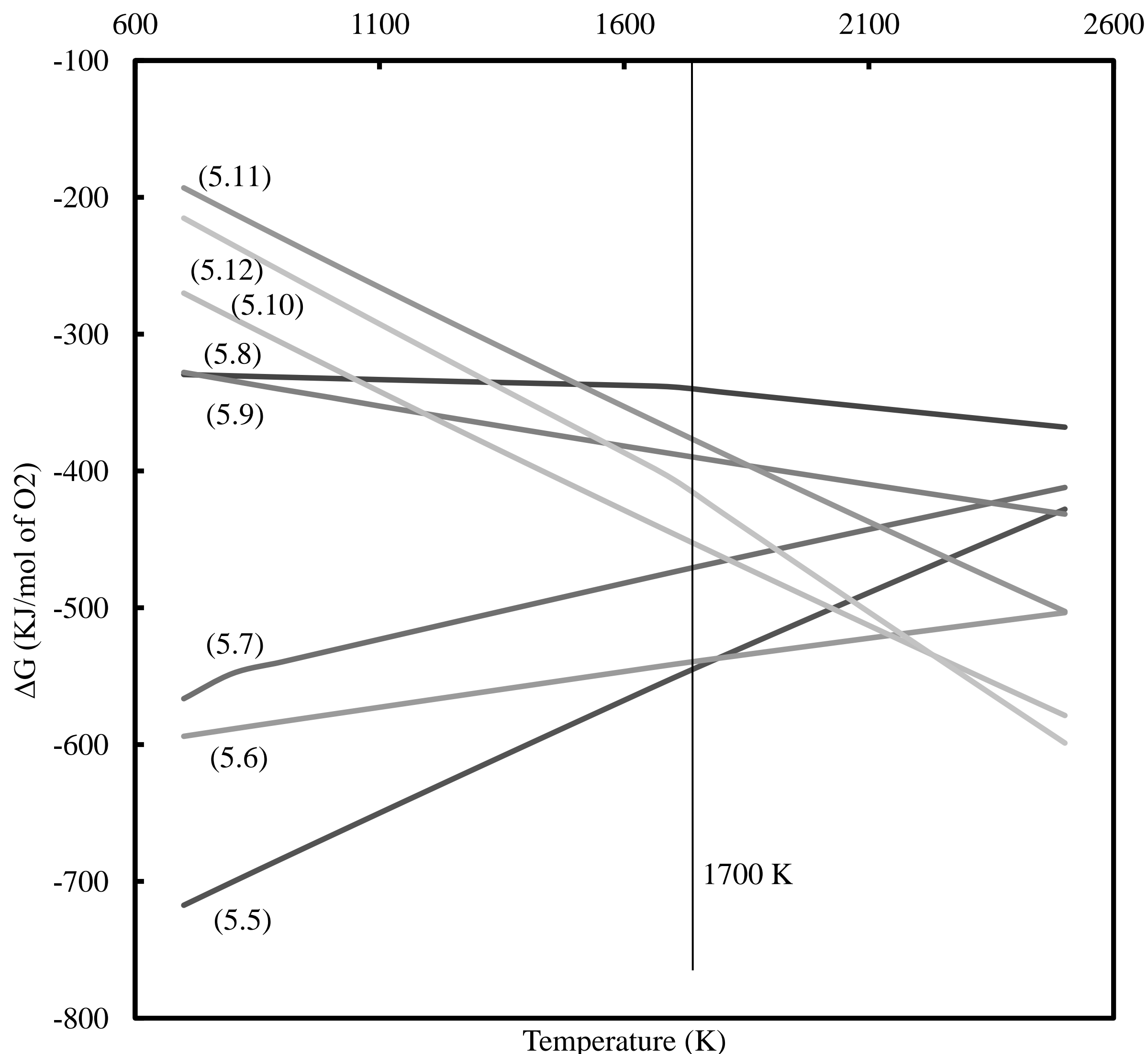

Fig. 5.3: Ellingham diagram for the oxidation reactions of SiC between temperatures of 700 K and 2400 K. The vertical line represents the 1700 K line.

The most probable reactions below a temperature of 1700 K were identified by considering the lowest Gibbs free energy change for all possible reactions. As seen in Figure 5.3, Reactions 5.5 – 5.7 have the lowest free energy values, meaning that they are the most probable reactions below this temperature. The reaction between phosphorus and oxygen, which forms phosphorus oxide, is shown in Reaction 5.13. Therefore the most probable reactions between SiC

and P_2O_5 below 1700 K are obtained by subtracting 5.13 from 5.5, 5.6, and 5.7. These are shown in Reactions 5.14 – 5.16.

$$\frac{4}{5}P + O_2 = \frac{2}{5}P_2O_5 \tag{5.13}$$

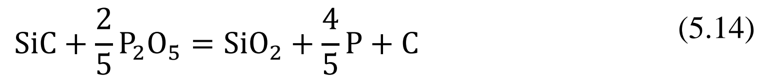

$$SiC + \frac{2}{5}P_2O_5 = SiO_2 + \frac{4}{5}P + C \tag{5.14}$$

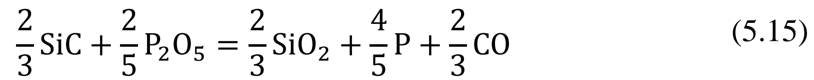

$$\frac{2}{3}SiC + \frac{2}{5}P_2O_5 = \frac{2}{3}SiO_2 + \frac{4}{5}P + \frac{2}{3}CO \tag{5.15}$$

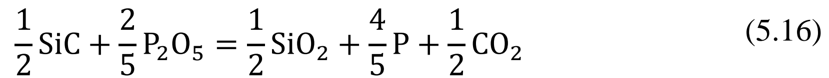

$$\frac{1}{2}SiC + \frac{2}{5}P_2O_5 = \frac{1}{2}SiO_2 + \frac{4}{5}P + \frac{1}{2}CO_2 \tag{5.16}$$

The Gibbs free energies of the most probable reactions between SiC and phosphorus oxide can be calculated by using the formula ΔG_5- ΔG_{13} (ΔG_{14}), ΔG_6- ΔG_{13} (ΔG_{15}) and ΔG_7- ΔG_{13} (ΔG_{16}). Hence, the condition for the decomposition reaction of SiC to occur in the presence of P_2O_5 can be is ΔG_{14}, ΔG_{15}, $\Delta G_{16} < 0$. The temperature dependencies of the Gibbs free energies of Reactions 5.14 – 5.16 are shown in Figure 5.4.

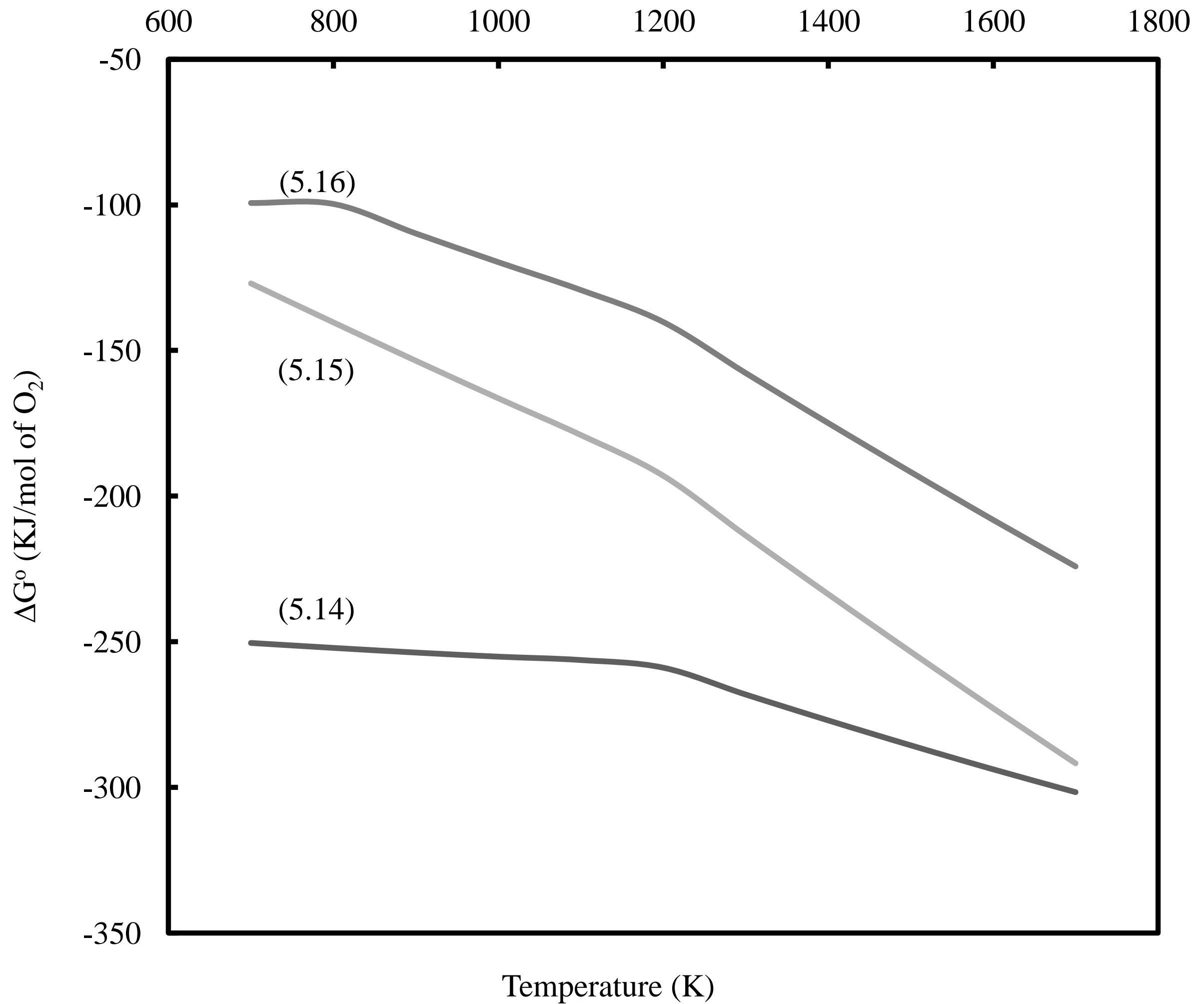

Fig. 5.4: Ellingham diagram for the most probable reactions between SiC and phosphorus oxide below 1700 K.

It is apparent from Figure 5.4 that the Gibbs free energy of the possible reactions between SiC and phosphorus oxide is negative for temperatures in the range of 700 K to1700 K. The standard free energies decrease with increasing temperatures, which leads to the increasing likelihood of the occurrence of Reactions 5.14, 5.15 or 5.16, or a combination thereof [15]. Comparisons can be made based on one mole of oxygen in the calculation of the Gibb free energy of reaction, which is the standard procedure for Ellingham diagrams in thermodynamics.

It is also practical at this point to consider an alternative reaction between SiC and phosphorus oxide, which produces phosphorus carbide. This reaction is shown in 5.17 [15].

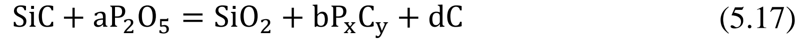

$$SiC + aP_2O_5 = SiO_2 + bP_xC_y + dC \qquad (5.17)$$

However, studies suggest that all phosphorus carbide stoichiometries have positive formation energies at ambient pressure [16], so the possibility of phosphorus carbide formation is extremely unlikely and can be ignored [15].

Recent research supports the use of boron oxide as a means of diffusing boron in SiC [17,18]. Tin et al. [18] presented electrically active boron-doping concentrations in the range of 10^{19} cm^{-3} using the VAID technique. Like phosphorus, boron can also be manipulated thermodynamically as a low temperature dopant in SiC. The reaction between boron and oxygen which forms boron oxide is represented below as Reaction 5.18. The the most probable reactions that occur between SiC and B_2O_3 below 1700 K are obtained by subtracting Reaction 5.18 from Reactions 5.5 – 5.7. These are shown as Reactions 5.19 – 5.21.

$$\frac{3}{4}B + O_2 = \frac{2}{3}B_2O_3 \qquad (5.18)$$

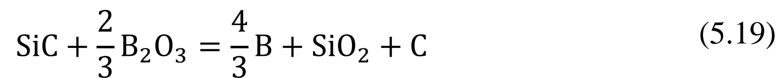

$$SiC + \frac{2}{3}B_2O_3 = \frac{4}{3}B + SiO_2 + C \qquad (5.19)$$

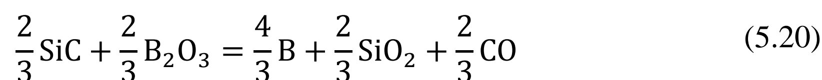

$$\frac{2}{3}SiC + \frac{2}{3}B_2O_3 = \frac{4}{3}B + \frac{2}{3}SiO_2 + \frac{2}{3}CO \tag{5.20}$$

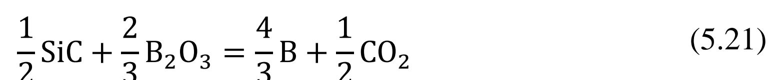

$$\frac{1}{2}SiC + \frac{2}{3}B_2O_3 = \frac{4}{3}B + \frac{1}{2}CO_2 \tag{5.21}$$

Therefore, the enthalpy of formation for the most probable reactions between SiC and boron oxide can be obtained by calculating ΔH_5- ΔH_{18} (ΔH_{19}), ΔH_6- ΔH_{18} (ΔH_{20}) and ΔH_7- ΔH_{18} (ΔH_{21}) [14]. Hence, the condition for the decomposition reaction of SiC in the presence of B_2O_3 to be a spontaneous is ΔH_{19}, ΔH_{20} or $\Delta H_{21} < 0$. The temperature dependencies of the enthalpies of Reactions 5.19 – 5.21 are shown in Figure 5.5. The enthalpy of formation is considered here due to the lack of of complete data for Gibbs free energy for the temperature range of 700 K to 1700 K.

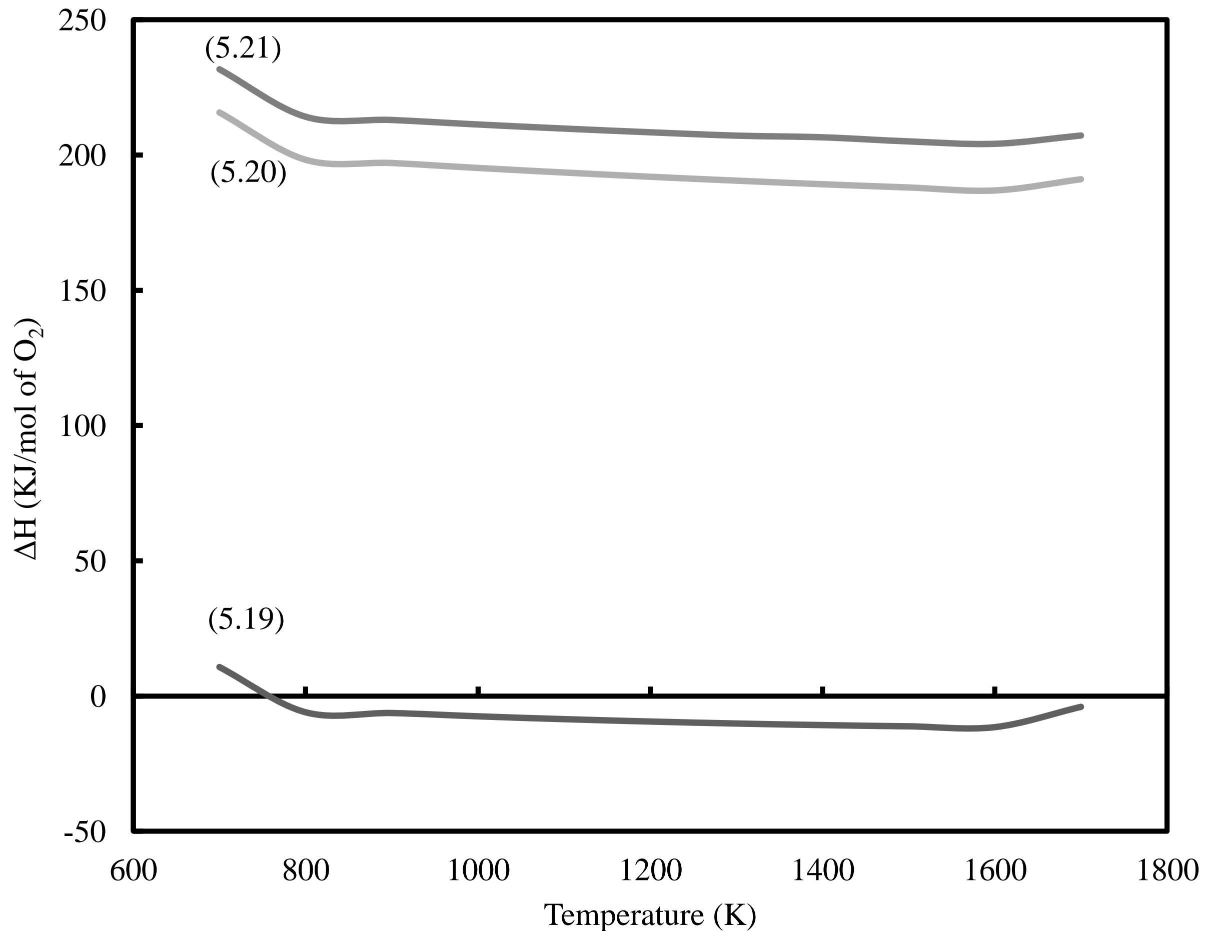

Fig. 5.5: Temperature dependence of the enthalpy of the reactions between SiC and boron oxide

It is evident from Figure 5.5 that the enthalpy is only negative for Reaction 5.19 when the temperature falls in the range between 700 K and 1700 K. Since the enthalpy of formation for Reactions 5.20 and 5.21 are positive for the indicated temperature range, it is unlikely that they will help decompose SiC.

Tin et al. [18] also compared the Gibbs free energies of formation (ΔG_f) of common oxides of impurities relevant to silicon carbide. Figure 5.6 shows the temperature dependence Gibbs free energy of formation for some common oxides. If SiO_2 has a lower free energy of formation than a particular impurity oxide, it implies that SiO_2 is more likely to form. This

causes the impurity oxide to dissociate with the formation of SiO_2 while freeing the impurity atoms to act as dopants.

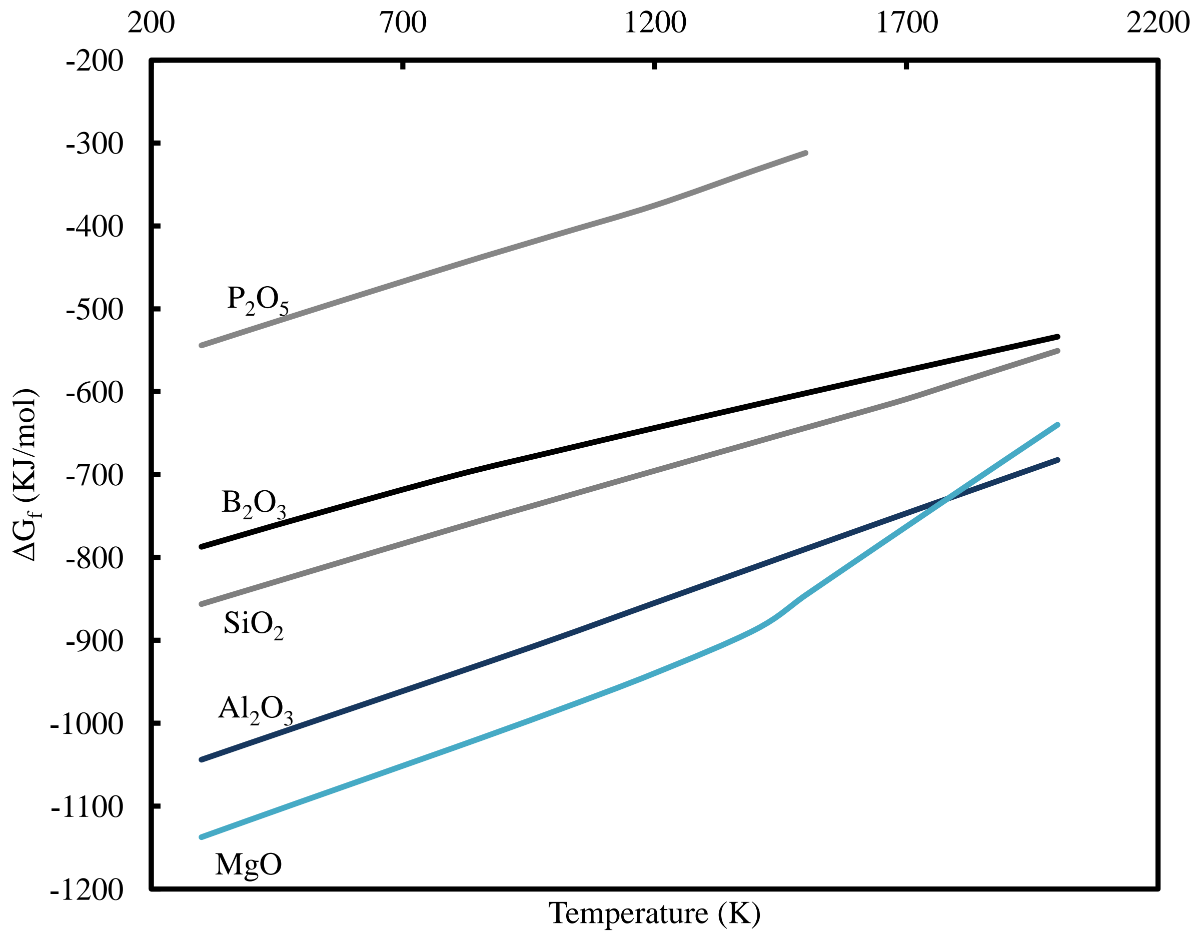

Fig. 5.6: Temperature dependence of the Gibbs free energy of formation for common oxides [18].

Figure 5.6 illustrates that this approach could explain the successful introduction of boron and phosphorus, but also that it may not be efficient for aluminum or magnesium doping because Al_2O_3 and MgO are more stable than SiO_2.

5.2.2 Ternary Phase Diagrams of Stability

The Gibbs phase rule allows for a maximum of three phases to coexist in equilibrium at any position in a ternary phase diagram, since temperature and pressure can be considered constant in a metal semiconductor system [19]. The Gibb's phase rule is given as:

$$f + p = c + 2 \tag{5.5}$$

where f is the number of degrees of freedom, c is the number of constituent elements and p is the number of phases present at any given point on the diagram. Any three phases in equilibrium form a triangle in a ternary phase diagram. At constant pressure and temperature, the Gibbs phase rule becomes $f + p = c$. Because a metal-SiC system has three components, the maximum number of phases that can be in equilibrium at any given point in the diagram is three. The boundaries of these phase regions can be discerned by calculating the tie lines. The maximum limit of 3 phases being permitted in equilibrium dictates that two tie lines cannot cross each other. Otherwise, there would be four phases in equilibrium which the Gibbs phase rule forbids [20].

To calculate the stable phases that must be connected by tie lines, all of the possible reactions for decomposition of the two phases have to be considered. If they all have positive Gibbs free energy, the reactions will not proceed. Thus, the two compounds are referred to as thermodynamically stable and can be depicted by a tie line in the ternary phase diagram [20].

In this section, stability considerations were discussed using Gibbs free energy and enthalpy of formation for the Ni-Si-C, Ni-O-Si, Ni-O-P and P-Si-C systems by constructing ternary phase diagrams of stability. The above systems were considered due to the presence of Si, C, P, O and Ni during the silicidation assisted impurity doping process.

SiC and a thin nickel film react to form nickel silicides and carbon in the form of amorphous precipitates [21]. In order to determine the stability of the nickel silicon carbide system, the Gibbs free energy for all possible reactions between nickel and SiC must be considered. The possible reactions between SiC and nickel are shown in Reactions 5.22–5.26. Figure 5.7 shows the Ellingham diagram for the formation of silicides.

$$\mathrm{Ni} + \frac{1}{3}\mathrm{SiC} = \frac{1}{3}\mathrm{Ni_3C} + \frac{1}{3}\mathrm{Si} \quad (5.22)$$

$$\mathrm{Ni} + 2\mathrm{SiC} = \mathrm{NiSi_2} + 2\mathrm{C} \quad (5.23)$$

$$\mathrm{Ni} + \mathrm{SiC} = \mathrm{NiSi} + \mathrm{C} \quad (5.24)$$

$$\mathrm{Ni} + \frac{2}{3}\mathrm{SiC} = \frac{1}{3}\mathrm{Ni_3Si_2} + \frac{2}{3}\mathrm{C} \quad (5.25)$$

$$\mathrm{Ni} + \frac{1}{2}\mathrm{SiC} = \frac{1}{2}\mathrm{Ni_2Si} + \frac{1}{2}\mathrm{C} \quad (5.26)$$

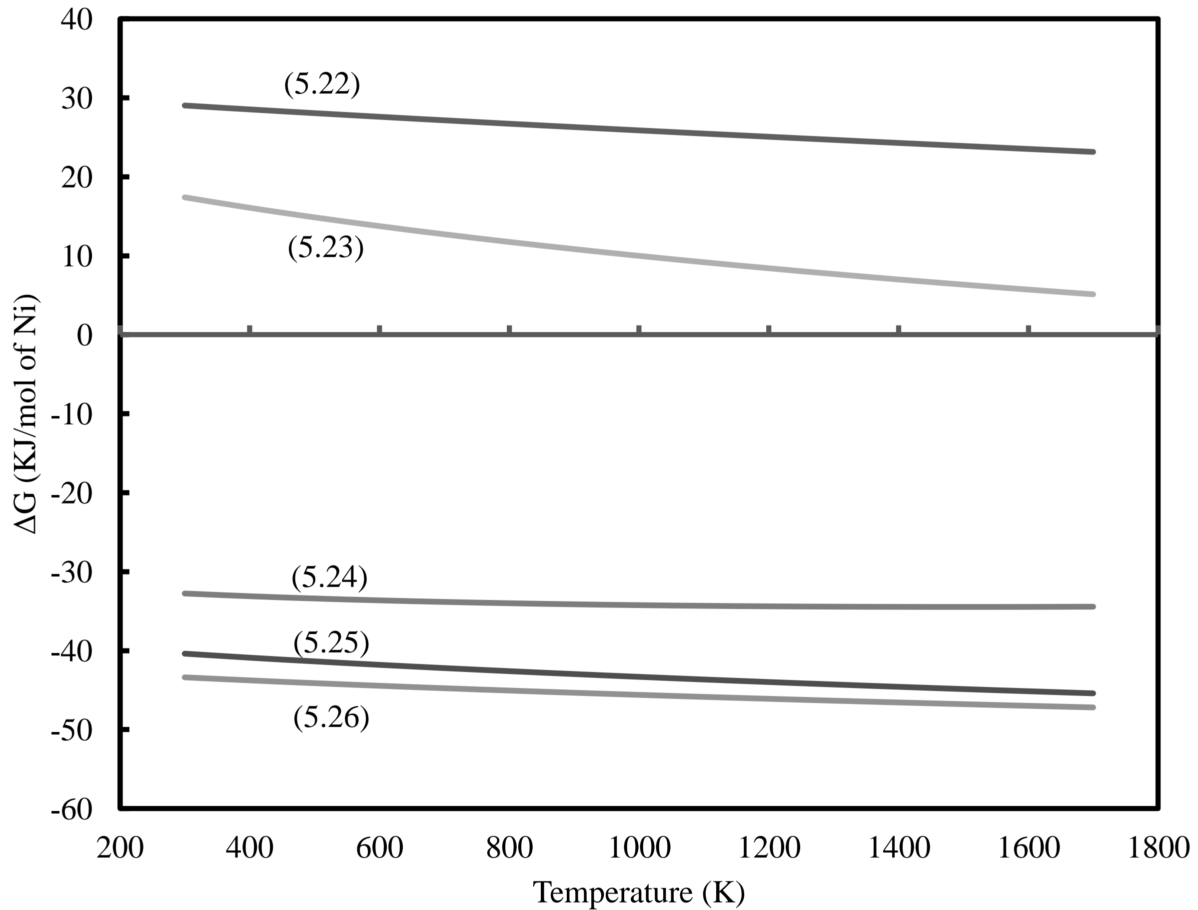

Fig. 5.7: Ellingham diagram for the silicide formation reactions.

As seen from the diagram, the formation of nickel carbide and $NiSi_2$ is not favorable due to the Gibbs free energy of Reactions 5.22 and 5.23 being positive for temperatures below 1700 K. The formation of Ni_2Si, Ni_3Si_2 and NiSi are favorable in the same temperature range since Reactions 5.24 – 5.26 have negative Gibbs free energies. Figure 5.8 shows the ternary phase diagram for the Ni-Si-C system at 900°C (1173 K).

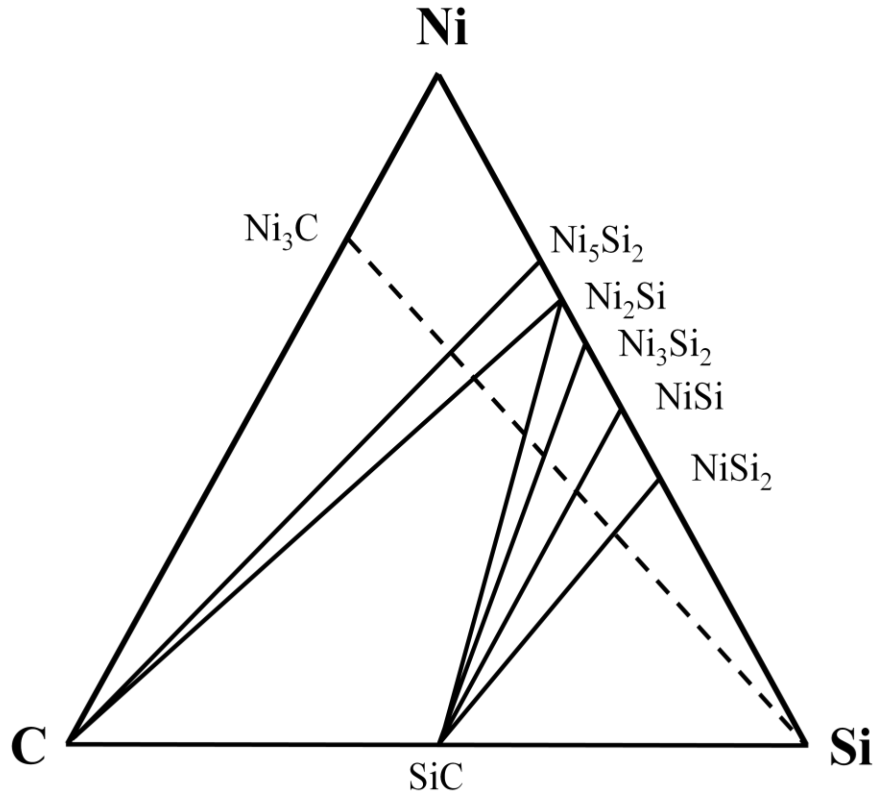

Fig. 5.8: Ni-Si-C ternary phase diagram at 900°C.

In the case of silicide formation on silicon, Ni_2Si is the first phase to form, followed by NiSi and $NiSi_2$. However, silicide formation on SiC requires additional energy for the decomposition of the SiC crystal, which leads to a different sequence for silicide formation [22]. For silicide formation in SiC, the formation of Ni_5Si_2 is the reaction that has the lowest Gibbs free energy [22]. Although Ni_5Si_2 is initially formed, the formation of Ni_2Si from Ni_5Si_2 becomes thermodynamically favorable, which leads to Ni_2Si being the dominant silicide at 900°C. Reactions 5.27 – 5.30 show the possible reactions for the formation of Ni_2Si, Ni_3Si_2, NiSi and $NiSi_2$:

$$2Ni_5Si_2 + SiC = 5Ni_2Si + C \quad (5.27)$$

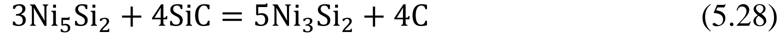

$$3Ni_5Si_2 + 4SiC = 5Ni_3Si_2 + 4C \quad (5.28)$$

$$Ni_5Si_2 + 3SiC = 5NiSi + 2C \quad (5.29)$$

$$Ni_5Si_2 + 8SiC = 5NiSi_2 + 8C \quad (5.30)$$

Levit et al. [22] presented the enthalpies of Reactions 5.27 - 5.30. The reaction for the formation of Ni_2Si from Ni_5Si_2 has an enthalpy change (ΔH) of -2.4 KJ/mol while the reactions for the formation of Ni_3Si_2, NiSi, and $NiSi_2$ from Ni_5Si_2 have enthalpies of +1.8, +7.1 and +19.2 KJ/mol respectively [22]. Therefore, Ni_2Si is the dominant silicide at 900^oC. This explains the tie lines in Figure 5.8 that connect Ni_2Si with SiC and Ni_2Si with C while there is no tie line connecting Ni_5Si_2 and SiC.

Determining the degree of stability of Ni in the presence of P_2O_5 requires the consideration of all of the possible reactions between Ni and P_2O_5. which are shown by Reactions 5.31 – 5.35. The Gibbs free energies of the reactions can be calculated using published data [13,14] and are shown in Table 5.1:

$$Ni + \frac{1}{5}P_2O_5 = NiO + \frac{2}{5}P \quad (5.31)$$

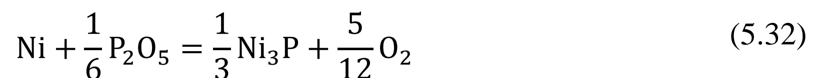

$$Ni + \frac{1}{6}P_2O_5 = \frac{1}{3}Ni_3P + \frac{5}{12}O_2 \quad (5.32)$$

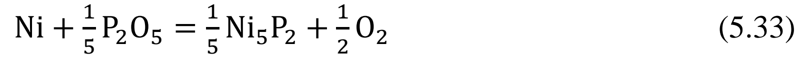

$$Ni + \frac{1}{5}P_2O_5 = \frac{1}{5}Ni_5P_2 + \frac{1}{2}O_2 \quad (5.33)$$

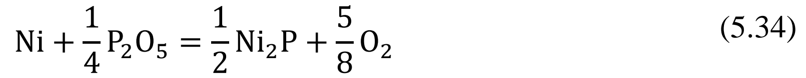

$$Ni + \frac{1}{4}P_2O_5 = \frac{1}{2}Ni_2P + \frac{5}{8}O_2 \quad (5.34)$$

Table 5.1: Gibbs free energies for 5.31 - 5.34 at 1200 K.

Reaction	ΔG (KJ/mol of Ni) at 1200 K (927°C)
5.31	+ 34.95
5.32	+ 82.12
5.33	+ 98.22
5.34	+ 138.57

As evident from Table 5.1, all possible reactions have positive Gibbs free energies, which indicates that P_2O_5 does not decompose in the presence of Ni at 1200 K. This is also shown in the ternary phase diagram for the Ni-O-P system (Figure 5.9) by the tie line connecting Ni and P_2O_5 to indicate stability.

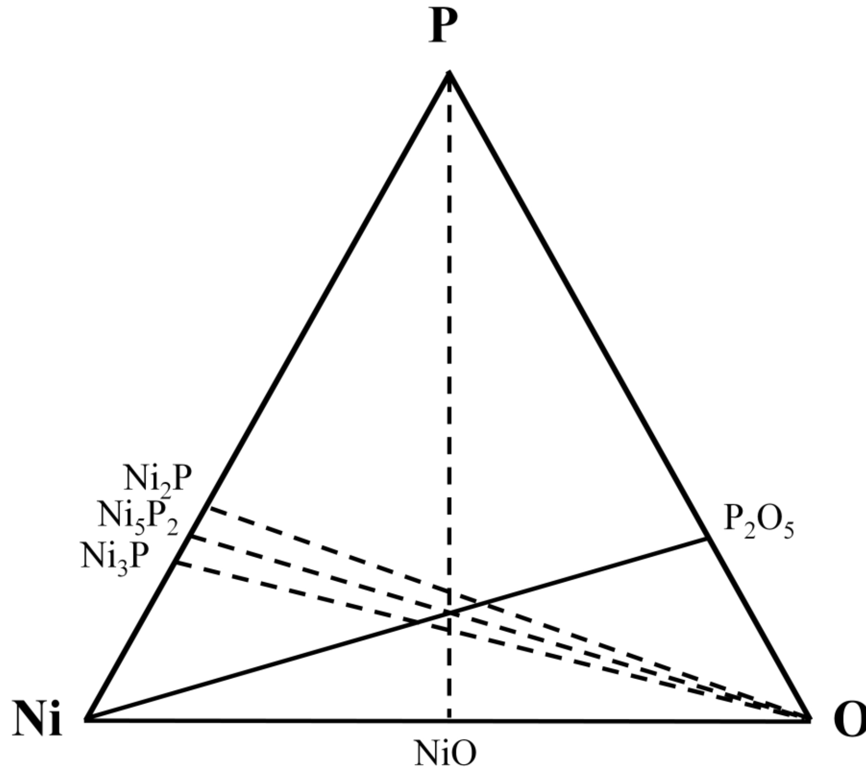

Fig. 5.9: Ni-O-P ternary phase diagram at 1200 K.

The degree of stability of Ni in the presence of SiO_2 depends on every possible reaction between Ni and SiO_2, all of which are shown in Reactions 5.35 – 5.39. The Gibbs free energies of the reactions can be calculated using published data [13,14] and are shown in Table 5.2.

$$\mathrm{Ni} + \frac{1}{2}\mathrm{SiO_2} = \mathrm{NiO} + \frac{1}{2}\mathrm{Si} \quad (5.35)$$

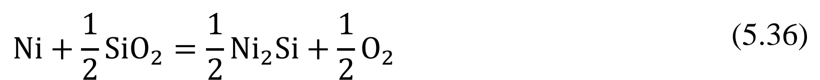

$$\mathrm{Ni} + \frac{1}{2}\mathrm{SiO_2} = \frac{1}{2}\mathrm{Ni_2Si} + \frac{1}{2}\mathrm{O_2} \quad (5.36)$$

$$Ni + 2SiO_2 = NiSi_2 + 2O_2 \quad (5.37)$$

$$Ni + SiO_2 = NiSi + O_2 \quad (5.38)$$

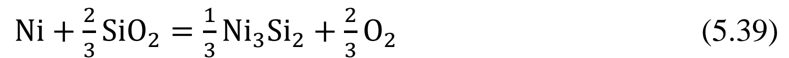

$$Ni + \frac{2}{3}SiO_2 = \frac{1}{3}Ni_3Si_2 + \frac{2}{3}O_2 \quad (5.39)$$

Table 5.2: Gibbs free energies for 5.35 - 5.39 at 1200 K.

Reaction	ΔG (KJ/mol of Ni) at 1200 K (927°C)
5.35	+ 215.67
5.36	+ 210.15
5.37	+ 834.78
5.38	+ 614.73
5.39	+ 399.87

As seen in Table 5.2, all possible reactions have positive Gibbs free energies, which indicates that SiO_2 does not decompose in the presence of Ni at 1200 K. This is also shown in the ternary phase diagram for the Ni-O-Si system (Figure 5.10) by the tie line connecting Ni and SiO_2 to indicate stability.

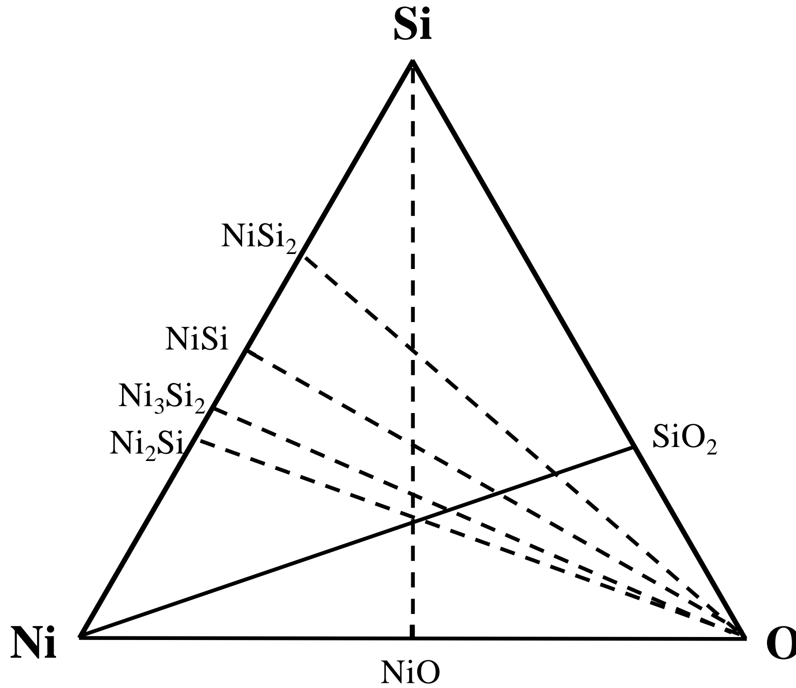

Fig. 5.10: Ni-O-Si ternary phase diagram at 1200 K.

The stability of phosphorus in the presence of SiC depends on the two possible reactions (5.40 and 5.41) that can result from the interaction. Calculations of Gibbs free energy for the two reactions reveal a ΔG value of +33.41 KJ/mol for the formation of silicon phosphide (SiP) and ΔG value of +389.83 KJ/mol for the formation of carbon phosphide (CP). This indicates that SiC is stable in the presence of elemental phophorus at 1200 K. This is also shown in the ternary phase diagram for the P-Si-C system (Figure 5.11) by the tie line connecting P and SiC to indicate stability.

$$\mathrm{SiC + P = SiP + C} \qquad (5.40)$$

$$\mathrm{SiC + P = CP + Si} \qquad (5.41)$$

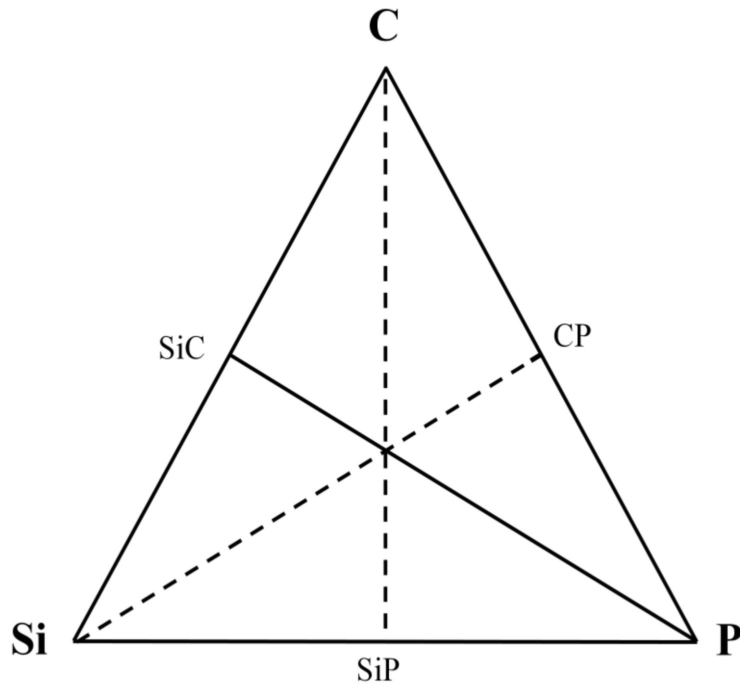

Fig. 5.11: P-Si-C ternary phase diagram at 1200 K.

After considering the variables and all of their potential combinations during the silicidation assisted impurity doping process, it can be deduced that nickel atoms from the thin Ni layer deposited on the P_2O_5 layer diffuse through the P_2O_5 layer without decomposing either P_2O_5 or SiO_2 while drawing out Si atoms from the SiC crystal to form Ni_2Si, thus assisting in silicon vacancy creation followed by dopant incorporation at 1200 K.

5.3 Dopant Sources for the VAID technique

5.3.1 Phosphorus and Boron

Spin-on dopants

The introduction of dopants in silicon substrates by using spin-on dopants followed by solid-state diffusion has been well documented and experimentally proven, and sufficiently high carrier concentrations are easy to achieve [23,24]. Zhu et al. [25] reported that the use of a spin-on dopant process for contact-doped single crystal silicon transistors on plastic substrates. High frequency silicon devices have been fabricated on plastic substrates using this process. Diffusion of phosphorus into silicon from a doped spin-on glass source using rapid thermal processing [24,26] has yielded sheet resistance as low as 15 Ω/□ and a surface carrier concentration in the range of 10^{20} cm^{-3} [26]. Bourdais et al. [23] studied emitter formation on polycrystalline silicon using rapid thermal diffusion from a spin-on dopant source. However, solid state diffusion of dopants in SiC is not well documented. The use of spin-on dopant solutions for doping silicon carbide is not a common practice and the successful development of this spin-on dopant method can provide an economical and simple way to dope SiC. Such a process would be useful in creating p-n junctions or in ohmic contact fabrication. Identification and development of phosphorus and boron dopant solutions for the implementation of the VAID technique is discussed in this section.

Phosphorus

The VAID process requires the use of an impurity oxide or carbide to aid in the creation of silicon vacancies. When considering phosphorus, oxide becomes the obvious choice because it is readily available in powder form as phosphorus oxide (P_2O_5). It can also be obtained as a liquid in the form of phosphoric acid (H_3PO_4). Sivoththaman et al. [27] studied the use of phosphoric acid as a spin-on solution for the formation of shallow junctions on silicon. However, investigations have shown that phosphoric acid does not have sufficient viscosity for the deposition of an even liquid layer on a complete sample wafer. Since the VAID process requires an even oxide layer on the semiconductor surface, an organic solvent would be an ideal candidate for the development of a spin-on dopant source.

Phosphorus spin-on dopants are available commercially but many formulations contain silica. Si-containing dopant sources must be avoided because additional Si in the layer prevents the silicon atoms from leaving and creating V_{Si} in the SiC lattice. For this work, a commercially available phosphorus spin-on dopant without silica was used for the implementation of VAID technique and the silicidation assisted doping technique. Since the VAID technique calls for a source of phosphorus oxide, the commercial dopant solution was analyzed using mass spectroscopy. Figure 5.12 shows the mass spectra of the dopant solution.

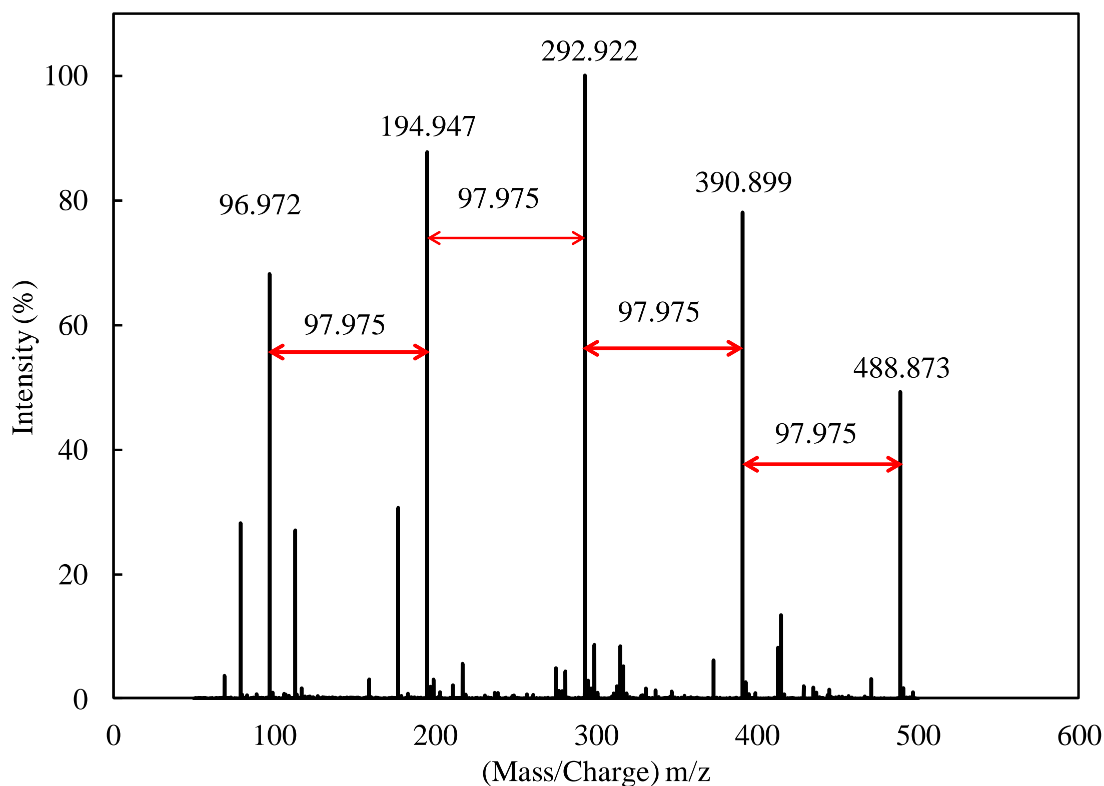

Fig. 5.12: Mass Spectrum of the phophorus dopant solution.

As seen from the mass spectrum, peaks are evident at 96.972, 194.947, 292.922, 390.899 and 488.873. The spectrum was obtained with an ion of negative charge and the mass of 96.972 corresponds to the dihydrogen phosphate anion ($H_2PO_4^-$). An average value of 97.975 between adjacent major peaks corresponds to the molar mass of phosphoric acid (H_3PO_4), which is 97.99g. Therefore, it can be concluded that the phosphorus dopant solution used in this work consists of phosphoric acid in an organic binding solvent, which allows it to be spun on the surface of a SiC sample. The experimental process for the VAID technique is discussed in detail in Section 6.1.5.1.1.

Boron

The VAID process for boron was implemented with a boron oxide solution prepared in the Auburn University semiconductor laboratory. Boron oxide (B_2O_3) is available commercially as a powder. Various combinations of solvents were considered for the preparation of a solution that could be effectively spun-on to a wafer. The best combination of solvents with the appropriate viscosity was a 1:1:2 mixture of ethanol, methanol, and isopropanol. Different masses of boron oxide were measured and dissolved in the solvent solution. The boron was effectively dissolved at approximately 60°C. The boron solution was then spun-on to sample by using a spin coater at spin speed of 2000 rpm (revolutions per minute) for 30 s. The organic solvent solution evaporated at the end of the spin coating process, leaving behind an evenly spread layer of boron oxide on the surface of the sample. Figure 5.13 (a-c) shows the Nomarski micrographs for the dopant solution deposited on SiC at different concentrations of B_2O_3. After being annealed in an oxygen ambient for 1 hr at 1300°C, the sample was immersed in buffered oxide etch to remove the SiO_2 layer that had formed on top of the SiC. As seen from Figure 5.13 (d), there is no major surface damage to the sample after the anneal at high temperature.

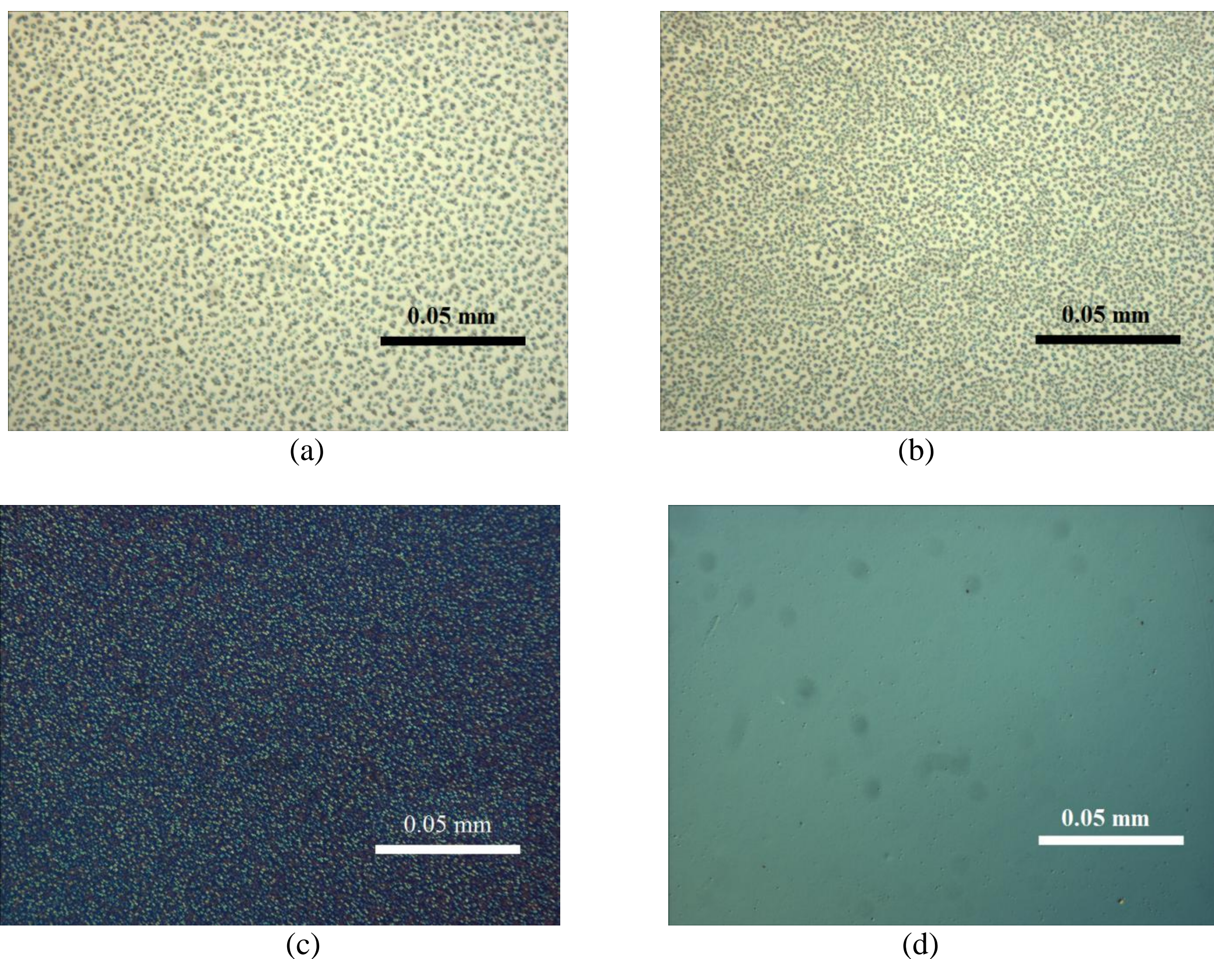

Figure 5.13: Nomarski micrographs for (a) 0.25 g (b) 0.497 g (c) 0.792 g of B_2O_3 in 20 ml of 1:1:2 ethanol, methanol and isopropanol solution. (d) After annealing sample shown in b at 1300°C.

Triethylborate, which is a commercially available organic based liquid source, can also be used as a dopant solution. This solution was spin-coated onto the sample at 1000 rpm and 2000 rpm. Figures 5.14(a) and 5.14(b) show the Nomarski micrographs for the spin-coated samples. As seen from the Figures, spin-coating at 1000 rpm was identified as the optimal spin speed. After being annealed in oxygen at 1300°C, the samples were immersed in buffered oxide etch to remove the SiO_2 layer. The sample showed considerable roughness after annealing, which is shown in Figure 5.14(c). Therefore, it can be reasoned that the solution prepared using

B_2O_3 powder was the most effective boron source for the VAID process. The experimental procedure for the VAID process for boron is discussed in detail in the experimental section in Chapter 6.

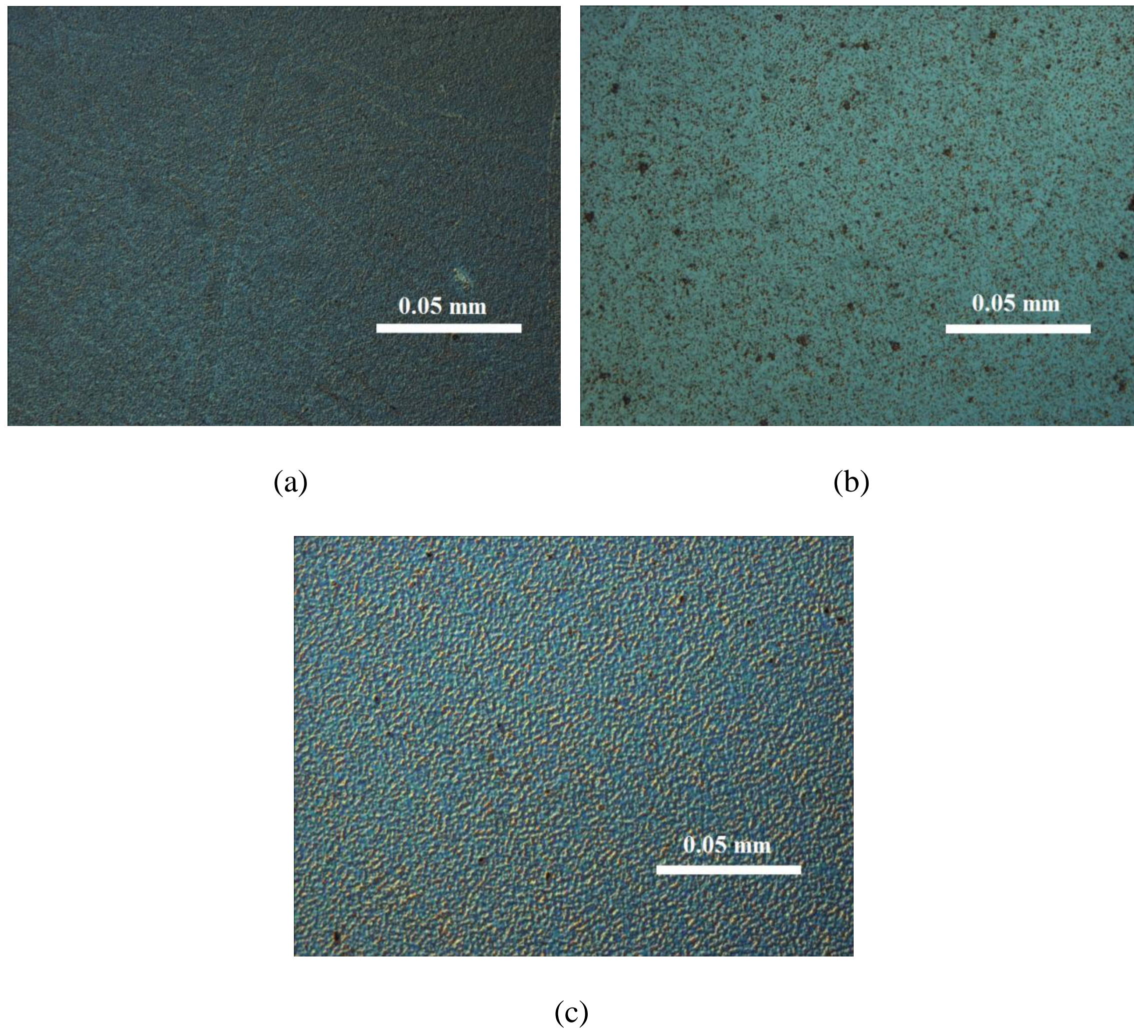

Fig. 5.14: Triethylborate spin-coated at (a) 1000 rpm (b) 2000 rpm. (c) Sample spin-coated at 1000 rpm after anneal in O_2 at 1300°C.

5.3.2 Electroless Plating

It is plausible that there are other variations and dopant solutions by which the VAID method can be implemented. One such method is electroless plating. Electroless nickel plating is an auto-catalytic chemical process used to deposit a layer of nickel-phosphorus or nickel-boron alloy on a solid surface. Since electroless nickel film contains 5-14% by weight of phosphorus, it is an attractive candidate for the silicidation assisted impurity doping process [28]. The nickel in electroless nickel film can form silicides and act as a catalyst for phosphorus diffusion at low temperatures.

Electroless nickel is generally used for the purpose of anti-corrosion or tribological coatings for metal parts in industry [29] and electroless nickel plating solution with different phosphorus content is available commercially. Electroless plating is an autocatalytic process of deposition by the immersion of a sample in a plating bath. The solution contains sodium hypophosphite (NaH_2PO_2), which acts as a reducing agent and provides electrons for the capture of Ni^{2+} cations. When in the plating solution, the sodium hypophosphite gives out the $H_2PO_2^-$ ions that are adsorbed to the surface [30]. This is shown in Reaction 5.42. During the binding process, atomic phosphorus is released which serves as the dopant atoms in the contact region when provided with adequate temperature.

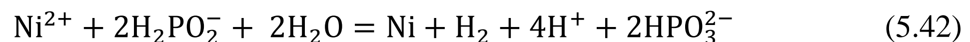

$$\mathrm{Ni^{2+} + 2H_2PO_2^- + 2H_2O = Ni + H_2 + 4H^+ + 2HPO_3^{2-}} \quad (5.42)$$

Electroless nickel has been used for fabrication of devices and contacts on other semiconductors [30,31]. Boulord et al. [30] demonstrated the formation of electroplated nickel contacts for silicon solar cells with contact resistivity of 10^{-4} Ωcm^2, but electroless nickel plating has not been studied in detail in terms of the fabrication of contacts for n-type SiC. The phosphorus content in the deposited electroless nickel film can be controlled by altering the pH, which affords a certain flexibility for the amount of phosphorus going into the lattice at the contact.

The experimental procedure is discussed in detail in the experimental section in Chapter 5. The successful deposition of a NiP thin layer on 4H-SiC through electroless nickel plating and ohmic contact characterization is reported in Chapter 6.

5.4 References

1. C. C. Tin, A. V. Adedeji, I. G. Atabayev, B. G. Atabaev, T. M. Saliev, E. N. Bakhranov, M. Li, S. P. Mendis and C. A. Ahyi, *U.S. Patent* 7,999,268. (2011).

2. M. Bockstedte, A. Gali, A. Mattausch, O. Pankratov and J. W. Steeds, *Phys. Stat. Sol.* (b) **245**, 1281 (2008).

3. F. Yan, *Low Temperature Photoluminescence Study on Defect Centers in Silicon Carbide*, DIssertation, University of Pittsburgh (2009).

4. T. Miyajima, N. Tokura, A. Fukumoto and H. Hayashi, *U.S. Patent* 6,133,120 (2000).

5. Y. Gao, S. I. Soloviev and T. S. Sudarshan, *Appl. Phys. Lett.* **83** (5), 905 (2003).

6. M. Laube, G. Pensl and H. Itoh, *Appl. Phys. Lett.* **74**(16), 2292 (1999).

7. V. Moroz, Y. S. Oh, D. Pramanik, H. Graoui and A. Foad, *Appl. Phys. Lett.* **87**, 051908 (2005).

8. D. J. Larkin, P. G. Neudeck, J. A. Powell, and L. G. Matus, *Appl. Phys. Lett.* **65**, 1659 (1994).

9. F. Gao, M. Posselt, V. Belko, Y. Zhang and W. J. Weber, *Nucl. Instrum. Meth.* B **218**, 74 (2004).

10. A. Mattausch, *Ab-initio theory of point defects and defect complexes in SiC*, Dissertation, University of Erlangen-Nuremberg (2005).

11. K. Negita, *J. Am. Ceram. Soc.* **69**(12), C308 (1986).

12. W. Greiner, L. Neise and H. Stöcker, *Thermodynamics and Statistical Mechanics*, Springer-Verlag (1995).

13. M.W. Chase, Jr., *NIST-JANAF Thermochemical Tables*, 4th Ed. National Institute of Standards and Technology, Gaithersburg, Maryland, (1998).

14. I. Barin, *Thermochemical data of pure substances*, 3rd Ed. VCH Publishers, New York (1995).

15. S. P. Mendis and C.C. Tin, *Mater. Res. Soc. Symp. Proc.* **1246**, B07 (2010).

16. J. N. Hart, N. L. Allan and J. M. Oliva, *Phys. Rev. B* **79**, 134115 (2009).

17. I. G. Atabaev, C. C. Tin, B. G. Atabaev, T. M. Saliev, E. N. Bakhranov, N. A. Matchanov, S. L. Lutpullaev, J. Zhang, N. G. Saidkhanova, F. R. Yuzikaeva, I. Nuritdinov, A. K. Islomov, M. Z. Amanov, Rusli and A. Kumta, *Mater. Sci. Forum* **600-603**, 457 (2009).

18. C. C. Tin, S. Mendis, K. Chew, I. Atabaev, T. Saliev, E. Bakhranov, B. Atabaev, V. Adedeji and Rusli, *Thin Solid Films* **518**, e118 (2010).

19. R. Beyers, K. B. Kim and R. Sinclair, *J. Appl. Phys.* **61**(6), 2195 (1987).

20. W. F. Seng and P. A. Barnes, *Mater. Sci. Eng.* **B76**, 225 (2000).

21. C. S. Lim, H. Nickel, A. Naoumidis and E. Gyarmati, *J. Mater. Sci*. **32**, 6567 (1997).

22. M. Levit, I. Grimberg and B. Z. Weiss, *J. Appl. Phys.* **80**(1), 167 (1996).

23. S. Bourdais, G. Beaucarne, A. Slaoui, J. Poortmans, B Semmache and C. Dubois, *Sol. Energy Mater. Sol. Cells* **65**, 487 (2001).

24. D. Mathiot, A Lachiq, A. Slaoui, S. Noël, J. C. Muller and C. Dubois, *Mater. Sci. Semicond. Process.* **1**, 231 (1998).

25. Z. -T. Shu, E. Menard, K. Hurley, R. G. Nuzzo and J. A. Rogers, *Appl. Phys. Lett.* **86**, 133507 (2005).

26. B. Hartiti, A. Slaoui, J. C. Muller, R. Stuck and P. Siffert, *J. Appl. Phys.* **71**, 5474 (1992).

27. S. Sivoththaman, W. Laureys, J. Nijs and R. Mertens, *Appl. Phys. Lett.* **71**(3), 392 (1997).

28. S. P. Mendis, C. C. Tin, M. T. Tin, T. Isaacs-Smith and E. R. Crandall, "*Electroless Nickel for n-type contact on 4H-SiC"*, Materials Science Forum – in press.

29. G. O. Mallory and J. B. Hajdu (Eds.), Electroless Plating: Fundamentals and Applications, American Electroplaters and Surface Finishers Society, Orlando, (1990).

30. C. Boulord, A. Kaminski, B. Canut, S. Cardinal and M. Lemiti, *J. Electrochem. Soc*. **157**, H742 (2010).

31. L. Lewis, D. P. Casey, A. V. Jeyaseelan, J. F. Rohan and P. P. Maaskant, *Appl. Phys. Lett.* **92**, 062113 (2008).

Chapter 6

Basic Experimental Methods

6.1 Standard Procedures

In this work, experiments were carried out to investigate the VAID process through oxidation and silicidation as discussed in Chapter 5. This chapter details the experimental procedures used to incorporate phosphorus into 4H SiC and the fabrication procedures used to characterize the SiC surface. 4H SiC wafers were diced into 5mm x 5mm samples, which were used for all experiments in this thesis. Three main types of 4H SiC were used, including n-type 4H-SiC for the fabrication and characterization of Schottky contacts and p-type 4H-SiC for the fabrication and characterization of ohmic contacts on doped samples. The epitaxial layers of both the n-type and p-type samples had a base-doping concentration of 10^{15}-10^{16} cm^{-3}. Semi-insulating 4H SiC was mainly used for physical analysis (EDX, RBS and SIMS).

6.1.1 Sample Cleaning

Prior to use, the samples were cleaned using both basic organic and Radio Corporation of America (RCA) cleaning processes. Meticulous cleaning is essential to remove any kind of particulate matter on the surface of the sample, including traces of organic, ionic or metallic contaminants [1-3]. Steps used in the cleaning process are listed below.

Organic Clean

- Immerse in acetone for 5 min.
- Immerse in trichloroethylene (TCE) for 5 min.
- Immerse in acetone for 5 min.
- Immerse in methanol for 5 min.
- Immerse in methanol for 5 min.
- Rinse in de-ionized water (DI water).
- Immerse in buffer oxide etch (BOE) for 4 min.
- Rinse in DI water for 2 min and dry with N_2 gas.

The first five steps are conducted in an ultrasonic bath to agitate and aid in the removal of impurities from the surface.

RCA Clean

- Immerse in a 1:1 solution of H_2O_2:H_2SO_4 for 15 min.
- Rinse with DI water for 2 min.
- Immerse in BOE for 1 min.
- Rinse with DI water for 2 min.
- Immerse in boiling 6:1:1 solution of DI water: H_2O_2: NH_4OH for 15 min.
- Rinse with DI water for 2 min.
- Immerse in BOE for 1 minute.

- Rinse with DI water for 2 min.
- Immerse in boiling 6:1:1 solution of DI water: H_2O_2: HCl for 15 min.
- Rinse with DI water for 2 min.
- Immerse in BOE for 1 minute.
- Rinse with DI water for 2 min.
- Dry with N_2 gas.

6.1.2 Photolithography

Photolithography is a necessary process for the fabrication of semiconductor electronic devices. Through this process, it is possible to transfer a particular pattern from a photomask onto a sample. Photolithography can also be described as a more sophisticated version of the photoengraving process. The required patterns are initially transferred onto photoresist, which is a light-sensitive chemical that coats the surface. Then, metal contacts can be deposited on the sample to transfer the pattern. This process allows control over the shape and size of the patterns, providing high resolution. Optical photolithography is limited to a minimum feature size of 1-2 μm. While this is sufficient for the purpose of this thesis, most modern electronics require feature sizes in the nm range, making optical photolithography inadequate. In these instances, electron beam lithography is used.

The Karl Suss MJB3 UV400 mask aligner at the Auburn University physics clean room facility was used in this work. This manually-controlled mask aligner is equipped with an optical microscope having magnification by factors of 5, 10, and 20, as well as an Hg lamp that provides

a UV light source with an output power of 160W. The resolution of the mask aligner is 2-3 μm and a schematic diagram of the aligner is shown in Figure 6.1.

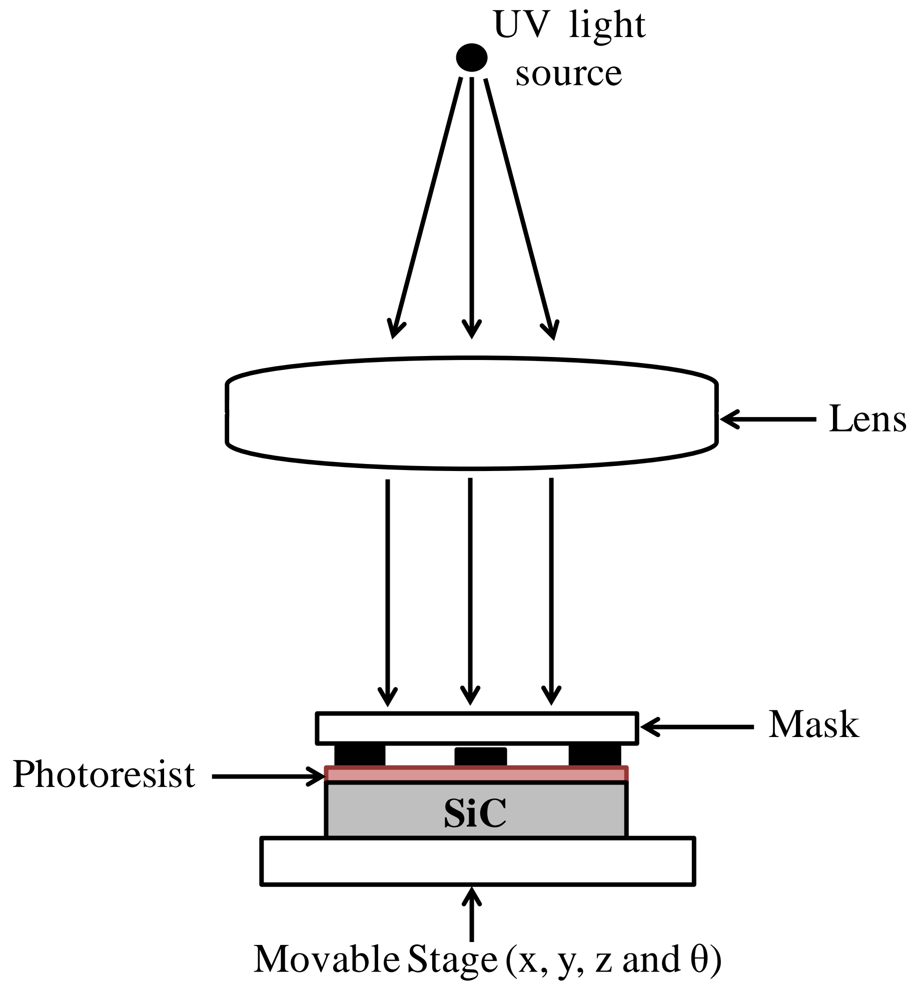

Fig. 6.1: Schematic diagram for mask aligner

The mask aligner is designed to accommodate a wafer with a maximum diameter of 4 in. Since each sample used in this work was only 5 mm x 5 mm in size, they were attached to the center of a silicon wafer with a diameter of 3 in using a water-soluble wax before photolithographic processing took place. The wafer holding the sample was coated with

photoresist (AZ 5214-EIR) using a spin-coater with a rotor speed of 4000 rpm for 30 s. The thickness of the photoresist layer on the sample was approximately 1.5 µm. The wafer was subsequently soft-baked for 1 min in an oven that was constantly maintained at 110°C. After soft-baking, the wafer was mounted on the mask aligner and the sample was aligned with the desired pattern on the mask. The sample was then exposed to ultraviolet (UV) light for 30 s.

The final step in the photolithographic process was development, in which a mixture of DI water and chemical developer (AZ 400K) was used. While still being mounted on 3-in wafers, the samples were immersed in the mixture for approximately 10-15 s, rinsed in DI water for 1 min, and blow dried using N_2. During development, the area which was been exposed to UV light disappeared, leaving behind the pattern of the mask on the sample. In some instances, image reversal is required and it can be achieved by hard-baking the sample for 1min at 110°C in the oven immediately after the first 30 s exposure, followed by a second UV exposure for 1 min without the photomask. This variation dissolves the photoresist, which is not exposed to UV light.

6.1.3 Metal Sputter Deposition

Sputter deposition is a process in which material is removed from a solid cathode by bombarding it with positive ions of a plasma and the removed material is deposited on the surface of the sample [4]. Collision of the ions with the material on the surface of the sputter target releases atoms leading to deposition on the sample. Figure 6.2 shows a schematic diagram of this process in the DC sputtering system at Auburn University.

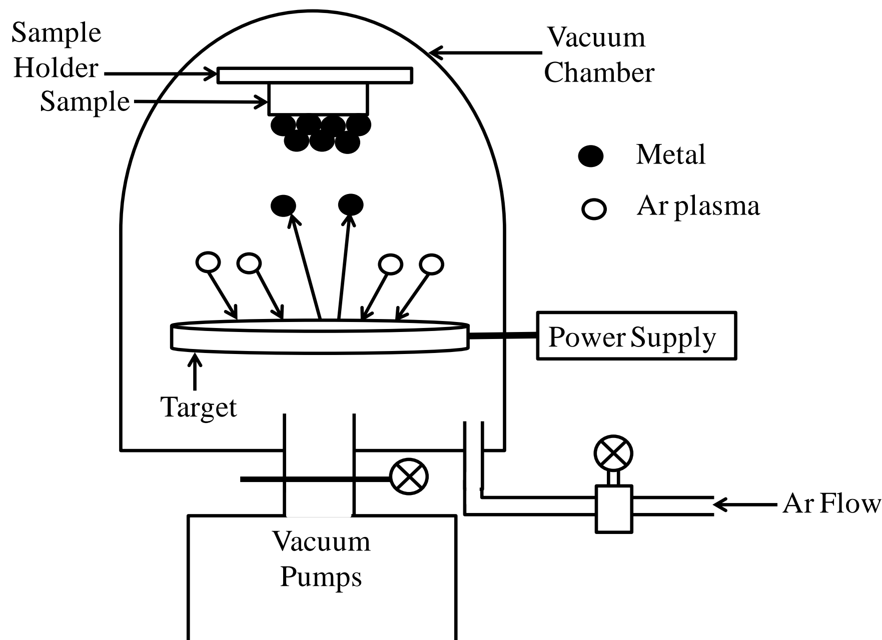

Fig. 6.2: Schematic diagram of the DC sputtering process [5,6].

Metals were sputter-deposited in an argon (Ar) plasma environment. A high vacuum of approximately $3x10^{-7}$ Torr was reached by using a turbo pump. Four 2″ diameter magnetron sputtering guns are available in the vacuum chamber. Four metals or alloys can be sputtered successively onto a sample without releasing the vacuum in this system and the sputter targets can be operated at a maximum DC power of 1000W. The 5 mm x 5 mm samples, which were still attached to 3-in Si wafers, were mounted on a circular holder which can be mechanically rotated to position directly above a specific sputter gun.

During the sputtering process, Ar gas flows at a rate of 100.0 sccm (standard cubic centimeters per minute). By using a valve to control the pumping speed of the turbo pump, the chamber pressure was allowed to rise to 18 mTorr. For 93% nickel/ 7% vanadium ($Ni_{93\%}V_{7\%}$) alloy, which was predominantly used as the ohmic contact metal in this work, the sputter current

was maintained at 0.25 A by controlling the voltage. Any impurities were removed from the target surface by pre-sputtering for 2 min before the sample is rotated into position for deposition. A total sputtering time of 8 min is used for ohmic contacts with a thickness of approximately 1500 Å.

6.1.4 Thermal Evaporation

This is one of the oldest techniques for depositing selected metals onto semiconductors. Through various methods, the metal required is heated to the point of evaporation and a thin film of the metal is formed on the surface of a sample. Evaporation requires a high vacuum in the deposition chamber so that the composition of the deposited metal can be controlled [1].

Figure 6.3 shows the schematic diagram of the thermal evaporation system used in this thesis. It is a simple filament evaporation system with a tungsten filament, which is capable of being heated to approximately 1500°C. Since this work called for the evaporation of pure Ni, an alumina-coated tungsten wire boat was used as seen in the insert in Figure 6.3.

In basic operation, the valves to the two mechanical roughing pumps are opened to lower the pressure of the chamber to an intermediate level ($\approx 2x10^{-2}$ Torr). Since a higher vacuum is required for evaporation, the valves to the mechanical pumps are closed and the valves to the turbo pumps are opened. This lowers the pressure of the chamber to approximately $5x10^{-6}$ Torr. After the chamber has been in a high vacuum for about 2 hrs, the power supply is turned on and the current to the filament is gradually increased until the Ni melts, which can be observed through a window in chamber. The high vacuum allows the evaporated metal particles travel

directly to the sample, which is placed above the tungsten boat. 15 s of evaporation after the observed melting deposits approximately 55 nm of nickel on the surface of the sample.

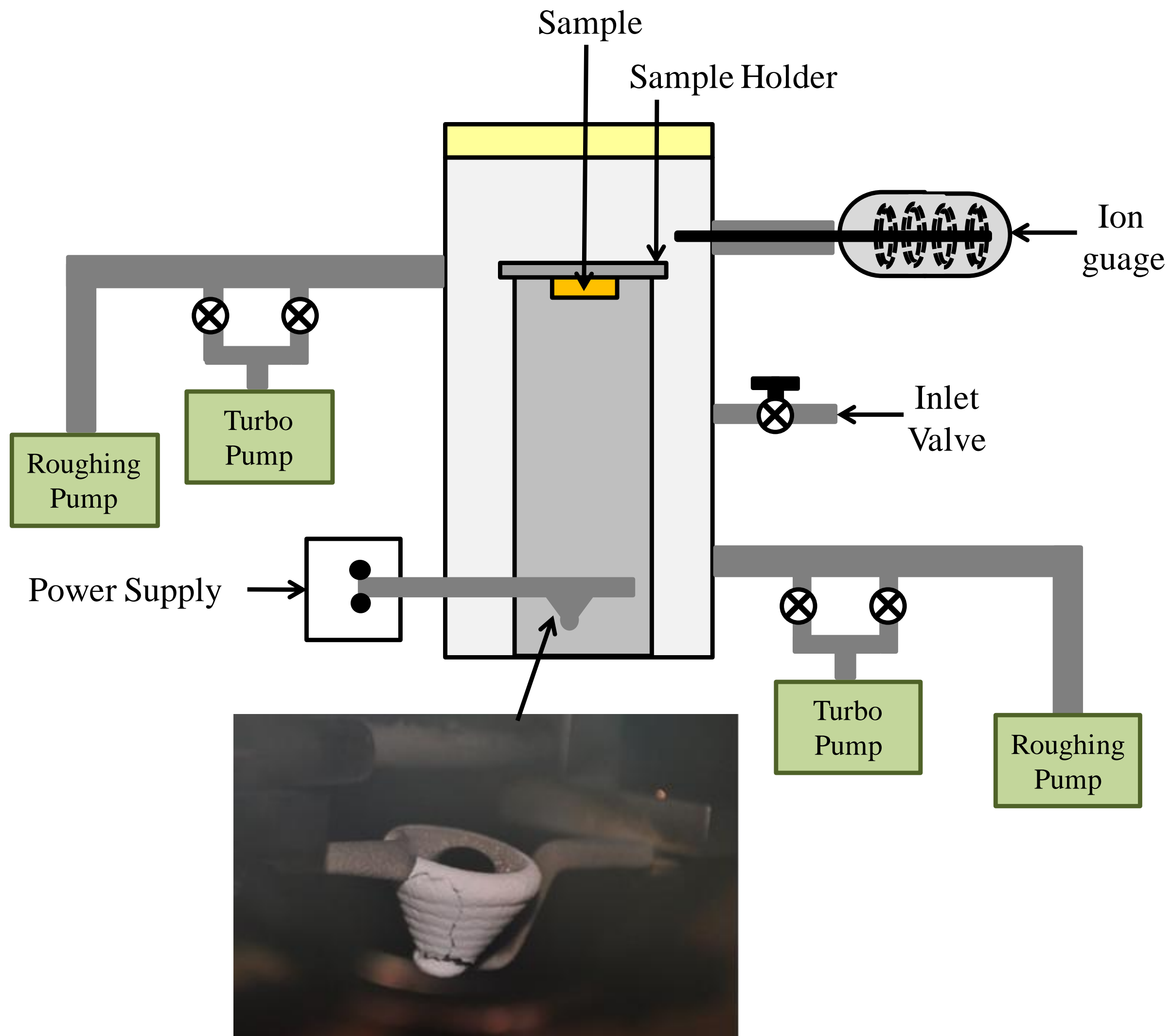

Fig. 6.3: Schematic diagram of thermal evaporation system.

6.1.5 Thermal Annealing

In this process, a sample is heated above a critical temperature for alloying with the substrate. This temperature must be maintained for a required amount of time in order for diffusion to occur. Afterwards, it is cooled to room temperature [7].

In the semiconductor industry, thermal annealing aids in the diffusion of dopant atoms into substitutional positions in the semiconductor lattice. In other instances, it is required to relieve internal stress at the metal semiconductor interface by inducing favorable reactions between the metal and the semiconductor [8].

6.1.5.1 Alumina Furnace

6.1.5.1.1 VAID Process

The alumina furnace used in this work primarily for the purpose of dopant diffusion is shown in Figure 5.4. It consists of an alumina tube as a heating chamber, which is connected to an oxygen gas line and an Argon gas line, with both lines connected to flow meters. The chamber is connected to a mechanical vacuum pump with the capacity to reach low vacuum levels (10^{-2}-10^{-1} Torr) as shown in the Figure 5.4. A one-way air flow valve is connected for use during gas flow. A maximum temperature of 1600^oC can be reached due to the 4 SiC rods that are used as heating elements.

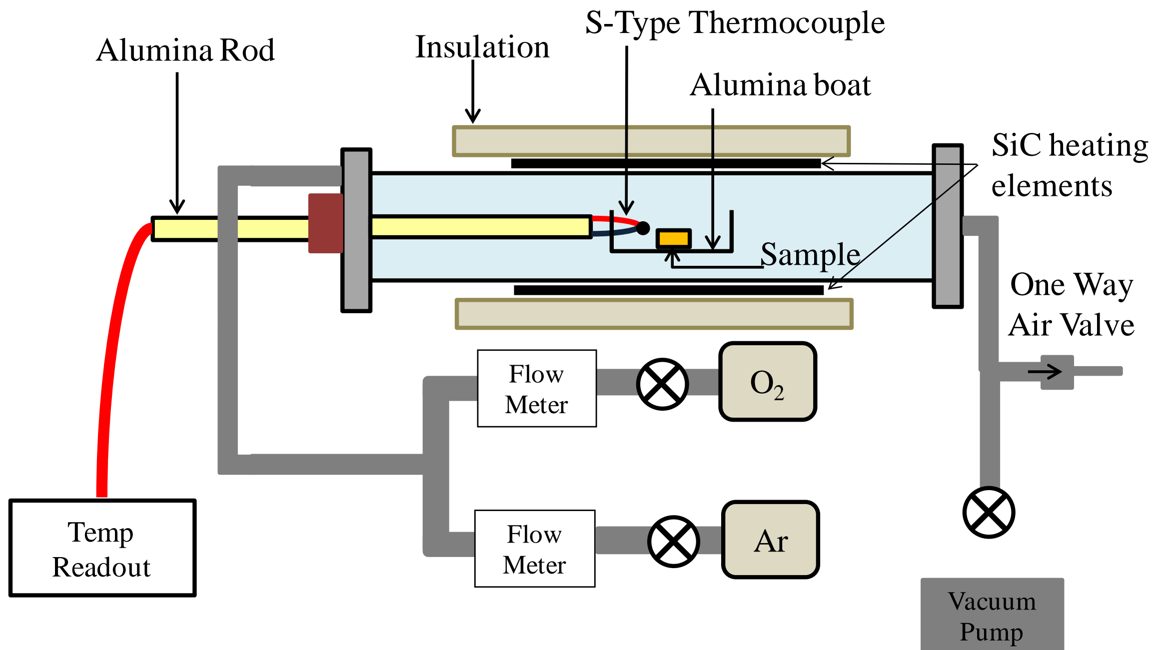

Fig. 6.4: Schematic diagram of alumina furnace.

The sample was placed on an alumina boat, which was attached to an alumina rod. This alumina rod could be moved inside the chamber to adjust the temperature of the sample. The temperature of the sample was monitored by an s-type thermocouple, which had been tunneled through the alumina rod.

Phosphorus diffusion

The samples were first cleaned using the standard organic and RCA cleaning processes. Then, as part of the dopant diffusion (VAID) process, a dopant solution was initially prepared (Section 5.3.1) and spun onto the surface of the SiC sample at the desired rotational speed. A speed of 1500 rpm was used when spinning the phosphorus solution and the boron solution was spun at 4000 rpm.

Figure 6.5 shows the VAID process for phosphorus diffusion. After spinning the dopant solution onto the surface, the SiC sample was heated to 650°C in O_2 for 30 min, which led to the formation of a glassy P_2O_5 layer on the surface. Then the sample was annealed in O_2 for 1 hr in the alumina furnace at a temperature ranging between 1150°C and 1400°C. After allowing the sample to cool down to room temperature while still in the furnace, it was immersed in buffered oxide etch (BOE) for 5 min to remove the SiO_2 layer that had formed on top of the sample as shown in the Figure 6.5

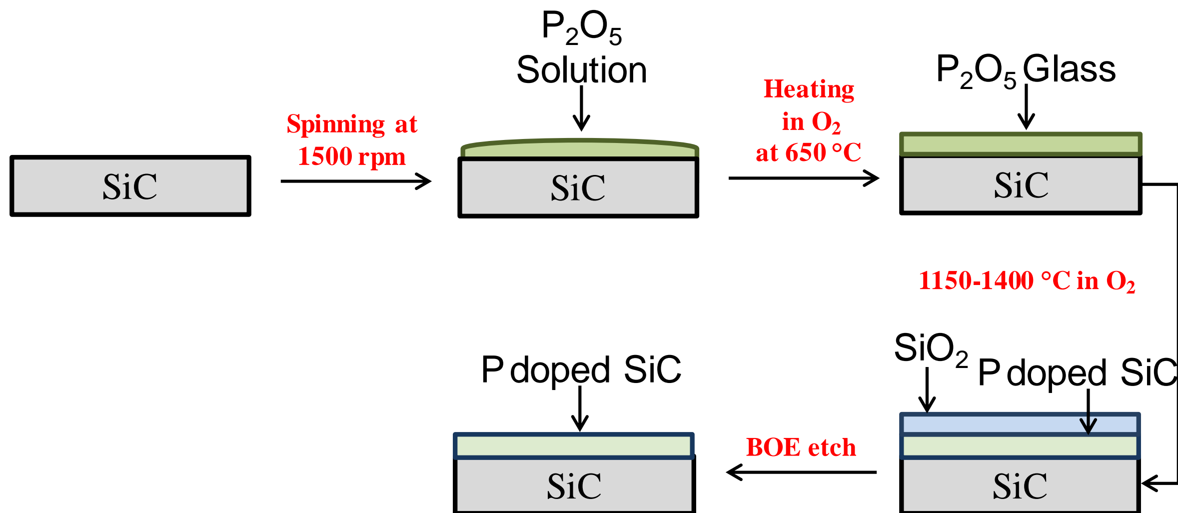

Fig. 6.5: Experimental process for phosphorus diffusion (VAID).

Silicidation assisted impurity doping

Figure 6.6 shows a variation of the above process where nickel was used as a catalyst for the dopant diffusion process. The phosphorus solution was spun on to the sample and heated in O_2 at 650°C to produce a P_2O_5 glassy layer. Then, pure nickel was thermally evaporated onto the sample as shown in Figure 6.6 by using the thermal evaporation system discussed in the previous

section. Subsequently, the SiC sample with the phosphorus oxide and nickel layers was annealed in an Ar ambient at 900°C for 1 hr. After the sample was cooled to room temperature, it was immersed in BOE to remove the top layers.

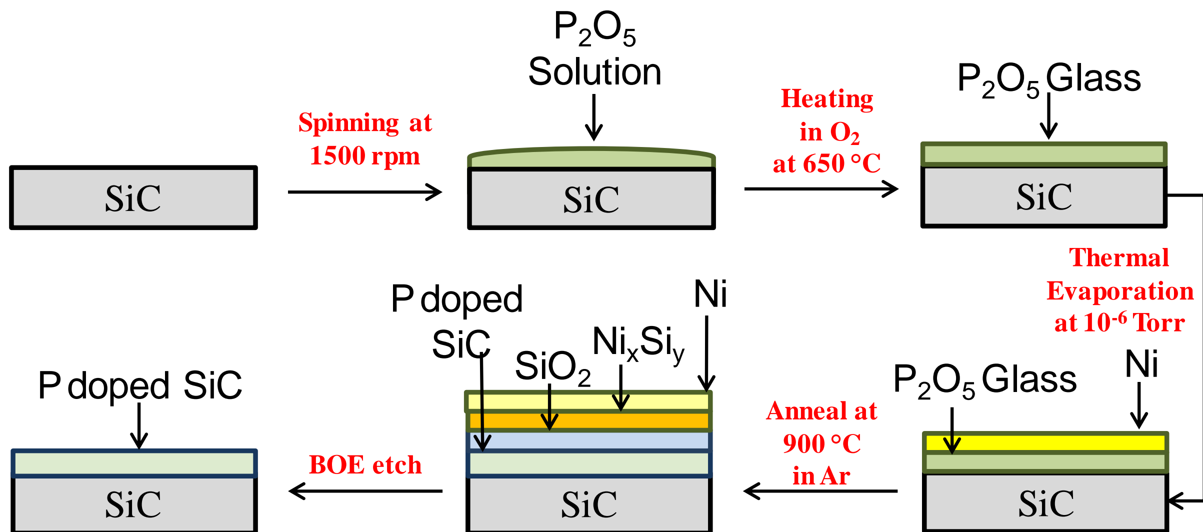

Fig. 6.6: Experimental process for silicidation assisted phosphorus diffusion.

Boron diffusion

The VAID process was also used to diffuse boron into SiC. After spinning-on the boron oxide solution at 4000 rpm, the boron oxide particles were observed to be evenly spread out on the sample (Figure 5.13). The sample was then heated in O_2 at 650°C for 30 min in the alumina furnace to form a glassy B_2O_3 layer. Afterwards the sample was annealed in O_2 for 1 hr in the alumina furnace at a temperature ranging between 1150°C and 1400°C. After the sample was cooled to room temperature, it was immersed in BOE to remove the top layer of B_2O_3. The boron diffusion process is shown in Figure 6.7.

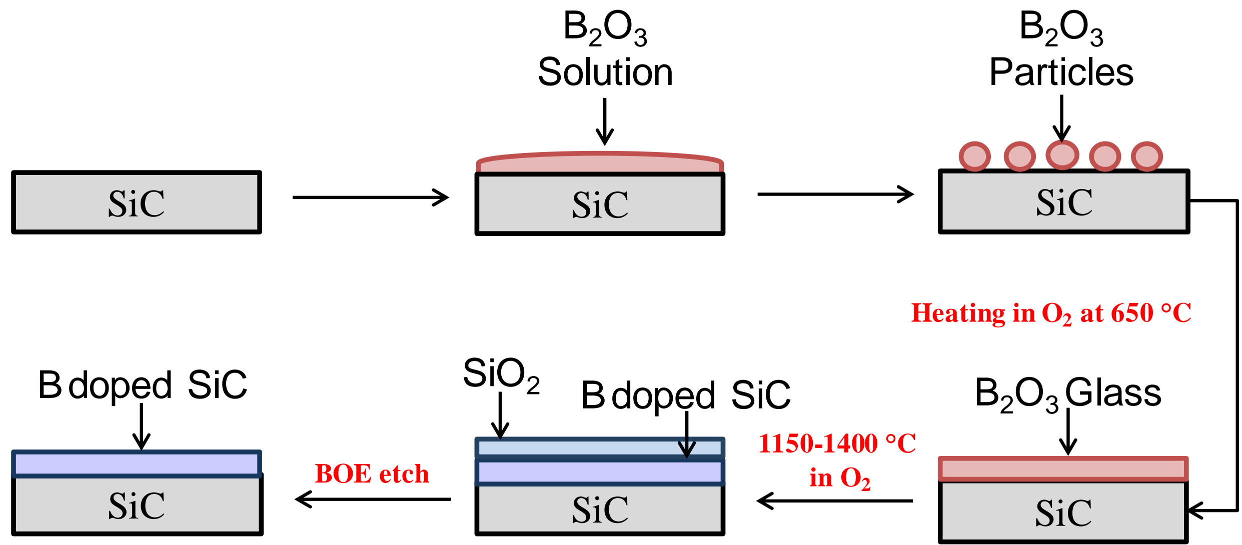

Fig. 6.7: Experimental process for boron diffusion (VAID)

6.1.5.1.2 Electroless Nickel Plating

n-type 4H-SiC samples with an n^- epilayer of about 2.5×10^{16} cm^{-3} carrier concentration on an n^+ substrate were used for the fabrication of ohmic contacts using electroless plated nickel. The high phosphorus version of the electroless nickel plating solution from Electrochemical Products Inc. was used for this work. A low phosphorus electroless plating solution from Transene Company, Inc., which is available from Alfa Aesar (Product # 44070), can also be used as it is specifically intended for semiconductor use.

After undergoing a standard organic clean (Section 6.1.1), the sample was immersed in BOE solution for about 1 min and rinsed in deionized water. The electroless nickel plating experimental process is shown in Figure 6.8. Electroless plating was carried out with the electroless nickel solution maintained at about 95°C while the pH level was maintained between

8 and 9 by adding ammonium hydroxide solution when necessary. Plating rate depends on surface morphology, as well as the doping concentration of the semiconductor. The deposition is faster on a highly-doped or rough (such as the lapped surface on the back of the samples) surface compared to a smoother or lightly-doped surface. After a thin, translucent layer was deposited (approximately 10–15 min), the samples were rinsed in deionized water and blow dried with N_2. The samples were then annealed at about 800°C for less than 5 min in argon. This step was found to be necessary to provide better adhesion of the plated NiP layer. Upon cooling to room temperature, the samples were etched with BOE for about 30 s. They were then placed into an electroless plating solution for less than 5 min depending on the desired thickness. The replated samples were then rinsed and blow dried.

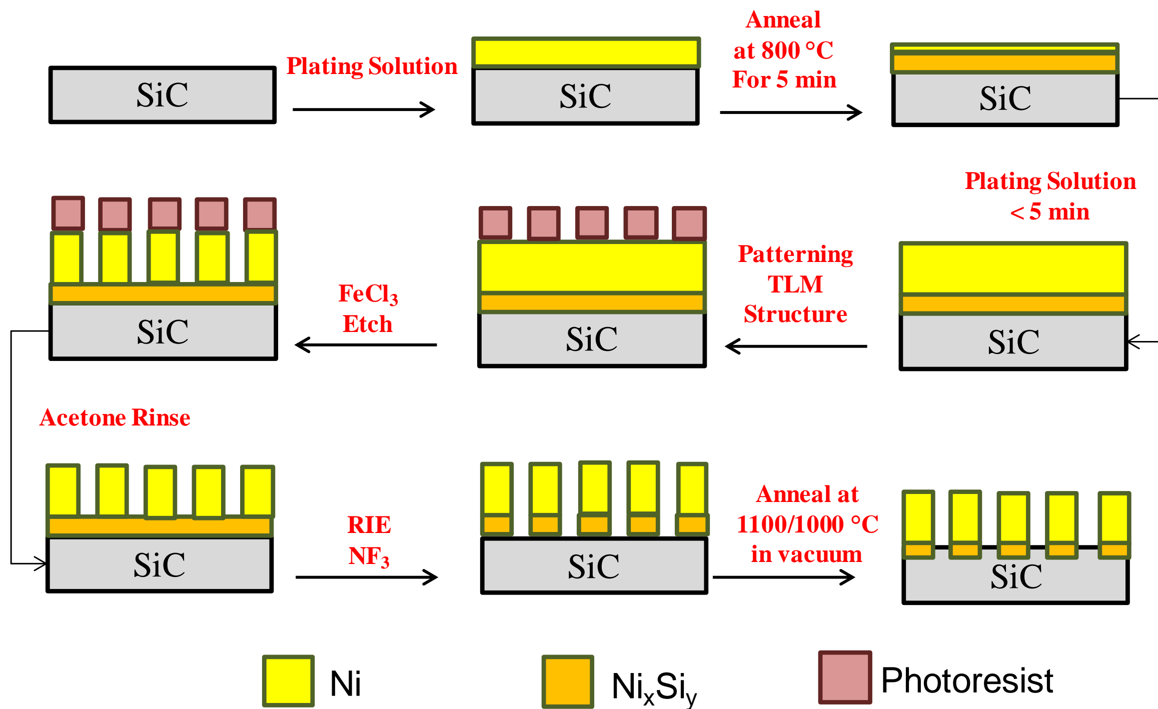

Fig. 6.8: Experimental process for the electroless nickel plating for ohmic contacts.

At this stage of the process, electron dispersive x-ray (EDX) spectoscopy and Rutherford backscattering spectroscopy (RBS) measurements (Chapter 7) were carried out on several samples to determine their composition, in addition to the depth profile of the nickel and phosphorus atoms in the deposited NiP layer. Some of the samples were patterned photolithographically for current-voltage (I-V) measurements and linear transmission line measurements (TLM). In order to improve adhesion of the NiP film to withstand lift-off and wet processing, the samples were annealed at 900°C in an argon ambient for about 5 min. Linear arrays of square pads were then defined by both chemical etching using $FeCl_3$ solution and RIE etching. After the etching, the samples were annealed at 1000°C/1100°C for 5 min at a pressure of approximately 2×10^{-7} Torr. I-V and TLM measurements were then carried out to determine the contact characteristics. The results are presented in Chapter 7.

6.1.5.2 Vacuum Annealing

A rapid thermal annealing system (RTA) was used for both ohmic contact anneals and dopant activation anneals. The system uses two thin carbon strips separated by 2" as the heating element. Rapid heat is attained by controlling the input voltage and the current through these strips. The sample was clamped down on the carbon strip for the ohmic contact anneal. It was put inside a SiC box, which was placed on the carbon strip for the dopant activation anneal. An s-type thermocouple was used to monitor the temperature when the sample was heated in the SiC box in an argon or nitrogen environment, while a pyrometer was used to measure the temperature when the sample was clamped directly onto the carbon strip. Using this system, a vacuum level of 2×10^{-7} Torr can be achieved while 1700°C is the maximum temperature limit.

6.1.5.2.1 Contact annealing

$Ni_{93\%}V_{7\%}$ was used as the preferred metal for ohmic contacts to the phosphorus-doped SiC in this work. The ohmic contacts were annealed at temperatures of 1000°C, 1100°C, and 1200°C for 5 min in a vacuum of 2 x 10^{-7} Torr, with the samples clamped directly onto the carbon strip. The pyrometer, which was directly above the chamber, was focused on the carbon strip adjacent to the sample.

6.1.5.2.2 Dopant Activation

After the dopants were introduced in to the SiC sample, it was turned over with its face down and placed inside a SiC box. The SiC box was moved onto the carbon heating strip and the temperature was monitored by an s-type thermocouple. After the system reaches a vacuum level of 2 x 10^{-7} Torr, a steady Ar flow is introduced in to the chamber. Activation temperatures of 1200°C and 1400°C were used for 30 min.

6.1.6 Reactive Ion Etching

There is no known wet chemical etch for single-crystal SiC at room temperature, so dry etching techniques are used when patterning SiC electronic devices. Yih et al. [9] reviewed the frequently used dry etching techniques in SiC device processing. The most commonly used process involves Reactive Ion Etching (RIE) of SiC in fluorinated plasmas. Figure 6.9 shows a basic schematic diagram of an RIE system. An etchant gas (NF_3 or SF_6) is injected between the

two electrodes, then an RF voltage is applied to the two electrodes and the voltage difference across the etchant gas produces the plasma [10].

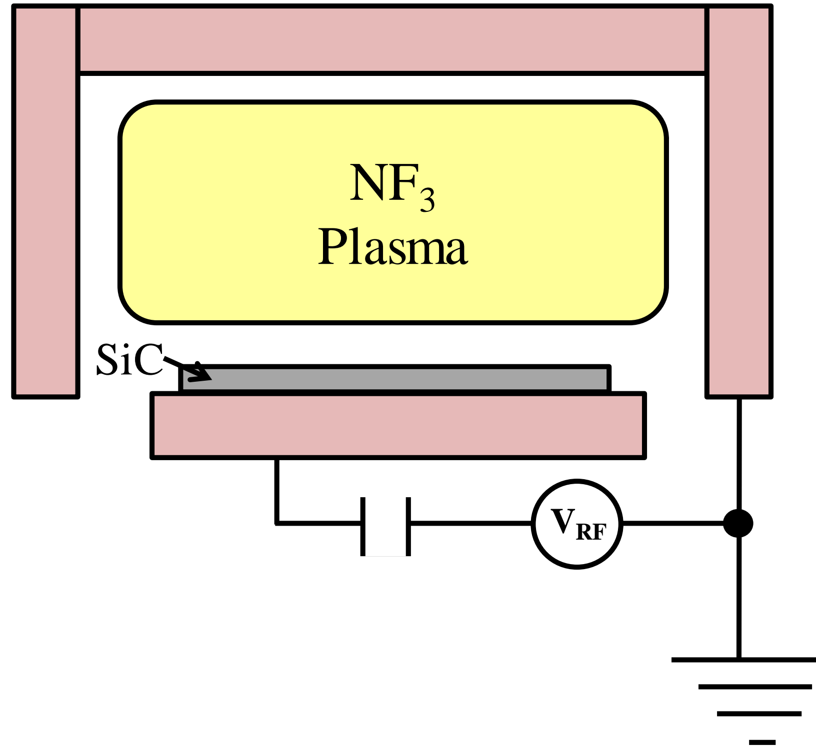

Fig. 6.9: Basic schematic diagram of an RIE system

The RIE system used in this work has a chamber which was initially pumped down to a vacuum of approximately 12 mTorr. NF_3 was used as the etchant gas and a nickel etch mask was photolithographically patterned for selective etching. For 4H-SiC, an etch rate of 90 nm/min was attained using the NF_3 plasma at an etch pressure of approximately 35 mTorr.

6.1.7 Ohmic Contact Fabrication for LTLM

Ohmic contacts were fabricated on phosphorus-doped 4H-SiC. Figure 6.10 shows the sequential process used for ohmic contact fabrication. Initially, patterns were made for the nickel etch masks and nickel was deposited using the plasma sputtering technique discussed in Section 6.1.3. The SiC was then etched using RIE. Following the RIE process, TLM structures were patterned by photolithography. Then $NiV_{7\%}$ layer was sputter deposited as ohmic contacts, which Figure 6.9 illustrates. Subsequently, the $NiV_{7\%}$ contacts were annealed using the RTA system and the annealing conditions explained in Section 6.1.5.1. Finally, the TLM structures were patterned for a second time and a gold layer was sputter deposited on top of the ohmic contact.

6.1.8 Schottky Contact Fabrication for CV Measurements

Schottky contacts were fabricated on phosphorus-doped 4H-SiC. Figure 6.11 shows the sequential process used for Schottky contact fabrication. Circular Schottky contacts were patterned using photolithography and $NiV_{7\%}$ was sputter deposited as Schottky contacts. A gold layer as a top contact was also deposited during the same process, as shown in Figure 6.11.

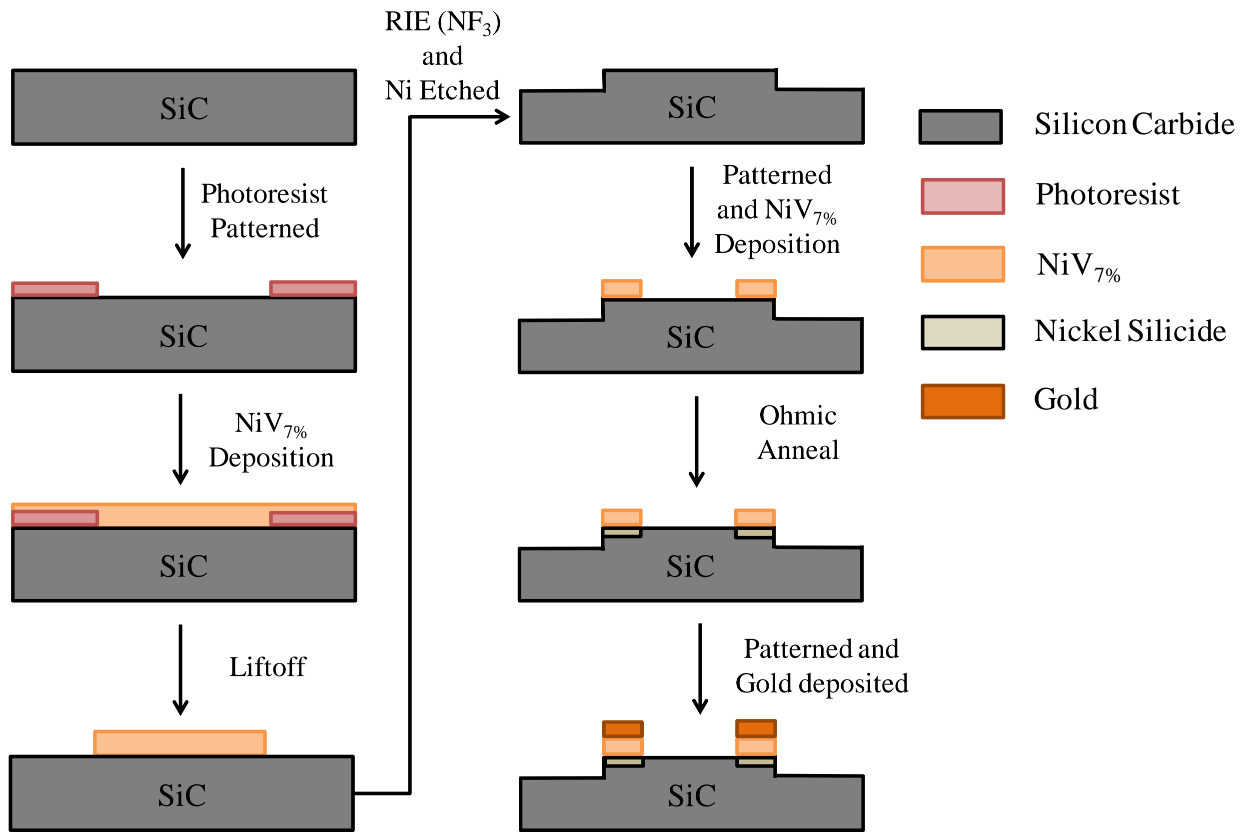

Fig. 6.10: Sequential process for ohmic contact fabrication

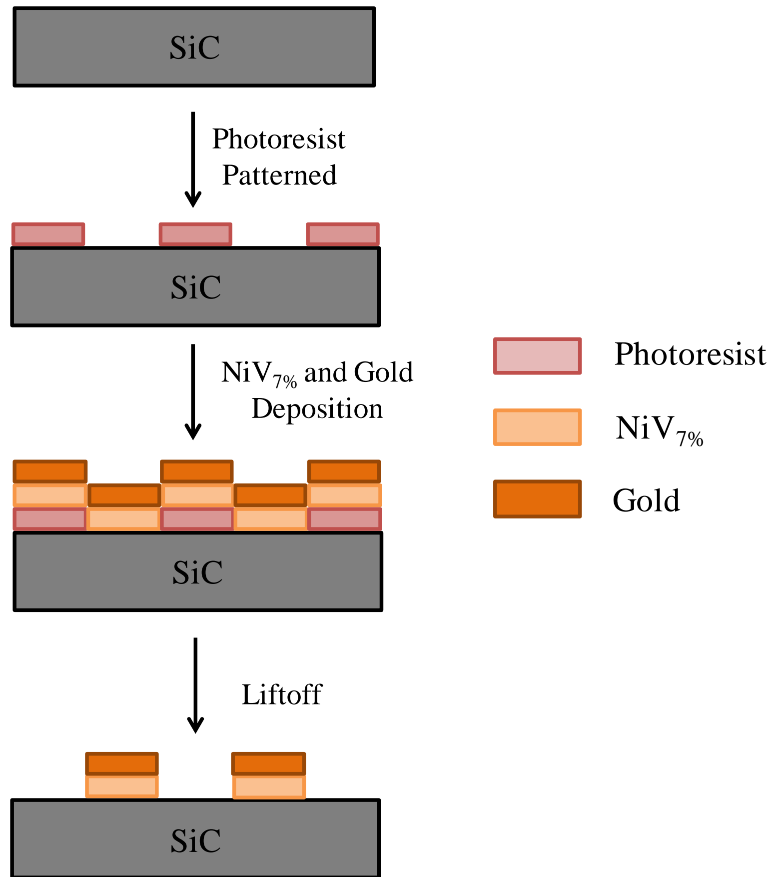

Fig. 6.11: Sequential process for Schottky contact fabrication

6.2 References

1. R. C. Jaeger, *Introduction to Microelectronic Fabrication,* 2nd Edition, G. W. Neudeck and R. F. Pierret (eds.) Prentice-Hall Inc. (2002).

2. W. Kern and D. A. Poutinen, *RCA Review,* **31**, 187-206 (1970).

3. W. Kern, *Semiconductor International*, pp. 94-99 (1984).

4. A. Elshabini and F. D. Barlow, *Thin Film Technology Handbook*, New York: Mcgraw-Hill, (1997).

5. S. M. Sze, *Semiconductor Devices*: *Physics and Technology*, New York: John Wiley & Sons, (1985).

6. L. Norin, S. McGinnis, U. Jansson and J. O. Carlsson, *J. Vac. Sci. Technol. A*, **15**, 3082 (1997).

7. J. D. Verhoeven, *Fundementals of Physical Metallurgy*, New York: John Wiley & Sons, (1989).

8. L. H. Van Vlack, *Elements of Materials Science and Engineering*, 6th edition, Addison-Wesley (1989).

9. P. H. Yih, V. Saxena and A. J. Steckl, *Physica Status Solidi (b)*, **202**, 605 (1997).

10. M. A. Lieberman and A. J. Lichtenberg, Principles of Plasma Discharges and Materials Processing, New York: John Wiley & Sons, (1994).

Chapter 7

Results and Discussion

This chapter discusses the applications of the VAID process and the silicidation assisted version of the VAID process, in fabrication of common device structures such as rectifying diodes and Ohmic contacts, as well as in the activation of implanted dopants.

7.1 VAID Process

7.1.1 Schottky Barrier Diodes on n^-/n^+ 4H-SiC

A solution of phosphorus oxide, discussed in Chapter 5, was spun-on to the surface of a 5 mm x 5 mm n^-/n^+ 4H-SiC sample using a spin-coater. The background carrier concentration of the epilayer was approximately 2.5 x 10^{16} cm^{-3}. The sample was then heated for 30 min at 650°C in oxygen, eliminating all traces of the solvent in the dopant solution, leaving a glassy layer containing phosphorus oxide according the procedure explained in Section 6.1.5.1.1. The sample was then annealed in oxygen at a temperature of 1300°C for 1 hr. After annealing, the sample was immersed in buffered oxide etch (BOE) to remove the silicon dioxide layer that formed on the surface. Schottky barrier diodes (SBD) were fabricated on the sample using sputtered nickel/vanadium ($Ni_{93\%}V_{7\%}$) gates. The SBD structures were patterned by photolithography followed by conventional lift-off. Standard capacitance-voltage (C-V) measurements were performed. Figure 7.1 shows the result of the C-V measurement in comparison to the control sample with a base concentration of 2.5 x 10^{16} cm^{-3} [1]. Current-voltage (I-V) measurements

were carried out on a Schottky contact pad and the highly doped bottom of the sample, and the results are shown in Figure 7.2.

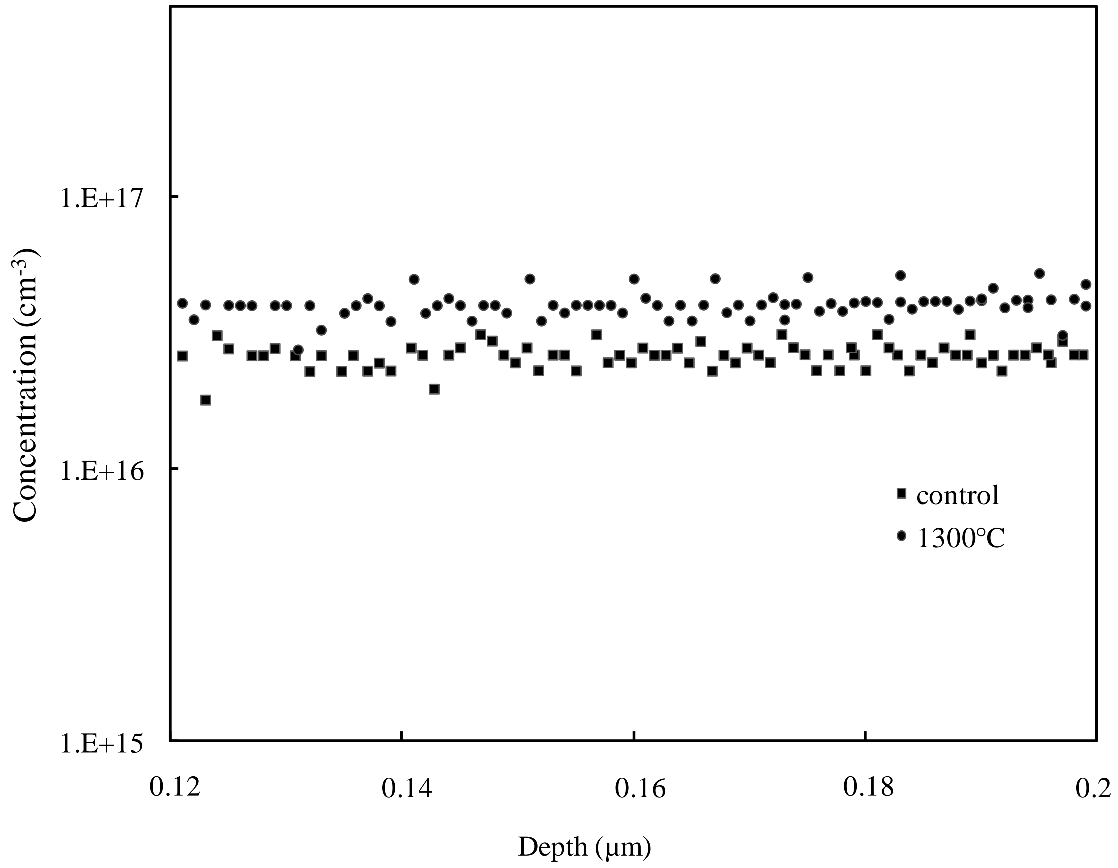

Fig. 7.1: Depth profile of concentration using C-V measurements for the Schottky barrier diode.

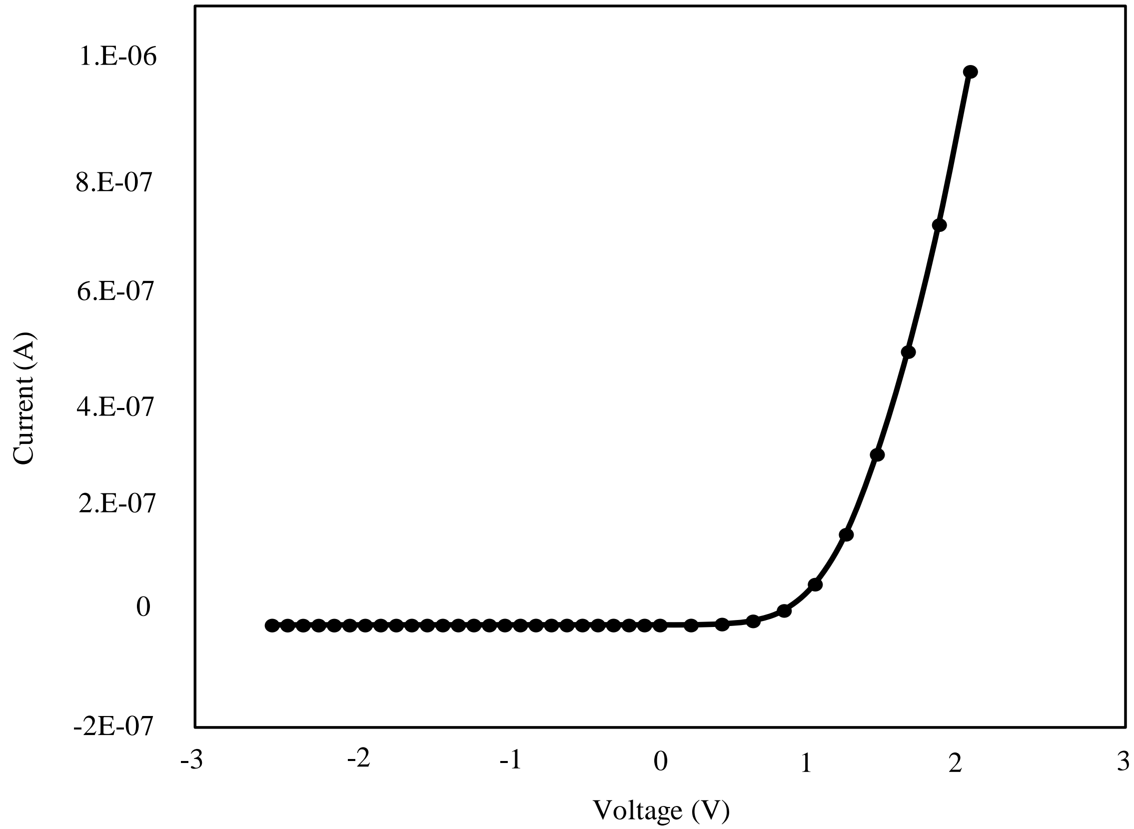

Fig. 7.2: I-V characteristic of a Schottky contact pad.

Electron dispersive x-ray (EDX) spectroscopy analyses were also performed on the sample and a spectrum is shown in Figure 7.2. Table 7.1 shows the average atomic percentages for carbon, silicon and phosphorus for the recorded EDX spectra.

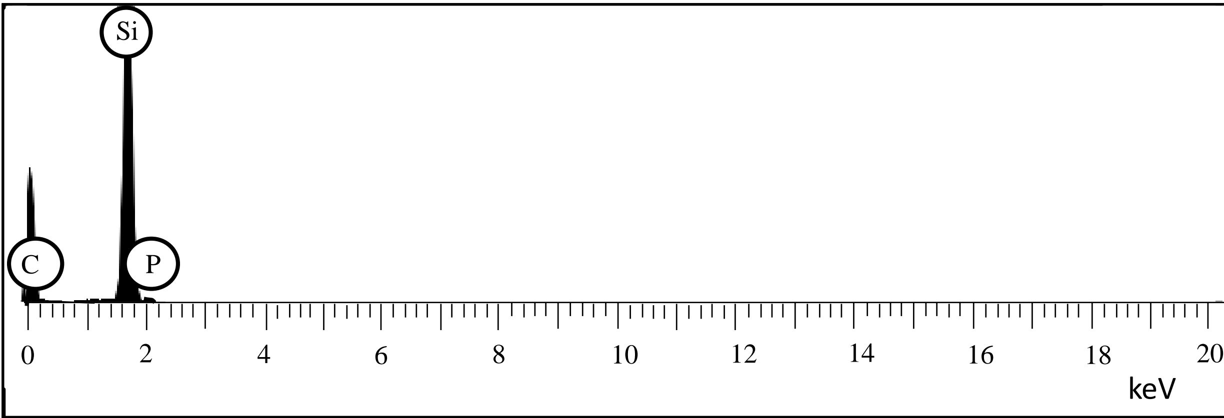

Fig. 7.3: EDX spectrum of the SBD sample

Table 7.1: Atomic percentages of elements in the SBD sample obtained using EDX.

Element	Spectrum 1 (Atomic %)	Spectrum 2 (Atomic %)	Spectrum 3 (Atomic %)	Average (Atomic %)
C	57.34	54.15	52.19	54.56 ± 2.60
Si	42.20	45.38	47.25	44.94 ± 2.55
P	0.46	0.47	0.56	0.50 ± 0.05

In Figure 7.1, the depth profile for the sample shows a doping concentration of approximately 4.5 x 10^{16} cm^{-3} and Figure 7.2 shows the Schottky characteristics of the contact. However, the EDX spectra for the same sample reveal an atomic percentage of approximately 0.5%, which relates to a phosphorus concentration of approximately 10^{19} cm^{-3}. This difference in doping concentrations can be explained by the fact that Figure 7.1 shows the tail end of the diffusion profile. A higher concentration is expected at the surface of the sample, which has been studied and is discussed in Section 7.1.2. Another reason for the discrepancy in concentrations is that phosphorus incorporation and activation are two separate mechanisms. To investigate this aspect, the nickel vanadium contacts were removed using a standard chemical etch and the

sample was annealed in an argon ambient at 1400°C for 30 min while face down inside a silicon carbide container. Following the annealing step, SBD structures were patterned on the sample and C-V measurements were taken. Figure 7.4 shows a higher dopant concentration, which is due to a higher activation percentage at 1400°C.

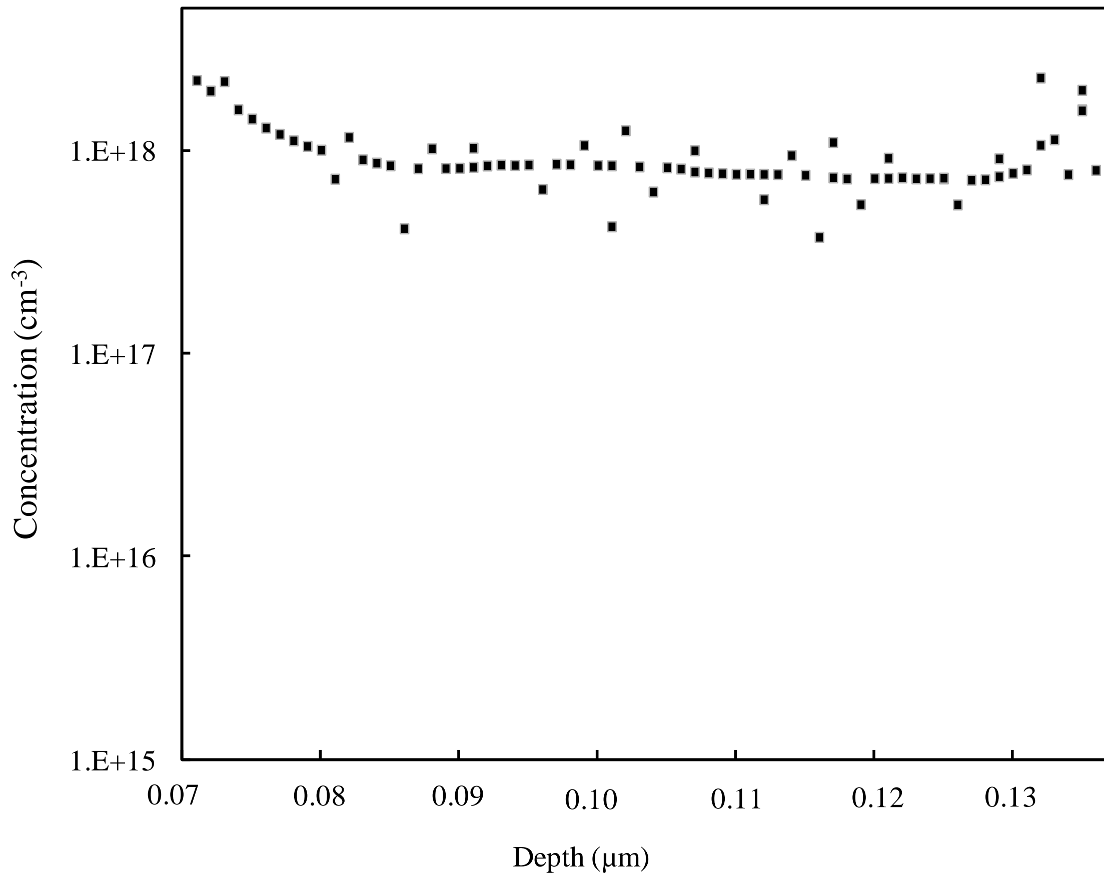

Fig. 7.4: Depth profile of dopant concentration using C-V measurements after dopant activation.

7.1.2 SIMS Profiles

Samples of 5 mm x 5 mm semi-insulating 4H-SiC substrate were used to investigate the phosphorus-doping profiles using secondary ion mass spectroscopy (SIMS). The phosphorus oxide solution was spun-on the surface using a spin-coater moving at 1500 rpm . The samples were then heated for 30 min at 650°C in oxygen to eliminate all traces of the solvent in the dopant solution, leaving a glassy layer containing phosphorus oxide according the procedure explained in Section 6.1.5.1.1. Next, the samples were annealed in oxygen at temperatures of 1200°C and 1400°C for 1 hr. Following the annealing step, the samples were immersed in BOE for 5 min to remove all traces of the silicon dioxide layer, that formed on the surface. SIMS analyses were performed on the samples and the results are shown in Figure 7.5.

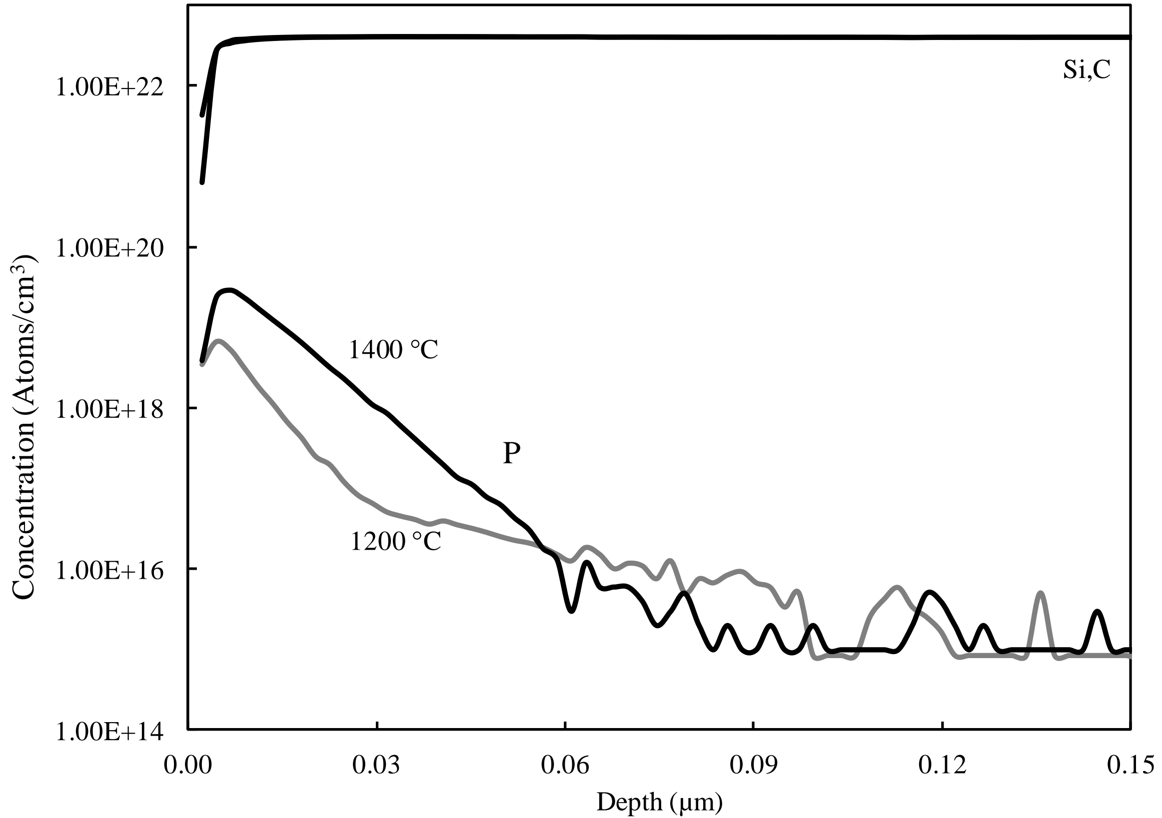

Fig. 7.5: SIMS analyses of the samples annealed at 1200°C and 1400°C.

The phosphorus concentration at the surface of the sample annealed at 1200°C is approximately 7 x 10^{18} cm^{-3}, but drops off steeply to 10^{16} cm^{-3} around a depth of 0.12 µm. In the sample annealed at 1400°C, the phosphorus concentration at the surface is approximately 3 x 10^{19} cm^{-3} which drops off steeply to 10^{16} cm^{-3} around 0.13 µm. Therefore, a high surface concentration of phosphorus can be achieved by using the VAID process on semi-insulating 4H-SiC. It is also consistent with the fact that the doping depth profiles obtained from C-V measurements in Section 7.1.1 show the tail end of the diffusion profile.

7.1.3 Activation of N Implants Using VAID

A nitrogen -implanted p^-/p^+ 4H-SiC sample was used to study the activation of implanted ions through the VAID process. The implanted impurity concentration was 4 x 10^{19} cm^{-3}. The phosphorus oxide solution was spun-on the surface at a speed of 1500 rpm using a spin-coater. Then, the sample was heated for 30 min at 650°C in oxygen to eliminate all traces of the solvent in the dopant solution, leaving a glassy layer containing phosphorus oxide according to the procedure explained in Section 6.1.5.1.1. The sample was then annealed in oxygen at a temperature of 1400°C for 1 hr. This was intended to replace the standard activation step in an argon ambient. Following the annealing step, the sample was immersed in BOE for 5 min to remove all traces of the silicon dioxide layer that had formed on the surface. Then the sample was photolithographically patterned for linear transmission line method (LTLM) measurements using the experimental procedure discussed in Section 6.1.7. $Ni_{93\%}V_{7\%}$ was used as the preferred metal for the n-type ohmic contact. The patterning step was followed by a contact anneal at 1000°C in a vacuum for 5 min according to the procedure discussed in Section 6.1.5.2.1. TLM measurements and I-V measurements were then carried out to determine the contact characteristics. Figure 7.6 shows the data from the TLM measurements. The contact resistance (R_c), sheet resistance (R_{sh}) and specific contact resistivity (ρ_c) were calculated using the TLM measurements. Table 7.2 lists R_c, R_{sh} and ρ_c.

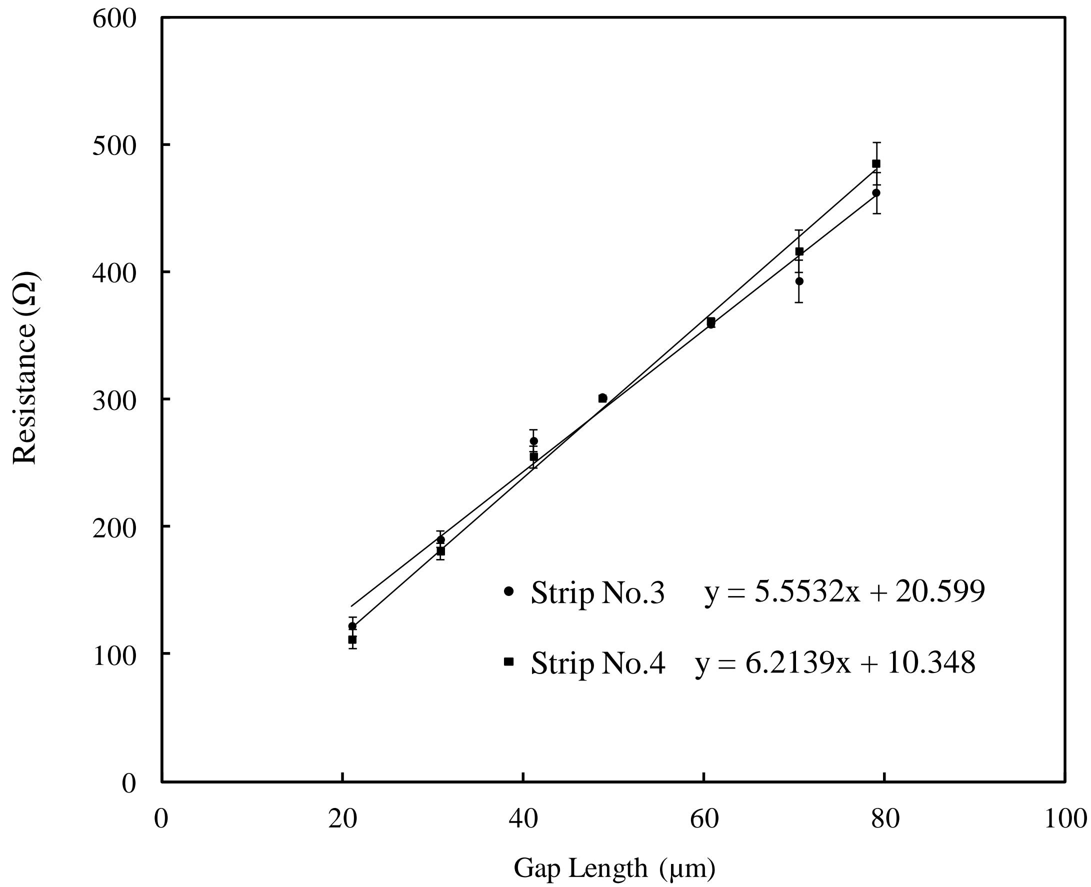

Fig. 7.6: TLM data for ohmic anneal at 1000°C.

Table 7.2: R_c, R_{sh} and ρ_c values for ohmic anneal at 1000°C.

Strip number	R_c (Ω)	R_{sh} (Ω/□)	ρ_c (Ωcm^2)
3	10.29	1072	3.7 x 10^{-5}
4	5.17	1193	8.5 x 10^{-6}
Average	7.73	1132	2.3 x 10^{-5}
Std. deviation	± 3.62	± 86	± 2.0 x 10^{-5}

As seen in Table 7.2, an average specific contact resistivity value of 2.3 x 10^{-5} Ωcm^2 was obtained using the VAID process on the nitrogen-implanted sample with an ohmic contact anneal of 1000°C. Li [2] reports specific contact resistivity in the range of 10^{-5} Ωcm^2 for n-type samples with an implant concentration of 4 x 10^{19} cm^{-3}, which have been activated at much higher temperatures (>1500°C). The average contact resistance was 7.73 Ω and the average sheet resistance was 1132 Ω/□. Following the TLM measurements, the ohmic contacts were annealed at 1100°C in vacuum for 5 min and TLM measurements were conducted. Figure 7.7 shows the TLM data and Table 7.3 shows the obtained values for R_c, $R_{sh,}$ and ρ_c. Figure 7.8 shows the I-V characteristic curve of the contacts between two adjacent pads.

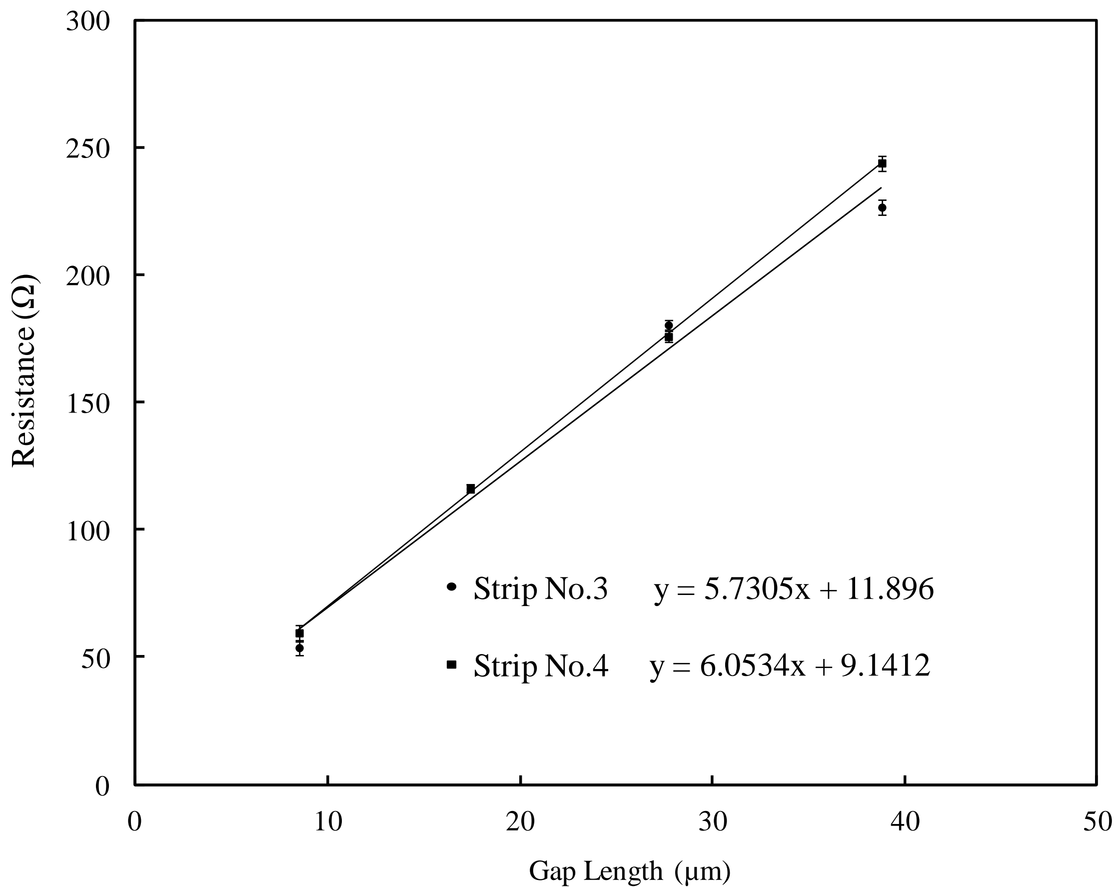

Fig. 7.7: TLM data for ohmic anneal at 1100°C.

Table 7.3: R_c, R_{sh} and ρ_c values for ohmic anneal at 1100°C.

Strip number	R_c (Ω)	R_{sh} (Ω/□)	ρ_c (Ωcm^2)
3	5.93	1111	1.1 x 10^{-5}
4	4.57	1164	6.8 x 10^{-6}
Average	5.25	1137	8.9 x 10^{-6}
Std. deviation	± 0.96	± 37	± 2.9 x 10^{-6}

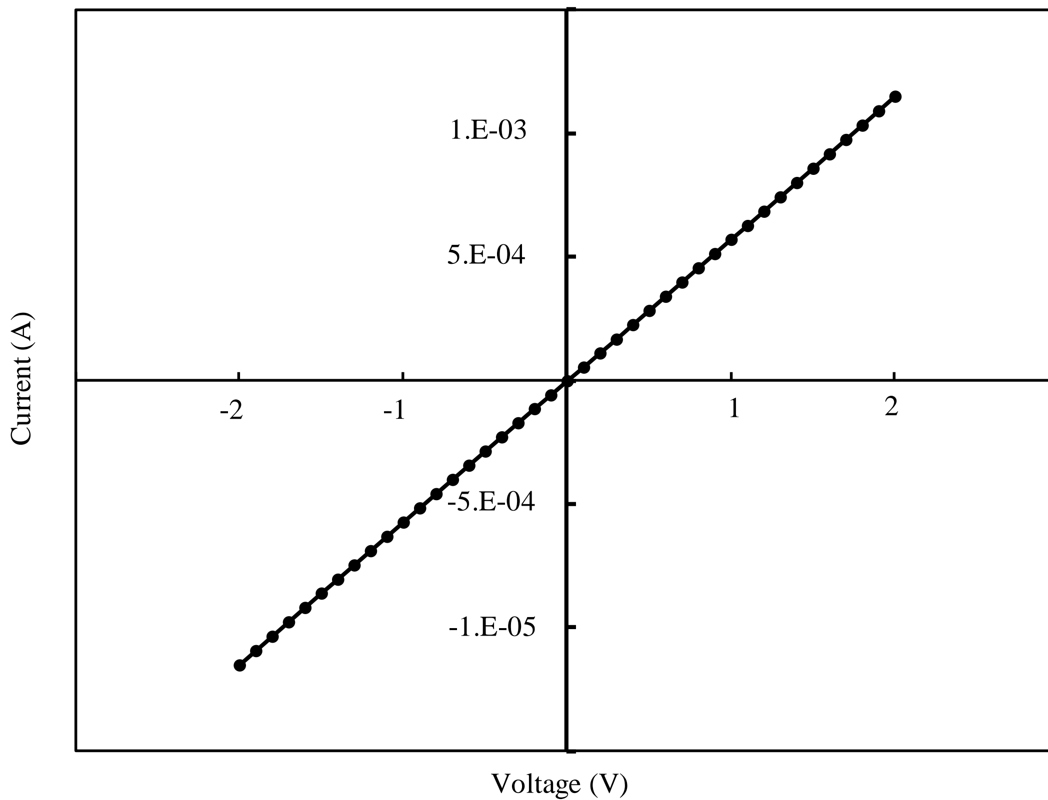

Fig. 7.8: I-V characteristic curve for the ohmic contacts annealed at 1100°C.

As seen from Table 7.3, an average specific contact resistivity of 6.8 x 10^{-6} Ωcm^2 has been calculated for the ohmic contacts annealed at 1100°C. This value is comparable to previously reported data for nitrogen- implanted samples with activation at high temperatures in excess of 1500°C. The average contact resistance was 5.25 Ω and the average sheet resistance was 1137 Ω/□. The I-V characteristic curve in Figure 7.10 confirms the ohmic nature of the contacts. Then the samples were annealed again at 1200°C in a vacuum for 5 min. TLM measurements were conducted on the samples. Figure 7.9 shows the TLM measurements and Table 7.4 shows the calculated values for R_c. R_{sh} and ρ_c.

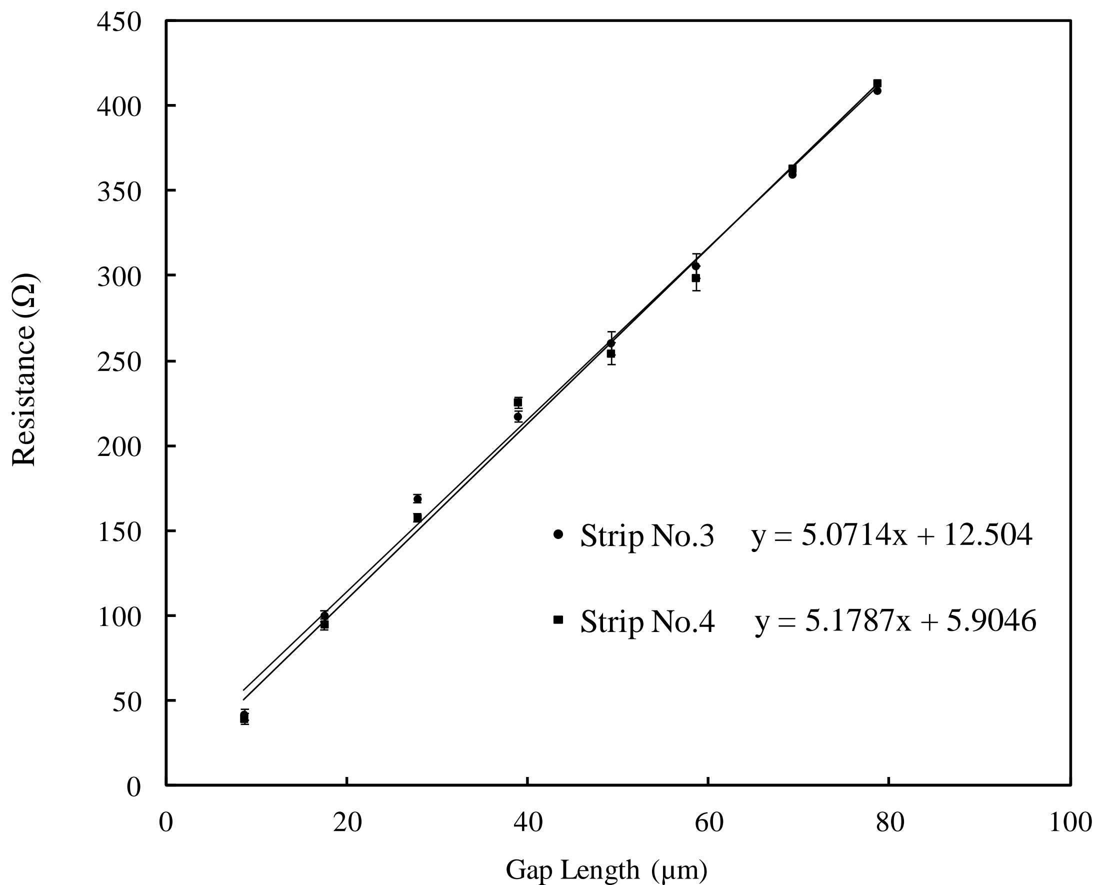

Fig. 7.9: TLM data for ohmic anneal at 1200°C.

Table 7.4: R_c, R_{sh} and ρ_c values for ohmic anneal at 1200°C.

Strip number	R_c (Ω)	R_{sh} (Ω/□)	ρ_c (Ωcm^2)
3	6.25	989	1.5×10^{-5}
4	2.95	1010	3.3×10^{-6}
Average	4.6	999	9.1×10^{-6}
Std. Deviation	± 2.33	± 15	$\pm 8.3 \times 10^{-6}$

As evident from Table 7.4, the average specific contact resistivity was 9.1×10^{-6} Ωcm^2, which showed no considerable change between the ohmic contact anneal at 1100°C and 1200°C. Therefore, the optimum temperature for the ohmic contact anneal was deduced to be 1100°C, which was the temperature used for the ohmic contact anneal in the following section. The average contact resistance was 4.6 Ω and the average sheet resistance was 999 Ω/□.

7.1.4 Ohmic Contact Characterization

Ohmic contacts to n-type 4H-SiC samples were characterized using TLM measurements. Two 5 mm x 5 mm p^-/p^+ 4H-SiC samples were used for the VAID process. The phosphorus oxide solution was spun-on the surface at a speed of 1500 rpm using a spin-coater. Then, the samples were heated for 30 min at 650°C in oxygen to eliminate all traces of the solvent in the dopant solution, leaving a glassy layer containing phosphorus oxide according the procedure explained in Section 6.1.5.1.1. The two samples were then annealed in oxygen at temperatures of 1300°C and 1400°C for 1 hr. Afterwards, they were immersed in BOE to remove any trace of silicon dioxide formed on the surface. At this stage, EDX analyses were performed on the

samples. Figure 7.10 shows the EDX spectra while Table 7.5 lists atomic percentages of the elements obtained using EDX.

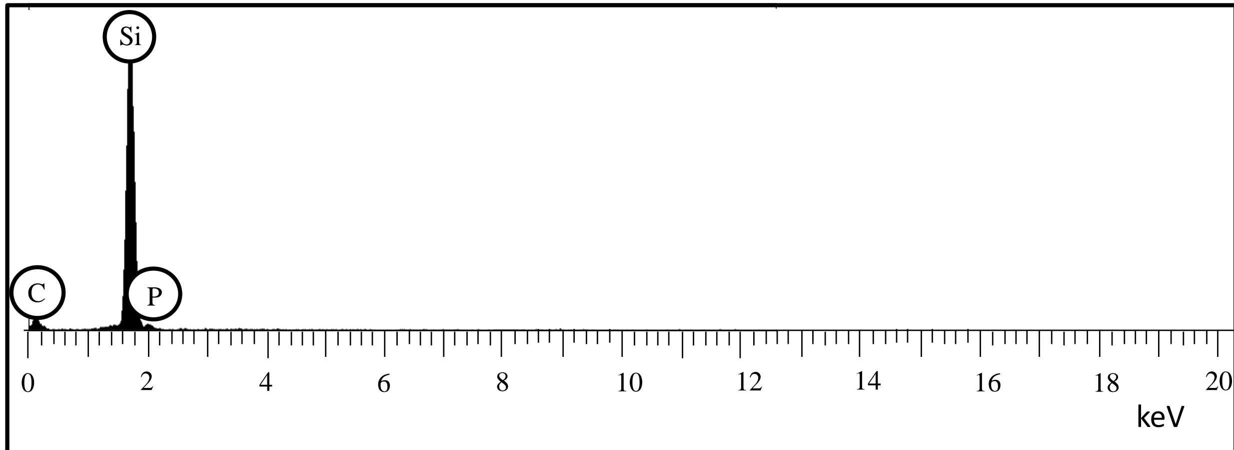

(a)

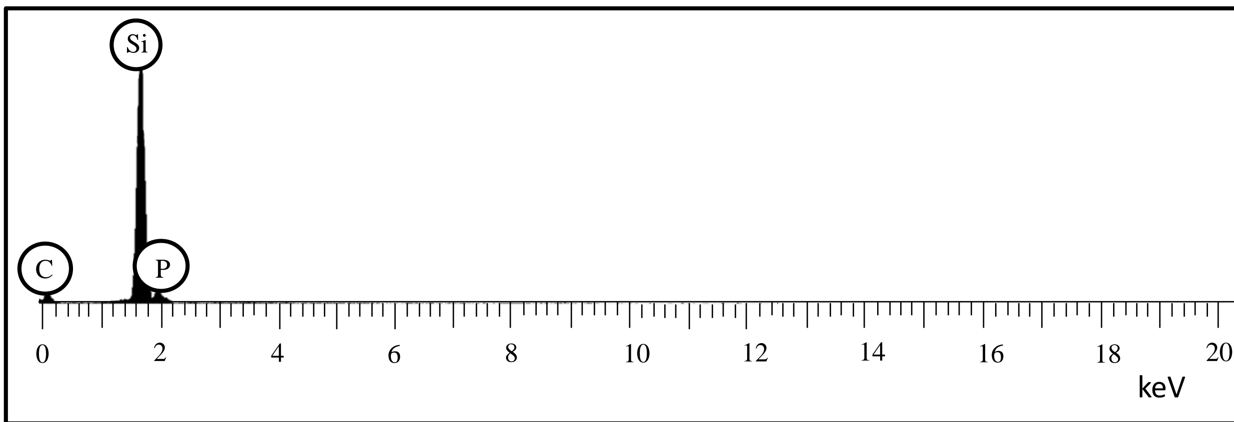

(b)

Fig.7.10: EDX spectrum for (a) sample annealed at 1300°C (b) sample annealed at 1400°C.

Table 7.5: Atomic percentages of elements obtained using EDX.

Element	Sample annealed at $1300^{o}C$ (Atomic %)				Sample annealed at $1400^{o}C$ (Atomic %)			
	Sp 1	Sp 2	Sp 3	Average	Sp 1	Sp 2	Sp 3	Average
C	54.74	56.80	56.04	55.86 ± 1.04	53.71	54.74	54.52	54.32 ± 0.54
Si	44.77	42.78	43.52	43.69 ± 1.01	45.75	44.76	45.00	45.17 ± 0.52
P	0.49	0.42	0.44	0.45 ± 0.04	0.54	0.50	0.48	0.51 ± 0.03

The results for the atomic percentage of phosphorus show approximately 0.5%, which is comparable to the EDX atomic percentages obtained in Section 7.1.1. After the EDX analyses, the samples were photolithographically patterned with $Ni_{93\%}V_{7\%}$ contacts for TLM measurements according to the process discussed in Section 6.1.7. After patterning, ohmic contact anneals were conducted at $1100^{o}C$ in vacuum for 5 min. TLM measurements and I-V measurements were taken to characterize the ohmic contacts. Figure 7.11 shows the TLM data for the two samples and Table 7.6 shows the calculated values for R_c. R_{sh} and ρ_c.

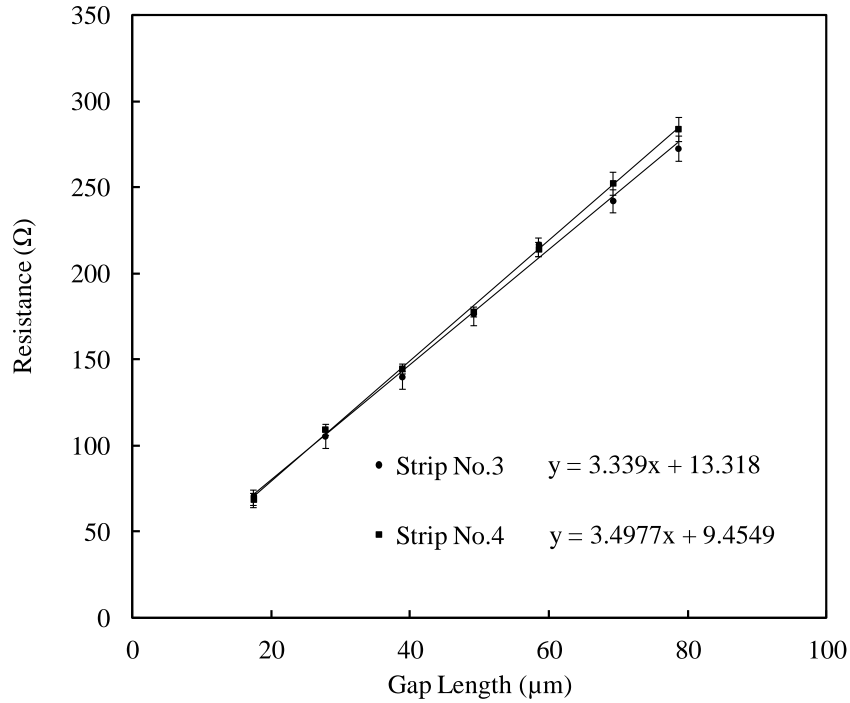

(a)

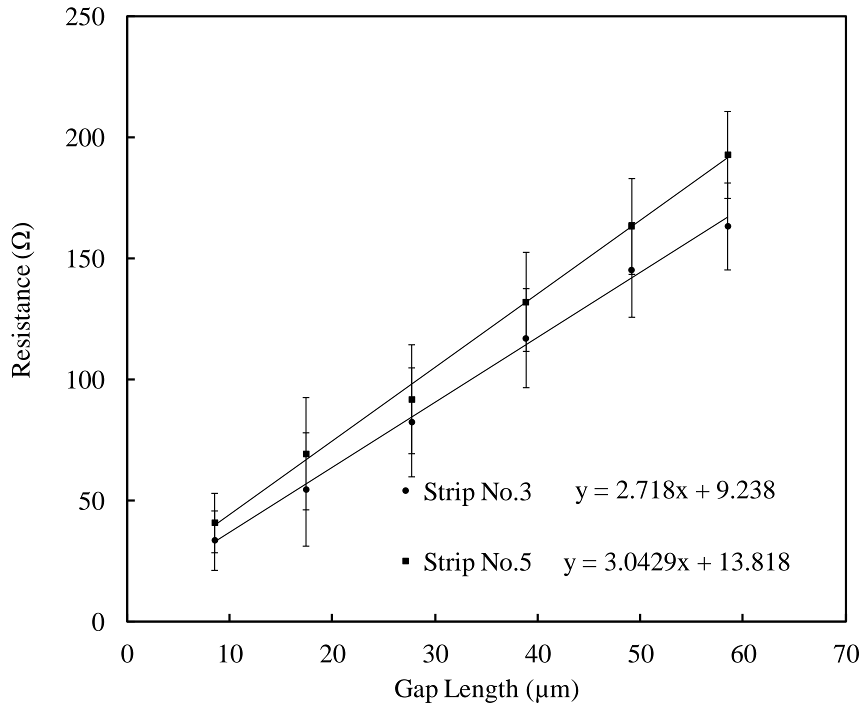

(b)

Fig. 7.11: TLM data for n-type doped sample (a) annealed at 1300°C in oxygen (b) annealed at 1400°C in oxygen.

Table 7.6: R_c, R_{sh} and ρ_c values for the sample (a) annealed at 1300°C in oxygen (b) annealed at 1400°C in oxygen.

Strip number	R_c (Ω)	R_{sh} (Ω/□)	ρ_c (Ωcm^2)
3	6.66	650	2.6×10^{-5}
4	4.72	674	1.2×10^{-5}
5	4.22	644	1.1×10^{-5}
Average	6.08	656	1.6×10^{-5}
Std. deviation	± 1.28	± 16	$\pm 8.4 \times 10^{-6}$

(a)

Strip number	R_c (Ω)	R_{sh} (Ω/□)	ρ_c (Ωcm^2)
3	4.62	530	1.5×10^{-5}
5	6.91	593	3.0×10^{-5}
6	7.17	600	3.2×10^{-5}
Average	6.23	575	2.6×10^{-5}
Std. deviation	± 1.40	± 39	$\pm 9.3 \times 10^{-6}$

(b)

As seen in Table 7.6(a), the VAID process sample annealed at 1300°C showed an average specific contact resistivity of 2.1×10^{-5} Ωcm^2. The average contact resistance for the sample was 6.08 Ω and the average sheet resistance was 656 Ω/□. In Table 7.6(b), the VAID process sample annealed at 1400°C showed an average specific contact resistivity of 2.6×10^{-5} Ωcm^2. The average contact resistance for the sample was 6.23 Ω and the average sheet resistance was 575 Ω/□. The difference between the two samples was that the sheet resistance was approximately 80

$\Omega/\square$ lower for the sample annealed at 1400°C. The values for specific contact resistivity were comparable $Ni_{93\%}V_{7\%}$ ohmic contacts to a nitrogen-implanted sample with an implant concentration of 1 x 10^{20} Ωcm^2 [2].

I-V measurements were conducted on the samples to confirm the ohmic nature of the contacts. Probes were connected to adjacent contact pads on the top surface of the sample. As seen in Figures 7.12(a) and (b), both samples showed ohmic characteristics. I-V measurements were also taken on the samples from top to bottom to confirm the presence of a p-n junction. Figures 7.13(a) and (b) shows the I-V characteristics of the p-n junctions on the VAID process samples.

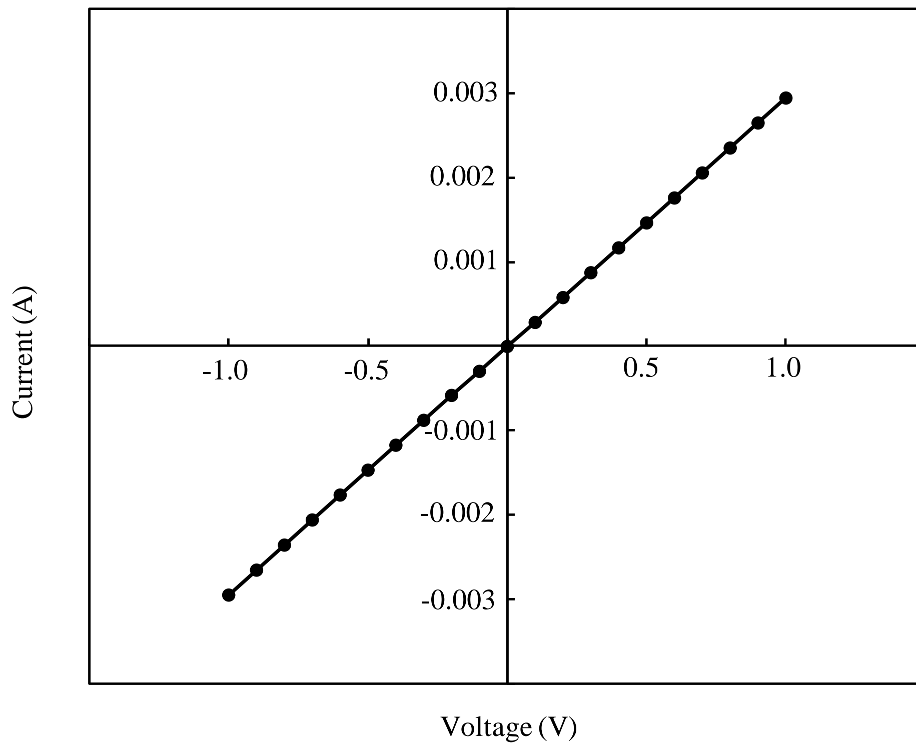

(a)

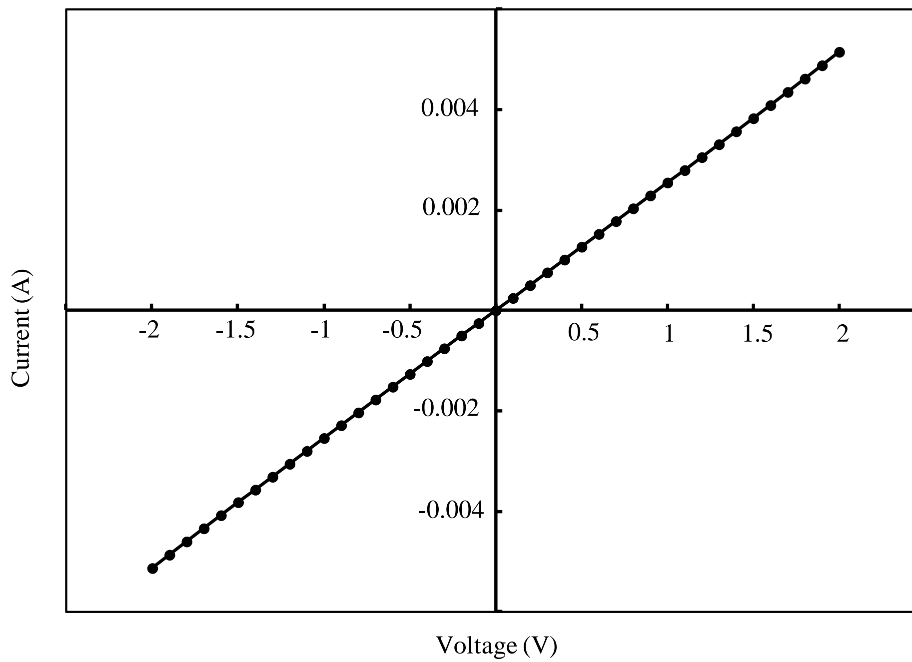

(b)

Fig. 7.12: I-V characteristics of the top surface for the sample (a) annealed at 1300°C (b) annealed at 1400°C.

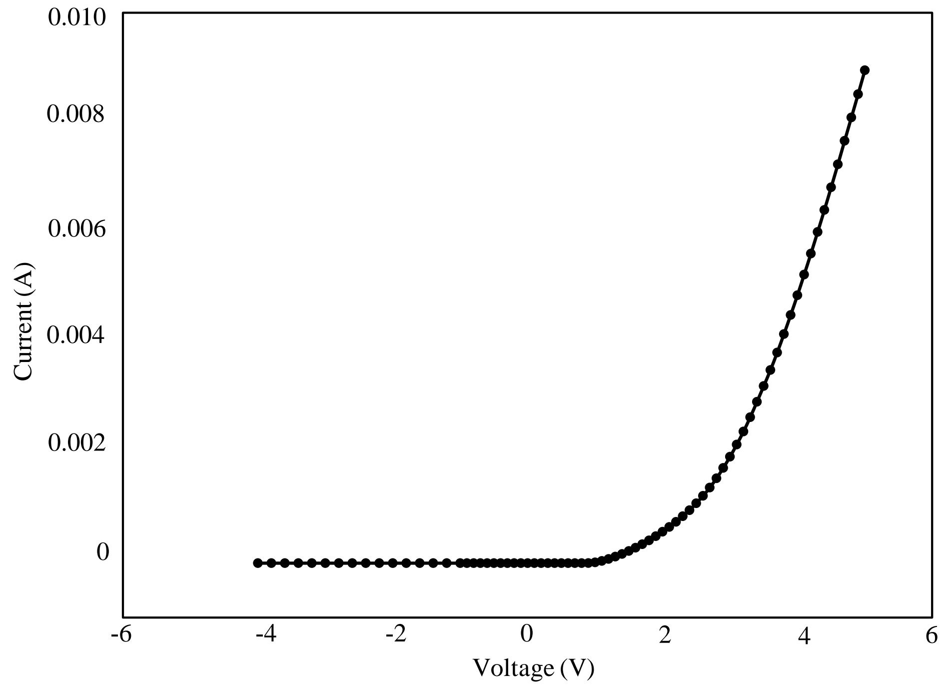

(a)

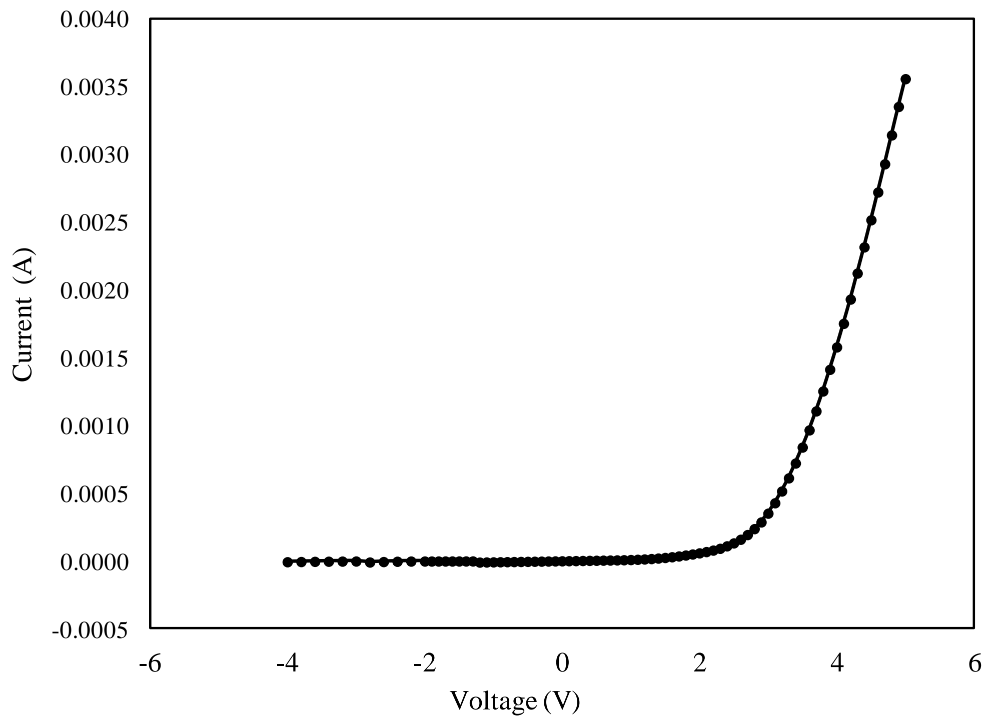

(b)

Fig. 7.13: p-n junction I-V characteristics for the sample (a) annealed at 1300°C (b) annealed at 1400°C.

7.2 Silicidation Assisted Impurity Doping

7.2.1 Schottky Barrier Diodes on n^-/n^+ 4H-SiC

The reaction between nickel and silicon carbide forms nickel silicide (Ni_2Si) starting at about 600°C. Up to 1050°C, Ni_2Si is the only silicide observed in the reaction zone [3]. The thermodynamic basis for this process is discussed in detail in Section 5.2.2. Since nickel readily draws out silicon from the silicon carbide surface, leaving behind silicon vacancies in the lattice, the introduction of a thin nickel layer on top of the phosphorus oxide film was studied by using 2 5 mm x 5 mm n^-/n^+ 4H-SiC samples. The background carrier concentration of the epilayer was approximately 2.5 x 10^{16} cm^{-3}. The experimental process began identically to the sample in Section 7.1.1. However, after the glassification of the phosphorus oxide layer at 650°C in oxygen for 30 min, a nickel film of 25~100 nm was deposited by thermal evaporation on top of the phosphorus oxide film. The samples containing nickel films were then annealed in argon for 1 hr at 650°C and 800°C. Subsequently, the samples were immersed in BOE to remove the oxide, silicide, and nickel layers. Another film of phosphorus oxide solution was formed on both samples and they were annealed at 1300°C in oxygen for 60 min. This step was intended to replenish the phosphorus on the surface of the SiC samples. Finally, the samples were immersed in BOE to remove the residual oxide layer. Simple Schottky devices were fabricated on the 2 samples [1]. C-V measurements were conducted and are shown in Figure 7.14. Current-voltage (I-V) measurements were performed on a Schottky contact pad and the highly doped bottom of the sample which was annealed at 800°C and the result is shown in Figure 7.15.

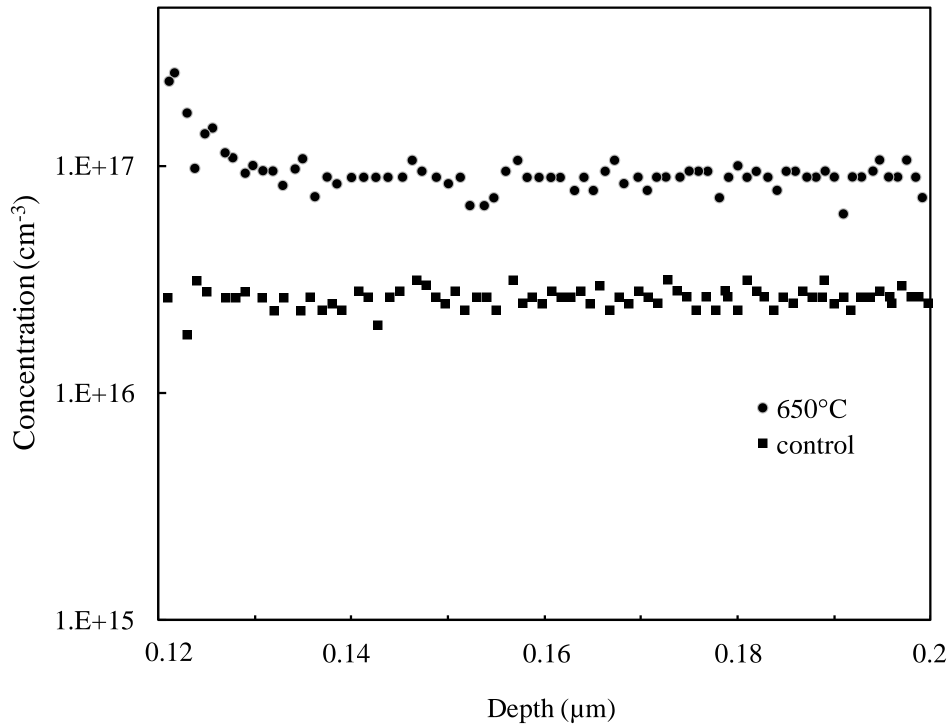

(a)

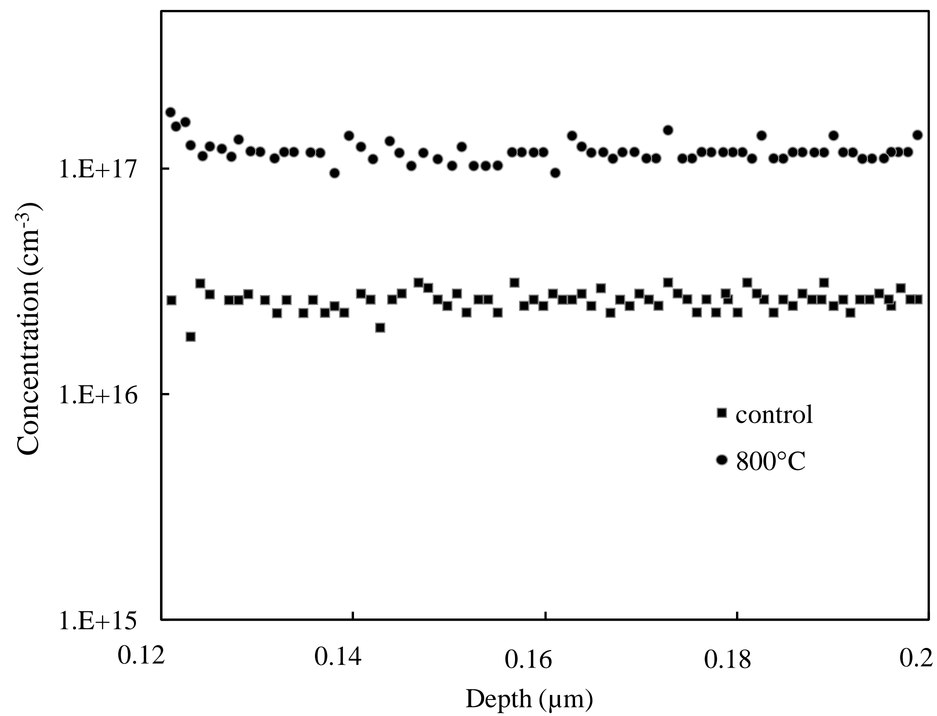

(b)

Fig. 7.14: Depth profile of concentration using C-V measurements for the Schottky barrier diode on the sample (a) annealed at 650°C (b) annealed at 800°C.

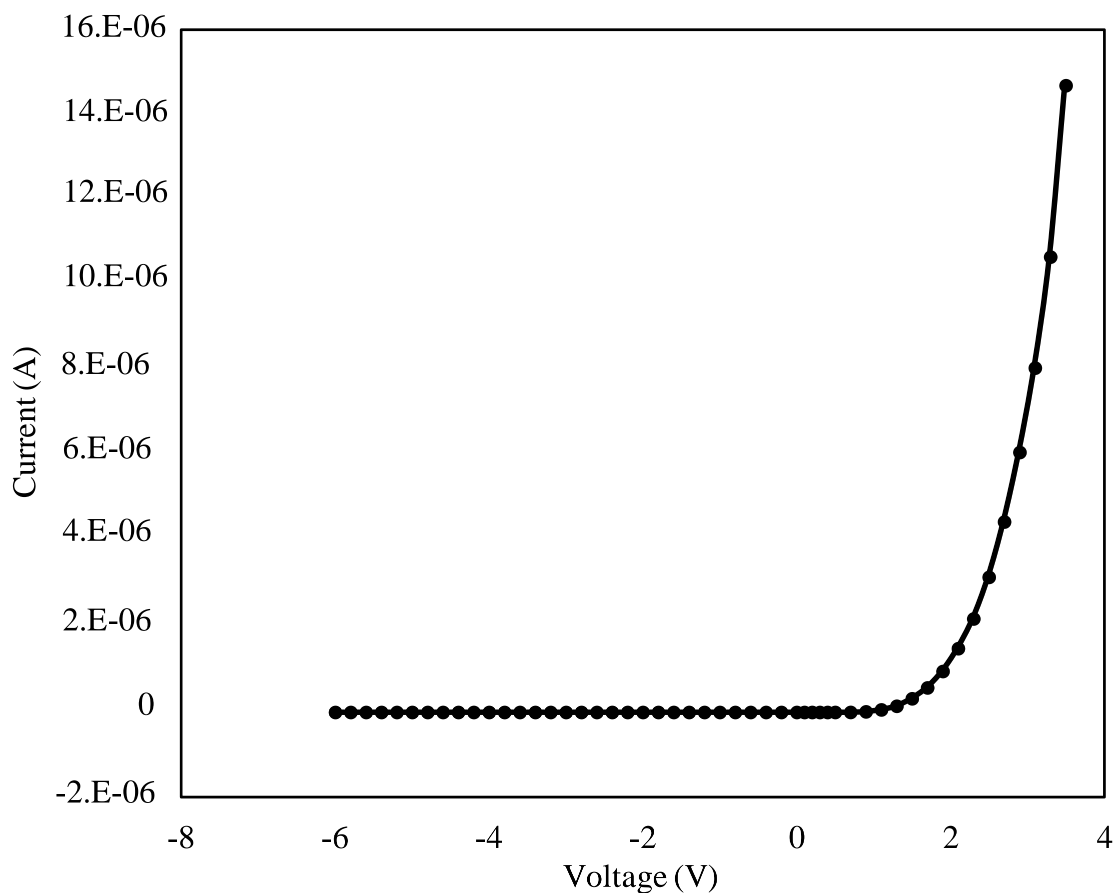

Fig. 7.15: I-V characteristic of a Schottky contact pad on the sample annealed at 800°C.

Electron dispersive x-ray (EDX) spectroscopy analyses were also performed on the samples and the spectra are shown in Figure 7.16. Tables 7.7(a) and (b) shows the atomic percentages for carbon, silicon and phosphorus for the recorded EDX spectra.

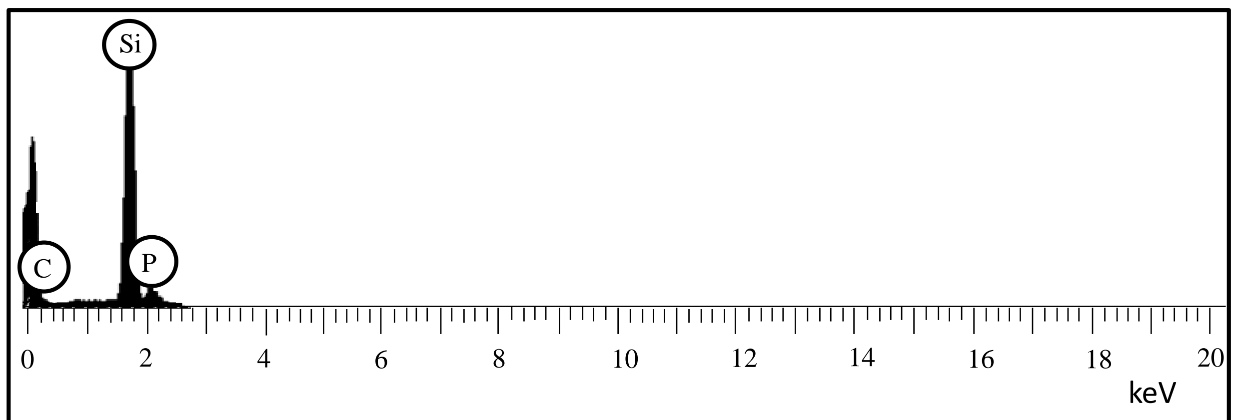

(a)

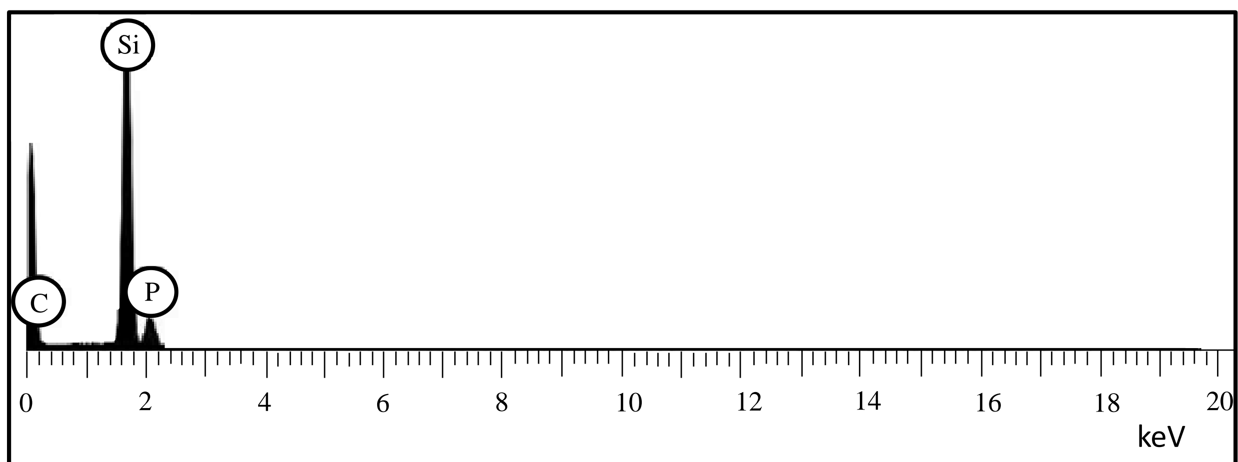

(b)

Fig. 7.16: EDX spectrum of the SBD sample (a) annealed at 650°C (b) annealed at 800°C.

Table 7.7: Atomic percentages of elements in the SBD sample obtained using EDX for the sample (a) with nickel annealed at 650°C (b) with nickel annealed at 800°C.

Element	Spectrum 1 (atomic %)	Spectrum 2 (atomic %)	Spectrum 3 (atomic %)	Average (atomic %)
C	57.79	54.15	52.18	54.71 ± 2.85
Si	40.60	45.38	47.25	44.41 ± 3.43
P	1.61	0.47	0.57	0.88 ± 0.63

(a)

Element	Spectrum 1 (atomic %)	Spectrum 2 (atomic %)	Spectrum 3 (atomic %)	Average (atomic %)
C	56.97	53.83	50.65	53.82 ± 3.16
Si	41.54	44.86	47.85	44.75 ± 3.15
P	1.49	1.31	1.50	1.43 ± 0.11

(b)

The depth profiles in Figure 7.16 for the samples show doping concentrations of approximately 6.9 x 10^{16} cm^{-3} and 1 x 10^{17} cm^{-3} respectively for the samples annealed at 650°C and 800°C. Figure 7.17 shows the Schottky characteristics of the contact. However, the EDX data for the samples revealed atomic percentages of approximately 0.5% and 1.4%, which related to phosphorus concentrations of approximately 10^{19}~10^{20} cm^{-3}. This difference in doping concentrations can be explained by the fact that Figures 7.14(a) and (b) show the tail end of the diffusion profiles. A higher concentration was expected at the surface of the sample which was investigated and reported in Section 7.2.2. In addition, phosphorus incorporation and activation

are two separate mechanisms. To investigate this aspect, the nickel vanadium contacts were removed using a standard chemical etch and the sample was further annealed in an argon ambient at 1400°C for 30 min while face down inside a silicon carbide container. Following the activation annealing step, SBD structures were patterned on the sample and C-V measurements were conducted. Figure 7.17 shows a higher dopant concentration, which was due to a higher activation percentage at 1400°C.

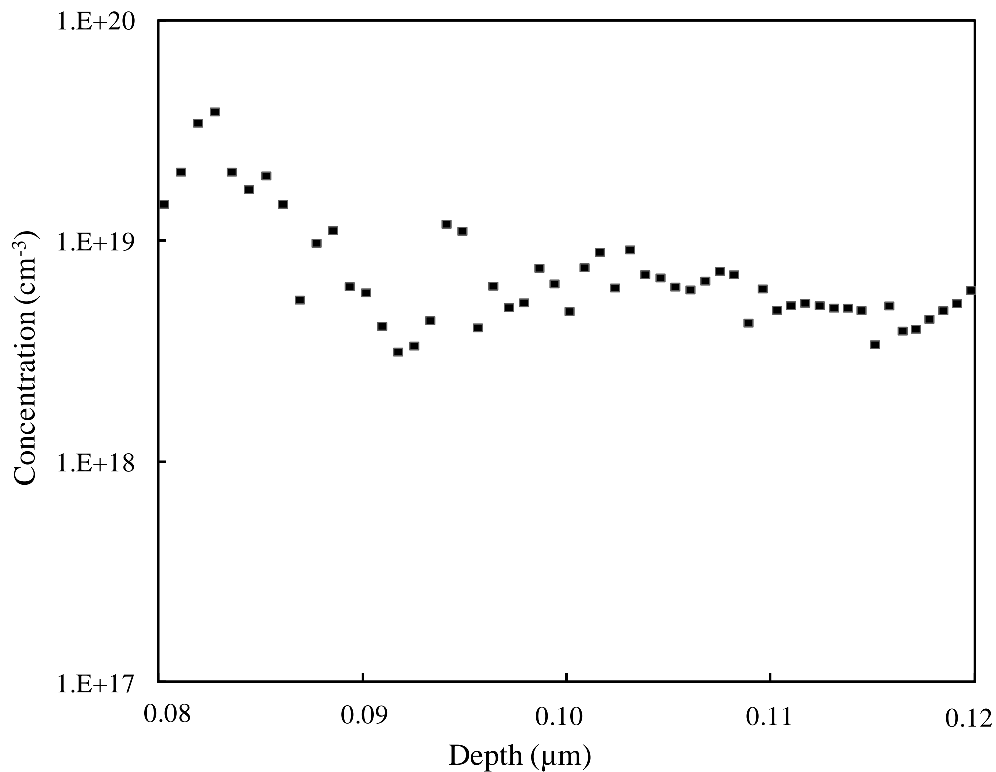

Fig. 7.17: Depth profile of dopant concentration using C-V measurements after sample activation for the sample with nickel annealed at 800°C.

Nomarski microscope images of the surface of the VAID process sample and the silicidation assisted impurity doped sample are shown in figureFigure 7.18. There appeared to be a slight surface degradation of the sample containing nickel, annealed at 800°C compared with

the VAID process sample discussed in 7.1.1, which might have led to a slightly uneven, higher atomic percentage of phosphorus.

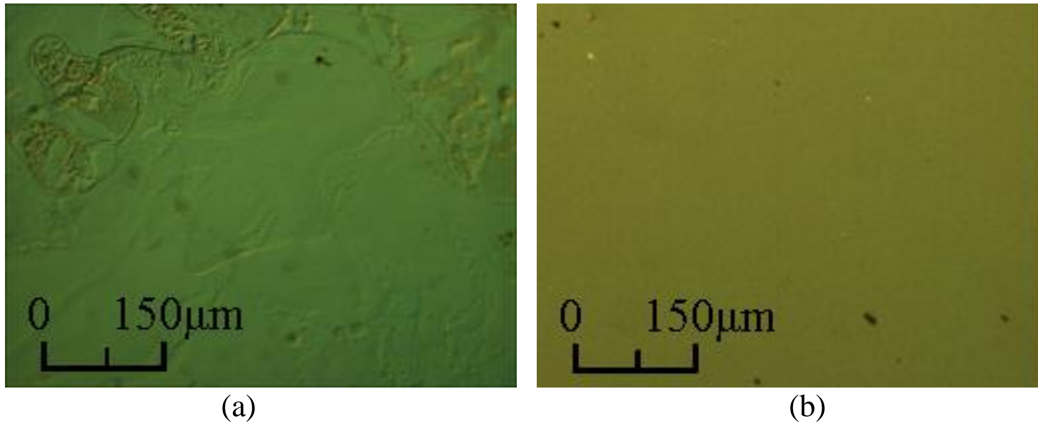

(a) (b)

Fig. 7.18: Nomarski microscope image of (a) the sample with nickel annealed at 800°C (b) the VAID process sample.

7.2.2 SIMS Profile and RBS Spectra

Samples of 5 mm x 5 mm semi-insulating 4H-SiC substrate were used to investigate the phosphorus-doping profiles achieved using the silicidation assisted impurity doping process. Secondary ion mass spectroscopy (SIMS) and Rutherford Backscattering Spectrometry (RBS) were used to physically characterize the doped samples. The phosphorus oxide solution was spun-on the surface at a speed of 1500 rpm using a spin-coater. The samples were then heated for 30 min at 650°C in oxygen to eliminate all traces of the solvent in the dopant solution, leaving a glassy layer containing phosphorus oxide according the procedure explained in Section 6.1.5.1.1. Following the glassification step, a thin nickel layer was deposited on top of the phosphorous oxide layer. RBS analysis (Figure 7.19) on one sample at this stage was completed to approximate the thickness of the two layers on the SiC surface.

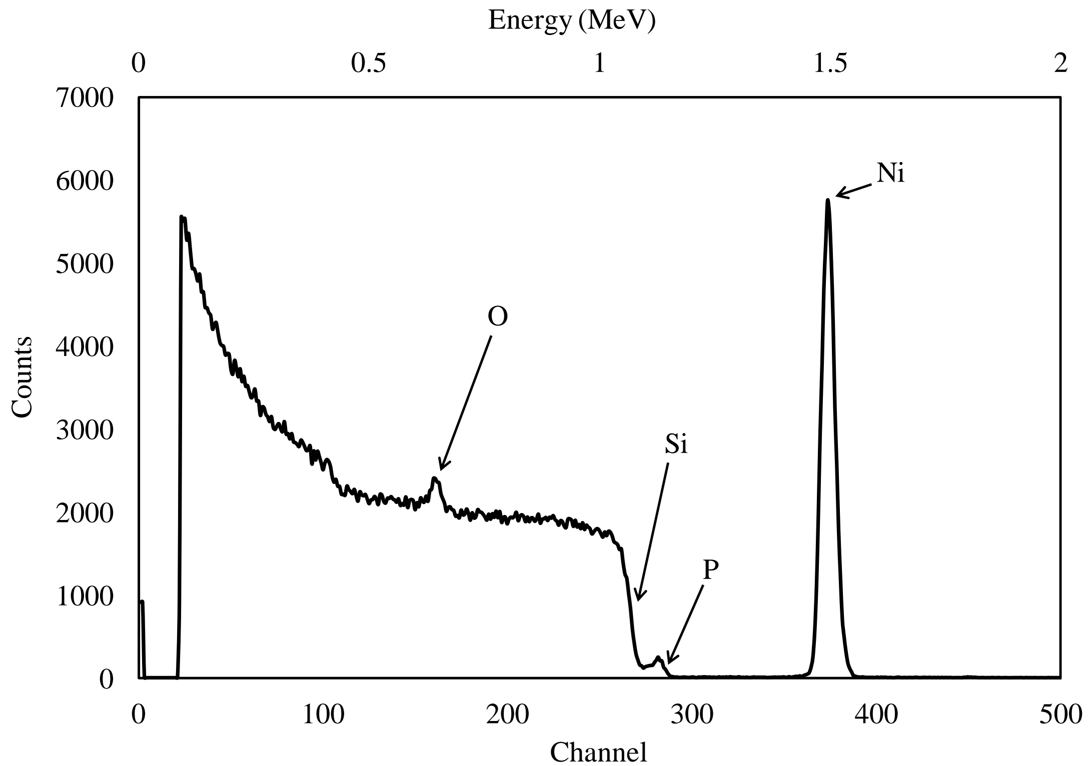

Fig. 7.19: RBS spectrum of the sample with the deposited layer before annealing in argon.

In Figure 7.19, the simulated fit for the RBS spectrum was approximately 25 nm of nickel and approximately 55 nm of the phosphorus oxide glassy layer on top of the SiC substrate. It was noted that nickel is clearly shown as a separate layer. Then three samples were annealed in argon for 1 hr at temperatures of 700°C, 900°C and 1000°C respectively. RBS analyses were conducted at this stage on the three samples. Figures 7.20(a), (b) and (c) show the diffusion of the nickel and phosphorus with SiC.

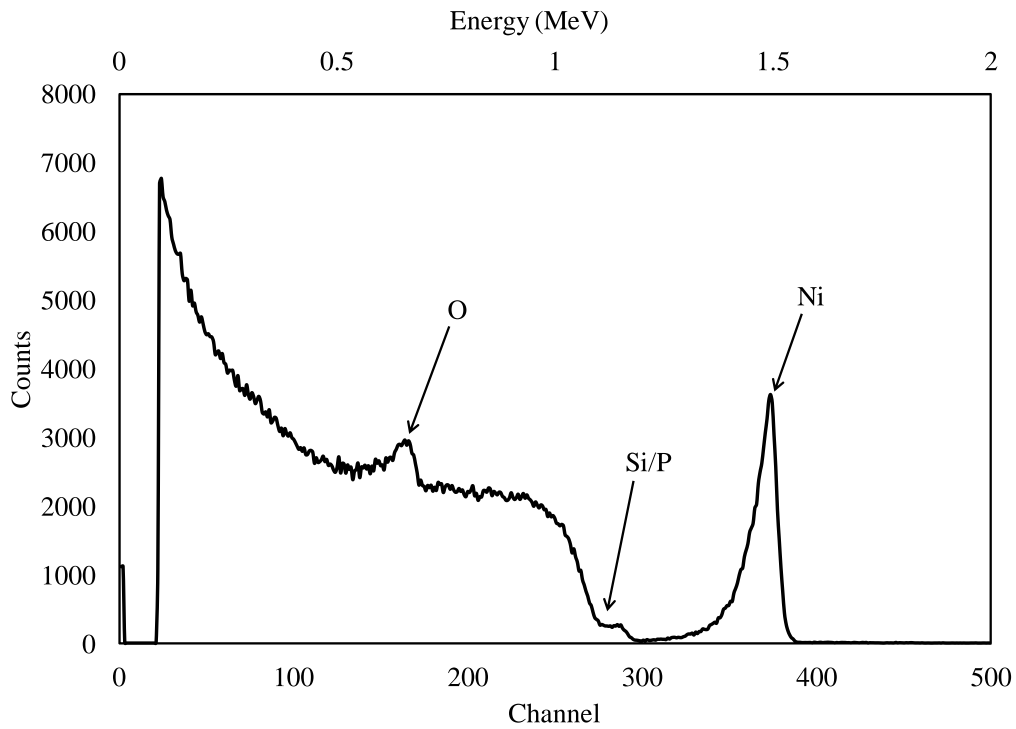

7.20(a)

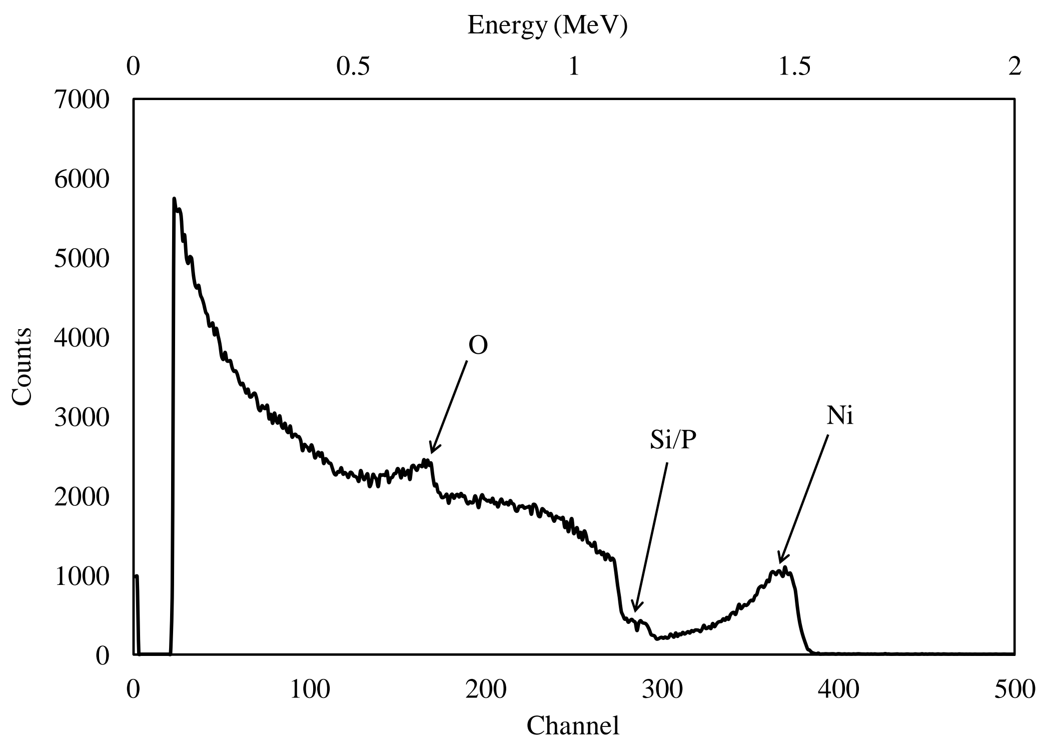

7.20(b)

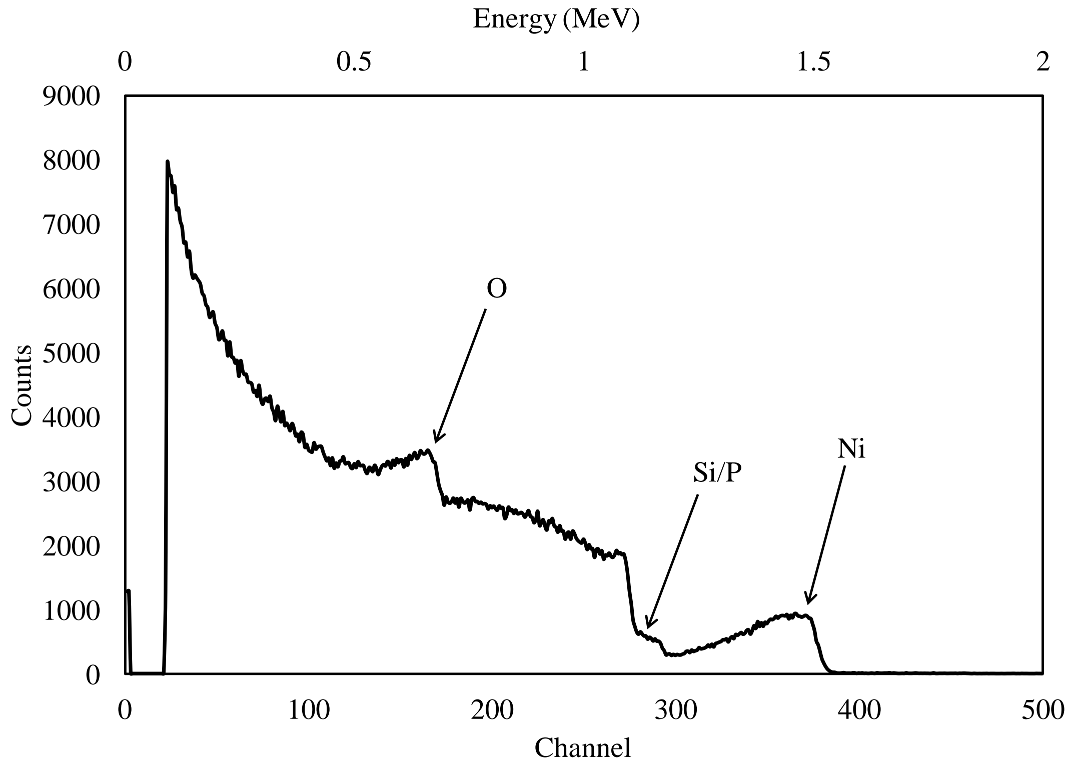

7.20(c)

Fig. 7.20: RBS analysis for the sample with nickel annealed in argon at (a) 700°C (b) 900°C (c) 1000°C.

Figure 7.20 depicts nickel's further diffusion towards the SiC substrate as the temperature increased. The distinctive nickel peak decreased in height and broadened with increasing temperature, which indicated the movement of nickel towards the SiC surface and possibly the formation of Ni_2Si. After RBS analyses, the samples were immersed in BOE to remove the oxide, silicide, and nickel layers. The top layers were easily removed on the samples annealed at 700°C and 900°C, revealing the SiC surface, but it was impossible to remove the top layers from the sample that was annealed at 1000°C. This implied that the Ni atoms diffused too deeply into the SiC to form nickel silicide, which cannot be removed by BOE. Therefore, 900°C was chosen as the annealing temperature to get the maximum number of dopants in without damaging the

surface when using this process. Subsequently, SIMS analysis was performed on the sample with nickel that was annealed at 900°C and the results are shown in Figure 7.21.

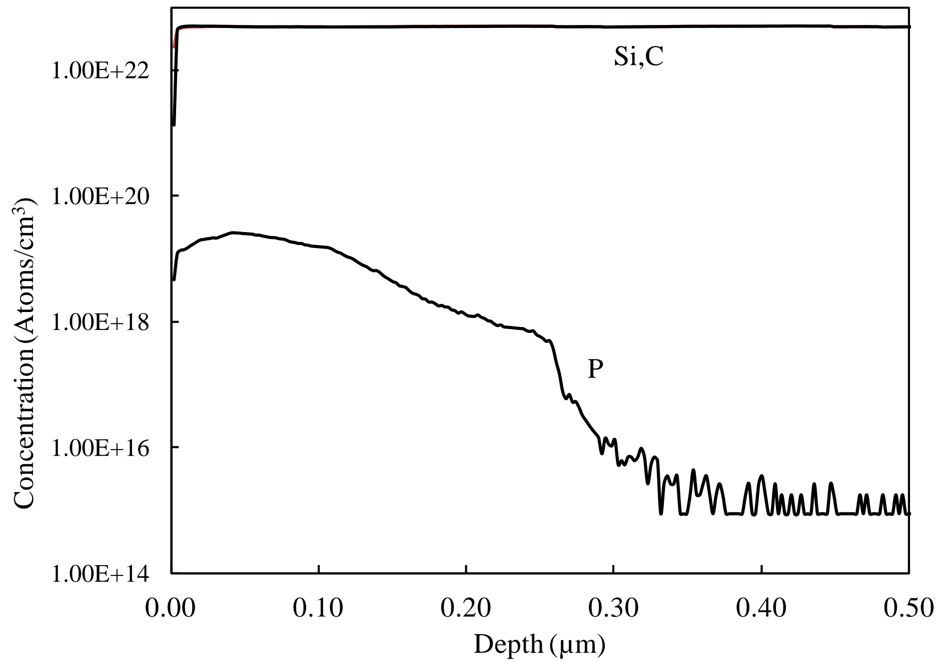

Fig. 7.21: SIMS analysis of the sample with nickel annealed at 900°C.

The phosphorus concentration at the surface of the sample annealed at 900°C was approximately 3 x 10^{19} cm^{-3}. The SIMS diffusion profile showed a phosphorus concentration of 10^{18} cm^{-3} , even past a depth of 0.2 μm, and dropped to 10^{16} cm^{-3} at a depth of 0.3 μm. This is a considerable improvement from the VAID process, in which the diffusion profile drops off steeply to 10^{16} cm^{-3} around a depth of 0.12~0.13 μm, as seen in Figure 7.5. Therefore, a high surface concentration of phosphorus was achieved on 4H-SiC using the silicidation-assisted impurity doping process while diffusing phosphorus deeper than it was when the VAID technique was used. It also explains the doping depth profile obtained from the C-V measurements in Figure 7.17.

7.2.3 Activation of N Implants using Silicidation Assisted Impurity Doping

A nitrogen-implanted p^-/p^+ 4H-SiC sample was used to investigate the activation of implanted ions using the silicidation assisted impurity doping process. The implanted impurity concentration was 4 x 10^{19} cm^{-3}. First, the implanted dopants were activated at 1350°C in argon for 30 min. The phosphorus oxide solution was then spun-on the surface at 1500 rpm using a spin-coater. Afterwards the sample was heated for 30 min at 650°C in oxygen to eliminate all traces of the solvent in the dopant solution, leaving a glassy layer containing phosphorus oxide explained in the procedure in Section 6.1.5.1.1. Following the glassification step, a thin nickel layer was deposited on top of the phosphorus oxide layer. Then the sample was annealed in argon for 1 hr at 900°C. After the annealing step, the sample was immersed in BOE for 5 min to remove all traces of the oxide, silicide and nickel layers that formed on the surface. Next, the sample was photolithographically patterned for the linear transmission line method (LTLM) measurements using the experimental procedure discussed in Section 6.1.7. $Ni_{93\%}V_{7\%}$ was used as the preferred metal for the n-type ohmic contact. The patterning step was followed by a contact anneal at 1000°C in a vacuum for 5 min according to the procedure discussed in Section 6.1.5.2.1. TLM measurements and I-V measurements were then conducted to determine the contact characteristics. Figure 7.22 shows the data from the TLM measurements. The contact resistance (R_c), sheet resistance (R_{sh}) and specific contact resistivity (ρ_c) were calculated using the TLM measurements. Table 7.8 lists R_c, R_{sh} and ρ_c.

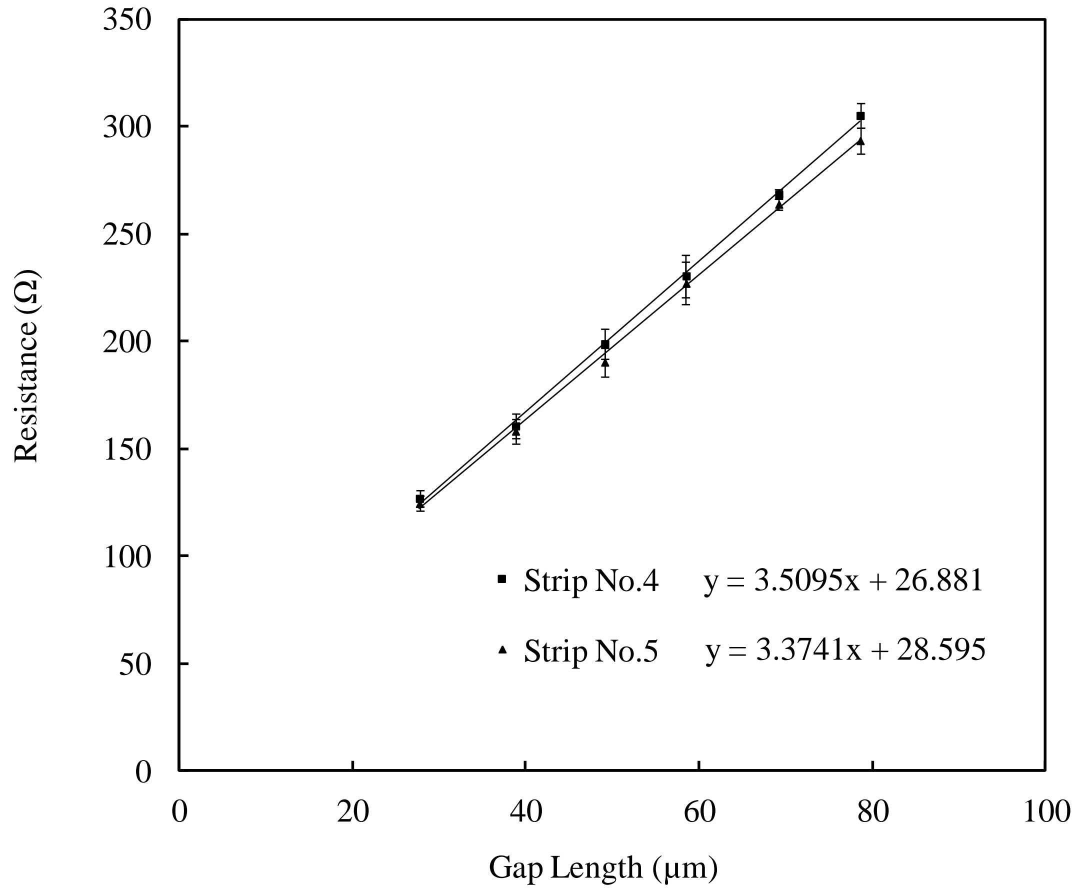

Fig. 7.22: TLM data for 1000°C ohmic anneal.

Table 7.8: R_c, R_{sh} and ρ_c values for ohmic anneal at 1000°C.

Strip number	R_c (Ω)	R_{sh} (Ω/□)	ρ_c (Ωcm^2)
3	16.33	674	1.5×10^{-4}
4	13.46	684	1.0×10^{-4}
5	14.29	657	1.2×10^{-4}
Average	14.69	672	1.2×10^{-4}
Std. deviation	± 1.48	± 14	$\pm 2.5 \times 10^{-5}$

Table 7.8 shows that an average specific contact resistivity value of 1.2 x 10^{-4} Ωcm^2 was obtained using the silicidation assisted doping process on the nitrogen-implanted sample with an ohmic contact anneal of 1000°C. This value was slightly higher than reported specific contact resistivity values for nickel vanadium ohmic contacts [2]. The average contact resistance was 14.69 Ω and the average sheet resistance was 672 Ω/□. Following the TLM measurements, the ohmic contacts were annealed at 1100°C in a vacuum for 5 min and TLM measurements were conducted. Figure 7.23 shows the TLM data and Table 7.9 shows the calculated values for R_c, R_{sh}, and ρ_c. Figure 7.24 shows the I-V characteristic of the contacts between two adjacent pads.

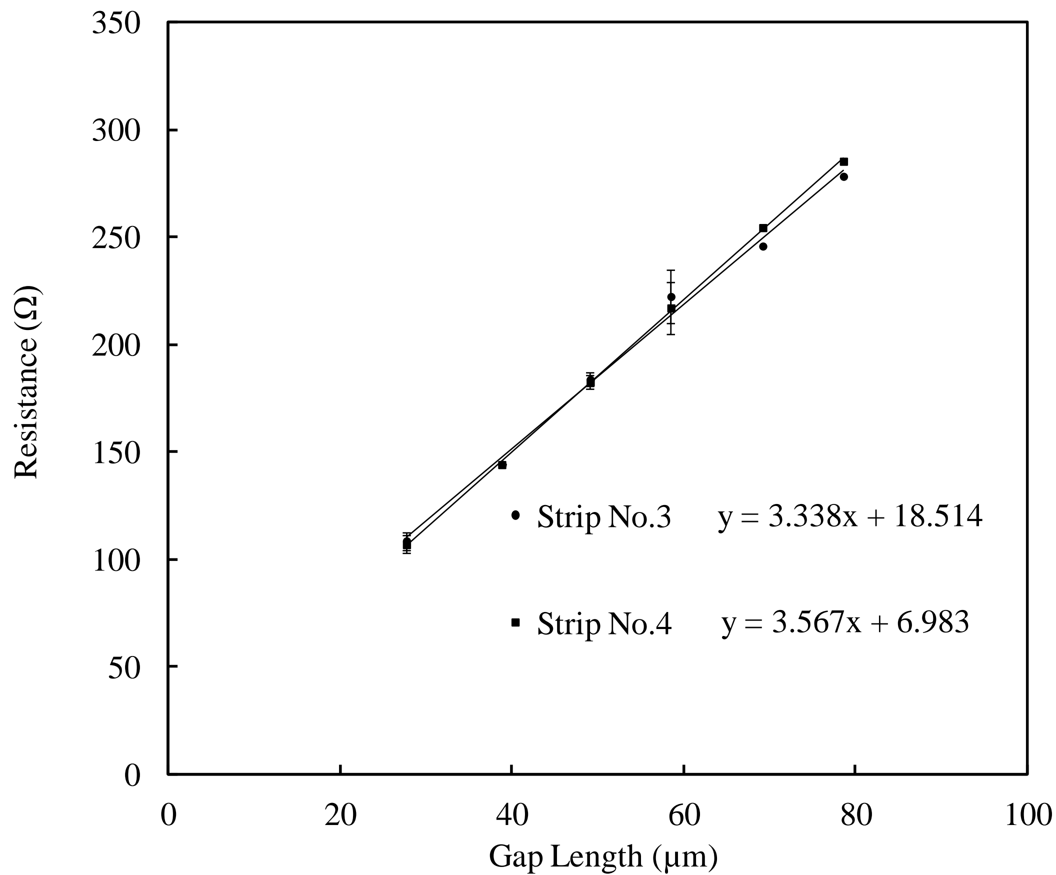

Fig. 7.23: TLM data for 1100°C ohmic anneal.

Table 7.9: R_c, R_{sh} and ρ_c values for the 1100°C ohmic anneal.

Strip number	R_c (Ω)	R_{sh} (Ω/□)	ρ_c (Ωcm²)
3	9.25	650	5.0×10^{-5}
4	3.49	694	6.6×10^{-6}
5	9.63	650	5.4×10^{-5}
Average	7.46	665	3.7×10^{-5}
Std. deviation	± 3.44	± 25	$\pm 2.62 \times 10^{-5}$

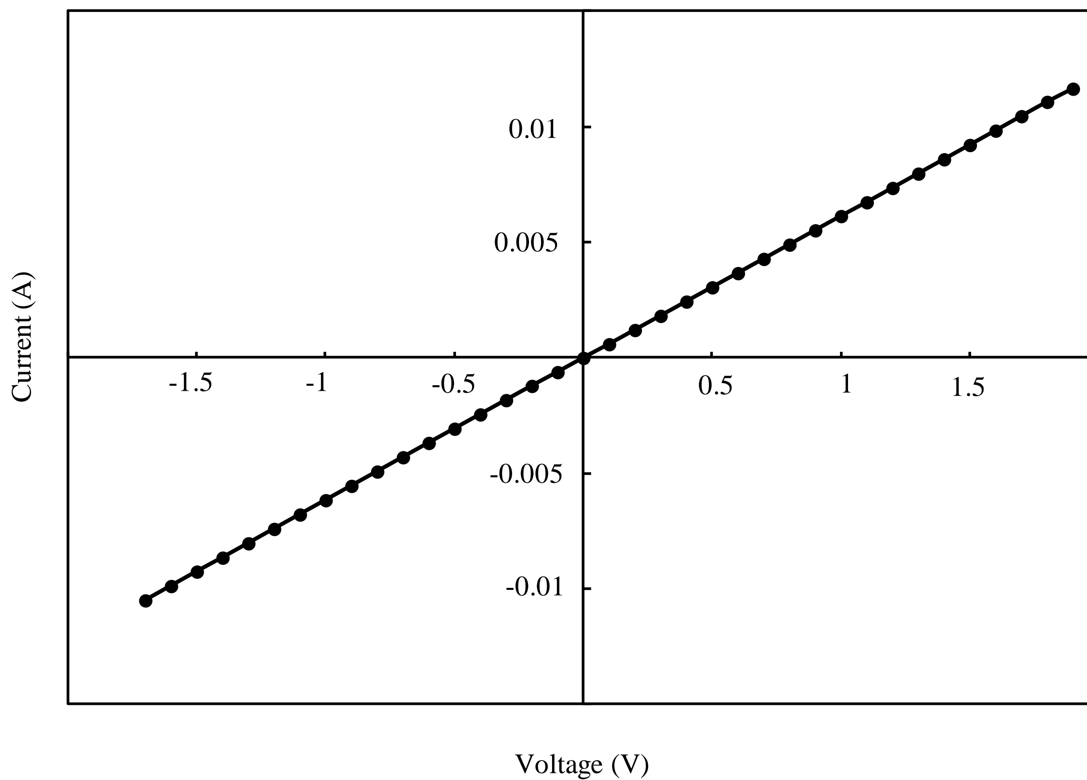

Fig. 7.24: I-V characteristic curve for the $Ni_{93\%}V_{7\%}$ ohmic contacts annealed at 1100°C.

Table 7.9 shows that the average specific contact resistivity was 3.7 x 10^{-5} Ωcm^2 for the ohmic contacts annealed at 1100°C. This value was comparable to previously reported data for nitrogen-implanted samples with activation at high temperatures in excess of 1400°C [2]. The average contact resistance was 7.46 Ω and the average sheet resistance was 665 Ω/□. The I-V characteristic curve in Figure 7.24 confirms the ohmic nature of the contacts. The sample was annealed again at 1200°C in a vacuum for 5 min and TLM measurements were conducted. Figure 7.25 shows the TLM measurements and Table 7.10 shows the calculated values for R_c. R_{sh} and ρ_c.

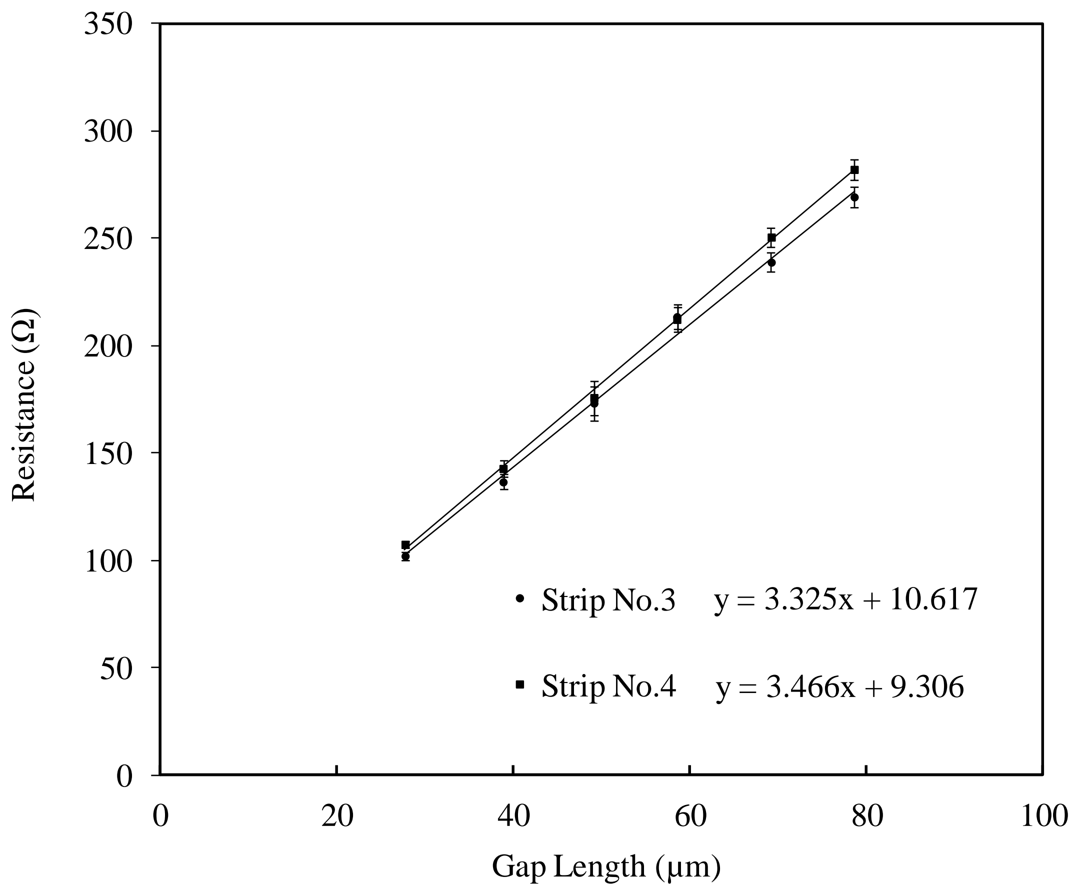

Fig. 7.25: TLM data for 1200°C ohmic anneal.

Table 7.10: R_c, R_{sh} and ρ_c values for the 1200°C ohmic anneal.

Strip number	R_c (Ω)	R_{sh} (Ω/□)	ρ_c (Ωcm^2)
3	5.31	648	1.6 x 10^{-5}
4	4.65	674	1.2 x 10^{-5}
5	5.09	646	1.5 x 10^{-5}
Average	5.02	656	1.5 x 10^{-5}
Std. deviation	± 0.34	± 16	± 2.1 x 10^{-6}

Table 7.10 shows that the average specific contact resistivity was 1.46 x 10^{-5} Ωcm^{2,} which implies that there was no considerable change between the ohmic contact anneals at 1100°C and 1200°C. The average contact resistance was 3.18 Ω and the average sheet resistance was 656 Ω/□, which are comparable to previously reported values for nitrogen-implanted (4 x 10^{19} cm^{-3}) samples activated at higher temperatures.

7.2.4 Ohmic Contact Characterization

Ohmic contacts to n-type 4H-SiC samples were characterized using TLM measurements. Two 5 mm x 5 mm p^-/p^+ 4H-SiC samples were used for the silicidation assisted impurity doping process. The phosphorus oxide solution was spun-on the surface at 1500 rpm using a spin-coater. The samples were then heated for 30 min at 650°C in oxygen to eliminate all traces of the solvent in the dopant solution, leaving a glassy layer containing phosphorus oxide according the procedure in Section 6.1.5.1.1. Following the glassification step, a thin nickel layer was

deposited on top of the phosphorous oxide layer. Then the sample was annealed in argon for 1 hr at 900°C. After the annealing step, the sample was immersed in BOE for 5 min to remove all traces of the oxide, silicide, and nickel layers that formed on the surface. At this stage, EDX analyses were performed on the samples. Figure 7.26 shows the EDX spectra while Table 7.11 lists the weight and atomic percentages of the elements obtained using EDX.

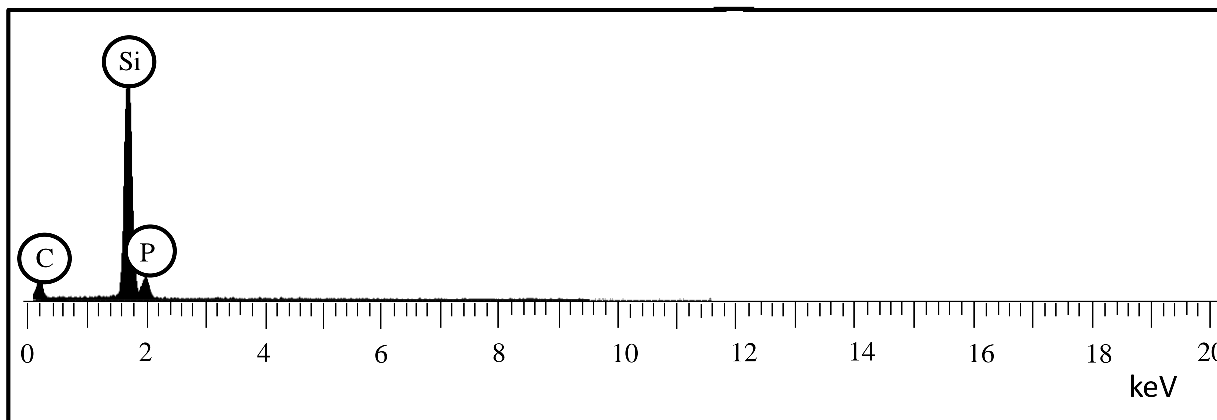

Fig.7.26: EDX spectrum for the sample with nickel annealed at 900°C.

Table 7.11: Atomic percentages of elements obtained using EDX for the sample.

Element	Spectrum 1 (atomic %)	Spectrum 2 (atomic %)	Spectrum 3 (atomic %)	Average (atomic %)
C	56.66	55.59	56.11	56.12 ± 0.54
Si	41.76	42.87	42.40	42.34 ± 0.56
P	1.58	1.53	1.49	1.53 ± 0.05

In Table 7.11, the results for the atomic percentages of phosphorus were approximately 1.5%, which was comparable to the EDX atomic percentages obtained in Section 7.2.1. After the EDX analyses, the two samples were annealed in argon for 30 min at temperatures of 1400°C

and 1500°C. Following the activation step, the samples were photolithographically patterned with $Ni_{93\%}V_{7\%}$ contacts for TLM measurements according to the process discussed in Section 6.1.7. After patterning, ohmic contact anneals were conducted at 1100°C in a vacuum for 5 min. TLM measurements and I-V measurements were carried out to characterize the ohmic contacts. Figure 7.27 shows the TLM data for the two samples and Table 7.12 shows the calculated values for R_c. R_{sh} and ρ_c.

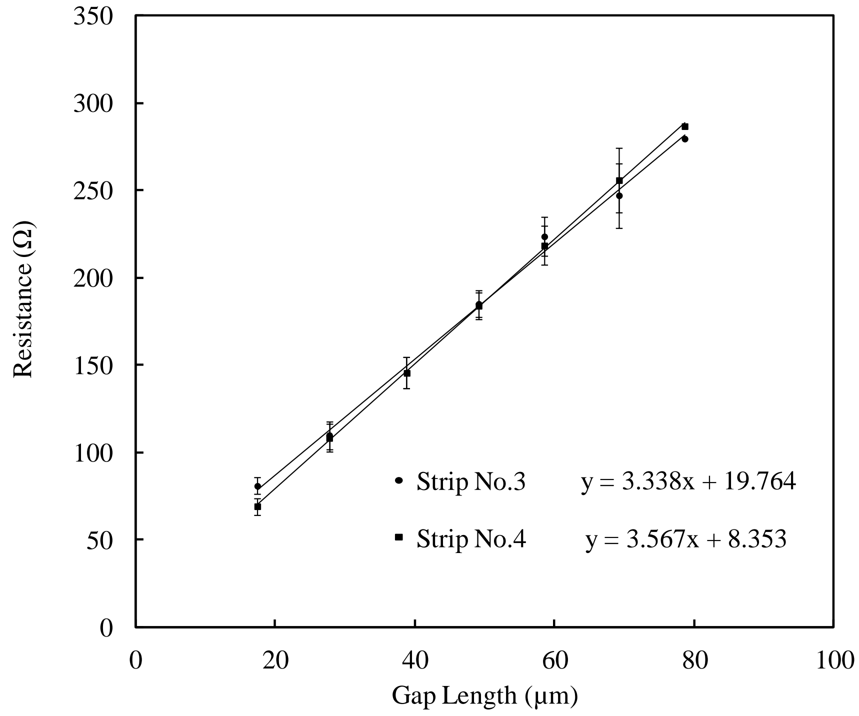

(a)

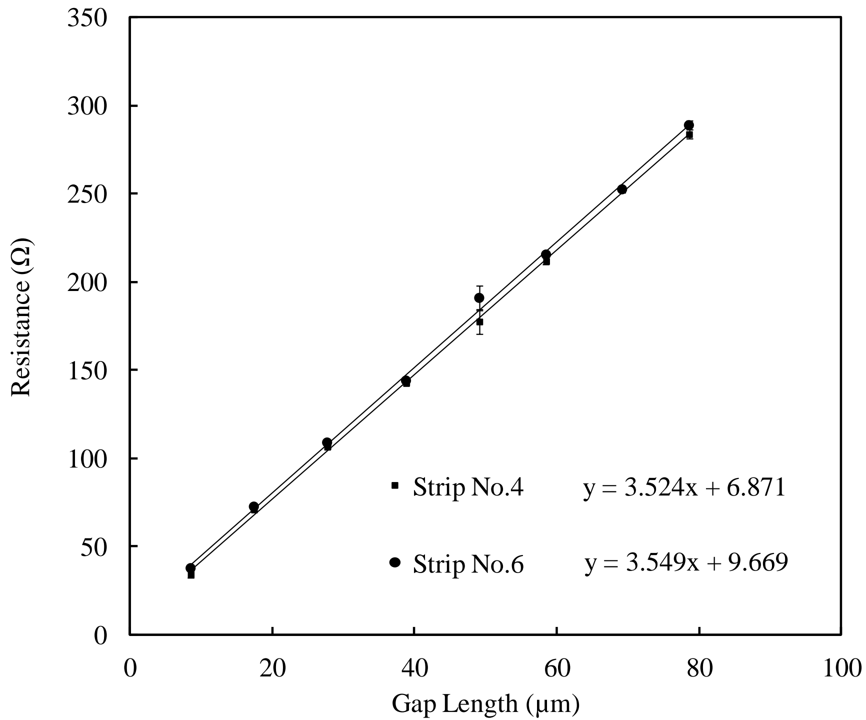

(b)

Fig. 7.27: TLM data for n-type doped sample (a) activated at 1400°C in argon (b) activated at 1500°C in argon.

Table 7.12: R_c, R_{sh} and ρ_c values for the sample (a) activated at 1400°C in argon (b) activated at 1500°C in argon.

Strip number	R_c (Ω)	R_{sh} (Ω/□)	ρ_c (Ωcm^2)
3	9.88	650	5.7×10^{-5}
4	4.18	694	9.5×10^{-6}
5	5.38	679	1.6×10^{-5}
Average	6.48	674	2.7×10^{-5}
Std. deviation	± 3.00	± 22	$\pm 2.6 \times 10^{-5}$

(a)

Strip number	R_c (Ω)	R_{sh} (Ω/□)	ρ_c (Ωcm^2)
3	3.77	682	7.9×10^{-6}
4	3.44	686	6.5×10^{-6}
5	3.82	684	8.1×10^{-6}
6	4.83	691	1.3×10^{-5}
Average	3.97	686	8.8×10^{-5}
Std. deviation	± 0.60	± 4	$\pm 2.8 \times 10^{-6}$

(b)

In Table 7.12(a), the sample activated at 1400°C had an average specific contact resistivity of 2.7×10^{-5} Ωcm^2. The average contact resistance for the sample was 6.08 Ω and the average sheet resistance was 656 Ω/□. The sample activated at 1400°C from Table 7.12(b) showed an average specific contact resistivity of 8.8×10^{-6} Ωcm^2. The average contact resistance for the sample was 3.97 Ω and the average sheet resistance was 686 Ω/□. The values for specific

contact resistivity were comparable to $Ni_{93\%}V_{7\%}$ ohmic contacts to a nitrogen-implanted sample with an implant concentration of 1 x 10^{20} Ωcm^2 activated at 1450°C [2].

I-V measurements were conducted on the samples to confirm the ohmic nature of the contacts, using probes connected to adjacent contact pads on the top surface of the sample. In Figures 7.28(a) and (b), both samples showed ohmic characteristics. These measurements were also taken on the samples from top to bottom to confirm the presence of a p-n junction. Figures 7.29(a) and (b) show the I-V characteristics of the p-n junctions. Figure 7.30 shows the blue light emitting diode (LED) fabricated by silicidation assisted impurity doping process.

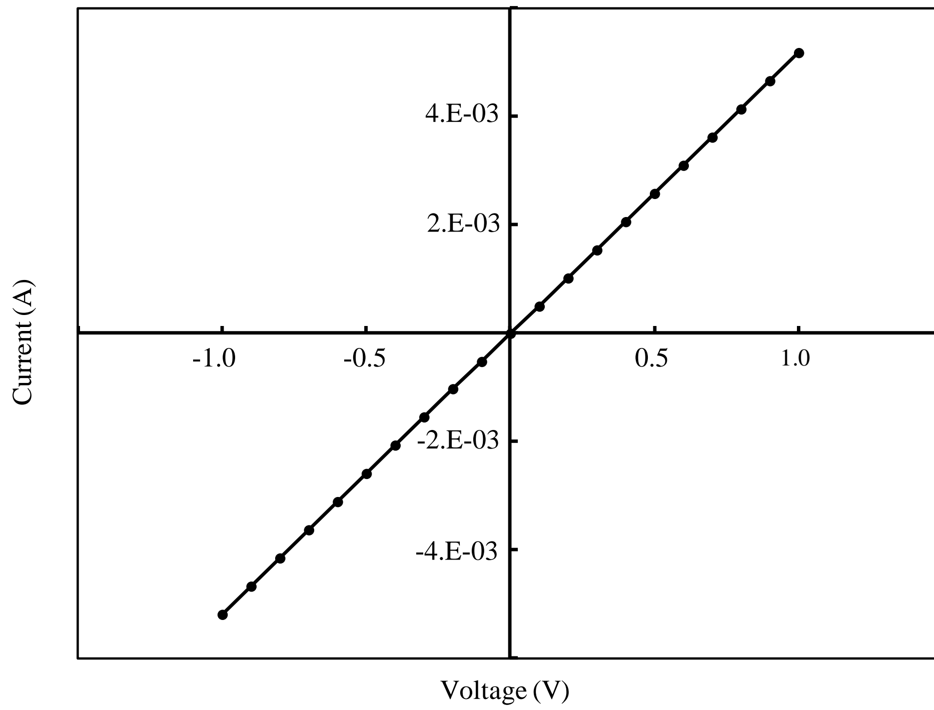

(a)

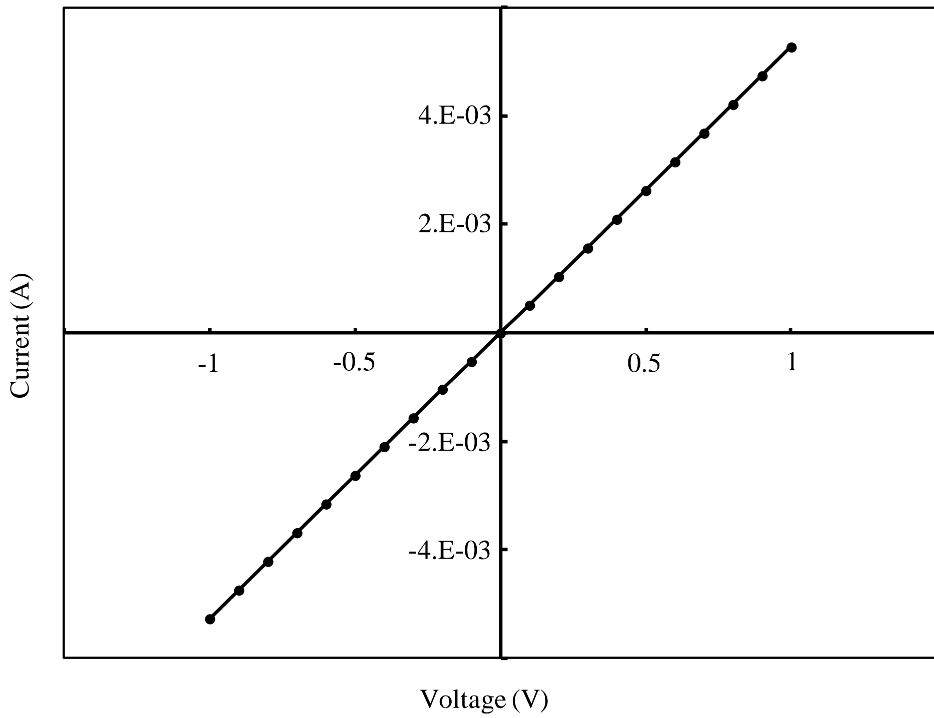

(b)

Fig. 7.28: I-V characteristics of the top surface for the sample (a) activated at 1400°C (b) activated at 1500°C.

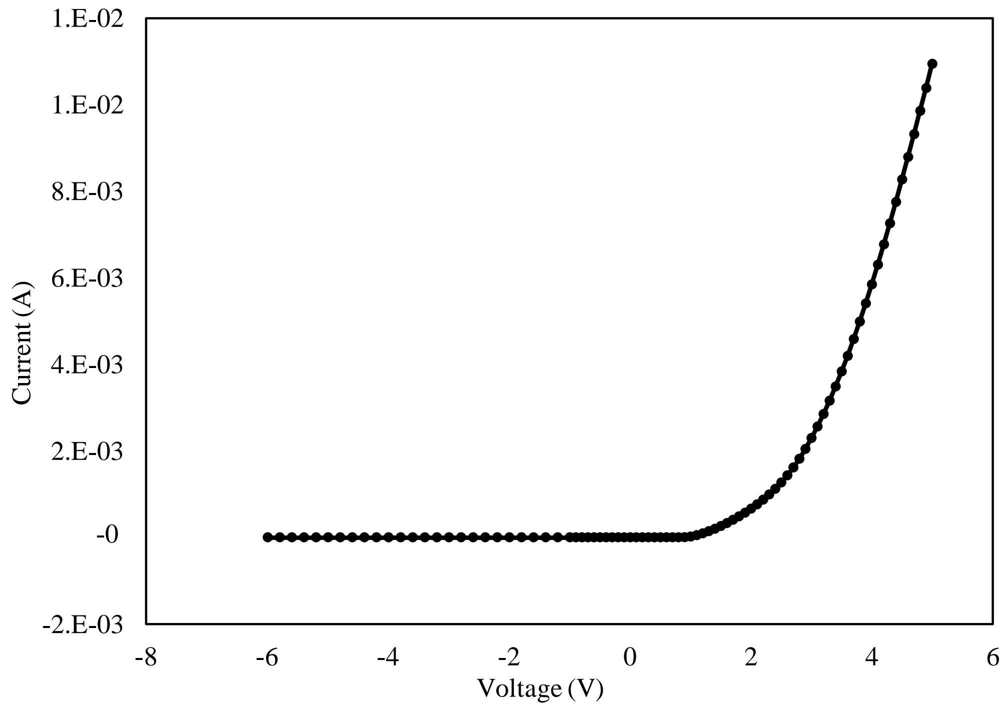

(a)

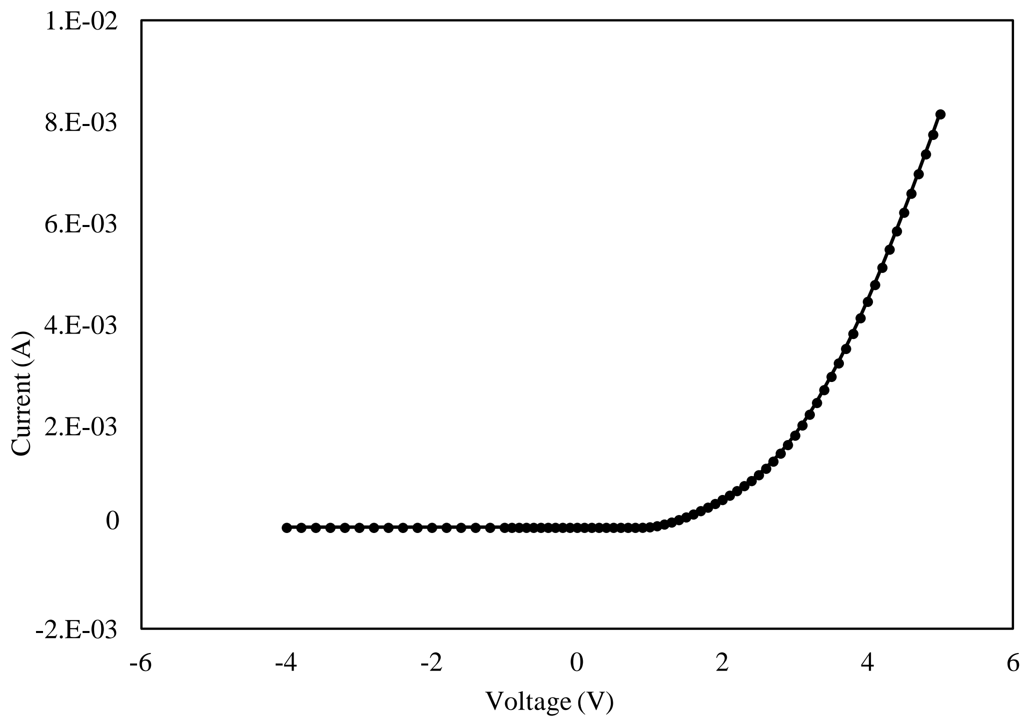

(b)

Fig. 7.29: p-n junction I-V characteristics for the sample (a) activated at 1400°C (b) activated at 1500°C.

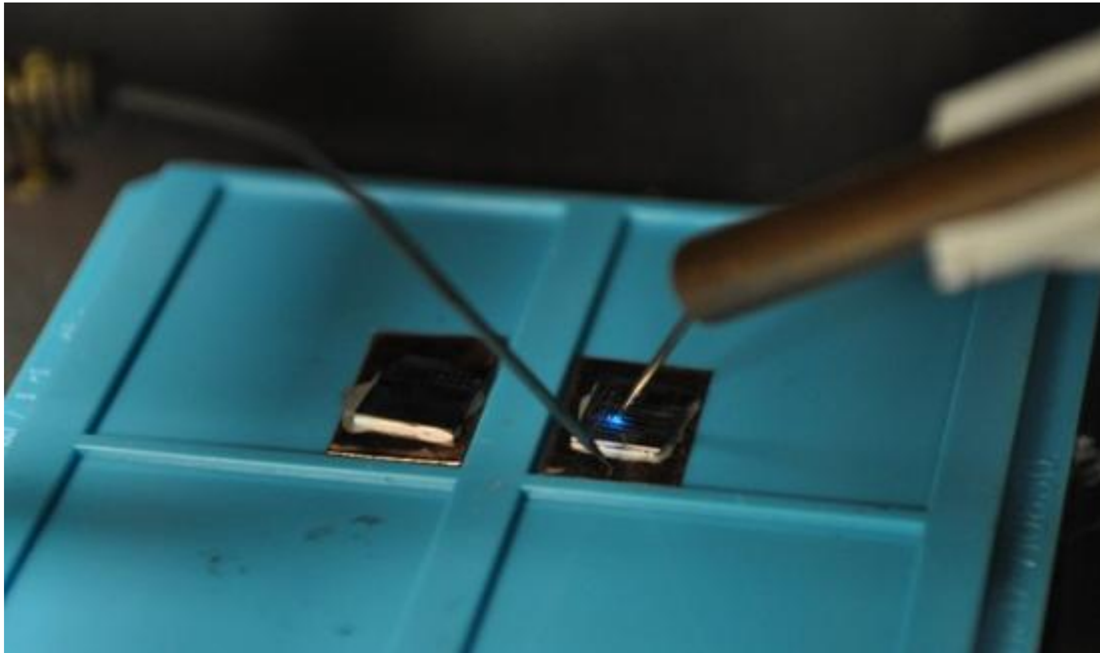

Fig. 7.30: Fabricated blue LED using silicidation assisted impurity doping technique.

7.3 Electroless Nickel Plating for Ohmic Contacts

Ni:P was plated onto the SiC sample and patterned for TLM measurements to characterize the contacts. The experimental procedure from electroless plating of nickel to patterning of contacts for TLM structures is discussed in detail in Section 6.1.5.1.2. After patterning the contacts, ohmic anneals were carried out in a vacuum for 5 min at temperatures of 1000°C and 1100°C.

Electron dispersive X-ray (EDX) spectroscopy was carried out on the sample after plating the Ni:P layer to characterize the weight and atomic percentages of the elements present. Figure 7.31 shows the EDX spectrum while Table 7.13 shows the weight and atomic percentages for the elements present in the surface region of the sample.

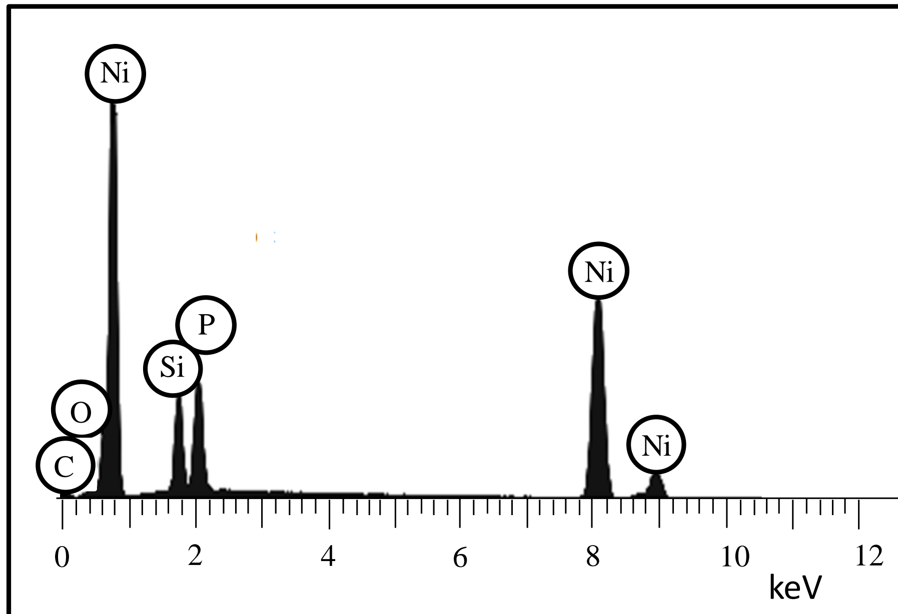

Fig. 7.31: EDX spectrum of an as-plated 4H-SiC sample.

Table 7.13: Surface composition of the 4H-SiC sample, as-plated and after anneal

Element	Atomic% (as-plated)	Atomic % (annealed at 1100°C)
C	14.18	31.20
SI	14.12	21.99
O	2.16	0
P	15.67	8.06
Ni	53.86	39.75

Table 7.13 shows that Si and C were from the substrate since they were about equal atomic percentages, but phosphorus appeared at a high concentration in the Ni:P layer, with atomic percentages of 15.67 before annealing and 8.06 afterwards. Rutherford backscattering

spectroscopy (RBS) analyses (Figure 7.32) were carried out on the samples to determine the composition as well as the depth profile of the nickel and phosphorus atoms in the deposited Ni:P layer before and after an ohmic anneal at 1000°C in vacuum for 5 min.

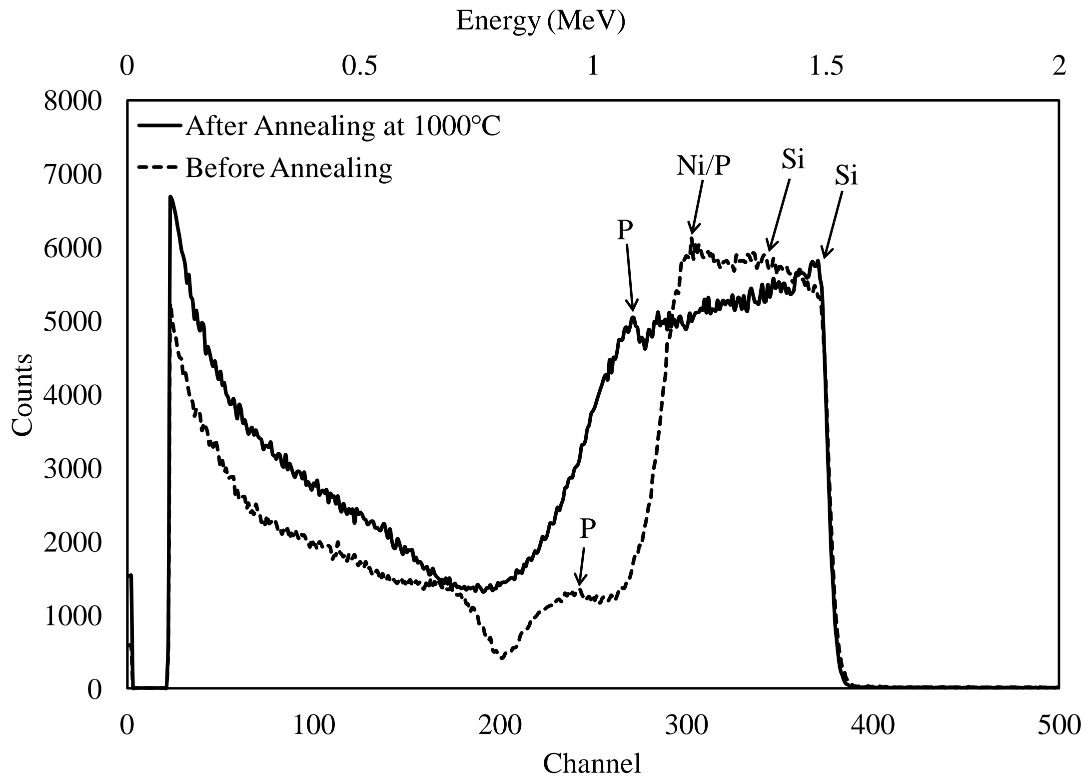

Fig. 7.32: RBS spectra of a Ni:P plated sample before and after annealing at 1000°C.

As seen in the RBS spectra, after annealing at 1000°C, the Ni:P alloyed with the SiC with significant diffusion of Ni into the SiC substrate, as well as outdiffusion of Si from the SiC substrate into the Ni:P layer. The RBS results also showed a rough interface between the Ni:P layer and the SiC substrate in the as-plated sample before annealing [4]. Figure 7.33 shows the I-V of a sample after annealing at 1000°C and 1100°C. The I-V curve after the anneal at 1000°C is slightly nonlinear. This could be due to interfacial contaminants, such as oxide from the

annealing, and ions from the plating solution. After further annealing at 1100°C in a vacuum for 5 min, the I-V data showed ohmic characteristics.

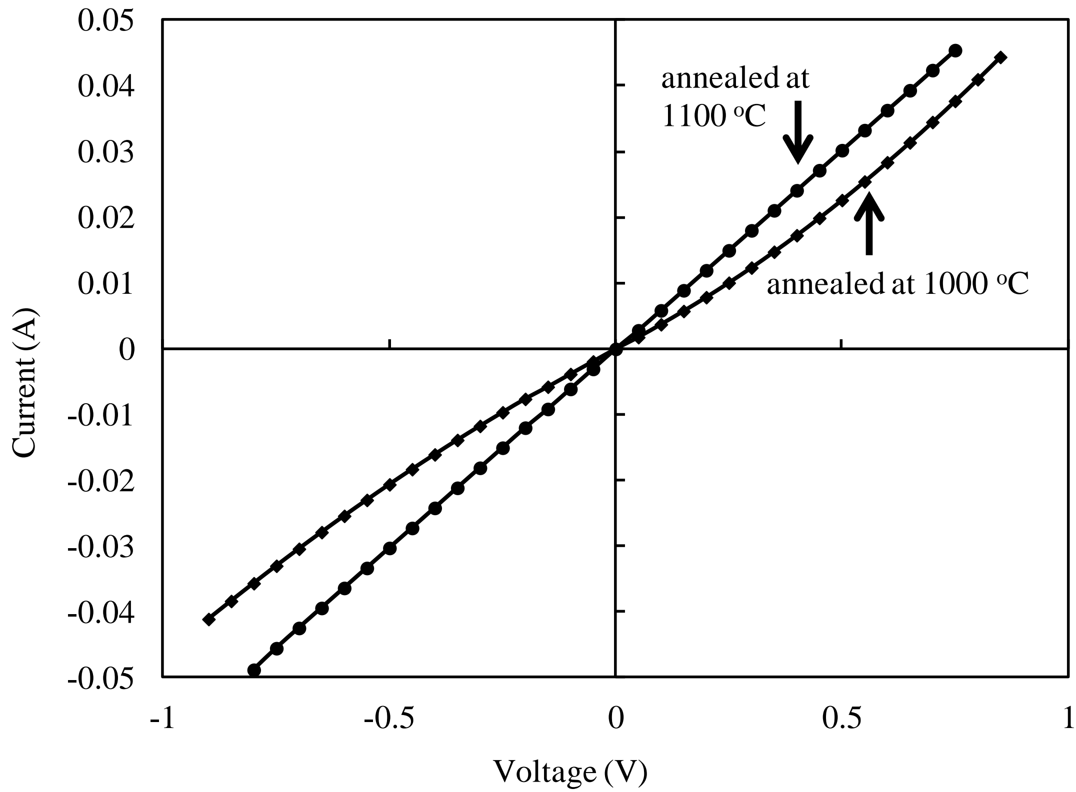

Fig. 7.33: I-V data for the sample annealed at 1000°C and 1100°C.

The sample patterned photolithographically for TLM structures was used to characterize the ohmic contacts. Figures 7.34(a) and (b) show the TLM data for the sample annealed at 1000°C and 1100°C respectively. Tables 7.14(a) and (b) show the calculated values for R_c. R_{sh} and ρ_c.

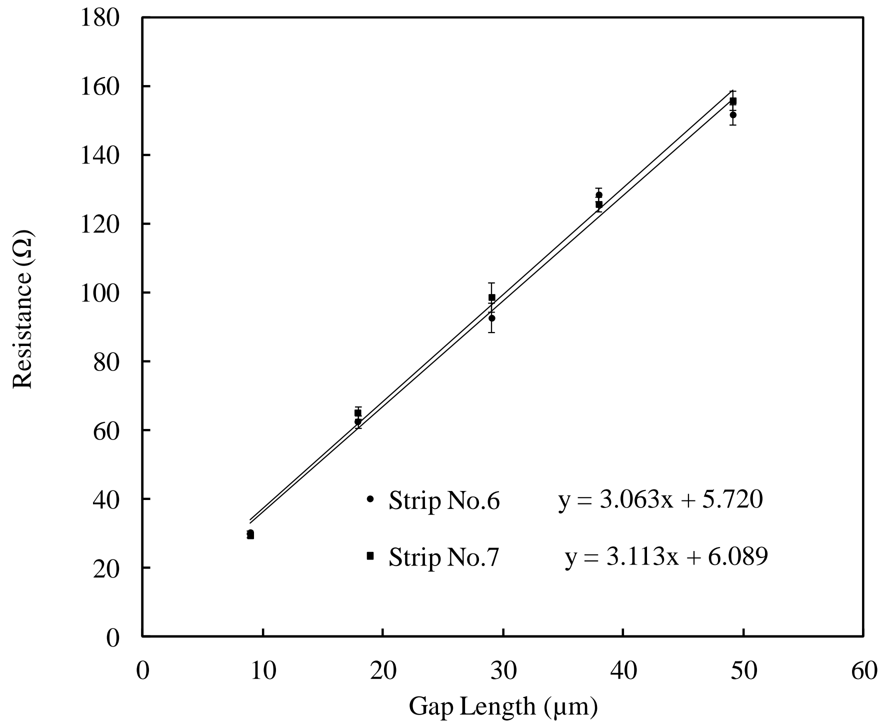

(a)

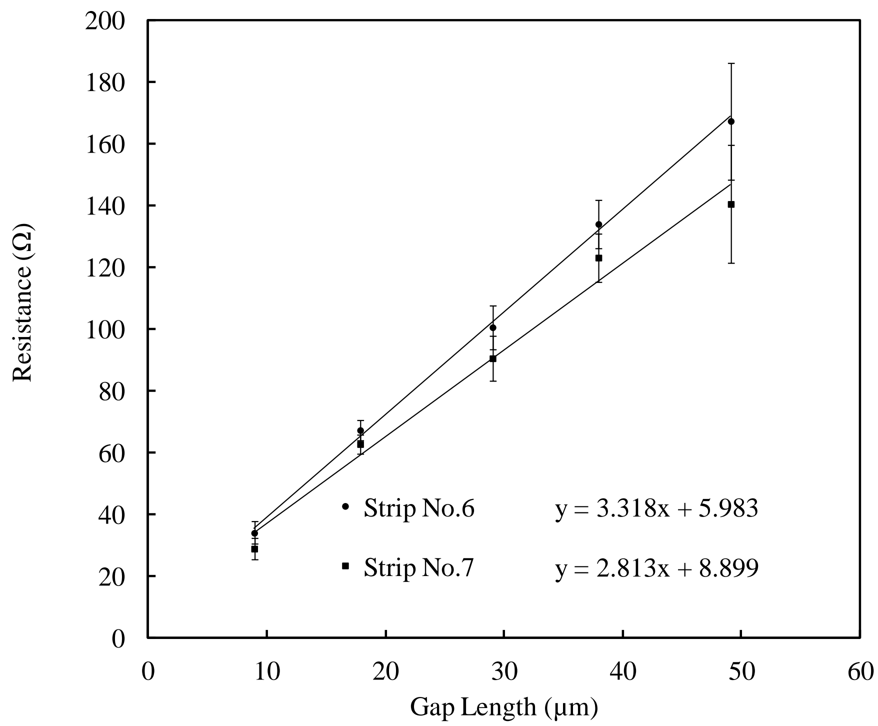

(b)

Fig. 7.34: TLM data plated sample (a) annealed at 1000°C (b) annealed at 1100°C.

Table 7.14: R_c, R_{sh} and ρ_c values for the sample (a) annealed at 1000°C (b) annealed at 1100°C.

Strip number	R_c (Ω)	R_{sh} (Ω/□)	ρ_c (Ωcm^2)
6	2.86	597	5.2×10^{-6}
7	3.04	607	5.8×10^{-6}
Average	2.95	602	5.5×10^{-6}
Std. deviation	± 0.13	± 7	$\pm 4.2 \times 10^{-7}$

(a)

Strip number	R_c (Ω)	R_{sh} (Ω/□)	ρ_c (Ωcm^2)
6	2.98	643	5.2×10^{-6}
7	4.45	546	1.4×10^{-5}
Average	3.72	595	9.4×10^{-6}
Std. deviation	± 1.04	± 69	$\pm 6.2 \times 10^{-6}$

(b)

The sample annealed at 1000°C had an average specific contact resistivity of 5.5×10^{-6} Ωcm^2. After annealing at 1100°C, the value increased to 9.4×10^{-6} Ωcm^2. The values of the specific contact resistivity were comparable to other published values of Ni-based ohmic contacts on SiC. However, it should be noted that the values reported here were obtained on lightly doped epilayers with carrier concentration of about 10^{16} cm^{-3}. Usually, such samples would require ion implantation to reduce contact resistance.

The results show that by intentionally creating vacancies through silicidation of nickel at the interface, it is possible to introduce phosphorus into the substrate and thus produce ohmic contacts. Some problems were encountered with electroless nickel plating in the form of

adhesion and selective area deposition. Adhesion could be improved by first annealing at about 800°C, or lower, for a few minutes before replating to increase thickness. Because of this annealing step, the fabrication of the contact pads requires RIE to remove residual nickel (or nickel silicide) from areas outside the contact pads.

7.4 References

1. S. P. Mendis and C.C. Tin, *Mater. Res. Soc. Symp. Proc.* **1246**, B07 (2010).

2. M. Li, *Ohmic Contacts to Implanted (0001) 4H-SiC*, Dissertation, Department of Physics, Auburn University (2009).

3. C. S. Lim, H. Nickel, A. Naoumidis and E Gyarmati, *J. Mater. Sci.* **32**, 6567 (1997).

4. S. P. Mendis, C. C. Tin, M. T. Tin, T. Isaacs-Smith, E. R. Crandall, "Electroless Nickel for n-type contact on 4H-SiC", *Mater. Sci. Forum* 2011 – in press.

Chapter 8

Conclusions and Future Work

8.1 Conclusions

This work presents new processes for efficient doping of SiC. The vacancy assisted impurity doping (VAID) and the silicidation assisted version of VAID were used to incorporate phosphorus into 4H-SiC. The thermodynamic basis for both processes were discussed using Gibb's free energy considerations and ternary phase diagrams of stability. Schottky and ohmic contacts to n-type 4H-SiC were characterized by electrical measurements. SIMS, EDX, and RBS analyses were used to physically characterize the surface composition of the doped samples.

Thermodynamic data were analyzed to confirm the possibility of phosphorus oxide decomposing SiC at the interface. The stability and formation of nickel silicides were thoroughly investigated for the silicidation assisted VAID technique and Ni_2Si formation was recognized as a catalyst for the impurity doping process, facilitating the mechanism by creating silicon vacancies.

SIMS analysis showed a phosphorus concentration in the range of 10^{19} cm^{-3} at the surface for the VAID process of annealing temperatures of $1200^{o}C$ and $1400^{o}C$, which is a sufficiently high doping concentration for the fabrication of ohmic contacts. For the silicidation assisted VAID process, SIMS results indicated phosphorus concentrations in the range of 10^{19} cm^{-3} going approximately 0.2 μm deeper than in the VAID process without nickel, with even lower annealing temperature at only $900^{o}C$. EDX analyses confirmed the presence of phosphorus with

atomic percentages of approximately 0.5% and 1.5%, respectively, for the VAID process and the silicidation assisted impurity doping process.

LTLM measurements were conducted on ohmic contacts fabricated using the VAID technique to confirm the high doping concentrations achieved by SIMS. High doping concentration in the range of 10^{18} ~ 10^{19} cm^{-3} is known to produce specific contact resistivity in the range of 10^{-5}–10^{-6} Ωcm^2. Electrical measurements revealed the possibility of reliable $Ni_{93\%}V_{7\%}$ ohmic contacts on n-type 4H-SiC using the two processes. TLM results showed specific contact resistivity values in the range of 10^{-5}–10^{-6} Ωcm^2, which was comparable to other published values for Ni ohmic contacts. Electroless nickel plating was used to form ohmic contacts on lightly doped n-type 4H-SiC and specific contact resistivity value of 5 x 10^{-6} Ωcm^2 was achieved. Due to its better adherence to the rough, back surface of the n-type substrate, it can be concluded that electroless nickel plating is a convenient method for broad area ohmic contact formation on the highly doped layer at the back of a sample.

In conclusion, significant progress has been made in lowering the temperature required for phosphorus thermal diffusion in 4H-SiC. The results show that by intentionally creating vacancies by using either the favorable thermodynamics of the oxidation or the silicidation of nickel at the interface, it is possible to introduce phosphorus into the substrate at high concentrations. Phosphorus atoms are expected to occupy the silicon vacancies, which increases the doping level in the surface region. Also, in the reaction of nickel with SiC, Si and C vacancies [1] and carbon clusters are created at the interface. The effect of the carbon clusters in this case is not understood, although some studies demonstrate that interfacial carbon helps in creating ohmic contacts between nickel and SiC [2,3].

8.2 Future Work

A more detailed study of the vacancy creation mechanisms is needed to completely understand the diffusion of phosphorus during the VAID process. A similar study of boron doping using the VAID process and the silicidation assisted version of VAID could be conducted using the same experiments used as this study. In addition to doping SiC with phosphorus and boron using the VAID process, other dopants can also be investigated in terms of thermodynamically favorable compounds. Other metals which form silicides with SiC can also be investigated on the basis of the silicidation assisted version of the VAID technique. Also, selective doping of SiC could be investigated using these two processes to fabricate devices such as MOSFETs.

The experimental VAID process and the silicidation version are significant achievements in the field of silicon carbide doping. The fact that the silicidation assisted impurity doping process can incorporate phosphorus in silicon carbide at a temperature as low as 900°C is especially significant when considering the current methods of doping and the high, restrictive temperature ranges involved. If perfected and further developed, this process has the potential to drastically reduce the processing cost of silicon carbide material and devices, which could lead to silicon carbide becoming a mainstream semiconductor material within the next decade.

8.3 References

1. I. P. Nikita, K. V. Vassilevski, N. G. Wright, A. B. Horsfall, A. G. O'Neill and C. M. Johnson, *J. Appl. Phys.* **97**, 083709 (2005).

2. W. Lu, W. C. Mitchel, G. R. Landis, T. R. Crenshaw and W. E. Collins, *Solid State Electron.* **47**, 2001 (2003).

3. M.G. Rastegaeva, A.N. Andreev, A.A. Petrov, A.I. Babanin, M.A. Yagovkina and I.P. Nikita, *Mater. Sci. Eng.* **B46**, 254 (1997).